MEASUREMENT OF THE STRANGE QUARK CONTRIBUTION TO THE VECTOR STRUCTURE OF THE PROTON

A Dissertation

Presented to

The Faculty of the Department of Physics

The College of William and Mary in Virginia

In Partial Fulfillment

Of the Requirements for the Degree of

Doctor of Philosophy

by

Sarah Katherine Phillips

2007

APPROVAL SHEET

This dissertation is submitted in partial fulfillment of

the requirements for the degree of

Doctor of Philosophy

Sarah Katherine Phillips

Approved by the Committee, November 2007

Professor David Armstrong, Physics
The College of William and Mary
Committee Co-chair

Associate Director Allison Lung, 12 GeV
Upgrade Project
Jefferson Lab
Committee Co-chair

Professor Marc Sher, Physics
The College of William and Mary

Assistant Professor Jeffrey Nelson, Physics
The College of William and Mary

Assistant Professor Kent Paschke, Physics
University of Virginia

ABSTRACT

The goal of the G^0 experiment is to determine the contribution of the strange quarks in the quark-antiquark sea to the structure of the nucleon. To this end, the experiment measured parity-violating asymmetries from elastic electron-proton scattering from $0.12 \leq Q^2 \leq 1.0$ (GeV/c)^2 at Thomas Jefferson National Accelerator Facility. These asymmetries come from the interference of the electromagnetic and neutral weak interactions, and are sensitive to the strange quark contributions in the proton. The results from the forward-angle measurement, the linear combination of the strange electric and magnetic form factors $G_E^s + \eta G_M^s$, suggest possible non-zero, Q^2 dependent, strange quark contributions and provide new information to understand the magnitude of the contributions. This dissertation presents the analysis and results of the forward-angle measurement.

In addition, the G^0 experiment measured the beam-normal single-spin asymmetry in the elastic scattering of transversely polarized 3 GeV electrons from unpolarized protons at $Q^2 = 0.15, 0.25$ (GeV/c)^2 as part of the forward-angle measurement. The transverse asymmetry provides a direct probe of the imaginary component of the two-photon exchange amplitude, the complete description of which is important in the interpretation of data from precision electron-scattering experiments. The results of the measurement indicate that calculations using solely the elastic nucleon intermediate state are insufficient and generally agree with calculations that include significant inelastic hadronic intermediate state contributions. This dissertation presents the analysis and results of this measurement.

Dedicated to the loving memory of my father
Paul Timothy Phillips II
1941 - 2004
and my grandfather
Josiah R. Gordon
1906 - 1997

ACKNOWLEDGMENTS

No one makes it through the long journey known as graduate school without the support and guidance of many other people, making me very aware of how woefully inadequate an acknowledgement section must be, especially if it is to have brevity and wit. I know that I cannot thank them all here, but there are so many in the G^0 Collaboration, Thomas Jefferson National Accelerator Facility and The College of William and Mary to whom I am indebted.

I would like to extend thanks to David Armstrong, whose excellent guidance and support inspired me throughout graduate school, and Allison Lung, who always encouraged me to do my best. David especially deserves to be thanked for his laughter when I came up with brilliant ideas like a pop-up dissertation and when I had originally entitled the last chapter of this dissertation "Omphaloskepsis".

Paul King and Julie Roche deserve the deepest gratitude, not just for guiding my analysis every step of the way, but for their friendship. I want to thank Dave Gaskell and Damon Spayde for their guidance in the polarization analysis, as we as for all the interesting physics discussions we would have. On that note, Jeff Martin and Klaus Grimm also always made shifts more fun with the discussions on physics and everything else. Steve Wells deserves thanks for his insightful thoughts about the transverse analysis. I also had a wonderful time sharing an office with the brilliant ladies of Hall C: Julie Roche, Tanja Horn, and Vipuli Dharmawardane.

I am indebted as well to my fellow G^0 graduate students, as we survived all those long night shifts and fighting with our analysis code together. We were quite a group: Jianglai Liu, who always cheerfully helped whenever I broke my code, Benoit Guillon, who always had such wonderful stories of life in France, Lars Hannelius, whose thoughtful discussions were always fun, and Kazutaka Nakahara, who knows in his heart that it will be me that takes over the world, not him. We all envied Jeff Secrest, Silviu Covrig, and Guillame Batigne, who managed to graduate a little ahead of us. May the G^0 backward angle students find such friendship.

I also had fun with graduate students and postdocs from the other halls and other experiments. I have fond memories of Ameya Kolarkar trying to get a decent photograph of Mark Dalton, Claire Gray and I during a Jefferson Lab Run-Around, Lisa Kaufman and I on shifts for HAPPEx, and Peter Monaghan trying to brainstorm the next Graduate Student Association event. I cherish the adventures I had while at conferences like an APS one I spent traveling in Colorado with Itaru Nakagawa, Sean Stave and Kazutaka Nakahara, a Gordon Conference in Maine with Vince Sulkosky, and a DNP Fall Meeting in Nashville, Tennessee with Matt Bellis and Ameya Kolarkar.

There are many people in Hall C and in the G0 Collaboration that have shared of their experience with me; who can forget sailing with Greg Smith, Herbert Bruer's lessons about detectors, Mark Pitt's lessons about the electron beam, Bill Vulcan's lessons about everything, Walter Kellner's and Joe Beaufait's abilities to make whatever I had dragged in work right, Serge Kox's favorite tabloids that he brought in to entertain the shift crew, the stories and medals from the latest race Jacques had run in, the never-ending kindnesses of Debbie Magaldi and the public relations people (and especially their endless help while I was part of the Quantum Diaries), Des Ramsay's and Larry Lee's humorous tales of physics adventures, Argentine tango lessons with Gary Rutledge, the magic of Steve Suhring's fiddle at a contradance, or the watching of a perfectly exquisite dawn with Hamlet Mkrtchyan after a quiet overnight shift?

My time at Jefferson Lab was further enriched by the opportunity to reign as the Empress of the Graduate Student Organization (it was only "President" until I got to it) and to work with Bob Welsh until his retirement and with Hari Areti thereafter. My only regret there is that I couldn't stay to work with Hari longer. I thank Andrew Puckett for taking over the GSA when I was finished being the benevolent dictator, and I hope that he will have as much enjoyment from it.

I have made many good friends at William and Mary, friends who I played hockey with on the Physics team, played video games with (and against) and laughed with at all the best parties: Aidan Kelleher (my co-gourmet), Vince Sulkosky, Joshua Moss (my best hockey coach), Melanie Collins, Keoki Seu, Bryan Moffit, Shannon Watson, Dandan Mao (my shopping co-conspirator), Justin Conroy, David Anderson, Brian Hahn, Dan Pechkis, Meghan Revelle, Sarah Chesney, Sadie Tedder, Allyn Powell, Erik Spahr, Aiyana Garcia, Malliga Suewattana (Cherry), Carla and Rita Schneider, Joe Katich, Stephen Coleman, Brian Glover, Dan Steiner, Jeff McIntyre, Michael Weissberger, William Cline, Crystal Bertoncini, Christopher Maher, Sadie Tedder, Nate Phillips, Kelly Kluttz, and Jeff Nelson.

My family has, of course, played a large part, especially my father, who passed away right after the forward-angle phase of the G^0 experiment finished running, and to whom this work is dedicated. I am sure he would be proud. I would also like to remember my two brothers here, Matthew and Stephen Phillips, who have both studied physics at various points in their lives and who both like to take things apart and blow things up as much as I do. I would also like to thank Jason Kalivas for being such a supportive friend, a friend who is closer than a brother.

Above all, I want to thank Jason Moscatello, for his wonderful friendship and his enduring love. I really couldn't have done it without you, my Beloved.

So, in summary, this work is dedicated to all of those who have shown me kindness, filled my life with color, and helped me on the road in this journey called life.

TABLE OF CONTENTS

Page

Acknowledgements . . . . . **ii**

List of Tables . . . . . **x**

List of Figures . . . . . **xii**

CHAPTER

1 Introduction **1**

1.1 Strange Quarks in the Nucleon 3

1.2 Beyond the Born Approximation 8

1.3 The G^0 Experiment 13

2 Theory **14**

2.1 Nucleon Vector Form Factors and Strangeness 14

2.2 Quark Decomposition of the Form Factors 18

2.3 Parity Violation in Electron Scattering 22

2.4 Electroweak Radiative Corrections 24

2.5 Theoretical Predictions for Strange Form Factors 28

2.5.1 Heavy Baryon Chiral Perturbation Theory (HBχPT) 28

2.5.2 Vector Meson Dominance (VMD) 30

2.5.3 Kaon Loop Models 33

2.5.4 Skyrme Model and Other Soliton Models 35

2.5.5 Constituent Quark Approach 37

2.5.6 Dispersion Relations 39

2.5.7 Lattice QCD 40

2.6 Summary of Estimates of Strangeness 42

2.7 Two Photon Exchange in Elastic Electron-Nucleon Scattering 43

2.7.1 Transverse Single Spin Asymmetries 44
2.7.2 Beyond the One-Photon Exchange Approximation 47
2.8 Theory Predictions for the Transverse Asymmetry A_n 48
2.8.1 Pion Electroproduction Threshold Region 49
2.8.2 Resonance Region 50
2.8.3 Intermediate and High-Energy, Forward Scattering 52
2.8.4 Hard Scattering Region 55
2.8.5 Two-Photon Exchange in Møller Scattering 56
2.9 A Summary about Two-Photon Exchange 56
2.10 Goals of the G^0 Physics Program 57
3 Survey of Related Experiments 59
3.1 Overview 59
3.2 Classic Parity-Violating Electron Scattering Experiments 59
3.3 Previous Strange Form-Factor Experiments 61
3.3.1 SAMPLE at MIT-Bates 61
3.3.2 HAPPEX at Jefferson Lab 64
3.3.3 PVA4 at MAMI 68
3.3.4 Summary of Previous PV Experiments 71
3.4 Previous Transverse Beam Spin Measurements 73
3.4.1 SAMPLE at MIT-Bates 74
3.4.2 PVA4 at MAMI 75
3.4.3 HAPPEX at Jefferson Lab 78
3.4.4 Summary of Previous Transverse Measurements 80
3.5 Remarks on Previous Experiments 81
4 The G^0 Experimental Apparatus 82
4.1 The G^0 Experiment 82
4.1.1 Experimental Technique 83
4.1.2 Experimental Design 84
4.2 Jefferson Lab Accelerator 88
4.3 The Polarized Electron Beam for G^0 89
4.3.1 The Polarized Source 90

4.3.1.1 Beam Position and Intensity Feedback 94
4.3.1.2 Leakage Beam 97
4.3.2 Accelerator and Beam Transport 99
4.3.2.1 Precession through the Møller Solenoid 100
4.3.3 Electron Beam Polarimetry 101
4.3.3.1 The Hall C Møller Polarimeter 102
4.3.3.2 Polarization Measurements 103
4.3.3.2.1 Optimizing the Spin Direction 104
4.3.3.2.2 Longitudinal Polarization Measurements 105
4.3.3.2.3 Transverse Polarization Measurements 107
4.3.3.2.4 Leakage Polarization Measurements 108
4.3.4 Monitoring the Electron Beam Quality 108
4.3.4.1 Beam Current Monitors 109
4.3.4.2 Beam Position Monitors 111
4.3.4.3 Beam Halo Monitoring System 113
4.3.4.4 Luminosity Monitors 115
4.3.4.5 Additional Beam Monitors 117
4.3.4.6 Beam Position Modulation and Energy Modulation 117
4.3.4.7 Beam Rastering System 118
4.4 The G^0 Target 118
4.4.1 The Target System 119
4.4.1.1 The Cryogenic Loop 119
4.4.1.2 Solid Targets 122
4.4.1.3 Target Control and Instrumentation 124
4.4.2 Target Performance and Systematics Studies 125
4.4.2.1 Target Boiling Studies 125
4.5 The G^0 Spectrometer 126
4.5.1 The Superconducting Magnet System (SMS) 127
4.5.2 The G^0 Focal Plane Detectors 129
4.5.2.1 North American Detectors 131
4.5.2.2 French Detectors 133
4.5.2.3 Detector Protection Systems 134

4.5.2.4 The Gain Monitoring System 135
4.6 The Electronics and Data Acquisition System 136
4.6.1 The G^0 Electronics 136
4.6.1.1 North American Electronics 139
4.6.1.2 French Electronics 141
4.6.1.3 Franco-American Hybrid Electronics 143
4.6.2 The Data Acquisition System 143
4.7 Summary 146
5 From Raw Asymmetries to Physics Asymmetries 147
5.1 Overview 147
5.2 Analysis Common to Both Datasets 149
5.2.1 Deadtime Corrections 151
5.2.2 Beam Polarization Correction 153
5.2.2.1 Longitudinal Polarization Analysis 153
5.2.2.2 Transverse Polarization Analysis 156
5.2.2.3 Determination of Physics Asymmetry Sign 157
5.3 Longitudinal Data Set 160
5.3.1 Time-of-Flight Particle Identification Cuts 161
5.3.2 Corrections for Helicity-Correlated Beam Properties 162
5.3.2.1 Helicity-Correlated Beam Parameters 162
5.3.2.2 Helicity-Correlated Beam Background Asymmetry 167
5.3.3 Corrections for Leakage Beam 169
5.3.4 Transverse Systematic Uncertainty 174
5.3.5 Physics Backgrounds 176
5.3.5.1 Background Decomposition 176
5.3.5.2 Background Correction 183
5.3.5.2.1 Detectors 1 through 14 184
5.3.5.2.2 Treatment of Detector 15 190
5.3.5.2.3 High Q^2 Peak of Detector 14 196
5.3.6 Electromagnetic Radiative Corrections 198
5.3.7 Determination of Q^2 201

5.3.8 The Physics Asymmetry 205
5.4 Transverse Data Set 206
5.4.1 Time-of-Flight Spectra and PID Cuts 208
5.4.1.1 Detectors 1 – 14 210
5.4.1.2 Detectors 15 and 16 211
5.4.2 Insertable Half-Wave Plate Reversal 211
5.4.3 Corrections for Helicity-Correlated Beam Properties: Beam Leakage, Beam Parameters and Linear Regression 212
5.4.4 Luminosity Monitors 215
5.4.5 Corrections for Physics Backgrounds 219
5.4.5.1 Dilution Factors 220
5.4.5.2 The Two-Step Method 221
5.4.5.3 Simultaneous Fit Method 226
5.4.5.4 Simple Monte Carlo 227
5.4.5.5 Comparison of Extracted Background Asymmetries 230
5.4.6 Corrected Asymmetries 232
5.4.7 Aluminum Frame Data 232
5.4.8 Discussion of Systematic Uncertainties 236
5.4.8.1 Phase Sensitivity Study 241
5.4.9 An Alternative Approach: Correcting via the Wiggles 244
5.4.10 Final Physics Asymmetries 247
5.5 Analysis Summary 248
6 From Physics Asymmetries to Physics Results 249
6.1 Longitudinal Data Set 249
6.1.1 Experimental Asymmetry Results 249
6.1.2 The Linear Combination $G_E^s + \eta G_M^s$ 250
6.1.3 Discussion of Results 252
6.1.4 Summary 256
6.2 Transverse Experimental Results 256
6.2.1 Extraction of Transverse Asymmetry A_n 256
6.2.2 Comparison with Theoretical Predictions 261

6.2.3 Summary 262
6.3 Conclusions 263
7 Concluding Remarks 264
7.1 Prospects for the Future 264
7.1.1 The Future of Strange Quark Physics 264
7.1.1.1 Other Measurements from G^0 267
7.1.2 Explorations of Two-Photon Exchange 267
7.1.3 The Future of PVES 270
7.2 Conclusions 273
BIBLIOGRAPHY 274

LIST OF TABLES

Table Page

2.1 Fundamental Fermion Charges 16

2.2 Electroweak Radiative Correction Factors 27

2.3 Theoretical Predictions for μ_s and $\langle r_s^2 \rangle$ 42

2.4 Transverse Asymmetry Predictions for G^0 (3 GeV, forward-angle) 57

3.1 Summary of Measurements of Parity-Violating Asymmetries from Strange-Quark Contribution Experiments Prior to G^0 71

3.2 Summary of $G_E^s + \eta G_M^s$ and Kinematics from Experiments at Forward Angles to Date 72

3.3 Summary of the Measurements of the Transverse Beam Spin Asymmetry Prior to G^0 80

4.1 Parameters for the G^0 Forward-Angle Measurement 86

5.1 Beam Polarization Uncertainty Sources 155

5.2 Transverse Polarization Values 157

5.3 Physics Asymmetry Sign Determination 160

5.4 Helicity-Correlated Beam Parameters 164

5.5 False Asymmetries Calculated from Linear Regression 168

5.6 Detector 15 Overall Systematic Uncertainties 195

5.7 Systematic Uncertainties for the Parity-Violating Asymmetries 206

5.8 Parity-Violating Physics Asymmetries from the G^0 Forward-Angle Measurement . 207

5.9 Kinematics for the Transverse Data Set 208

5.10 Comparison of Regression-Corrected and Uncorrected Transverse Asymmetries . . 215

5.11 Dilution Factors, Transverse Data Set 221

5.12 Extracted Background Asymmetry – Two-Step Method 226

5.13 Extracted Background Asymmetries – Simultaneous Method 227

5.14 Simple Monte Carlo Results 230

5.15 Extracted Background Asymmetries 231

5.16 Corrected Measured Elastic Transverse Asymmetries 233

5.17 Transverse Asymmetries from Aluminum 236

5.18 Systematic Uncertainties for the Transverse Asymmetries 238

5.19 Uncertainties for the Transverse Asymmetries 240

5.20 Comparison of Extracted Transverse Elastic Asymmetries 245

5.21 Transverse Elastic Asymmetries and Uncertainties 247

6.1 Final Published Parity-Violating Physics Asymmetries 250

6.2 $G_E^s + \eta G_M^s$ from the G^0 Forward-Angle Measurement 252

6.3 Published Transverse Elastic Asymmetries and Uncertainties 257

6.4 Sources of Systematic Uncertainties for the Transverse Asymmetry Measurement . 258

6.5 Transverse Asymmetry Results 261

7.1 Anticipated G^0 Backangle Transverse Statistical Precision 268

LIST OF FIGURES

Figure Page

1.1 Ratio of G_E/G_M by Rosenbluth Separation compared to Polarization Transfer Measurements . . . 12

2.1 Feynman Diagram for Elastic ep Scattering . . . 15

2.2 Feynman Diagrams for One-Quark Radiative Corrections . . . 25

2.3 More Feynman Diagrams for Radiative Corrections . . . 26

2.4 Feynman Diagram for Vector Meson Dominance . . . 30

2.5 Feynman Diagram for Kaon Loop Calculations . . . 33

2.6 Feynman Diagrams for Two-Photon Exchange . . . 45

2.7 Definition of Coordinate System . . . 46

2.8 Transverse Asymmetry Calculations by Diaconescu and Ramsey-Musolf . . . 49

2.9 Transverse Asymmetry Calculation for 0.2 GeV by Pasquini and Vanderhaeghen . 51

2.10 Transverse Asymmetry Calculations by Pasquini and Vanderhaeghen . . . 52

2.11 Transverse Asymmetry Calculations by Afanasev and Merenkov . . . 53

2.12 Transverse Asymmetry Calculations by Gorchtein . . . 54

2.13 Transverse Asymmetry Calculations by Pasquini and Vanderhaeghen . . . 55

3.1 Schematic of a Module of the SAMPLE Apparatus . . . 62

3.2 Schematic of the SAMPLE Experimental Apparatus . . . 62

3.3 SAMPLE Results at $Q^2 = 0.1$ (GeV/c)^2 . . . 64

3.4 SAMPLE Deuterium Results as a Function of Q^2 . . . 64

3.5 Schematic Overview of the HAPPEX Experiment in Hall A . . . 65

3.6 Results from the HAPPEX Experiment at $Q^2 = 0.1$ (GeV/c)^2 67

3.7 Schematic of the PVA4 Experimental Apparatus 69

3.8 PVA4 Energy Spectrum Histogram 69

3.9 Results from Previous Experiments at $Q^2 = 0.1$ (GeV/c)^2 72

3.10 Measured Transverse Beam Spin Asymmetries from the SAMPLE Experiment . . 75

3.11 SAMPLE Transverse Beam Spin Asymmetry Results at $Q^2 = 0.1$ (GeV/c)^2 75

3.12 Measured Transverse Beam Spin Asymmetries from PVA4 76

3.13 PVA4 Transverse Beam Spin Asymmetry Results at $Q^2 = 0.106$ and $Q^2 = 0.230$ (GeV/c)^2 76

3.14 PVA4 Transverse Beam Spin Asymmetry Results at $Q^2 = 0.106$ and $Q^2 = 0.230$ (GeV/c)^2 77

3.15 Preliminary PVA4 Transverse Beam Spin Asymmetry Backward-Angle Results at $Q^2 = 0.23$ (GeV/c)^2 78

4.1 Schematic of G^0 Spectrometer Optics 83

4.2 Diagram of the CEBAF Accelerator 90

4.3 Coordinate System for Spin Precession 101

4.4 Diagram of the Møller Polarimeter 104

4.5 Diagram of the Møller Polarimeter Optics 105

4.6 Polarization Data and Fit from a Spin Dance Calibration 106

4.7 Photograph of the Halo Monitoring System 114

4.8 Electron Rates for the Luminosity Monitors 116

4.9 Placement Diagram for the Luminosity Monitors 116

4.10 Schematic of the Target Loop 119

4.11 Schematic of the Target Manifold 122

4.12 Photograph of the G^0 Spectrometer in Hall C 126

4.13 Photograph of Detector Assembly in the JLab Cleanroom 132

4.14 Flowchart of the G^0 Electronics for the Forward-Angle Measurement 137

4.15 Flowchart of the Data-Acquisition System for the Forward-Angle Measurement . . 143

5.1 Time-of-Flight Spectrum for Detector 8 150

5.2 Beam Polarization Versus Date for the G^0 Experiment 154
5.3 Time-of-Flight Spectrum for Detector 8 161
5.4 Fractional Yield versus Beam Position in x, Octant 2, Detector 1 166
5.5 Fractional Yield versus Beam Position in x, Octant 6, Detector 1 166
5.6 Linear Regression Slopes in x versus Octant for Detector 1 167
5.7 G^0 Histogram Showing Cuts and Leakage Spectrum 170
5.8 Raw Asymmetries versus the Leakage Correction, Proton Cut 173
5.9 Raw Asymmetries versus the Leakage Correction, Cut3 173
5.10 Background Yield Studies for Detector 1 178
5.11 Background Yield Simulation Comparison for Detector 4 178
5.12 Evolution of Background Asymmetry versus Time-of-Flight 180
5.13 Comparison of Measured σ_{total} from SAPHIR and KAON-MAID Calculations . . . 182
5.14 Hyperon Contributions to Backgrounds 183
5.15 Total Hyperon Contribution to the Background 183
5.16 Yield Fit for Octant 2, Detector 8 185
5.17 Asymmetry Fit for Octant 2, Detector 8 185
5.18 Background Yield "Lozenge" 188
5.19 Background Asymmetry "Kink" 189
5.20 Background Yield Evolution for Detectors 12, 13, 14, and 16 191
5.21 Background Linear Yield Fits for Detector 15 Background Interpolation 191
5.22 Comparison of Background Yield Determination Methods for Detector 15 192
5.23 Fitted Background Asymmetry Evolution for Detectors 12, 13, 14, and 16 193
5.24 Interpolated Background Asymmetries for Octant 3, Detector 15 193
5.25 Fit to the Measured Asymmetries for Octant 3, Detector 15 193
5.26 Yield Fit for the High Q^2 Peak of Detector 14 196
5.27 Asymmetry Fit for the High Q^2 Peak of Detector 14 196
5.28 Feynman Diagrams of Various Radiative Corrections 199
5.29 Ratio of Radiative Corrected and Uncorrected Asymmetries versus Detector 201
5.30 Elastic Proton Rate versus SMS Current 203

5.31 Difference Between Elastic Proton ToF and Pion ToF versus Detector 204
5.32 ToF PID Cuts for the Transverse Data, Detector 1–8 Cuts, NA 208
5.33 ToF PID Cuts for the Transverse Data, Detector 1–8, French 208
5.34 Raw Transverse Asymmetries versus Octant for Detector 1–8 209
5.35 Raw Transverse Asymmetries versus Octant for Detector 9–12 209
5.36 Detector 15 Time-of-Flight Cuts, French 210
5.37 Detector 15 Time-of-Flight Cuts, NA 210
5.38 Detector 16 Time-of-Flight Cuts, French 212
5.39 Detector 16 Time-of-Flight Cuts, NA 212
5.40 Raw Transverse Asymmetries versus Octant for Detector 13–14 213
5.41 Raw Transverse Asymmetries versus Octant for Detector 15 and 16 213
5.42 Insertable Half-Wave Plate Reversal Plots 214
5.43 Raw Asymmetries versus Octant for Detectors 1–8, No Leakage Correction 215
5.44 Raw Asymmetries versus Octant for Detectors 1–8, With Leakage Correction . . . 215
5.45 Helicity-Correlated Beam Parameter Asymmetries 216
5.46 Beam Halo Background Asymmetries 216
5.47 Electron Scattering Rates for the Luminosity Monitors 217
5.48 Luminosity Monitor Position Diagram 217
5.49 Helicity-Correlated Lumi Asymmetries for the Transverse Data 218
5.50 Lumi Asymmetries versus ϕ, Free Fit 219
5.51 Lumi Asymmetries versus ϕ, Constrained Offset Fit 219
5.52 Lumi Asymmetries versus ϕ, Constrained to Calculated Spin Precession 220
5.53 Lumi Asymmetries versus ϕ, Constrained Offset and to Calculated Spin Precession 220
5.54 Example Fit for Dilution Factor Determination 221
5.55 NA Background Fits, Two-Step Method 223
5.56 French Background Fits, Two-Step Method 223
5.57 Azimuthal Background Asymmetry Fits, Two-Step Method 224
5.58 Linear Background Asymmetry Fits, Two-Step Method 224
5.59 NA Background Fits, No Dilution Correction 225

5.60 French Background Fits, No Dilution Correction 225
5.61 NA Background Fits, Simultaneous Method 228
5.62 French Background Fits Simultaneous Method 228
5.63 Azimuthal Background Asymmetry Fits, Simultaneous Method 229
5.64 Linear Background Asymmetry Fits, Simultaneous Method 229
5.65 Corrected Elastic Asymmetries, Two-Step Method 234
5.66 Corrected Elastic Asymmetries, Simultaneous Method 234
5.67 Transverse Aluminum Asymmetry versus Octant 235
5.68 Raw Cut3 Asymmetries versus Run Number, No Beam Leakage Correction 237
5.69 Raw Cut3 Asymmetries versus Run Number, With Beam Leakage Correction . . . 237
5.70 Effects of Phase ϕ_0 on Extracted Transverse Asymmetry 243
5.71 Asymmetry Correction Using Extracted $A_\perp$ 246
5.72 Asymmetry Correction Using Extracted $A_\perp$, Constrained Fits 246

6.1 $A_{physics}$ and A_{NVS} versus Q^2 (Linear plot) 251
6.2 $A_{physics}$ and A_{NVS} versus Q^2 (Log plot) 251
6.3 $G_E^s + \eta G_M^s$ versus Q^2 253
6.4 World Data of $G_E^s + \eta G_M^s$ for $Q^2 = 0.1$ (GeV/c)^2 254
6.5 $G_E^s + \eta G_M^s$ at $Q^2 = 0.23$ (GeV/c)^2 255
6.6 $G_E^s + \eta G_M^s$ at $Q^2 = 0.48$ (GeV/c)^2 255
6.7 Defined Coordinates for the G^0 Transverse Measurement 259
6.8 Measured Asymmetry versus ϕ with Sinusoidal Fits 260
6.9 Transverse Asymmetry Results vs. θ_{CM} with Theoretical Predictions 261

7.1 G^0 Backward-Angle Measurement Schematic 265
7.2 G^0 Backward-Angle Detectors Photograph 265
7.3 G^0 Backward-Angle Coincidence Pattern 266
7.4 G^0 Backward-Angle Electron Coincidence Data 266
7.5 Anticipated G^0 Backangle Transverse Results 269

7.6 CAD Drawing of the Q_{Weak} Apparatus 271

7.7 Q_{Weak} Plot of the Calculated Running of the Weak Mixing Angle 272

MEASUREMENT OF THE STRANGE QUARK CONTRIBUTION TO THE VECTOR STRUCTURE OF THE PROTON

CHAPTER 1

Introduction

Much of the study of modern physics is focused on achieving two basic goals: an understanding of the fundamental constituents of matter and the interactions that take place between them. Most of the matter that makes up the visible universe is made of nucleons, which are the protons and neutrons that bind together, forming the nuclei of the atoms around us. However, despite the fact that protons and neutrons have been carefully studied since their discovery in the beginning of the twentieth century [1–4], there is a surprising lack of understanding of the fundamental structure of the two nucleons.

Ever since the first evidence that the proton had internal structure, when Frisch and Stern's measurement [5] of the proton's magnetic moment showed a value of $\mu_p \sim 2.5\mu_N$ (instead of the 1 μ_N expected of a point-like Dirac particle), and Alvarez and Bloch's measurement of the neutron's magnetic moment to be $\mu_n \sim -1.93\mu_N$ [6], the internal structure of the nucleon has been investigated. Experiments at SLAC in the early 1970's using deep inelastic scattering (DIS) [7] showed that nucleons are comprised of point-like Dirac particles, which became known as quarks. This led the way for the development of the Standard Model and Quantum Chromodynamics, which are the theories used to describe composite particles such as nucleons in terms of their constituent elementary particles (such as quarks) and the carriers of the strong force that binds

them together (the gluons). The Standard Model (SM) of elementary particle physics attempts to describe the enormous number of fundamental and composite particles that have been observed and the laws that govern their interactions. In this model there are six different flavors of quarks (listed by increasing mass): u up, d down, s strange, c charm, b bottom (beauty), and t top (truth). All hadrons, which are strongly interacting composite particles, are composed of quarks.

The theory of quantum chromodynamics (QCD) is considered to be the correct microscopic picture for descriptions of hadrons, and it successfully describes hadronic phenomena at very short distance scales (high momentum transfer), where the bound systems of quarks have relatively simple properties. The short distance scale physics that has been calculated from QCD agrees well with deep-inelastic scattering data [7] and e^+e^- annihilation data [8] that have been collected over the past 30 years. QCD attempts to describe these phenomena by describing the interaction between quarks through the exchange of color gauge fields, or gluons. Within the hadrons there is a quark-gluon sea, where quarks and anti-quarks can fluctuate in and out of existence by pair-producing from the gluon fields. Using this theory, the interactions of the quarks at short distance scales (high energy) can be described using a converging perturbation expansion. This is not very successful at large distance scales (low energy) of order of the size of a nucleon, however, as the strong coupling constant α_s becomes too large for the perturbation expansion to converge. Because of this lack of understanding of the non-perturbative nature of the interaction of quarks and gluons, many of the fundamental properties of the internal structure of the nucleon are still a mystery.

At long distance scales, about the size of the hadron itself, the picture is quite incomplete. Models exist that employ effective degrees of freedom and are more or less motivated directly by observation or by QCD. They are the present standard in this regime, although lattice QCD is able to calculate some low energy observables and will be able to calculated more in the near future. The descriptions of hadron structure that will develop from lattice results and models will require careful measurements of low energy properties to guide this development. Although constituent

quark models are successful in the description of low-energy phenomena such as the hadronic mass spectra, charges and magnetic moments, these models should fit into the more fundamental theory of QCD.

This raises one of the great questions of nuclear physics: how can the gap between QCD and our current description of nuclei and nuclear forces in terms of hadrons be bridged? This dissertation discusses two measurements designed to further the knowledge of the nucleon. The first measurement investigates the contribution of strange quarks to the properties of the nucleon, and the second measurement studies the imaginary part of the two-photon exchange amplitude and the contributions of hadronic inelastic intermediate states to this amplitude.

1.1 Strange Quarks in the Nucleon

In QCD, the nucleon is described as primarily being composed of three valence quarks, which are surrounded by a quark-gluon sea filled with ever increasing numbers of sea quarks, anti-quarks and gluons, in what is known as the QCD vacuum. In the sea, quark-antiquark pairs can be created and annihilated through pair production in the gluon field. The proton is made of three valence quarks, two u quarks and one d quark, surrounded by a sea of gluons and quark-antiquark ($q\bar{q}$) pairs ($u\bar{u}$, $d\bar{d}$, $s\bar{s}$, ...). The neutron shares the same description other than the three valence quarks are two d quarks and an u quark.

This sea plays an important role at these distance scales. These gluons carry about half of the the overall nucleon momentum. The overall spin of the nucleon appears to only come partially from the spin carried by quark degrees of freedom; the rest comes from quark orbital angular momentum and gluon spin [9]. Although the strange quarks only exist in the nucleon in the quark sea, they could have significant contributions to nucleon structure. The sea u and d quark contributions are indistinguishable from their valence counterparts, but as there are no valence s quarks, their contribution could be observed. The overall strangeness of the proton is zero, but the distribution of the strange quarks within the nucleon could be non-uniform, similar to the charge distribution

within the neutron. To develop a complete understanding of nucleon structure, the contribution of strange quarks is important, as they are exclusively part of the quark-antiquark sea. Furthermore, the antiquark pairs partly reflect the gluon contributions that undoubtedly play an important role, just as they do at smaller distance scales.

There are suggestions that the strange quark-antiquark pairs in the sea could make a significant contribution to nucleon structure. Experimental constraints can be placed on Δu, Δd, and Δs (the helicity of a quark flavor in the nucleon) by studying the strange quark's spin contribution using the polarized deep-inelastic scattering of electrons or muons from nucleons, where the cross section is characterized by two polarization structure functions $g_1(x, Q^2)$ and $g_2(x, Q^2)$. In the simplest analysis, by defining the quark helicity content as $\Delta q_i \sigma_\mu = \langle p, \vec{\sigma} | \bar{q}_i \gamma_\mu \gamma_5 q_i | p, \vec{\sigma} \rangle$, the g_1 sum rule can be expressed as to first order

$$\sum_0^1 g_1(x) dx = \frac{1}{2} \left(\frac{4}{9} \Delta u + \frac{1}{9} \Delta d + \frac{1}{9} \Delta s \right), \tag{1.1}$$

where the contributions of the quark and anti-quark contributions from a particular flavor are combined together. Using the Bjorken sum rule [10, 11] and its SU(3) generalization, a solution can then be found. Several experiments at CERN [12, 13], SLAC [14, 15], and DESY [16] have made measurements to determine g_1 over a large kinematic range. As an example, the results of the measurement by the European Muon Collaboration (EMC) [12] for the spin contribution of constituent quarks to the overall spin of the proton, combined with earlier results from SLAC [17], found the value of the spin-dependent structure function, g_1^p, of the proton to be [12]

$$\int_0^1 g_1^p dx = 0.126 \pm 0.010 \pm 0.015. \tag{1.2}$$

This is in contradiction with the calculated value of 0.189 ± 0.005 from the Ellis-Jaffe sum rule [18], which neglects contributions from the strange quark. The combined analysis yielded

$$\begin{aligned} \Delta u &= 0.391 \pm 0.016 \pm 0.023 \\ \Delta d &= -0.236 \pm 0.016 \pm 0.023 \\ \Delta s &= -0.095 \pm 0.016 \pm 0.023 \end{aligned}$$

which shows that the strange sea quarks are polarized anti-parallel to the proton spin, and have a contribution of 19% to the overall proton spin (of $\frac{1}{2}$). However, more recent measurements have suggested a smaller contribution for Δs [19–21].

The momentum distribution of strange quarks in the nucleon can be determined from measurements of oppositely signed muons (dimuons) from muon neutrino ν_μ deep inelastic scattering. The muons come from charmed particle production from a charged current interaction with a strange or down quark. Charm production from the down quark is Cabbibo-suppressed, so the dimuons are most sensitive to the strange sea. The charmed hadrons decay semi-muonically into a final state with two oppositely charged muons, with one from the weak vertex, the other from the charm decay. The momentum distributions of s and $\bar{s}$ quarks in the nucleon were studied by the measurement of charm production in deep-inelastic neutrino scattering through the detection of dimuons by the NuTeV experiment at Fermilab [22–24]. The NuTeV collaboration at Fermilab reported a non-zero result for the strangeness contribution to the nucleon's longitudinal momentum at $Q^2 = 16$ (GeV/c)^2, reporting that the fraction of the nucleon momentum carried by strange sea quarks (s and $\bar{s}$) to that by the non-strange sea was [25, 26]:

$$\frac{2\int_0^1 dx(s+\bar{s})}{\int_0^1 dx(u+\bar{u}+d+\bar{d})} = 0.42 \pm 0.07 \pm 0.06. \tag{1.3}$$

It is expected that the light sea quarks (u, d, and s) carry about 5% of the proton momentum in the parton model [27]. However, although this points to the existence of the strange sea, it is difficult to interpret the momentum fraction in the parton model in terms of more familiar observables. The NuTeV analysis also reported that the asymmetry in the $s(x)$ and $\bar{s}(x)$ momentum distributions is $\int x[s(x) - \bar{s}(x)]dx = -0.0009 \pm 0.0014$, consistent with zero [22].

Neutral current elastic neutrino-nucleon scattering can also be used to probe for strange sea quark effects. The standard model axial current is purely isovector in the case that the strange matrix element vanishes; this current can be predicted exactly from the known charged current axial matrix element. Deviations can be interpreted as contributions from heavier quarks. Cross section data was taken at Brookhaven National Lab (BNL) and fitted using nucleon electromagnetic

form factors, yielding a result of $\Delta s = -0.15 \pm 0.09$ [28]. This is consistent with the deep inelastic data, but has large uncertainties because of the limited precision of the cross section data [29].

Another method used to investigate strange quark effects is to study the sigma term in pion-nucleon scattering in order to determine the strange-quark contribution to the mass of the nucleon [30–32]. This method is actually one of the original motivations for investigating the strange sea. In this analysis, it is expected that in the limit of vanishing quark masses, the nucleon mass should approach some non-zero value M_0 associated with the gluon quark mass and the $q\bar{q}$ condensate. In reality, with nonzero quark mass, the nucleon mass is modified and has several additional terms. The analysis involves separating the nucleon mass into each of its valence and non-valence quark components :

$$M_N = M_0 + \sigma_s + \sigma, \tag{1.4}$$

where M_N is the nucleon mass, M_0 is the mass of the gluon sea and the $q\bar{q}$ condensate, $\sigma_s = \frac{1}{2M_N}\langle N|m_s s\bar{s}|N\rangle$, and $\sigma = \frac{1}{2M_N}\langle N|\frac{m_u+m_d}{2}(u\bar{u} + d\bar{d})|N\rangle$, where m_u, m_d, and m_s are the u, d, and s quark masses, with σ_s and σ representing the contributions from the strange sea and the non-strange sea, respectively. To provide the needed constraints, the value of σ is obtained from πN scattering data, with another constraint coming from utilizing hyperon mass relations to give insight into the contributions from the quark masses. In the simple quark picture, $\langle N|s\bar{s}|N\rangle = 0$, which would imply that the value from πN scattering should agree with the value from the hyperon mass limit. However, the two values do not agree, which can be explained by postulating the existence of the $s\bar{s}$ contribution to nucleon structure, with an overall strange quark contribution of $\frac{\langle N|s\bar{s}|N\rangle}{\langle N|(u\bar{u}+d\bar{d})|N\rangle} \simeq 0.1$, implying that $M_0 \simeq 765$ MeV and $\sigma \simeq 130$ MeV. However, more recent analyses [33, 34] suggest somewhat larger values for the sigma term, which leads to $f \simeq 0.2, M_0 \simeq 500$ MeV, and $\sigma_s \simeq 375$ MeV. Work on refining this analysis is ongoing [31, 35, 36].

These measurements all give hints that strange quarks may provide a significant contribution to the properties of the proton, but it is clear that other measurements are required to fully determine the role of the strange sea quarks.

In addition to the above methods, strange contributions can be probed in another way. Contributions of the strange sea quarks to the static charge and magnetization distributions (e.g. magnetic moment) of the nucleon can be determined from experiments measuring the neutral weak scattering of electrons from protons and neutrons.

The electroweak probe is a well-understood way of measuring observables at low energies as well as high energies. Experiments have been using electron scattering for the last fifty years to study the electromagnetic structure of the nucleon. The functions that describe the nucleon electromagnetic structure contain the information about the underlying nucleon charge and magnetism distributions, providing fundamental information about the underlying quark distributions. Hofstadter *et al.* [37, 38] used electron-proton scattering to use the electromagnetic interaction to determine the internal structure of the proton by measuring the proton charge and magnetic form factors in the 1950's. The electromagnetic form factors describe the charge and magnetization distributions within the nucleon, and are now well-measured over a wide range of kinematics.

After the unification of descriptions of the electromagnetic and weak interactions (which describes the electromagnetic and weak interactions of fundamental and composite particles) in the early 1970's, it became possible to consider comparing the electromagnetic and weak observables to extract information [39, 40]. The photon and weak gauge bosons have precisely related couplings to the point-like quarks of the QCD Lagrangian, making it possible to extract structure information according to quark flavor.

Kaplan and Manohar, in 1988, put forth the idea that the form factors that describe the charge and magnetization distributions due to the strange quarks, known as the strange electric and magnetic form factors G_E^s and G_M^s, could be determined by measuring the neutral weak electromagnetic form factor of the nucleon $G_{E,M}^{Z,p(n)}$ [40]. Shortly thereafter, McKeown and Beck proposed that the neutral weak electromagnetic form factor could be investigated using parity-violating elastic electron-proton scattering [41, 42]. Since then, there have been many experimental efforts to make these measurements and determine the strange quark contributions to the nucleon

using this technique, including the G^0 experiment.

Unlike the axial and scalar matrix elements, the s-quark contributions to the vector currents of the nucleon (ordinary charge and magnetization currents) can be determined more directly. By comparing measurements of neutral weak and electromagnetic elastic scattering, the s-quark contributions can be extracted. [40–42]. The only assumptions that need to be made are that the proton and neutron both obey charge symmetry [43] (under an isospin rotation the proton's u quarks become d quarks in the neutron and vice versa) and that the quarks are all point-like, spin $\frac{1}{2}$ Dirac particles. Because of this, the measurements can provide a clean basis from which to describe low energy hadron structure.

The primary goal of the G0 experimental program is to provide information on the structure of the nucleon through measurements of the role of strange quarks in the charge and magnetization distribution of the proton. The information gained from these measurements yields direct insight into the properties of the quark-gluon sea. This dissertation reports on the first phase of this experiment, the forward-angle parity-violation measurement of the G^0 experiment.

1.2 Beyond the Born Approximation

Elastic electron-nucleon scattering has been very successfully used as a tool to access information on hadron structure for the past several decades. The development of new technology and more advanced techniques have enabled electron-nucleon scattering experiments to achieve unprecedented and ever improving precision, which is still improving. These advances have allowed researchers to measure previously unattainable quantities of hadron structure, such as electroweak form factors, parity-violating effects, transition form factors, spin-dependent structure functions, nucleon polarizabilities, and so forth.

Experiments utilizing elastic electron-nucleon scattering are usually treated in the single-photon exchange approximation, called the Born approximation. Higher-order processes, such as two-photon exchange, are generally treated as small radiative corrections. The validity of

this approximation was investigated by experimental and theoretical work done to establish the magnitude of any corrections for higher-order processes in the 1960's and 1970's, when electron-nucleon scattering was measured systematically at the Stanford Linear Accelerator Center (SLAC) in order to study nucleon electromagnetic form factors. Experimentally, the validity of the one-photon exchange approximation (and the magnitude of two or multi-photon exchange effects) could be tested by comparing the difference between electron-nucleon and positron-nucleon cross sections, because the one-photon exchange cross section depends quadratically on the lepton charge. The comparisons of the electron-nucleon and the positron-nucleon scattering cross sections revealed that they were consistent with equal cross sections [44, 45]. However, the precision attainable in these investigations in the 1960's and 1970's was insufficient to measure two-photon effects at the few percent level of the cross section, a likely magnitude for two-photon exchange contributions due to a suppression factor $\alpha = \frac{e^2}{(4\pi)} \simeq \frac{1}{137}$.

Recognizing the limitations of the one-photon approximation, theorists have been calculating corrections to elastic electron-nucleon scattering of order e^2 relative to the Born approximation for a long time [46, 47]. The calculations with one photon being "soft" (having a vanishingly small four-momentum) were done, as the infrared divergences associated with the soft photon cancel against infrared divergences from soft bremsstrahlung. However, the contributions arising from both photons being "hard", that is when the momentum transfer of both of the individual photons is large, were not calculated because of a lack of sufficient knowledge of the intermediate hadronic state.

Early estimates of the two-photon exchange contribution with two hard photons were done by Drell and collaborators in the late 1950's, where a non-relativistic model including the nucleon and the lowest nucleon resonance contribution, the $\Delta(1232)$ was used to find that the cross sections were affected at the $\sim 1\%$ level by the resonance contribution to the two-photon exchange diagram [48,49]. As the calculation was non-relativistic in nature, this result was limited to an electron beam energy of $\lesssim 1$ GeV. Later works calculated two-photon exchange effects at higher energies [50, 51],

with Greenhut [51] calculating the contribution of higher nucleon resonance intermediate states with masses up to 1.7 GeV. The calculations showed that the real (or dispersive) part of the two-photon exchange amplitude gave an electron-to-positron cross section ratio that deviated from unity at the 1–2% level in the region of a few GeV.

Significant interest was recently renewed in two-photon exchange, when it was argued that contributions from the real part of this amplitude play a role in the discrepancy between the Rosenbluth separation and the polarization transfer measurements of the ratio of the proton's elastic form factors G_E^p/G_M^p [52]. The elastic electromagnetic form factors of the nucleon characterize its internal structure, describing the charge and current distributions within it. The elastic cross section for electron-proton scattering can be written in terms of the electric ($G_{E_p}(Q^2)$) and magnetic ($G_{M_p}(Q^2)$) Sachs form factors as

$$\frac{d\sigma}{d\Omega} = \frac{\alpha^2 E_e' \cos^2\frac{\theta_e}{2}}{4E_e^3 \sin^4\frac{\theta_e}{2}} \left[G_{E_p}^2 + \frac{\tau}{\epsilon} G_{M_p}^2\right] \left(\frac{1}{1+\tau}\right), \tag{1.5}$$

where E_e' and θ_e are the scattered electron's energy and angle, E_e is the incident electron's beam energy, $\tau = Q^2/4M^2$, M is the proton mass, and ϵ is the virtual photon longitudinal polarization, given by

$$\frac{1}{\epsilon} \equiv 1 + 2(1+\tau)\tan^2\frac{\theta}{2}. \tag{1.6}$$

The ratio of G_E/G_M has been measured by several collaborations [53–56] with unpolarized measurements using the Rosenbluth separation technique [57]. In this method, the separation of $G_{E_p}^2$ and $G_{M_p}^2$ is done by measuring the elastic electron-nucleon cross section at a fixed Q^2 over a range of ϵ values. These varying ϵ values are obtained by changing the beam energy and the scattered electron angle. Measurements of the proton form factors using this method yield uncertainties of only a few percent on both G_{E_p} and G_{M_p} for $Q^2 < 1$ (GeV/c)^2, with results indicating that $G_{E_p}/G_{M_p} \simeq 1$. Above $Q^2 = 1$, the uncertainties for G_{E_p} become larger because as Q^2 increases, the cross section becomes dominated by G_{M_p}, making the extraction of G_{E_p} more difficult.

Advances in the technology to produce high-quality polarized electron beams have enabled

experiments [58–60] to measure the ratio of the nucleon electromagnetic form factors using, instead, the polarization transfer technique. In this method, the form factors are measured by scattering longitudinally polarized electrons from a proton (hydrogen) target, which results in a transfer of polarization to the recoil proton. The transferred polarization has only two non-zero components, P_t perpendicular to, and P_l parallel to the proton momentum in the scattering plane, given by [61, 62]

$$I_0 P_t = -2\sqrt{\tau(1+\tau)} G_{E_p} G_{M_p} \tan\frac{\theta_e}{2}, \tag{1.7}$$

$$I_0 P_l = \frac{1}{M}(E_e + E_{e'})\sqrt{\tau(1+\tau)} G_{M_p}^2 \tan^2\frac{\theta_2}{2}, \tag{1.8}$$

where $I_0 = G_{E_p}^2 + \frac{\tau}{\epsilon} G_{M_p}^2$. Combining the above two equations yields the ratio

$$\frac{G_{E_p}}{G_{M_p}} = -\frac{P_t}{P_l}\frac{(E_e + E_{e'})}{2M}\tan\left(\frac{\theta_e}{2}\right). \tag{1.9}$$

The two recoil polarization components are measured simultaneously in the polarimeter, and as neither the beam polarization nor the polarimeter analyzing power needs to be known, the systematic uncertainties are small. Surprisingly, the results of these measurements are quite inconsistent with the results of the Rosenbluth experiments. The polarization transfer data feature a sharp decline in the ratio $\mu_p G_{E_p}/G_{M_p}$ with increasing Q^2, which indicates that G_{E_p} falls faster then G_{M_p}. A global Rosenbluth analysis of the cross section measurements [53] is shown with Jefferson Lab polarization transfer measurements from References [58, 59] in Figure 1.1, which clearly shows the large discrepancy between the two techniques [63]. The extraction of G_{E_p}/G_{M_p} from these measurements assumes that there is only the exchange of a single photon between the electron and the nucleon. Given this intriguing problem, a precise measurement of two-photon exchange processes could be quite enlightening.

In order to reach greater precision with electron scattering experiments, it is important to understand two-photon exchange effects and their contributions to different observables. Although the two-photon exchange contribution is small, it is comparable to the parity-violating elastic electron-nucleon scattering asymmetry [64], and recent parity-violation measurements have had to consider possible systematic corrections due to this effect. In addition, a good understanding

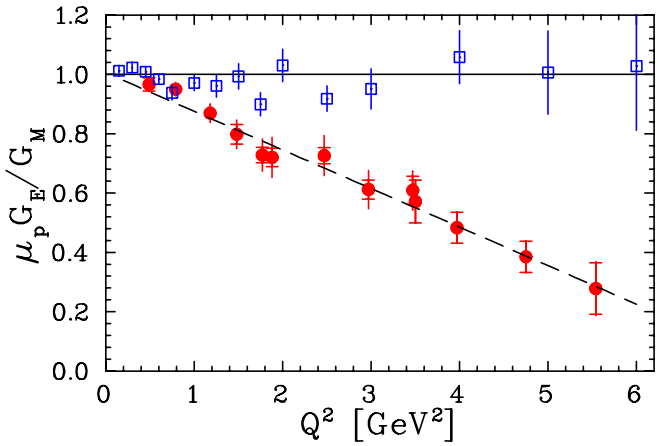

FIG. 1.1: *The ratio of the electric to magnetic form factor from Rosenbluth separation measurements (hollow squares) and from Jefferson Lab measurements of recoil polarization (solid circles). Figure from [63] of data from [53], [58], and [59].*

of two-photon exchange contributions can be extended to calculations of diagrams that appear in other processes, such as γZ and W^+W^- box diagrams, which are important corrections in precision electroweak experiments [65]. Thus, empirical verification of the theoretical framework for this effect is beneficial.

These issues have spurred a significant amount of theoretical activity and provided motivation for a precise evaluation. A precise measurement of the imaginary (absorptive) part of the two-photon exchange amplitude can be done by measuring the single-spin asymmetry in elastic electron-nucleon scattering, where either the beam spin or the target spin is polarized normal (transversely) to the scattering plane, as discussed in [66, 67]. Although challenging, due to the small size of the asymmetry, this was measured by the G^0 collaboration as part of the systematic studies. Although the primary goal of the G^0 experiment is to measure the asymmetry from the elastic scattering of longitudinally polarized electrons off an unpolarized hydrogen target (protons) in order to determine the contribution of the strange sea quarks to the charge and magnetization of the proton, the experiment also performed a measurement of transverse beam spin asymmetries, in order to determine the possible contribution of any systematic false asymmetry in the longitudinal measurement that would arise from any residual transversely-polarized beam component. As noted

above, these data are a measurement of the imaginary part of the two photon exchange amplitude, providing valuable information on this contribution to the electron-scattering amplitude. This dissertation also reports how this measurement was performed and how these data were analyzed to obtain this important information on this higher-order process.

1.3 The G^0 Experiment

The goal of the G^0 experiment is to determine the strange quark contribution to electric and magnetic properties of the nucleon, that is, to determine the values of the strange electric and magnetic form factors G_E^s and G_M^s. The experiment will achieve this ambitious goal by measuring the neutral weak form factor via parity-violating elastic electron scattering, a very precise yet challenging technique. To accomplish this, several phases of measurements must be taken and many experimental techniques and methods had to be developed or refined to meet the challenges of this experiment. This dissertation discusses the first part of the G^0 experiment, the forward-angle measurement, and the challenges that were overcome to make that measurement successful. In addition, this dissertation reports a second measurement performed by the G^0 collaboration of the imaginary part of the two-photon exchange amplitude through the transverse asymmetry in the scattering of transversely polarized electrons from unpolarized protons. Both of these measurements will be described in detail in the following chapters, and will conclude with the results of the experiment and some thoughts about the future directions of these experiments.

CHAPTER 2

Theory

The goal of the G^0 experiment is to determine the strange electric and strange magnetic form factors G_E^s and G_M^s by measuring the neutral weak form factor $G_{E,M}^Z$, which is accessed through parity-violating elastic electron-proton scattering [27, 68–70]. The form factors of the nucleon characterize its internal structure, describing the charge and current distributions within it, and thus, the contributions of the quarks to that structure. The first part of this chapter describes the physics behind that measurement. The second half of the chapter is devoted to a discussion of two-photon exchange in electron scattering and the investigation of this effect by the measurement of transverse asymmetries.

2.1 Nucleon Vector Form Factors and Strangeness

On the simplest level (to first order) the interaction of an electron with a nucleon in elastic electron scattering can be described by two processes represented by the two Feynman diagrams in Figure 2.1: the electromagnetic interaction, with the exchange of a single photon (γ), and the neutral weak interaction, with the exchange of the single vector boson (Z^0).

There is an invariant amplitude that is associated with each process represented in these

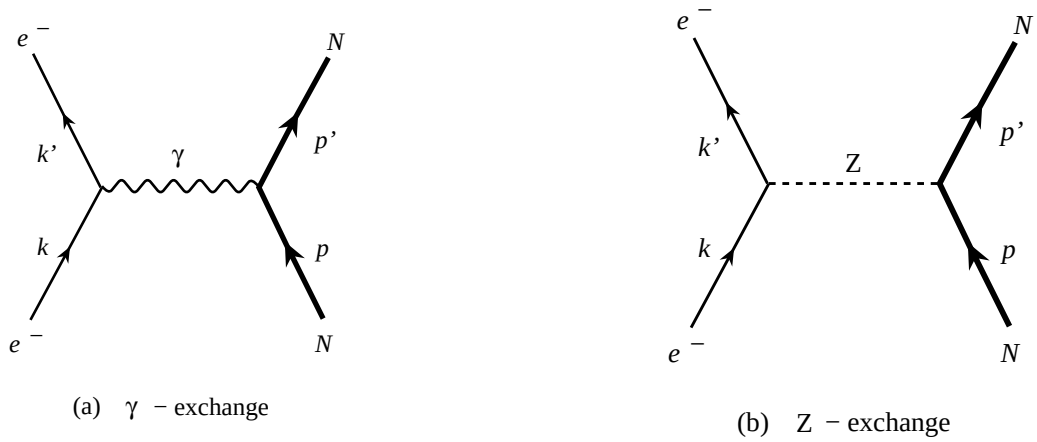

FIG. 2.1: *The Feynman diagrams describing the first-order interaction processes for the elastic scattering of an electron from a nucleon. The incoming and outgoing four-momentum for the electron and the nucleon are given by k and k' and p and p'. The four-momentum of the exchanged boson is defined as $q \equiv p' - p = k - k'$ and $Q^2 \equiv -q^2 > 0$.*

diagrams, that sum together to the overall invariant amplitude for the interaction: $\mathcal{M} = \mathcal{M}_\gamma + \mathcal{M}_\mathcal{Z} + ...$, with higher-order processes denoted by the ellipses. These amplitudes for the scattering of a lepton from a hadronic electromagnetic current and a weak neutral current, as shown in Figure 2.1, can be expressed using the underlying fundamental electroweak interactions between quarks and leptons. The couplings of the fundamental fermions to the γ and the Z^0 are written as [68]

$$i\alpha e_f \gamma^\mu, \tag{2.1}$$

$$i\tfrac{gM_Z}{4M_W}\gamma^\mu(g_V^f + g_A^f\gamma_5), \tag{2.2}$$

where α is the electromagnetic coupling strength, g is the weak coupling strength, M_Z is the mass of the Z boson, M_W is the mass of the W boson, e_f is the fermion's electromagnetic charge, g_V^f is the fermion's vector weak charge, and g_A^f is the fermion's axial weak charge, where the values to all these charges can be found listed in Table 2.1.

From here, it is simple to write the invariant amplitudes of the leptonic currents l and hadronic

Fermion	e_f	g_V^f	g_A^f
ν_e, ν_μ, ν_τ	0	1	-1
e^-, μ^-, τ^-	-1	$-1+4\sin^2\theta_W$	1
u, c, t	$\frac{2}{3}$	$1-\frac{8}{3}\sin^2\theta_W$	-1
d, s, b	$-\frac{1}{3}$	$-1+\frac{4}{3}\sin^2\theta_W$	1

TABLE 2.1: *The electromagnetic and weak charges of the fundamental fermions, from [68]*

currents J of the nucleon, using the electromagnetic and weak couplings listed in Table 2.1:

$$\mathcal{M}_\gamma = \frac{4\pi\alpha}{q^2} e_l l^\mu J_{\gamma\mu} \tag{2.3}$$

$$\mathcal{M}_Z = -\frac{G_F}{2\sqrt{2}}(g_V^l l^\mu + g_A^l l^{\mu 5})(J_{Z\mu} + J_{Z\mu 5}), \tag{2.4}$$

where $q \equiv p' - p = k - k'$, k is the four-momentum of the incident electron, k' is the four-momentum of the scattered electron, p and p' are the four-momentum of the target and recoil nucleon, and $G_F = \frac{g^2}{4\sqrt{2}M_W^2}$ is the Fermi coupling constant (the combination of the weak coupling constant and the W boson mass into one constant) [68]. Note that this is in the set of units where $\hbar c = 1$. The Q^2 dependence in $\mathcal{M}_\mathcal{Z}$ due to the Z propagator has been neglected, as these invariant amplitudes are derived in a kinematic regime where $Q^2 \ll M_Z$ [68].

As the lepton currents only involve point-like fundamental Dirac particles, the form of l^μ and $l^{\mu 5}$ are uncomplicated and can be expressed as [68]

$$l^\mu \equiv \bar{u}_l \gamma^\mu u_l \tag{2.5}$$

$$l^{\mu 5} \equiv \bar{u}_l \gamma^\mu \gamma_5 u_l \tag{2.6}$$

where u_l represents the lepton spinor, which depends on the four-momentum of the lepton, k or k', and on the spin state s or s'.

However, because of the hadron's internal structure (being a composite particle made of quarks), hadronic currents are much more complicated than the leptonic currents. Since they are made of point-like quarks, the nucleon current can be expressed as a sum of the quark current operators. The currents J_μ^{EM}, J_μ^{NC}, and $J_{\mu 5}^{NC}$ are the hadronic matrix elements of the electromagnetic,

vector, and axial-vector quark current operators [68]:

$$J_\mu^{EM} \equiv \langle N|\hat{J}_\mu^{EM}|N\rangle \tag{2.7}$$

$$J_\mu^{NC} \equiv \langle N|\hat{J}_\mu^{NC}|N\rangle \tag{2.8}$$

$$J_{\mu 5}^{NC} \equiv \langle N|\hat{J}_{\mu 5}^{NC}|N\rangle \tag{2.9}$$

where $|N\rangle$ represents our nucleon (either a proton or a neutron). We will return to these shortly.

The nucleon has extended structure, and so form factors are defined to parameterize this structure. Assuming Lorentz invariance, the electromagnetic vector current for a spin-$\frac{1}{2}$ particle like the nucleon can be expressed as [71]

$$J_\mu^\gamma = \bar{\mathcal{U}}_N \left(F_1(q^2)\gamma_\mu + i\frac{F_2(q^2)}{2M}\sigma_{\mu\nu}q^\nu \right) \mathcal{U}_\mathcal{N}, \tag{2.10}$$

where $\mathcal{U}_\mathcal{N}$ represents the nuclear spinors, N is the hadron (p or n), and F_1 and F_2 are the Dirac and Pauli form factors. The Dirac and Pauli form factors are often expressed in the form of the Sachs charge (electric) and magnetic form factors, which are defined as linear combination of the former [71]

$$G_E(Q^2) = F_1(Q^2) - \tau F_2(Q^2), \tag{2.11}$$

$$G_M(Q^2) = F_1(Q^2) + F_2(Q^2), \tag{2.12}$$

$$\tau = \frac{-q^2}{4M_N^2} = \frac{Q^2}{4M_N^2}. \tag{2.13}$$

At $Q^2 = 0$, the electric and magnetic form factors are the charge and magnetic moments of the respective nucleon:

$$G_E^{p,\gamma}(0) = 1 \qquad G_M^{p,\gamma}(0) = +2.793; \tag{2.14}$$

$$G_E^{n,\gamma}(0) = 0 \qquad G_M^{n,\gamma}(0) = -1.913; \tag{2.15}$$

where the proton magnetic moment is defined as one nuclear magneton (μ_N). The neutral weak electric and magnetic form factors G_E^Z and G_M^Z also reduce to the weak charge e^Z and the weak magnetic moment μ^Z for each nucleon. A simplistic way to think about these form factors goes

thusly: in the Breit frame (where $\mathbf{p}' = \mathbf{p}$), the Sachs form factors are the Fourier transforms of the nucleon charge and magnetic moment distributions [71].

The axial current of the nucleon can be expressed in terms of the neutral weak axial form factor G_A^{eN}:

$$J^Z_{A,\mu} = \bar{\mathcal{U}}_N G_A^{eN}(q^2)\gamma_\mu\gamma_5\mathcal{U}_\mathcal{N}, \tag{2.16}$$

which allows us to express the total hadronic neutral weak current (the sum of the neutral weak vector and axial currents) as

$$J^\mu_Z = \bar{N}\left(F_1^{ZN}(q^2)\gamma_\mu + i\frac{F_2^{ZN}(q^2)}{2M}\sigma_{\mu\nu}q^\nu + G_A^{eN}\gamma^\mu\gamma_5\right)N. \tag{2.17}$$

2.2 Quark Decomposition of the Form Factors

As mentioned earlier (Equations 2.7, 2.8, and 2.8), the overall electromagnetic and neutral weak hadronic currents may be expressed in terms of the currents of the quarks in the nucleon. The quark currents may be written as (assuming the quarks are point-like Dirac particles) [68]:

$$\hat{J}^\gamma_\mu = \sum_q e^q\bar{u}_q\gamma_\mu u_q, \tag{2.18}$$

$$\hat{J}^\gamma_Z = \sum_q g_V^q\bar{u}_q\gamma_\mu u_q, \tag{2.19}$$

$$\hat{J}^{\gamma 5}_Z = \sum_q g_A^q\bar{u}_q\gamma_\mu\gamma_5 u_q, \tag{2.20}$$

where e_q, g_V^q and g_A^q represent the electromagnetic or neutral weak currents, q denotes the quark flavor, and u_q is the spinor for the quark flavor q. The sum is for all six quark flavors, but because of suppression due to the mass of the heavier quark flavors, it is sufficient to only sum the three lightest quark flavors: u, d, and s, as they would have the most significant contribution [40]. The nucleon current can then be expressed in terms of the quark currents as [68]

$$J^\mu_\gamma = \langle N|\hat{J}^\mu_\gamma|N\rangle \tag{2.21}$$

$$= \left\langle N|\sum_q e^q\bar{u}_q\gamma_\mu u_q|N\right\rangle. \tag{2.22}$$

That is

$$J^{\mu}_{\gamma} = \sum_f e_f \bar{\mathcal{U}}_N \left[F_1^{fN} \gamma^{\mu} + F_2^{fN} \frac{i\sigma^{\mu\nu} q_\nu}{2M} \right] \mathcal{U}_{\mathcal{N}} \tag{2.23}$$

$$J^{\mu}_{Z} = \sum_f g_V^f \bar{\mathcal{U}}_N \left[F_1^{fN} \gamma^{\mu} + F_2^{fN} \frac{i\sigma^{\mu\nu} q_\nu}{2M} \right] \mathcal{U}_{\mathcal{N}} \tag{2.24}$$

$$J^{\mu 5}_{Z} = \sum_f g_A^f \bar{\mathcal{U}}_N G_A^{fN} \gamma^{\mu} \gamma_5 \mathcal{U}_{\mathcal{N}}, \tag{2.25}$$

where f is a quark flavor and q_ν represents one component of the four-momentum transferred by the exchanged boson. By equating the quark form factors and the equations for the electromagnetic and neutral weak currents, we find that the form factors F_1 and F_2 can be written as linear combinations of the currents of the six different quark flavors (or in our case, the three lightest):

$$F^{\gamma}_{1,2} = \sum_q e_q F^q_{1,2} \tag{2.26}$$

$$F^{Z}_{1,2} = \sum_q g^q_V F^q_{1,2} \tag{2.27}$$

$$G^{e}_{A} = \sum_q g^q_A G^q_A. \tag{2.28}$$

These can be expressed in the form of the Sachs form factors as

$$G^{\gamma}_{E,M} = \sum_q e_q G^q_{E,M} \tag{2.29}$$

$$G^{Z}_{E,M} = \sum_q g^q_V G^q_{E,M} \tag{2.30}$$

$$G^{e}_{A} = \sum_q g^q_A G^q_A \tag{2.31}$$

which results in five equations for the nucleon form factors written in terms of six unknown quark form factors. By factoring out the quark charges, the proton's electromagnetic and neutral weak vector form factors can then be expressed as

$$G^{\gamma,p}_{E,M} = \frac{2}{3} G^u_{E,M} - \frac{1}{3} G^d_{E,M} - \frac{1}{3} G^s_{E,M} \tag{2.32}$$

$$G^{Z,p}_{E,M} = \left(1 - \frac{8}{3}\sin^2\theta_W\right) G^u_{E,M} - \left(1 - \frac{4}{3}\sin^2\theta_W\right) \left(G^d_{E,M} + G^s_{E,M}\right) \tag{2.33}$$

with the neutral weak axial currents of the quarks giving the axial current

$$G^p_A = G^u_A - (G^d_A + G^s_A). \tag{2.34}$$

The contributions of the antiquarks in the sea are included above. The quarks and antiquarks contribute to the matrix elements $G^f_{E,M,A}$ with opposite signs because of their opposite signs; thus, if the spatial distributions of the s and $\bar{s}$ quarks were the same, their charges would cancel, forcing G^s_E to vanish as well [27].

By assuming charge symmetry, one can write the electromagnetic neutron form factors in terms of the proton matrix elements. This assumption asserts that the distribution of the u and $\bar{u}$ quarks in the proton is the same as the distribution of the d and $\bar{d}$ quarks in the neutron and vice versa (that is, by exchanging u and d quarks and $\bar{u}$ and $\bar{d}$ quarks and vice versa, a proton becomes a neutron). By isospin symmetry, this means:

$$G^{u,p}_{E,M} = G^{d,n}_{E,M} \equiv G^u_{E,M}, \quad G^{d,p}_{E,M} = G^{u,n}_{E,M} \equiv G^d_{E,M}, \quad G^{s,N}_{E,M} \equiv G^s_{E,M}, \tag{2.35}$$

$$G^{u,p}_A = G^{d,n}_A \equiv G^u_A, \qquad G^{d,p}_A = G^{u,n}_A \equiv G^d_A, \qquad G^{s,N}_A \equiv G^s_A. \tag{2.36}$$

Using this assumption, we can write out the neutron form factors as

$$G^{\gamma,n}_{E,M} = \frac{2}{3}G^d_{E,M} - \frac{1}{3}G^u_{E,M} - \frac{1}{3}G^s_{E,M} \tag{2.37}$$

$$G^{Z,n}_{E,M} = \left(1 - \frac{8}{3}\sin^2\theta_W\right) G^d_{E,M} - \left(1 - \frac{4}{3}\sin^2\theta_W\right)\left(G^u_{E,M} + G^s_{E,M}\right), \tag{2.38}$$

with the neutral weak axial currents of the quarks giving the axial current

$$G^n_A = G^d_A - (G^u_A + G^s_A). \tag{2.39}$$

Thus, $G^{Z,p}_{E,M}$ can also be written out as

$$G^{Z,p}_{E,M} = \left(1 - 4\sin^2\theta_W\right) G^{\gamma,p}_{E,M} - G^{\gamma,n}_{E,M} - G^s_{E,M}. \tag{2.40}$$

This all shows that with known electromagnetic form factors, a precision measurement of $G^{Z,p}_{E,M}$ would enable the decomposition of the electric and magnetic form factors into the contributions from the individual quark flavors, as the vector current contributions from the quark flavors may

be written as (for the proton case):

$$G_{E,M}^{u,p} = \left(3 - 4\sin^2\theta_W\right) G_{E,M}^{p,\gamma} - G_{E,M}^{p,Z} \tag{2.41}$$

$$G_{E,M}^{d,p} = \left(2 - 4\sin^2\theta_W\right) G_{E,M}^{p,\gamma} + G_{E,M}^{n,\gamma} - G_{E,M}^{p,Z} \tag{2.42}$$

$$G_{E,M}^{s,p} = \left(1 - 4\sin^2\theta_W\right) G_{E,M}^{p,\gamma} - G_{E,M}^{n,\gamma} - G_{E,M}^{p,Z}. \tag{2.43}$$

The form factors $G_{E,M}^{\gamma}$ for both protons and neutrons have been measured to such a precision that they are treated as known quantities for the purposes of the G^0 experiment. The goal of the G^0 experimental program is to determine $G_{E,M}^{s}$.

So why is the experiment called G^0? The flavor decomposition of the proton form factors can also be written in terms of the SU(3) flavor generators (that is, for the three lightest quarks). For the vector current, the singlet, isovector, and octet form factors can be written as

$$G_{E,M}^{(0)} = \frac{1}{3}\left(G_{E,M}^{u} + G_{E,M}^{d} + G_{E,M}^{s}\right), \tag{2.44}$$

$$G_{E,M}^{(3)} = \frac{1}{2}\left(G_{E,M}^{u} - G_{E,M}^{d}\right), \tag{2.45}$$

$$G_{E,M}^{(8)} = \frac{1}{2\sqrt{3}}\left(G_{E,M}^{u} + G_{E,M}^{d} - 2G_{E,M}^{s}\right). \tag{2.46}$$

Using these, the electromagnetic and weak form factors of the proton can be expressed as

$$G_{E,M}^{\gamma,p} = G_{E,M}^{(3)} + \frac{1}{\sqrt{3}} G_{E,M}^{(8)}, \tag{2.47}$$

$$\begin{aligned} G_{E,M}^{Z,p} &= -G_{E,M}^{(0)} + \left(2 - 4\sin^2\theta_W\right) G_{E,M}^{(3)} + \left(\frac{2}{\sqrt{3}} - \frac{4}{\sqrt{3}}\sin^2\theta_W\right) G_{E,M}^{(8)} \\ &= -G_{E,M}^{(0)} + \left(2 - 4\sin^2\theta_W\right) G_{E,M}^{\gamma,p}. \end{aligned} \tag{2.48}$$

With a measurement of the neutral weak form factor $G_{E,M}^{Z,p}$, combined with measurements of the proton electromagnetic form factors $G_{E,M}^{\gamma,p}$, the flavor singlet form factor of the proton, $G_{E,M}^{(0)}$, can be determined, which contains the desired information about $G_{E,M}^{s}$. Thus, the experiment is named after the flavor singlet proton form factor.

2.3 Parity Violation in Electron Scattering

The question then is how does one access the neutral weak current experimentally? As the cross section for electron-proton scattering is proportional to the square of electromagnetic and neutral weak amplitudes, $\sigma \propto |\mathcal{M}_\gamma + \mathcal{M}_Z|^2$, it would seem that such a measurement could provide access to the neutral weak current. However, the neutral weak current of interest is strongly suppressed compared to the electromagnetic current in a direct measurement. Therefore, a direct measurement is not very feasible. However, the parity-violating nature of the weak interaction makes it possible to make the measurement by using parity-violating electron scattering, which is the technique that the G^0 experiment employs. For the record, the neutral weak current of the nucleon can actually be measured in two ways: by using elastic neutrino scattering [29, 72] or via parity-violating electron scattering [40–42].

The scattering of unpolarized electrons from nucleons is dominated by the electromagnetic currents of the electron and nucleon. The electromagnetic properties of the proton, as approximated by single-photon exchange, are rather well-known, measured by previous experiments. Vector currents (such as the photon) exchanged in the electromagnetic interaction conserve parity. However, the neutral weak currents do not. As the weak currents carry equal parts vector and axial-vector components, they violate parity (space inversion) maximally. Because the weak interaction violates parity [73–76], the interference of the electromagnetic and weak currents also violates parity [41, 42]. This property is the basis of parity-violation measurements, as it gives insight into the neutral weak amplitude.

To observe this small effect, a comparison must be done between the experiment and its "mirror image", as the cross section contains a pseudo scaler component which changes sign in the mirror image of the experiment, resulting in an asymmetry between the two measurements, just as in the ground-breaking experiments by Wu *et al.* [77–79] and Garwin *et al.* [80]. In a parity-violating electron scattering experiment, this mirror measurement is done by reversing the (pseudoscaler) beam helicity with respect to the beam's momentum.

As the cross section is $\sigma \propto |\mathcal{M}^{\gamma} + \mathcal{M}^{Z}|^2$, the parity-violating asymmetry for the scattering of longitudinally polarized electrons from unpolarized protons is defined as the difference of the cross section measured for each beam helicity state divided by the sum:

$$A_{PV} \equiv \frac{\sigma_+ - \sigma_-}{\sigma_+ + \sigma_-}, \tag{2.49}$$

where $\sigma_{+,-}$ denotes the cross section for each helicity state. The measured parity-violating asymmetry can be written in terms of the electromagnetic and neutral weak proton form factors as [68]

$$A_p = -\frac{G_F Q^2}{4\pi\alpha\sqrt{2}} \frac{\epsilon G_E^{\gamma,p} G_E^{Z,p} + \tau G_M^{\gamma,p} G_M^{Z,p} - (1 - 4\sin^2\theta_W)\epsilon' G_M^{\gamma,p} G_A^e}{\epsilon (G_E^{\gamma,p})^2 + \tau (G_M^{\gamma,p})^2} \tag{2.50}$$

where $\epsilon = (1 + 2(1+\tau)\tan^2\frac{\theta_e}{2})^{-1}$, $\epsilon' = \sqrt{\tau(1+\tau)(1-\epsilon^2)}$, and $\tau = \frac{Q^2}{4M_p}$.

However, the parity-violating asymmetry seen in electron-proton scattering is very small. The small size of the asymmetry is because it is determined by the ratio of the neutral weak and electromagnetic propagators. As the ratio is $\frac{\mathcal{M}^{Z}}{\mathcal{M}^{\gamma}}$, and M_γ is larger than M_Z by about a factor of 10^5, the measured asymmetries are of order parts-per-million (ppm), making these experiments very challenging [27, 68].

The measured asymmetry has an angular kinematic dependence, making measurements of the asymmetry mostly sensitive to $G_E^{Z,p}$ and $G_M^{Z,p}$ at forward scattering angles, and predominantly $G_M^{Z,p}$ and G_A^e at backward scattering angles. The axial term vanishes at 0°, the electric term vanishes at 180°, and the magnetic term contributes independently of angle. Thus, it is possible to kinematically separate the electric and magnetic terms by conducting measurements of the parity-violating asymmetry at both forward and backward angles. This angular dependence is key in the strategy of the G^0 experimental program. The forward-angle measurement resulted in a determination of a linear combination of G_E^s and G_M^s. By then performing subsequent backward-angle measurements of G_M^s and G_A^e, the separation can be accomplished. However, in order to have enough information to do the separation, backward-angle angle measurements must be done on both hydrogen, which has an asymmetry that is sensitive to G_M^s and G_A^e, and deuterium, which has an asymmetry with an enhanced sensitivity to G_A^e. The asymmetry from a measurement with

a deuterium target can be expressed as a linear combination of the individual proton and neutron asymmetries weighted by their cross sections. As this makes it so that G_M^s and G_A^e have different contributions, there is enough information to make a complete separation when combined with the other two measurements.

Various experiments have measured the parity-violating asymmetry and have attempted to optimize the measurements for sensitivity to particular form factors. The G0 experiment performed forward-angle measurements at eighteen Q^2 points, as well as backward-angle measurements on hydrogen and deuterium at a couple of Q^2 values, in order to do a complete separation of the three unknown quantities (G_E^s, G_M^s, G_A^e) at these Q^2 values. This dissertation discusses the forward-angle measurement.

2.4 Electroweak Radiative Corrections

Although the first-order electromagnetic and neutral weak interactions are the processes of interest (and are the dominant ones), important higher-order electroweak processes do contribute to electroweak-nucleon scattering, and so there must be corrections made to account for them [81–83]. These higher-order processes are generally considered as small radiative corrections to the ordinary Z^0 exchange diagram, on the order of 1% corrections to the lowest order predictions [27]. However, these corrections do have some uncertainty. The uncertainty in the calculation of the contribution of these higher-order effects is an important systematic background for any experiment measuring strangeness effects.

These higher-order processes in effect modify the coupling constant (weak vector and axial charges) at the interaction vertex in the scattering diagrams. The radiative corrections account for this. The R values are the corrections made to the six weak charges. The R_V parameters (introduced in [68]) characterize the difference between the value of the parameters for the one-quark radiative corrections at the tree level and their full expressions. These corrections are classified into three types [68]: those due to one-quark processes, those due to many-quark processes, and

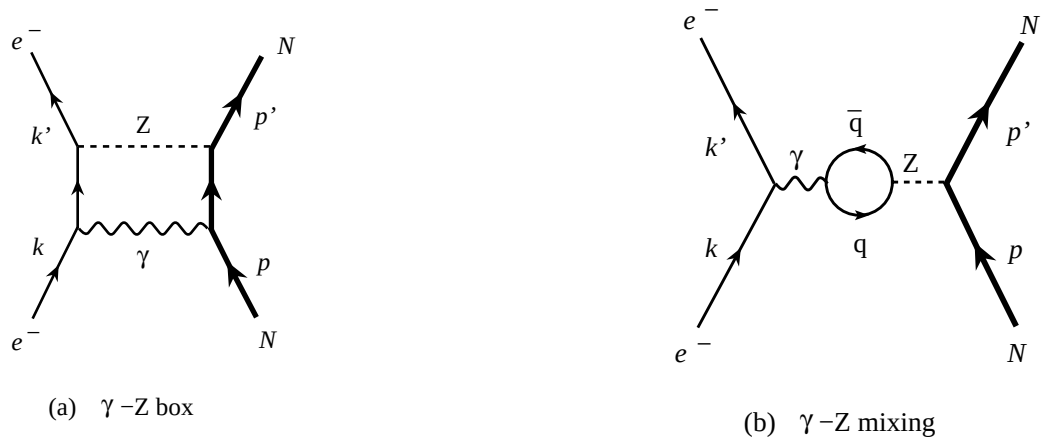

FIG. 2.2: *The Feynman diagrams describing two of the one-quark processes that contribute to the electroweak radiative corrections. Diagram (a) is a $\gamma - Z$ box diagram, while (b) pictorially describes $\gamma - Z$ mixing.*

those due to the heavy quark renormalization of light quark operators.

There is another aspect to be considered for these computations. To calculate these corrections, the theory has to use a renormalization scheme to make the calculations finite. The renormalization scheme used in this work is the modified minimal subtraction scheme ($\overline{MS}$), which is a widely used one, and depends on a renormalization scale μ that is generally set to the mass of the Z boson ($M_Z = 91.19$ GeV) [84].

One class of electroweak radiative corrections are classified as one-quark diagrams, because they involve interactions with only one quark in the hadron. A couple of these are depicted in Figure 2.2, but there are many more of these to higher and higher order. The first diagram is a $\gamma - Z$ box, while the second, the $\gamma - Z$ mixing diagram, is also referred to as the vacuum polarization correction due to its similarity to an analogous concept in QED. The corrections for these processes are purely electroweak and can be calculated fairly well in the Standard Model. They have a small Q^2 dependence [68,85]. For this work, it is assumed that the present calculations for the one-quark corrections are sufficiently reliable. The values of the one-quark standard-model parameters were taken from the Particle Data Book [86], where they were calculated in the $\overline{MS}$

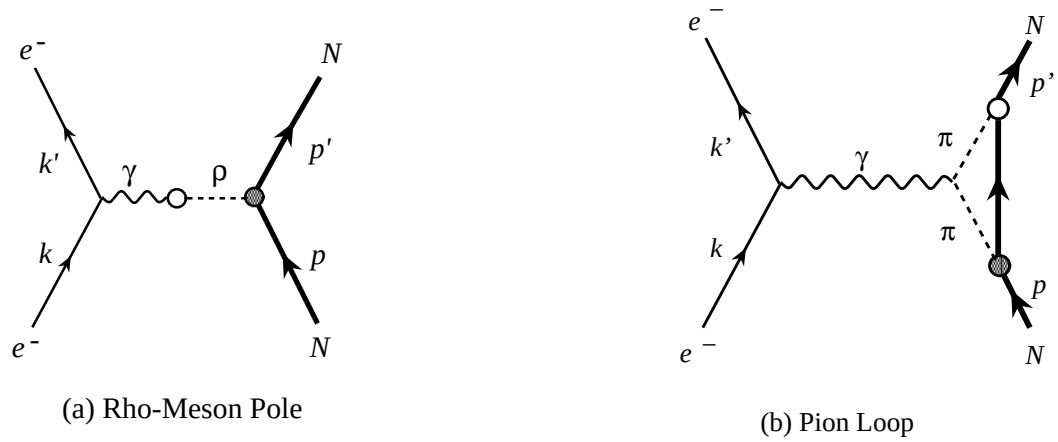

FIG. 2.3: *The Feynman diagrams describing two of the many-quark processes that contribute to the electroweak radiative corrections. Diagram (a) is a rho meson pole diagram, while (b) pictorially describes the pion loop process. The filled circles denote parity-violating meson nucleon vertices while the open circles represent parity conserving (strong and electromagnetic) vertices.*

scheme. However, there are still uncertainties involved with these calculations. For example, calculation of the $\gamma - Z$ box diagram involving only a nucleon intermediate state can be reliably calculated; full calculations of the $\gamma - Z$ box diagram must take into account excited hadronic states, which are not well understood [27].

Uncertainties from hadronic structure come from another class of electroweak corrections, the ones referred to as many-quark corrections. These many-quark corrections arise from interactions that involve more than one quark in the hadron, such as the exchange of (weak) Z bosons between the quarks during the scattering, which modifies the nucleon axial coupling. Some of these diagrams are sometimes referred to as anapole terms. An example of these types of diagrams can be seen in the pion loop in Figure 2.3, where a parity-violating pion emission occurs because of the weak interaction between the quarks. The pion is then absorbed through the strong interaction, which is parity-conserving. Unfortunately, these are difficult corrections to calculate, as the strong coupling constant α_S is too strong in this kinematic region to use perturbative QCD. Hadronic models then must be used to calculated these corrections, leading to rather large uncertainties as it is impossible to include all virtual hadronic states. Happily, the contribution of the many-quark processes only

Factor	Value	Factor	Value
$\sin^2\theta_W$	0.23120	g_A	1.2545
G_F	1.16637×10^{-5}	Δs	-0.084 ± 0.040
$R_V^{T=1}$	-0.0140914	$R_A^{T=1}$	-0.1727633
$R_V^{T=0}$	-0.0091121	$R_A^{T=0}$	-0.2526596
$R_V^{(0)}$	-0.0111789	$R_A^{(0)}$	-0.5517526
R_V^p	-0.0447091	R_V^n	-0.0117890

TABLE 2.2: *Electroweak radiative correction factors [82, 83]; values taken from the Particle Data Book, 2004 [86] and are evaluated in the $\overline{MS}$ renormalization scheme.*

affect the axial contribution. Zhu *et al.* performed a calculation of the "anapole" correction to the axial form factor using heavy baryon chiral perturbation theory (HBχPT) to compute the many-quark diagrams, yielding values of $R_A^{T=1} = -0.087(0.35)$ and $R_A^{T=0} = -0.015(0.20)$ [85].

The heavy quark corrections come from the fact that the heavier quark flavors (c, b, and t) were neglected in the calculations for the hadronic (neutral current coupling) currents. Happily, these effects are very small when calculated, only $\Delta v < 10^{-4}$ for the vector coupling and $\Delta A < 10^{-2}$ for the axial coupling [40], and so these contributions are considered negligible.

With all the radiative corrections, the parity-violating asymmetry on the proton can be written as (Q^2 dependences dropped for clarity) [82, 83]

$$\begin{aligned} A(ep) = -\frac{G_F Q^2}{4\pi\alpha\sqrt{2}} \Bigg\{ & (1-4\sin^2\theta_W)(1+R_V^p) - (1+R_V^n)\frac{\epsilon G_E^p G_E^n + \tau G_M^p G_M^n}{\epsilon (G_E^p)^2 + \tau (G_M^p)^2} \\ & -(1+R^{(0)})\frac{\epsilon G_E^p}{\epsilon (G_E^p)^2 + \tau (G_M^p)^2} G_E^s - (1+R^{(0)})\frac{\tau G_M^p}{\epsilon (G_E^p)^2 + \tau (G_M^p)^2} G_M^s \\ & -\frac{(1-4\sin^2\theta_W)\epsilon' G_M^p}{\epsilon (G_E^p)^2 + \tau (G_M^p)^2} G_A^e \Bigg\}, \end{aligned} \tag{2.51}$$

where $\tau = \frac{Q^2}{4M_p^2}$, $\epsilon = \frac{1}{1+2(1+\tau)\tan^2\frac{\theta}{2}}$, $\epsilon' = \sqrt{\tau(1+\tau)(1-\epsilon^2)}$, θ is the laboratory electron scattering angle, M_p is the proton mass, and

$$G_A^e = -2(1+R_A^{T=1})G_A^{T=1} + \sqrt{3}R_A^{T=0}G_A^{(8)} + (1+R_A^{(0)})G_A^s, \tag{2.52}$$

and some of the numerical values for the calculations are shown in Table 2.2.

2.5 Theoretical Predictions for Strange Form Factors

In spite of the theoretical difficulties, there have been many efforts to calculate the strange-quark contributions to nucleon properties (for reviews, see References [27, 68–70], for example). Unfortunately, calculations for strange quark effects are in the realm of non-perturbative QCD since $m_s \sim \Lambda_{QCD}$, so estimations have been done using a variety of methods that include various theoretical models and lattice calculations. Many of the estimates focus on estimating the contribution to the strange magnetic moment, μ_s, and the strangeness radius, ρ_s, as these values quantify the contribution at $Q^2 = 0$, that is,

$$\mu_s = G_M^s(Q^2 = 0); \quad \rho_s \equiv \left.\frac{dG_E^s}{d\tau}\right|_{\tau=0}, \tag{2.53}$$

where $\tau = \frac{Q^2}{4M^2}$. The strange charge radius is commonly used as well, which has dimensions of length (unlike ρ_s, which is dimensionless):

$$\langle r_s^2 \rangle = -6\left.\frac{dF_1^s}{dQ^2}\right|_{Q^2=0}; \quad \rho_s = -\frac{2}{3}M_p^2\langle r_s^2\rangle - \mu_s, \tag{2.54}$$

although one must be careful in how it is interpreted [70, 87]. This section will give an overview of the efforts to estimate strange quark effects, starting with calculations using various models of the nucleon to estimate the strangeness content and ending with lattice QCD calculations, which employs first-principles to describe the existence of the $s\bar{s}$ pairs in the sea through gluon splitting.

2.5.1 Heavy Baryon Chiral Perturbation Theory (HBχPT)

The obvious choice to use to estimate strange form factors would be Heavy Baryon Chiral Perturbation Theory (HBχPT). Chiral perturbation theory has been used for some time very effectively to predict and interpret a variety of low-energy properties of the nucleon.

However, to calculate strangeness effects, HBχPT must be extended from SU(2), which only has the u and d quarks, to SU(3). The idea is that in the limit where the light quark masses (u, d, and s) vanish, the QCD Lagrangian possesses an exact $SU(3)_L \times SU(3)_R$ symmetry [27], which can then be used to relate a set of observables to another, or to use a set of measured quanti-

ties to predict another [88]. By including the kaon loops, addition counterterms are introduced, and although most of these can be constrained by the experimental electromagnetic moments of the baryon octet, two of the counterterms are flavor-singlet counterterms that require knowledge of strangeness radius and magnetic moment, as these counterterms contain the information on short-distance hadronic effects that cannot be determined from existing measurement using chiral symmetry. The leading, long-distance loop contributions for the strangeness magnetic moment and radius are calculable, but it is unknown whether the leading order effects are dominant over the unknown terms from the same or lower order from the chiral Lagrangian [88]. This creates a situation where the answer must be measured to calculate the answer, which isn't terribly helpful. Because of this, HBχPT cannot be used to predict nucleon strangeness [88]. Thus, to make predictions for the nucleon's strangeness moments, additional model-dependent assumptions must be made.

However, even with this rather severe limitation, it is possible to get some information out of HBχPT. Hemmert, Meissner and Steininger found that the Q^2 behaviour of G_M^s is dictated by the kaon loop diagram up to the order of $p^3(\mathcal{O}(p^3))$ in the chiral expansion. This diagram has an analytical and parameter free form [89]. Hemmert, Kubis and Meissner then derived an expression of $G_M^s(Q^2)$ to $\mathcal{O}(p^3)$ in terms of the two unknown counterterms, which they constrained using the data from SAMPLE and HAPPEx (see Chapter 3). By doing this, they obtained values of $\langle r_s^2 \rangle_E = 0.05 \pm 0.09$ fm^2 for the strangeness radius and $\mu_s \sim 0.18$ n.m. for the strangeness magnetic moment [90]. When extended to $\mathcal{O}(p^4)$, though, the calculation indicated a significant amount of cancellation between the $\mathcal{O}(p^3)$ and $\mathcal{O}(p^4)$ contributions [91]. Because of this, the Q^2 slope of the strange magnetic moment is very sensitive to the unknown coefficient of the $\mathcal{O}(p^4)$ counterterm, and so the sign and magnitude of μ_s are not well constrained by the calculation.

The unknown counterterms makes the use of chiral perturbation theory to calculate the strange contributions very difficult. However, by making model assumptions about the underlying physics, estimates can be made, as we will see in the next sections.

2.5.2 Vector Meson Dominance (VMD)

Although chiral perturbation theory cannot be used alone to calculate predictions for strangeness properties of the nucleon, it can be used as a framework for calculation, with the assumption of model-dependent method used to estimate the size of the chiral counterterms [27]. One approach that has proven to be useful is to estimate the size of the counterterms by using vector and axial-vector meson exchange contributions, or Vector Meson Dominance (VMD). The principle is that the photon in an interaction can fluctuate electromagnetically into an intermediate vector meson, which is a neutral, spin-1, parity-odd meson. The vector meson then interacts via the strong force with the hadron, as illustrated in Figure 2.4. The lightest vector mesons and their approximate quark compositions are

$$\rho_0\ (770\ \text{MeV}) = \frac{1}{\sqrt{2}}(u\bar{u} - d\bar{d}), \quad \omega_0(783\ \text{MeV}) = \frac{1}{\sqrt{2}}(u\bar{u} + d\bar{d}), \tag{2.55}$$

$$\phi_0(1020\ \text{MeV}) = s\bar{s}. \tag{2.56}$$

The ρ is an isovector meson; ω and ϕ are isoscaler mesons.

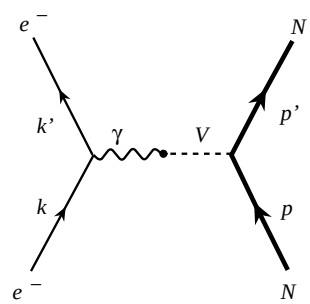

FIG. 2.4: *Feynman diagram illustrating vector meson dominance, where the photon fluctuates into an intermediate vector meson, V, which interacts with the hadron.*

Using VMD, the nucleon matrix element $\langle N|\hat{\mathcal{J}}^{\mu}_{EM}|N\rangle$ is expressed as the summation over intermediate vector states by

$$\langle N|\hat{\mathcal{J}}^{\mu}_{EM}|N\rangle = \sum_V f_V \frac{1}{m_V^2 - q^2}\langle N|V^{\mu}|N\rangle, \tag{2.57}$$

where m_V is the mass of the intermediate meson V, $q^2 < 0$ is the four-momentum transfer squared of the photon, and f_V is the vector meson photon coupling constant. The couplings f_V that are associated with the strange matrix elements $\langle 0|\bar{s}\gamma_\mu s|V\rangle$, where $\langle 0|$ is the vacuum state, could be used to derive the information we seek; however, those couplings are unknown.

However, the flavor content of the vector meson wavefunctions is known, and by assuming vector meson dominance, dispersion relations for the nucleon form factors can be expressed as [27, 88]

$$F_1^a(q^2) = F_1^a + \sum_V \frac{q^2 a_V^a}{m_V^2 - q^2} \tag{2.58}$$

$$F_2^a(q^2) = \sum_V \frac{m_V^2 b_V^a}{m_V^2 - q^2}. \tag{2.59}$$

Höhler *et al.* [92, 93] determined the residues at the vector meson poles by a global three-pole fit (of electron-nucleon scattering cross section data), where they identified the first pole as the ω, the second as the ϕ, and the third as a higher mass vector meson V' to take into account any contributions from higher resonances. With the residues, the counterterms are evaluated as

$$b^a = \left(\frac{\Lambda_\chi}{2M_N}\right) \sum_V b_V^a \tag{2.60}$$

$$c^a = \sum_V \left(\frac{\Lambda_\chi}{m_V}\right)^2 a_V^a. \tag{2.61}$$

Their results implied a significant strangeness contribution, which was argued by Jaffe [94]. Mergell *et al.* [95] used this same method in an updated version of this analysis, although with the inclusion of constraints from perturbative QCD and unitarity. The analysis supported the earlier conclusions.

Jaffe [94] evaluated the strange residues at the ω, ϕ poles in terms of the isoscaler electromagnetic residues by

$$\frac{a_\omega^s}{a_\omega^{I=0}} = -\frac{\sqrt{6}\sin\epsilon}{\sin(\epsilon + \theta_0)} \tag{2.62}$$

$$\frac{a_\phi^s}{a_\phi^{I=0}} = -\frac{\sqrt{6}\cos\epsilon}{\cos(\epsilon + \theta_0)}. \tag{2.63}$$

The term $\epsilon = 0.053 \pm 0.005$ is the mixing angle between the ω, ϕ states and the pure vector meson

states:

$$\omega = \cos\epsilon\omega_0 - \sin\epsilon\phi_0, \quad \phi = \sin\epsilon\omega_0 + \cos\epsilon\phi_0. \tag{2.64}$$

The term $\theta_0 = \tan^{-1}\frac{1}{\sqrt{2}}$ is the "magic" angle of octet-singlet mixing that gives the flavor pure states ω_0 and ϕ_0. To obtain the strange residues for the higher mass vector state, Jaffe made the assumption that the form factor F_1 vanishes as $\frac{1}{q^2}$ and that F_2 vanishes as $\frac{1}{q^4}$; he then applied the pole residuals from Höhler's fits. By doing this, he obtained values of $\mu_s = -0.31 \pm 0.09$ and $\langle r_s^2 \rangle_E \sim 0.14 \pm 0.09$ fm^2. An updated analysis was performed by Hammer, Meissner, and Drechsel that was based on the Mergell fit [96]. From this analysis, they obtained $\mu_s = -0.25 \pm 0.03$ and $\langle r_s^2 \rangle_E = 0.22 \pm 0.03$ fm^2. Forkel also made a similar calculation, which was in good agreement with the other results [97].

Ramsey and Ito [88] calculated the leading, non-analytic loop contribution from χPT using the ω and ϕ pole residuals from Höhler's isoscaler fit [92] to constrain the counterterms. This approach yielded results of $\mu_s = 1.85$ for the strangeness moment and $\langle r_s^2 \rangle_E \sim 0.36$ fm^2 for the strangeness radius, a somewhat larger result than the three-pole fits [94, 96]. This arises from a lesser cancellation between the ϕ pole and the continuum than that between the ϕ and the third higher mass poles in the other analysis approaches. The large value of μ_s comes from the large kaon loop contribution to the isoscaler anomalous magnetic moment, which requires large counterterms to balance it.

There are some caveats with this approach, however. The values obtained are very sensitive to the $\omega - \phi$ mixing angle ϵ and to the representation of the form factors in terms of three poles, especially the second resonance with the ϕ due to its large strangeness content. The representation of the high-energy continuum as a zero-width pole raises some concern, and Forkel has shown that using QCD asymptotics reduces the size of the strangeness couplings from the three-pole results by a factor of two to three [97]. In addition, the asymptotic constraints used in the three-pole calculation requires the inclusion of more poles with unknown masses and residues to be consistent with quark counting rules, leading to even more ambiguity [88].

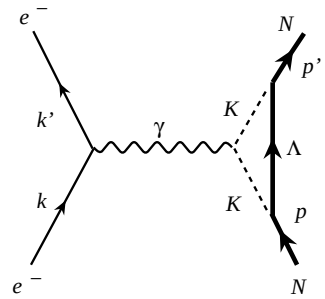

FIG. 2.5: *Feynman diagram illustrating kaon loop calculations, where the nucleon fluctuates into a kaon and a hyperon (a Λ), where the photon can couple to either, and then fluctuates back to the original proton.*

2.5.3 Kaon Loop Models

Another approach to compute strangeness matrix elements is to just disregard the requirement of a consistent chiral expansion and include a kaon loop contribution. This model is intuitively simple, where the strangeness of the proton is modeled by a meson-hyperon intermediate state that can interact with the exchange photon or Z. This only requires that the nucleon fluctuates into a kaon (K) and a hyperon (Y), where the photon can couple to either, and then the s and $\bar{s}$ quarks annihilate, leaving the original proton, as shown in Figure 2.5. This type of model is sometimes called the kaon cloud model, as the kaon is further away from the center of the nucleon due to its smaller mass compared to the hyperon. As the s and $\bar{s}$ quarks are spatially separate, there is an asymmetric and non-zero strange charge and magnetization distribution within the proton. An interesting feature of these calculations is that because the kaon is on the outside and has a negative strangeness, this would make the strangeness radius negative, neglecting recoil effects [98]. The $K - \Lambda$ fluctuation could also make μ_s negative [99].

However, this procedure introduces divergences, so a cutoff procedure must be used. Donoghue and Holstein suggested the introduction of a dipole regulator into the chiral loop [100, 101]

$$F(q^2) = \left(\frac{\Lambda^2}{\Lambda^2 - q^2}\right)^2, \tag{2.65}$$

where q is the loop momentum and Λ is the cutoff scale. They showed that by doing this, the chiral structure was maintained; however, consistent power counting was lost. Also, contact or seagull terms must be introduced to satisfy the Ward-Takahashi identities and preserve gauge invariance, which introduces some ambiguity in the choice of terms that can result in a large spread in the final calculations [102]. There is also a cutoff scale dependence [88].

Several calculations have been done using this method. Ramsey-Musolf and Burkardt [102] performed the calculation using a $K\Lambda$ loop and the phenomenological meson-baryon form factors from the Bonn-Jülich potential at the hadronic vertices to prevent UV divergence. Seagull terms were used to preserve gauge invariance, and the cutoff scale was chosen to have a range of 1 to 2 GeV. The results gave a moderately negative value for the strangeness moment $\mu_s = -0.31 \pm 0.05$ n.m., as well as for the strangeness charge radius, $\langle r_s^2 \rangle_E = -0.03 \pm 0.003$ fm^2.

A somewhat different approach was taken by Pollock, Koepf, and Henley, who performed a calculation of strangeness moments using a cloudy bag model [103]. The cloudy bag model is based on the earlier MIT bag model [104]. In this model, weakly-interacting quarks are confined in bags (or bubbles) of perturbative vacuum. The bags are stabilized from collapsing to the QCD vacuum phase by the pressure from the Heisenberg energy of the quark states [27]. No free quarks exist outside of the bag. Unfortunately, this model breaks chiral symmetry. The cloudy bag model takes the MIT bag and repairs the broken chiral symmetry at the bag's surface by introducing a pion (meson) field that couples to the confined quarks [105,106]. The inverse of the bag dimension then sets the cutoff parameter. Using this model with a bag radius of about 1.1 fm, determined by fitting experimental nucleon EM form factors, they determined values of $\mu_s = -0.026$ n.m. and $\langle r_s^2 \rangle_E = -0.012$ fm^2 [103].

Cohen, Forkel, and Nielson proposed an approach that combines the kaon loop method with the vector-meson dominance approach [98,107]. The results of the two methods cannot simply be added together, as double counting issues then arise. Instead, they calculated the intrinsic nucleon strange matrix elements by kaon loops and the isoscalar matrix elements using Höhler's empirical

fits, which were then mixed using the VMD assumption with only ω and ϕ poles. Because of the mixing, both the intrinsic component and the vector meson mixing contribute. This method yielded results of $\mu_s \sim -0.28$ n.m. and $\langle r_s^2 \rangle_E = -0.042$ fm^2. However, this analysis is very sensitive to the size of the $\omega - \phi$ mixing parameter ϵ [27]. Meissner *et al.* also performed a calculation using a combination of the kaon loop and VMD models [108]. In this treatment, the excited intermediate states with K^* and Σ were included in the $K - \Lambda$ loop, but $\omega - \phi$ mixing was neglected. This calculation yielded results of $+0.003$ n.m. and $+0.002$ fm^2 for μ_s and $\langle r_s^2 \rangle_E$.

Despite its appealing intuitive simplicity, other authors have questioned some of the assumptions of the kaon loop calculations. Malheiro and Melnitchouk raised the concern that the one-meson current used in the method violates Lorentz covariance [109] and showed that contributions from this violation cause the calculated value of μ_s to become small and positive at $+0.01$ n.m. [109]. A quark-level calculation that included the OZI allowed intermediate loops of $K^* - Y^*$ by Geiger and Isgur yielded values of $\mu_s \sim +0.035$ n.m. and $\langle r_s^2 \rangle_E \sim -0.04$ fm^2 [110], although they noted that the signs arise from the cancellations of large contributions from many intermediate states. Barz *et al.* then made a complementary hadronic calculation of the K^* contribution by using both a one-loop calculation and a dispersion analysis [111], which confirmed the findings of [110] that the K^* can have as significant a contribution as the K.

2.5.4 Skyrme Model and Other Soliton Models

The Skyrme model was one of the first methods used to calculate strangeness effects. In the 1960's, Skyrme presented the idea that baryons are solitons in the non-linear sigma model [112]. Some twenty-years later, Witten took the model and showed that QCD becomes equivalent to an effective field theory of mesons at the limit of a large number colors (large N_c QCD) [113, 114], laying the groundwork for the successful calculation of various static nucleon properties by Adkins *et al.* under the Skyrme model [115].

The Skyrme Lagrangian is

$$\mathcal{L} = \frac{1}{16}F_\pi^2 \mathrm{Tr}(\partial_\mu U \partial_\mu U^\dagger) + \frac{1}{32e^2}\mathrm{Tr}\left[(\partial_\mu U)U^\dagger, (\partial_\nu U)U^\dagger\right]^2, \tag{2.66}$$

where U is an SU(2) matrix, F_π is the pion decay constant, and the entire last term was introduced to stabilize the solitons [115]. From this Lagrangian, the soliton solution is found

$$U_0(x) = \exp\left[iF(r)\vec{\tau}\cdot\hat{x}\right], \tag{2.67}$$

where we have used what is known as the hedgehog ansatz and have forced the boundary conditions as $F(0) = \pi$ and $F(\infty) \to 0$. Using variational methods, this system can be solved and used to successfully describe various aspects of nucleon structure.

However, the extension of this SU(2) Skyrme model approach to SU(3) and thus include strangeness effects is not a trivial exercise. Additional model dependence must be introduced [116–118], and the various treatments used contain ambiguities [119]. In addition, SU(3) flavor symmetry breaking becomes an issue. To deal with this problem, Weigel, Schechter and Park [119] introduced terms involving nonminimal derivative couplings into the Lagrangian. After the quantization of the collective and radial excitations, they diagonalized the Hamiltonian, treating the symmetry breaking term exactly. The results of this yielded moderate negative values for both the strangeness charge radius and magnetic moment of $\langle r_s^2\rangle_E = -0.11$ fm^2 and $\mu_s = -0.13$ n.m., respectively.

This calculation only considered pseudoscalar mesons; in further studies Park and Weigel [120] added vector mesons into the model. The results of the studies showed a drop in the magnitudes of both quantities by a factor or two, with a change of sign in the strangeness radius. This discrepancy indicates some of the uncertainty in the Skyrme model predictions.

There are other concerns about the accuracy of Skyrme model predictions in addition to concerns about ambiguities introduced by the extension to SU(3). The Skyrme model is justified in the large N_c limit of QCD, casting doubt as to the accuracy of predictions of quark sea effects in the real $N_c = 3$ world. In the Skyrme model, the strangeness current is evaluated by taking

the difference between the baryon number and hypercharge currents $J^s_\mu = J^B_\mu - J^Y_\mu$, leading to a situation where the predictions for strangeness matrix elements are obtained by taking the (small) difference of two large and uncertain quantities. This casts doubt as to their reliability [27, 98].

There is a related approach to the Skyrme model called the chiral soliton-quark model. In this model, the interaction of the quarks with the chiral fields is described with a linear sigma Lagrangian for which a stable soliton solution for the meson fields can be found by imposing the same hedgehog ansatz. As with the Skyrme model, the soliton solution is identified as a baryon. Again, as with other models, the extension to SU(3) to include strangeness is not trivial, and these models share many of the same potential concerns as the Skyrme models.. Calculations of strangeness effects using the chiral soliton-quark model were done by Silva, Kim, and Goeke [121], and they reported results of $\mu_s \sim 0.12$ n.m. for the strange magnetic moment and $\langle r^s_s \rangle_E \sim -0.1$ fm^2 for the strangeness radius. Another closely related method is to bosonize the NJL model (a description of which is at the end of Section 2.5.5), which gives a Lagrangian that can be solved by Skyrme methods to get the stable soliton solution, although with some model dependence [122].

2.5.5 Constituent Quark Approach

Another method that can be used to calculate strange quark effects is called the constituent quark approach. The idea of this method is to account for the internal quark structure of the nucleon by representing it in terms of constituent (U, D) quarks whose substructure consists partly of $s\bar{s}$ pairs. This came about from the suggestions of Kaplan and Manohar [40].

The problem is how to take the quark sea structure into account. One way is to assume that the constituent quarks are themselves coupled to mesons by a chiral quark method. Using this concept, studies by Ramsey-Musolf and Ito estimated the effect of constituent U and D quarks fluctuating into a kaon and a constituent S quark [88]. To determine the axial coupling of the constituent quark to the kaon, the constituent quark calculation of the nucleon's axial charge with its experimental value in neutron beta decay of $g_A \simeq 1.27$. The results for both μ_s and $\langle r^2_s \rangle_E$

are small and negative. However, the calculation has model-dependent assumptions. As such loop calculations are themselves divergent and the singlet channel quantities are unknown, a hadronic form factor with a cutoff scale $\Lambda = \Lambda_\chi$ was introduced to avoid infinities, and the validity of the simple one-loop kaon approximation was assumed.

Hannelius, Riska, and Glozman further extended this chiral quark model framework by including contributions from pseudovector K^* loops and $K - K^*$ radiative transition loops [99, 123]. The vector loops serve to help stabilize the calculation from sensitivity to the size of the regulator provided that a cutoff of order the chiral symmetry breaking scale is chosen. The loops did not add significant strangeness, and the resulting strangeness moments are $\mu_s = -0.05$ n.m. and $\langle r_s^2 \rangle_E = 0.02$ fm^2, where there was also a substantial cancellation between the kaon and K^* loop contributions. In addition to the uncertainty from the remaining cutoff dependence, there is uncertainty introduced because of the loop diagram involving the $K - K^* - \gamma$ vertex. Another calculation was done by Lyubovitskij *et al.* using the perturbative chiral quark model [124], which treated the valence quarks as though moving in a perturbative Goldstone meson cloud. To determine the cutoff scale of the effective confinement field the quarks feel, a fit is done to the charge radius of the proton, much like above. The one-loop perturbative calculation then yielded values of μ_s and $\langle r_s^2 \rangle_E$ that were small and negative, and in agreement with [88].

Unfortunately, the chiral quark model has an additional concern other than the usual model dependencies that plague everybody else: double-counting, because it is unknown whether the $Q\bar{Q}$ bound states in the theory should be separated from the Goldstone bosons or not [88].

Another approach to tackle the question of how to take the quark sea structure into account is to use the Nambu Jona-Lasinio (NJL) model [125]. This model is an effective field theory that involves relativistic fermions that interact through four-point vertices that respect chiral symmetry. The idea is that if a massless quark is exposed to a nonzero $\langle q\bar{q} \rangle$ condensate, it becomes a massive pseudoparticle, the constituent quark, breaking chiral symmetry. To introduce strangeness into the constituent quarks, there must be a flavor mixing interaction, which was done [126, 127] through

a mean field approximation to the NJL model, where the terms come from 6-quark interactions involved in the determinant. Forkel *et al.* performed a calculation using this method, and obtained a strangeness charge radius of $\langle r_s^2 \rangle_E = +0.0169$ fm^2 [98]. A related approach is to bosonize the NJL model, and then solve the effective topological soliton by Skyrme methods [122].

2.5.6 Dispersion Relations

Yet another way to calculate strangeness content is by using dispersion relations. This technique shares a similarity to the use of effective field theory, as both are based in general principles, although in the case of dispersion relations those principles are causality and analyticity instead of chiral symmetry as in chiral perturbation theory.

Working with the standard Dirac and Pauli form factors $F_1^{(s)}$ and $F_2^{(s)}$, we can write the mean square strangeness radius and magnetic moment as [128]

$$\langle r_s^2 \rangle = 6 \frac{dF_1^{(s)}}{dQ^2}\bigg|_{Q^2=0}, \tag{2.68}$$

$$\mu_s = F_2^{(s)}(0). \tag{2.69}$$

To obtain the dispersion relation for the $F_i^{(s)}(t)(i = 1, 2)$, where t is real, assumptions must be made that an analytic continuation $F_i^{(s)}(z)$ exists in the upper half plane that approaches $F_i^{(s)}(t)$ as $z \to t + i\epsilon$, has a branch cut on the real axis for t greater than some threshold t_0, and that $\frac{F_i^{(s)}(z)}{z^n} \to 0$ as $z \to \infty$ for non-negative integers n in the upper half plane. Cauchy's theorem then yields these relations:

$$F_1(t) = F_1(0) + \frac{t}{\pi} \int_{t_0}^{\infty} \frac{Im[F_1(t')]}{t'(t'-t)} dt', \tag{2.70}$$

$$F_2(t) = \frac{1}{\pi} \int_{t_0}^{\infty} \frac{Im[F_2(t')]}{(t'-t)} dt'. \tag{2.71}$$

In this case, $F_1^{(s)}(0) = 0$, as the nucleon carries no net strangeness, and the unsubtracted dispersion relation is used for $F_2^{(s)}(t)$ since one would like to predict the value of the magnetic form factor at $t = 0$. The integral can be represented by the sum over all possible stable intermediate states. The threshold t_0 is the production threshold of the lowest possible intermediate state. The $Im[F_{1,2}(t')]$

are often called the spectral functions, as they imply dynamical contributions to the form factors from the intermediate states. The general dispersion relation includes all possible on-shell intermediate states, unlike VMD, which only includes a few off-shell vector meson resonance [129]. For the isoscalar and strangeness form factors, the allowable continuum includes 3π, 5π, $K\bar{K}$, $N\bar{N}$, etc. Naturally, the $K\bar{K}$ is generally focused on, as it is the lightest state containing strangeness. The first evaluation of this was done by Ramsey-Musolf, Hammer and Drechsel [128]. The contribution of $K\bar{K}$ to the strangeness spectral function can be written in terms of a product of the amplitudes of $\gamma \to K\bar{K}$ and $K\bar{K} \to N\bar{N}$; however, direct data exist only when $t > 4m_N^2$, forcing the need for models or extrapolation. In [130], the authors addressed this problem by calculating the scattering amplitudes of $K\bar{K} \to N\bar{N}$ under the Born approximation in both the physical and unphysical regions.

Ramsey-Musolf and Hammer further refined this analysis in following papers [128, 129, 131]. Instead of using the Born approximation in the unphysical region, they used an analytical continuation of the experimental $K - N$ scattering amplitudes. They reported results of $\mu_s \sim 0.28$ n.m. and $\langle r_s^2 \rangle_E \sim 0.42$ fm^2 in Ref [131].

However, there are some issues with this method. Unlike χPT, dispersion relations do not involve a systematically controlled approximation. The assumption that the lowest OZI-allowed state $K\bar{K}$ is the dominant contribution to the continuum may not be entirely true. Despite being OZI violating processes, the contributions from light multi-meson intermediate states could be significant. It was shown by Hammer and Ramsey-Musolf that the effects of $3\pi \to \omega$ or $3\pi \to \rho\pi \to \phi$ can enhance the 3π contribution up to the same scale as the $K\bar{K}$ continuum [132].

2.5.7 Lattice QCD

There is another approach, very different than the hadronic-type models described above, where observables from strongly interacting field theories such as μ_s and r_s are numerically calculated numerically from first principles. This is know as lattice QCD (or LQCD). This method

is non-perturbative and computational, and is done by applying QCD on a discrete lattice of space-time points.

Lattice field theory is based on the idea of Feynman's path integral [84,133], where a functional integral over fields on a lattice is used to approximate Green's functions, allowing the calculation of physical observables [84,134]. By introducing a discretely-spaced lattice to replace the continuum, the inverse of the lattice spacing provides a natural momentum cutoff, eliminating the possibility of unphysical infinities. In addition, because of the finite number of lattice sites, numerical computation becomes computationally possible. LQCD calculations converge much more rapidly with large quark masses. As a result, the calculations are done at several large quark masses, then extrapolated using χPT to the masses of physical quarks, usually by a technique called chiral extrapolation.

The primary allure of LQCD is that it should be free of the model dependencies that plague the other hadronic models. However, it suffers from a limiting unwieldiness, as the application of LQCD to computing the contributions from $q\bar{q}$ loops and using quarks with their physical masses is at present computationally prohibitive. As computers improve, so does the ability to do LQCD calculations. To make up for this computational limitation, many of the LQCD calculations use the quenched approximation, where quarks are assumed not to be dynamical, so these calculations of the QCD sea effects have uncertainties.

There have been several calculations using LQCD. Dong, Liu, and Williams calculated values (in the quenched approximation, with a simple extrapolation to physical valence masses) of $G_M^s(0) \equiv \mu_s = -0.36 \pm 0.20$ and $\langle r_s^2 \rangle_E = -0.061 \pm 0.003 \rightarrow -0.16 \pm 0.06$ fm^2 [135]. After improving their Monte Carlo technique, they reported an updated value of $\mu_s = -0.28 \pm 0.10\ \mu_N$ [136]. Lewis, Wilcox, and Woloshyn performed calculations of strangeness effects using a quenched chiral extrapolation, reporting a value of $\mu_s = 0.05 \pm 0.06$ [137]. Leinweber *et al.* [138] took a different approach, combining the constraints of charge symmetry with new chiral extrapolation techniques and low-mass quenched lattice QCD simulations to account for the difference between the quark

Type of Calculation	μ_s (μ_N)	r_s^2(fm^2)	Reference
HBχPT	~ 0.18	0.05 ± 0.09	[90]
VMD	-0.31 ± 0.09	$\sim 0.14 \pm 0.09$	[94]
VMD	-0.25 ± 0.03	0.22 ± 0.03	[96]
χPT+VMD	1.85	~ 0.36	[88]
Kaon Loop	-0.31 ± 0.05	-0.03 ± 0.003	[102]
Cloudy Bag Model	-0.026	-0.012	[103]
Kaon Loop and VMD	~ -0.28	-0.042	[98, 107]
Kaon Loop and VMD	$+0.003$	$+0.002$	[108]
Skyrme Model	-0.13	-0.11	[119]
Chiral Soliton	~ 0.12	~ -0.1	[121]
NJL Soliton Model	$-0.05 \leq \mu_s \leq +0.25$	$-0.25 \leq r_s^2 \leq -0.15$	[122]
Chiral Quark	-0.05	0.02	[123]
Dispersion Relations	~ 0.28	~ 0.42	[131]
Lattice QCD	0.05 ± 0.06	—	[137]
Lattice QCD	-0.046 ± 0.019	—	[138]

TABLE 2.3: *A brief summary of some of the theoretical predictions for μ_s and r_s^2.*

masses in the calculation and their physical values. Using the ratios of the valence u quark contribution to the magnetic moment of the proton and neutron to the Σ^+ and Ξ^0 (respectively), the experimentally measured values of the baryon moments, and charge symmetry, they obtained a result of $-0.046 \pm 0.019\ \mu_N$.

As the lattice QCD calculations become more precise due to improvements in lattice techniques, and chiral extrapolation techniques, as well as advances in computing power, precision measurements will certainly be needed to guide the theoretical progress.

2.6 Summary of Estimates of Strangeness

This section has provided a brief overview of a sampling of the calculations for strange quark contributions to nucleon structure using a variety of theoretical models, and although far from exhaustive, it does give an idea of the various flavors of models employed to estimate strange quark effects on the nucleon's charge and magnetic properties, as well as the rather wide range of the predictions. Some of the uncertainties and limitations of these different approaches have been remarked upon as well. A summary of the results of some of these calculations is shown in Table

2.3 for the convenience of the reader.

2.7 Two Photon Exchange in Elastic Electron-Nucleon Scattering

The rest of this chapter discusses the theory behind the second measurement that is covered in this dissertation. Elastic electron-nucleon scattering has been used very successfully for several decades to study hadron structure. The electromagnetic interaction provides a powerful tool to investigate nucleon structure, and experiments measuring the form factors of the nucleon historically have successfully made use of the Born approximation, where only a single photon is exchanged. The elastic electromagnetic form factors of the nucleon characterize its internal structure, describing the charge and current distributions within it. However, as the measurements have become more precise, it has become apparent that the neglected higher-order processes have become a more significant systematic uncertainty, motivating the need for theoretical understanding and experimental characterization.

The primary goal of the G^0 experiment is to measure the parity-violating asymmetries from the elastic scattering of longitudinally-polarized electrons from unpolarized protons in order to use these asymmetries to determine the contribution of strange sea quarks to the charge and magnetization of the nucleon. However, the experiment included the taking of data from which other very interesting and important physics can be extracted about the electromagnetic probe in the elastic scattering of electrons from protons.

In addition to the primary parity-violating measurement, the experiment also performed a measurement of asymmetries using a beam polarized transversely to the beam motion, in order to determine the possible contribution of any systematic false asymmetry in the longitudinal measurement that would arise from any residual transversely-polarized beam component. Unlike the parity-violating longitudinal (i.e. helicity-dependent) asymmetry, the transverse beam single-spin asymmetry is a parity-conserving quantity that arises from two-photon exchange or higher-order processes. Although the two-photon exchange contribution is small, it can be comparable to

the parity-violating elastic electron-nucleon scattering asymmetry [64], and recent parity-violation measurements have had to consider possible systematic corrections due to this effect. However, the data of this measurement is very interesting for much more than a systematics check, as it contains valuable information on two-photon exchange physics. These data are of interest because as experiments in electron scattering are reaching higher levels of precision, the need has arisen to understand these higher-order corrections such as two-photon exchange, and how they affect different observables.

In this section, the theoretical formalism for the imaginary part of the two-photon exchange amplitude will be discussed, followed by brief discussions of calculations in various regions: the threshold region, the resonance region, the diffractive region (corresponding to high energy and forward angles), and the hard scattering region. For a thorough review of this topic, see Carlson and Vanderhaeghen [139].

2.7.1 Transverse Single Spin Asymmetries

The elastic scattering of electron from protons at leading order involves the exchange of a single photon, followed by higher-order processes such as two-photon exchange. A schematic illustrating the electron-proton scattering amplitude through second-order for one-photon and two-photon exchange is shown in Figure 2.6. Elastic electron-proton scattering is often approximated as a single photon exchange process (known as the Born approximation). This is possible because of the small value of the electromagnetic coupling constant $\alpha \approx 1/137$, and so higher order processes, such as two-photon exchange, are treated just as small "radiative corrections".

The two-photon exchange process involves the exchange of two virtual photons with an intermediate hadronic state that includes the ground state and all excited states. There are several observables that are directly sensitive to two-photon effects. The real (or dispersive) part of the two-photon exchange amplitude can be measured through the difference between elastic electron and positron scattering cross sections off a nucleon [140, 141]. The two-photon exchange process also can produce a single-spin asymmetry in electron scattering [67], from either the scattering of

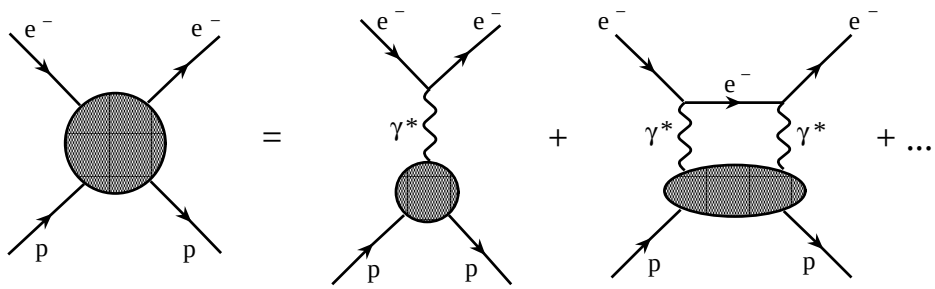

FIG. 2.6: *Feynman diagrams of the electron-proton scattering amplitude expanded through second-order for one-photon and two-photon exchange.*

transversely polarized electrons from unpolarized nucleons or from the scattering of unpolarized electrons from a transversely polarized nucleon target [67,140,141]. These measurements access the imaginary (or absorptive) part of this amplitude. In addition, efforts have been made to determine the magnitude of two-photon exchange effects in a quantitative way from the electron-proton scattering data by studying deviations from the Rosenbluth formula [142,143]. In the G^0 experiment, the second method was used, where the transverse single-spin asymmetry was measured using a transversely-polarized electron beam on an unpolarized proton target, so that is the focus of this section.

The beam-normal single-spin asymmetry, or transverse asymmetry A_n, is sensitive to the imaginary part of the two-photon exchange amplitude in the elastic scattering of transversely polarized electrons from unpolarized nucleons, and arises from the interference of the one-photon and two-photon exchange amplitudes [67]

$$A_n = \frac{2A_{1\gamma}\Im(A_{2\gamma})}{|A_{1\gamma}|^2}, \tag{2.72}$$

where the symbol $\Im$ represents the imaginary part. Time-reversal invariance forces A_n to vanish in the Born approximation, so it is of relative order $\alpha = \frac{e^2}{4\pi} \approx \frac{1}{137}$. Furthermore, A_n must vanish in the chiral limit and so is suppressed by the ratio of the electron's rest mass to the beam energy, leading to an asymmetry on order of $10^{-5} - 10^{-6}$ for $\simeq$ GeV electrons. Hence, measurement of A_n is challenging. An analogous case is the target normal single-spin asymmetry, where the target

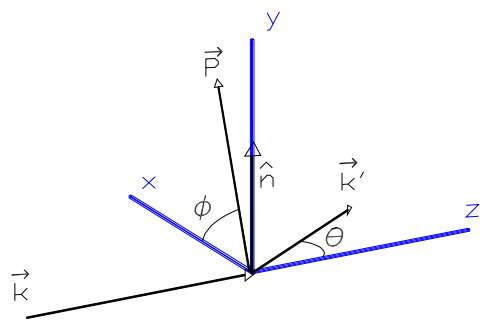

FIG. 2.7: *A schematic of the coordinate system. Shown are the incident and scattered electron wave vectors* $\mathbf{k}$ *and* $\mathbf{k}'$*, respectively, the unit vector* $\hat{n}$*, the polarization vector* $\mathbf{P}$*, and the angles* θ *and* ϕ*, where* $\vec{P} \cdot \hat{z} = 0$*. Figure from [145].*

is polarized normal to the scattering plane, which is also sensitive to the imaginary part of the two-photon exchange amplitude, and gives an asymmetry on order of 10^{-2} [66, 67, 144].

For a beam polarized normal to the scattering plane, the transverse asymmetry is defined as

$$A_n = \frac{\sigma_\uparrow - \sigma_\downarrow}{\sigma_\uparrow + \sigma_\downarrow}, \tag{2.73}$$

where $\sigma_\uparrow(\sigma_\downarrow)$ represents the cross section for the elastic scattering of electrons with spins parallel (anti-parallel) to the normal polarization vector defined by

$$\hat{n} \equiv \frac{\vec{k_e} \times \vec{k'}}{|\vec{k_e} \times \vec{k'}|}, \tag{2.74}$$

where $\vec{k_e}$ and $\vec{k'}$ are the three-momenta for the incident and scattered electron, as shown in Figure 2.7. The scattering angle is positive for the electron scattering to beam left (the Madison convention). The measured asymmetry A_{meas} can be written as $A_n \vec{P_e} \cdot \hat{n}$, where $\vec{P_e}$ is the incident electron beam polarization. Because of the term $\vec{P_e} \cdot \hat{n}$, A_{meas} is dependent on the azimuthal scattering angle ϕ, which is manifested as a sinusoidal dependence in A_{meas} versus ϕ. A_{meas} has a zero crossing where the scattering plane contains the incident electron polarization vector. A_{meas} vanishes for forward scattering ($\theta_e = 0°$) and backward scattering ($\theta_e = 180°$), and also if the electron polarization vector is longitudinal. The target normal beam asymmetry can be defined in

the same manner.

2.7.2 Beyond the One-Photon Exchange Approximation

The transverse asymmetry due to two-photon exchange can be expressed using the formalism developed for the general amplitude for electron-nucleon elastic scattering [146]. This parameterization uses six complex functions, $\tilde{G}_M(\nu, Q^2)$, $\tilde{G}_E(\nu, Q^2)$, and $\tilde{F}_i(\nu, Q^2)$, $i = 3, \ldots, 6$, dependent on ν, the energy transfer to the proton, and Q^2, the four-momentum transfer. In the Born approximation, these functions reduce to the usual magnetic and electric form factors $G_M(Q^2)$, $G_E(Q^2)$, and to $\tilde{F}_i = 0$, so the $\tilde{F}_i$ and phases associated with G_M, G_E must come from processes with the exchange of two or more photons. A_n is proportional to the imaginary part of the combination of $\tilde{F}_3$, $\tilde{F}_4$, $\tilde{F}_5$ and for a beam polarized perpendicularly to the scattering plane can be expressed as [140, 147]

$$A_n = \frac{2m_e}{Q}\sqrt{2\epsilon(1-\epsilon)}\sqrt{1+\frac{1}{\tau}}\left(G_M^2 + \frac{\epsilon}{\tau}G_E^2\right)^{-1} \times \left\{-\tau G_M \Im\left(\tilde{F}_3 + \frac{1}{1+\tau}\frac{\nu}{M^2}\tilde{F}_5\right) - G_E \Im\left(\tilde{F}_4 + \frac{1}{1+\tau}\frac{\nu}{M^2}\tilde{F}_5\right)\right\} + \mathcal{O}(e^4), \qquad (2.75)$$

where $\Im$ denotes the imaginary part. Thus, A_n is a function of Q^2 and the center-of-mass scattering angle θ_{CM}, with the intermediate hadronic state information contained in the $\tilde{F}_i$. The beam normal spin asymmetry vanishes when $m_e = 0$, as it involves an electron helicity flip.

In an analogous manner, the target normal spin asymmetry A_{targ}, where the target is polarized normal to the scattering plane, can be expressed as [140, 147]

$$A_{targ} = \frac{2\epsilon(1+\epsilon)}{\tau}\left(G_M^2 + \frac{\epsilon}{\tau}G_E^2\right)^{-1}\left\{-G_M \Im\left(\delta\tilde{G}_E + \frac{\nu}{M^2}\tilde{F}_3\right) + G_E \Im\left[\delta\tilde{G}_M + \left(\frac{2\epsilon}{1+\epsilon}\right)\frac{\nu}{M^2}\tilde{F}_3\right]\right\} + \mathcal{O}(e^4), \qquad (2.76)$$

when neglecting terms that correspond with electron helicity flip (*i.e.* setting $m_e = 0$). In both A_n and A_{targ}, it can be seen that they vanish in the Born approximation, and are therefore of order e^2.

2.8 Theory Predictions for the Transverse Asymmetry A_n

There have been several calculations of the transverse asymmetry (examples of such for the G^0 experiment include [139, 140, 147–149]), but the primary theoretical difficulty in calculations of the two-photon exchange amplitude is the large uncertainty in the contribution of the inelastic hadronic intermediate states. As the calculations require both the proton elastic form factors (elastic contribution) and the excitation amplitudes to other intermediate states, e.g. πN (inelastic contribution), experimental verification is important to test the framework of the calculations. However, at the present experimental information on A_n is scarce (see Chapter 3 on experimental measurements). This section will discuss some of these calculations, primarily ones in the kinematics of the G^0 transverse measurement, but will a brief discussion of other relevant calculations in other regimes, particularly those of companion experiments.

There has been quite a bit of theoretical activity on this subject, much of it quite recent due to efforts to explain the discrepancy in the proton elastic form factor measurements. The first calculations of the transverse beam asymmetry from the scattering of a spin-$\frac{1}{2}$ particle from a nuclear target were done by N. F. Mott in the late 1920's and early 1930's [150, 151], and neglect proton recoil and internal structure. These calculations are the basis for a method of polarimetry for low-energy (a few MeV) electron beams [152]. The first estimates of the target normal single-spin asymmetry in elastic electron-nucleon scattering were performed by DeRujula and his collaborators [67, 144]. In these early works, the calculations were done with the nucleon intermediate state (the elastic or nucleon pole contribution), with an estimation of the inelastic contribution for a very forward approximation. The beam normal transverse asymmetry was calculated within this approximation by Afanasev *et. al* as well [141].

More recent predictions for the transverse beam spin asymmetry have been done using a variety of models for the intermediate hadronic states. The various models can be grouped according to how they treat those intermediate states.

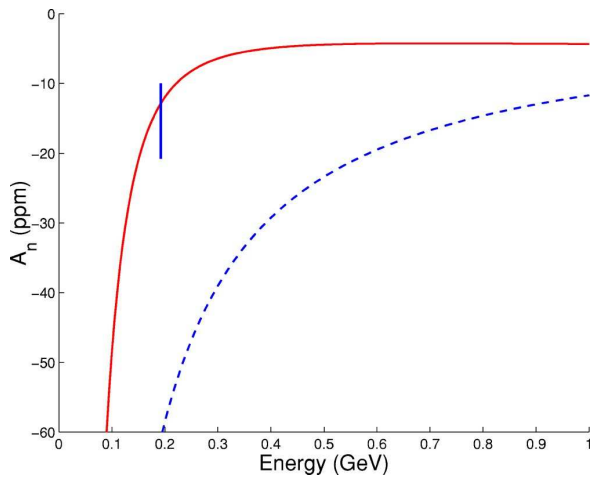

FIG. 2.8: *The calculation for the transverse asymmetry at the SAMPLE kinematics by Diaconescu and Ramsey-Musolf. The dashed line represents the leading-order result; the solid line denotes the full calculation. Figure taken from [153]; Data point from [145].*

2.8.1 Pion Electroproduction Threshold Region

The transverse asymmetry in the low energy, elastic scattering of transversely-polarized electrons from protons was studied using an effective theory of electrons, protons, and photons by Diaconescu and Ramsey-Musolf [153, 154]. The goal of the calculation was to determine if the discrepancy between the low-energy SAMPLE transverse beam spin experimental result for the vector analyzing power and the original scattering calculation by Mott could be resolved using effective field theory. If this approach was successful, the same technique could be employed to the electroweak box corrections for electroweak observables such as the ones for neutron and nuclear β-decay.

In the calculations, only the electron, photon, and nucleon were considered as dynamical degrees of freedom, since the SAMPLE measurement corresponded to kinematics close to the pion electroproduction threshold. This corresponds to the use of heavy baryon chiral perturbation theory (HBχPT) with the pions integrated out, providing a systematic expansion of A_n in powers of p/M, where M is the nucleon mass and p is either the incident electron energy E or electron mass m. Up to second order in p/M, the prediction for A_n was free of unknown parameters and included all

contributions that arise uniquely from one-loop, two-photon exchange parameters. The calculation showed that the inclusion of all one-loop effects through second order in $\mathcal{M}_{\gamma\gamma}$ and all terms in $\mathcal{M}_{\gamma}$ to second order is sufficient to resolve the disagreement between the measured SAMPLE result and the original simplest potential scattering predictions by Mott, which corresponds to the $\mathcal{O}(p/M)^0$ contribution (an infinitely heavy target). The calculation for the vector analyzing power A_n is shown in figure 2.8 versus energy for fixed scattering angle, $\theta = 146.1°$. In the plot, the dashed line is the leading order result, and the solid line is the full calculation; the SAMPLE result is shown at $E = 192$ MeV.

This EFT approach worked well for the SAMPLE result, despite the lack of dynamical pions in the calculation and the fact that the SAMPLE kinematics are just above the pion production threshold. However, this prediction did not work for the measurement of A_n at higher energies by the A4 collaboration at Mainz. This is unsurprising given that the Mainz energies are well beyond the valid limit of this EFT, and addition dynamical degrees of freedom such as the π or $\Delta(1230)$ resonance probably need to be included.

A full calculation for the N intermediate state for this kinematical region was done by Pasquini and Vanderhaeghen [140]. The calculation is model independent, involving only on-shell $\gamma^* NN$ matrix elements. However, the inclusion of threshold pion electroproduction contributions that arise from the πN intermediate states partly cancels the elastic contributions, which reduces the effect, as can be seen in Figure 2.9. The matrix elements are fairly well-known in this low-energy region, leading to a puzzle as to why the calculation is not in better agreement with the somewhat larger asymmetry measured by the SAMPLE experiment [145].

2.8.2 Resonance Region

If the transverse asymmetry is measured at energies below or around the two-pion production threshold, the electroproduction amplitudes used in the calculations of the intermediate states are relatively well known, since pion electroproduction experiments can be used as input. Conversely, as the transverse asymmetry is sensitive to the electroproduction amplitudes on the nucleon, the

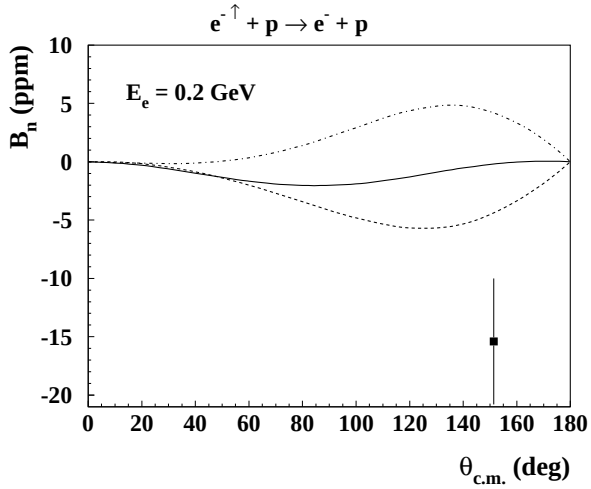

FIG. 2.9: *The transverse asymmetry (denoted as B_n) for a beam energy of 0.2 GeV as a function of the center-of-mass scattering angle θ_{cm}. The dashed curve represents the nucleon intermediate state, the dashed-dotted line the πN contribution, and the solid curve the sum of both contributions. Figure taken from [140]; Data point from SAMPLE [145].*

asymmetry could provide information on resonance transition form factors.

Pasquini and Vanderhaeghen [140] used this method to calculate the imaginary part of the two-photon exchange amplitude, by relating the amplitude to the contribution of $X = N$ and $X = \pi N$ intermediate state contributions through unitarity. The πN intermediate state contributions were assessed using the phenomenological MAID analysis [155] to obtain the corresponding pion electroproduction amplitudes. Both resonant and non-resonant pion production mechanisms are included in the MAID analysis. The results of the calculation show that at forward angles, the quasi-real Compton scattering at the endpoint $W = W_{max}$ only yields a very small contribution. However, it grows larger going to backward angles, because the quasi-real Compton scattering contribution is the opposite sign as the remainder of the integrand, which determines the location of the absolute maximum value of the transverse asymmetry.

The results for the full calculation (solid line) of A_n are shown in Figure 2.10 for beam energies of 0.3, 0.424, 0.570, and 0.855 GeV, along with the results for only the nucleon intermediate state (the dashed line) and the πN inelastic contribution (dashed-dotted line). At these energies, the nucleon intermediate state has a relatively small contribution compared to the inelastic states,

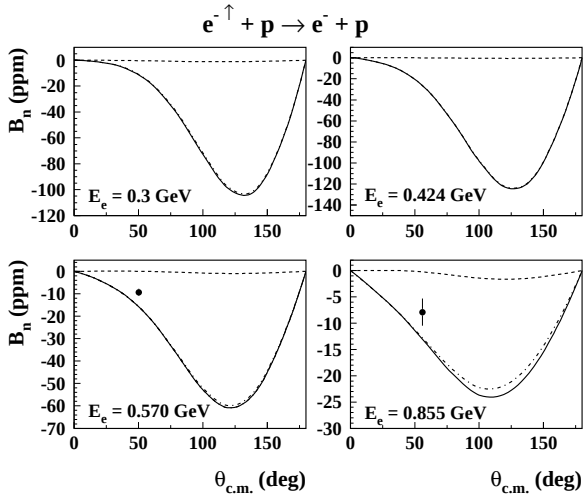

FIG. 2.10: *The transverse asymmetry (denoted as B_n) for various beam energies as a function of the center-of-mass scattering angle θ_{cm}. The dashed curve represents the nucleon intermediate state, the dashed-dotted line the πN contribution, and the solid curve the sum of both contributions. Figure taken from [140]; Data points from A4 [156].*

making A_n primarily a measure of the inelastic part. The transverse asymmetries are large in the backward-angle region, because of the quasi-real Compton scattering near singularity. The transverse asymmetry has been measured in this energy region by the A4 collaboration (see Section 3.4.2). At forward angles, the predicted asymmetries are compatible, although the calculation somewhat overpredicts the absolute size of the asymmetry in this range [156]. However, asymmetries of this size ($\sim$ 100 ppm around $\theta_{CM} = 150°$) in the backward-angle range have recently been observed in preliminary results by the A4 collaboration [157]. More backward-angle transverse asymmetry data has also recently been taken by the G^0 collaboration in this energy region (see Section 7.1.2).

2.8.3 Intermediate and High-Energy, Forward Scattering

The calculations for the transverse asymmetry become somewhat easier in the extreme limit of very high energies and very forward scattering angles (known as the diffractive limit). In this limit, A_n is dominated by the quasi-real Compton singularity, and can be expressed rather simply in terms of the total photo-absorption cross section on the proton, $\sigma_{tot}^{\gamma p}$ [148, 158, 159]. A_n is then

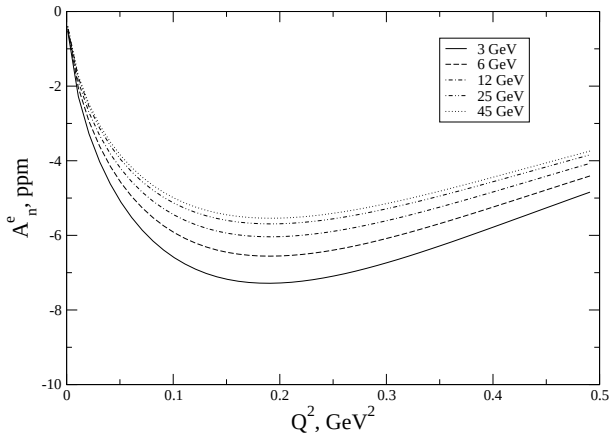

FIG. 2.11: *The transverse asymmetry for various beam energies as a function of the four-momentum transfer Q^2. The solid curve represents the kinematics of the G^0 experiment (3 GeV). Figure taken from [148].*

given by the analytical expression

$$A_n = -\frac{m_e\sqrt{Q^2}\sigma_{tot}^{\gamma p}}{8\pi^2}\frac{G_E}{\tau G_M^2 + \epsilon G_E^2}\left[\log\frac{Q^2}{m_e^2} - 2\right]. \tag{2.77}$$

The logarithmic enhancement factor comes from the quasi-real Compton singularity, and is the cause of the relatively large magnitude of A_n. Using this expression, estimates were done for different parameterizations of the total absorption cross section [148], which seem to be in agreement with preliminary result for the transverse proton asymmetry measured by E158 at SLAC, an experiment that is primarily an e^-e^- scattering experiment [139].

However, the situation becomes much more complicated at intermediate energies. The diffractive expression above no longer rigorously applies in this region, and thus corrections to the diffractive limit result to account from the deviation from forward scattering must be calculated, as has been done in [148] and [149] using different model approaches.

Afanasev and Merenkov used an optical theorem to evaluate the transverse asymmetry in terms of the total photoproduction cross section on the proton [148, 160]. They found that the asymmetry has logarithmic and double logarithmic enhancement that arises from the contributions of hard collinear quasi-real photons. The results of the calculations are shown in Figure 2.11. At

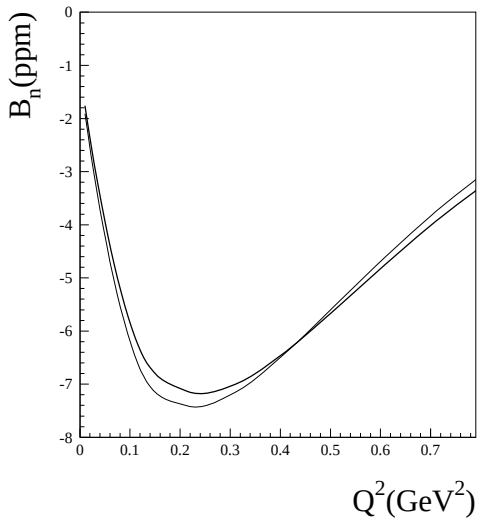

FIG. 2.12: *The transverse asymmetry for a beam energy of 3 GeV as a function of the four-momentum transfer Q^2 for forward angle scattering. The thick curve represents the leading t contribution; the thin curve corresponds to the full calculation including the subleading terms of t. Figure taken from [149].*

small Q^2, the asymmetry follows the high-energy diffractive behaviour of total photoproduction cross section on the photon, while at higher Q^2 the asymmetry starts to decrease in magnitude due to introduced exponential terms. For the G^0 kinematics at 3 GeV, the magnitude is $\sim 6-7$ ppm.

Gorchtein calculated the transverse asymmetry at forward angles using a model which combined forward-angle DIS input with the phenomenological t-dependence (where t denotes the four-momentum transfer) taken from the Compton scattering differential cross section $d\sigma/dt$ measured at high energies and low t values [158, 159], as proposed by [148]. The calculation was then extended in a later work that included subleading t terms [149]. The results reported in [149] are presented in Figure 2.12. The leading terms in t clearly dominates the calculation, and results in a prediction of about -7 ppm for the Q^2 range of the G^0 experiment.

Pasquini and Vanderhaeghen [140] performed calculations for the transverse asymmetry by extending the method employed for lower energies to a beam energy of 3 GeV. The result of these calculations are shown in Figure 2.13, where the elastic contribution (dashed), inelastic contribution (dashed-dotted), and total contribution (solid) curves are shown as a function of center-of-mass

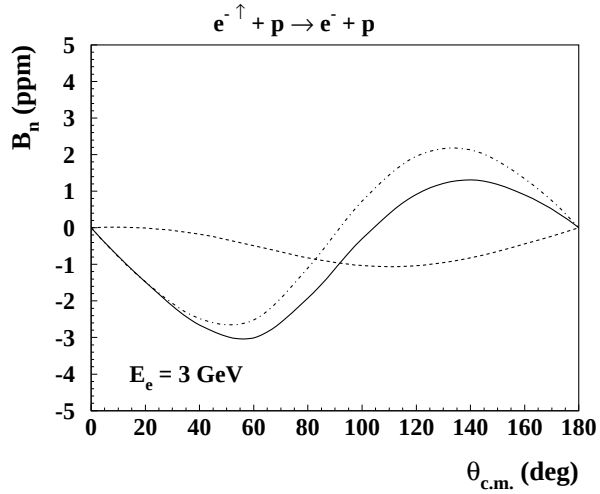

FIG. 2.13: *The transverse asymmetry (denoted as B_n) for a beam energy of 3 GeV as a function of the center-of-mass scattering angle θ_{cm}. The dashed curve represents the nucleon intermediate state, the dashed-dotted line the πN contribution, and the solid curve the sum of both contributions. The πN intermediate states are estimated for $W < 2$ GeV. Figure taken from [140].*

scattering angle. In the figure, it is clear that the elastic contribution is not a significant contribution, especially in the forward-angle range. Interestingly, the inelastic contribution changes sign around $\theta_{cm} \approx 90°$. However, a possible limitation of this calculation comes from the fact that the πN contribution is only known for $W < 2$ GeV, whereas the upper integration range is $W_{\max} \approx 2.55$ GeV. This could introduce an additional negative component to A_n, especially in the forward-angle region.

The calculations of the transverse asymmetry in [148, 149, 160] are in basic agreement with the reported preliminary results from the HAPPEX collaboration [161] (see Section 3.4.3).

2.8.4 Hard Scattering Region

The hard scattering region is the region where both photons are hard and the momentum transfer is large ($Q^2 \gg M^2$). Chen and collaborators [162] calculated the contribution of two-photon exchange to elastic electron-nucleon scattering at large momentum transfer through the scattering off a parton located in a proton by relating the process on a nucleon to generalized parton distributions (GPDs). The authors found that these contributions largely resolve the discrepancy between the Rosenbluth and recoil polarization measurements. Both the beam and the target

transverse asymmetries have been estimated through the scattering off a parton embedded in the nucleon through GPDs in Refs. [147, 163]. A precision measurement of the transverse target asymmetry using a polarized ^{3}He target is planned in Hall A at Jefferson Lab[1], which will give information on the elastic electron-neutron transverse asymmetry from two-photon exchange at large momentum transfer.

2.8.5 Two-Photon Exchange in Møller Scattering

Two-photon exchange processes can also be accessed by measuring the beam normal spin asymmetry for polarized Møller scattering, $e^{-\uparrow}e^- \rightarrow e^-e^-$. This transverse asymmetry arises from a QED rescattering phase. Theoretical calculations of the beam normal spin asymmetry have been calculated by several authors [66, 153, 164–167], with the most recent theoretical work focused on estimating the size of possible radiative corrections due to this effect for the E158 experiment at SLAC [168, 169]. The E158 experiment performed a measurement of the transverse asymmetry in Møller scattering at a $Q^2 \approx 0.05$ (GeV/c)^2 and a beam energy of about 46 GeV. The collaboration announced a result of a few ppm and a negative sign, with the final results forthcoming in the near future.

2.9 A Summary about Two-Photon Exchange

In this section, an overview of two-photon exchange and the transverse asymmetries measured in the elastic scattering of transversely polarized electrons from nucleons has been presented, along with theoretical calculations covering a rather wide kinematical range. Despite difficulties in calculating the inelastic contribution of the hadronic intermediate states, the calculations indicate that the inelastic contribution is significant, and first measurements of A_n by the SAMPLE collaboration [145] and the A4 collaboration [156] (see section on these measurements) indicate that models including only the nucleon elastic state are insufficient. Other preliminary data suggest that the elastic contribution alone is insufficient [157, 161].

[1] JLab experiment E05-015, spokespersons T. Averett, J.P. Chen, and X. Jiang

Calculation	$A_n(Q^2 = 0.15)$	$A_n(Q^2 = 0.25)$	Reference
Afanasev and Merenkov	-7.3 ppm	-7.2 ppm	[148]
Gorchtein	-7.2 ppm	-7.5 ppm	[149]
Pasquini and Vanderhaeghen	-1.6 ppm	-2 ppm	[140]

TABLE 2.4: *Calculations of the transverse asymmetry at 3 GeV for the G^0 forward-angle measurements at $Q^2 = 0.15$ (GeV/c)^2 ($\theta_{cm} = 20.2°$) and $Q^2 = 0.25$ (GeV/c)^2 ($\theta_{cm} = 25.9°$).*

The G^0 measurement is at a higher beam energy (3 GeV) and forward angles, where the πN intermediate states are predicted to be a significant contribution to A_n [140]. Furthermore, this beam energy falls in a transition range between models. At energies below the two-pion production threshold, the πN intermediate state contribution can be calculated using pion electroproduction amplitudes based on experimental input. Above that limit, the πN contribution is not well known, and there could be additional contributions to A_n [140]. At very high energies and forward scattering angles (the diffractive limit), A_n can be expressed simply in terms of the total photo-absorption cross section using the optical theorem [148, 158]. For the present intermediate energy [148, 149], corrections to the diffractive limit result have been calculated. A summary of the predictions relevant to the G^0 transverse measurement is shown in Table 2.4.

2.10 Goals of the G^0 Physics Program

As stated earlier, the goal of the G^0 is to determine the values of the strange electric and magnetic form factors of the nucleon, G_E^s and G_M^s. To completely separate the electric, magnetic, and axial form factors, three independent measurements are required, so the G^0 experimental program includes a forward-angle measurement, which is the scope of this dissertation, a backward-angle measurement using a hydrogen target, and a backward-angle measurement using a deuterium target. The forward-angle measurement resulted in the linear combination $G_E^s + \eta G_M^s$ for 18 Q^2 values between 0.1 and 1.0 (GeV/c)^2. The two backward-angle measurements were each recently done at two Q^2 values, 0.23, 0.62 (GeV/c)^2, allowing a complete separation at those points. The analysis of these data is currently underway.

However, the G^0 experiment is not the only experiment studying these effects, nor could it map the entire range alone. The next chapter discusses some of these companion experiments and their goals.

CHAPTER 3

Survey of Related Experiments

3.1 Overview

Over the last thirty years, parity-violating electron scattering has become an important experimental tool, especially in the last decade, where this technique has been used to investigate the contribution of the quark-antiquark sea of the nucleon to its electromagnetic structure. These very challenging experiments have become possible with the development and improvement of many experimental techniques which facilitate the measurement of the parity-violating asymmetries at the parts-per-million level. In this chapter, an overview of some of the pioneering experiments utilizing parity-violating electron scattering will be given, followed by summaries of measurements by previous and contemporary experiments to provide a context for the G^0 experiment.

3.2 Classic Parity-Violating Electron Scattering Experiments

Parity-violating electron scattering experiments are difficult to perform due to the extremely small asymmetries of only a few parts-per-million that are being measured and the need to therefore keep the statistical and systematic errors even smaller. Many of the experimental techniques

needed to gain the necessary statistical precision and to control systematic errors, such as the development of a source of a high-quality, intensely polarized electron beam and the ability to control and accurately measure the properties of the beam such as the polarization, were developed by the pioneering deep inelastic eD parity experiment at SLAC in the late 1970's [170, 171]. The experiment observed parity-violating asymmetries in the inelastic scattering of longitudinally polarized electrons of energy between 16.2 and 22.2 GeV from unpolarized liquid deuterium and liquid hydrogen targets at a $Q^2 = 1.6$ (GeV/c)^2. The techniques were further developed in the quasi-elastic beryllium experiment at Mainz in the 1980's [172]. In this experiment, polarized electrons were scattered off a ^{9}Be target at an energy of 300 MeV at angles from $115° \leq \theta \leq 145°$. After the corrections for the beam polarization of 44% and for background processes, they reported a measurement of $A = -9.4 \pm 1.8_{stat} \pm 0.5_{sys}$ ppm. Both of these experiments sought to test the standard model by using the measured asymmetries to compute a value for $\sin^2\theta_W$, where θ_W is the Weinberg angle (also called the weak mixing angle), to compare to the value predicted by the standard model. Their values agreed with the value predicted by electroweak theory, within the error bars of the measurements. These experiments were followed by the elastic carbon measurement at MIT-Bates that further refined the experimental techniques, publishing results in 1990 [173]. In this experiment, the parity-violating asymmetry from the elastic scattering of polarized electrons from ^{12}C nuclei was measured to compute the isoscaler vector hadronic coupling constant $\tilde{\gamma}$ as another test of the standard model. The observed asymmetry was $A = 0.60 \pm 0.14_{stat} \pm 0.02_{syst}$ ppm, yielding a value of $\tilde{\gamma}$ that agreed with the prediction of the standard model.

These classic experiments were all directed toward tests of the electroweak standard model. However, the next generation of parity-violating electron scattering experiments has taken the focus of this technique at the facilities at MIT-Bates, Jefferson Lab, and MAMI in a new direction and has successfully used this technique to investigate the spin-flavor structure of the nucleon.

3.3 Previous Strange Form-Factor Experiments

Recent parity-violating electron scattering experiments, including the G^0 experiment, have been focused on measuring the strange-quark electric and magnetic form factors of the nucleon. This section discusses other experiments that have been performed, or are currently running, that have the goal of measuring the strange vector form factors at various kinematics using this technique.

3.3.1 SAMPLE at MIT-Bates

The first experiment to measure the strange magnetic form factor of the proton was the SAMPLE experiment at the MIT-Bates Laboratory, which took data from 1998 to 1999 [174, 175]. The experiment performed three measurements of parity-violating asymmetries from electron scattering: a first measurement on a liquid hydrogen target at a beam energy of 200 MeV [176–178, 180], a second measurement at the same beam energy on a liquid deuterium target [177–180], and a third measurement on a liquid deuterium target at a beam energy of 125 MeV [179, 180]. The first two measurements correspond to an average Q^2 of 0.1 $(\mathrm{GeV}/c)^2$, and the third to $Q^2 = 0.038$ $(\mathrm{GeV}/c)^2$.

The experiment measured the parity-violating asymmetries at an angle of $\theta_e \sim 145°$ by detecting the elastically backward-scattered electrons from the unpolarized 40 cm-long hydrogen or deuterium target with an air Čerenkov detector system, as can be seen in Figure 3.1. The detector system consisted of an array of ten ellipsoidal mirrors placed symmetrically around the beam axis that focused the Čerenkov light from the passage of the electrons through the air onto a group of ten corresponding eight-inch photomultiplier tubes, as illustrated in Figure 3.2. The signals from the phototubes were integrated over a period of 60 μs, digitized by the ADCs, then read out by the data acquisition system. The 40 μA longitudinally-polarized beam was generated from a bulk GaAs electron source, with a polarization of about 37%. The beam was pulsed at 600 Hz (each pulse with a duration of about 25 μs); the helicity was flipped pseudo-randomly. The combination

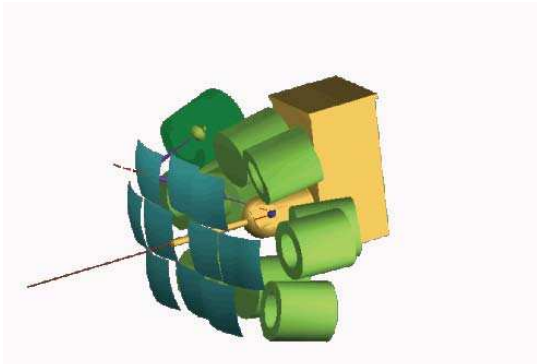

FIG. 3.1: *A schematic of the SAMPLE apparatus. Portions of the scattering chamber and lead shielding have been cut away for clarity. Backscattered electrons from the target are detected in the air Čerenkov detectors at an average scattering angle of about 145°. The detectors consist of ten ellipsoidal mirrors that reflect the Čerenkov light into ten phototubes facing them. Figure taken from [180]*

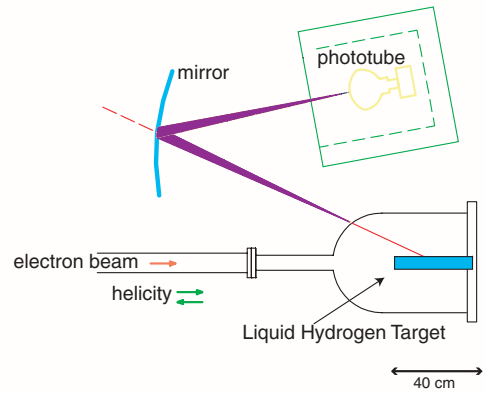

FIG. 3.2: *A schematic of one of the modules of the SAMPLE experimental apparatus. Ten of these mirror-phototube pairs are placed symmetrically around the beam axis. The Čerenkov light from the electrons back-scattered from the target were reflected and focused by the mirrors onto the phototubes. Figure taken from [177].*

of the large solid angle of the detectors ($\Delta\Omega \approx 1.5$ sr) and the high luminosity of the polarized beam allowed the experiment to measure the small asymmetries in a relatively short amount of time.

The measurements were performed at backward angles, so the asymmetry is mostly sensitive to the linear combination of G_M^s and G_A^e, the nucleon strange magnetic and axial form factors, and not the strange electric form factor. Making the measurements on both hydrogen and deuterium targets enabled the collaboration to extract the electron-proton axial form factor and the strange magnetic form factor.

The measured asymmetry for the hydrogen measurement was [180]

$$A_p(Q^2 = 0.1) = -5.61 \pm 0.67_{stat} \pm 0.88_{sys} \text{ ppm} \tag{3.1}$$

$$= -5.56 + 3.37 G_M^s + 1.54 {G_A^e}^{(T=1)} \text{ ppm.} \tag{3.2}$$

By combining this result with the theoretically predicted value for the isovector component of the axial form factor of ${G_A^e}^{(T=1)} = -0.83 \pm 0.26$ by Zhu et al. [85], the value of G_M^s obtained is

$$G_M^s(Q^2 = 0.1) = 0.37 \pm 0.20_{stat} \pm 0.26_{sys} \pm 0.07_{FF} \tag{3.3}$$

in which the last uncertainty is due to the uncertainty in nucleon electromagnetic and axial form factors. From the analysis of the 200 MeV data taken with the deuterium target, the measured asymmetry was [180]

$$A_d(Q^2 = 0.1) = -7.77 \pm 0.73_{stat} \pm 0.72_{sys} \text{ ppm} \tag{3.4}$$

$$= -7.06 + 0.72 G_M^s + 1.66 G_A^{e\,(T=1)} \text{ ppm.} \tag{3.5}$$

Using only these two data sets, the values of the form factors were determined to be

$$G_M^s(Q^2 = 0.1) = 0.23 \pm 0.36_{stat} \pm 0.40_{sys} \tag{3.6}$$

and

$$G_A^{e\,(T=1)}(Q^2 = 0.1) = -0.53 \pm 0.57_{stat} \pm 0.50_{sys}, \tag{3.7}$$

which are in excellent agreement with [85] and the determination from the hydrogen data alone [180]. These calculations assume that $G_E^s = 0$. The two results are shown in Figure 3.3 plotted in the space of G_M^s versus $G_A^{e\,(T=1)}$. The blue diagonal band is the hydrogen measurement and the red band is the deuterium, where the inner and outer bands represent the statistical and total uncertainties. The larger pink ellipse representing the 1σ error ellipse is obtained from combining the two experimental results and the smaller yellow ellipse is the 1σ contour obtained by combining the hydrogen result with the theoretical $G_A^{e\,(T=1)} = -0.83 \pm 0.26$ by Zhu et al. [85], which is the theoretical prediction shown in the vertical light green band.

The third SAMPLE measurement was carried out in order to provide another experimental determination of $G_A^{e\,(T=1)}$. This measurement was made with a deuterium target and a beam energy of 125 MeV, corresponding to a Q^2 of 0.038 (GeV/c)^2. The asymmetry was found to be [179, 180]

$$A_d(Q^2 = 0.038) = -3.51 \pm 0.57_{stat} \pm 0.58_{sys} \text{ ppm} \tag{3.8}$$

$$= -2.14 + 0.27 G_M^s + 0.76 G_A^{e\,(T=1)} \text{ ppm.} \tag{3.9}$$

Although no hydrogen data were taken at $Q^2 = 0.038$, the two measurements on deuterium can be compared to the predicted theoretical values by assuming a value for G_M^s at $Q^2 = 0.038$, as

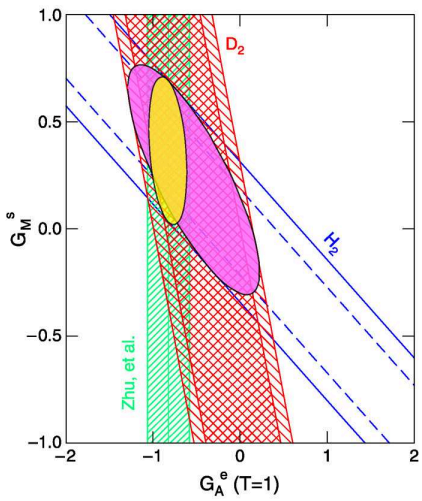

FIG. 3.3: *The results from the SAMPLE data taken at 200 MeV and $Q^2 = 0.1$ $(GeV/c)^2$. The results are shown in the space of G_M^s versus $G_A^{e\,(T-1)}$, along with the theoretical calculation of $G_A^{e\,(T-1)}$ by [85]. The ellipses correspond to a 1-σ overlap of the two experimental data sets (larger) and the combination of only the hydrogen data and theory by [85] (smaller). Figure taken from [180]*

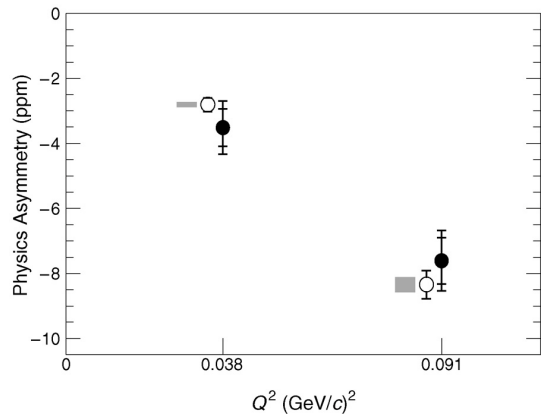

FIG. 3.4: *The results from the two SAMPLE deuterium measurements plotted as a function of Q^2 along with the theoretical predictions (open circles, offset for clarity) with the value of $G_A^{e\,(T-1)}$ from [85], assuming $G_M^s = 0.15$ nuclear magnetons. The grey bands represent the change in the physics asymmetry corresponding to a change in G_M^s of 0.6 n.m. Figure taken from [179, 180]*

the deuterium asymmetry only has a weak dependence on G_M^s. A comparison between the data and the theoretical predictions are shown in Figure 3.4, where a constant value of $G_M^s = 0.15$ is assumed. The shaded grey areas represent the variation in the theory corresponding to a change in G_M^s of 0.6 nuclear magnetons. The good agreement indicates that $G_A^{e\,(T=1)}$ has a weak Q^2 dependence, which is consistent with theory [180].

3.3.2 HAPPEX at Jefferson Lab

The first measurements of parity-violating electron scattering at Jefferson Lab were performed by the Hall A Proton Parity Experiment, known as HAPPEX. The goal of the experiment is to measure the strange-quark contribution to the nucleon. In the experiment, forward-scattered electrons from the interaction of the electron beam with the target are focused by two high-resolution spectrometers onto detectors set in the focal plane, as seen in Figure 3.5. To date, there have been three HAPPEX measurements:

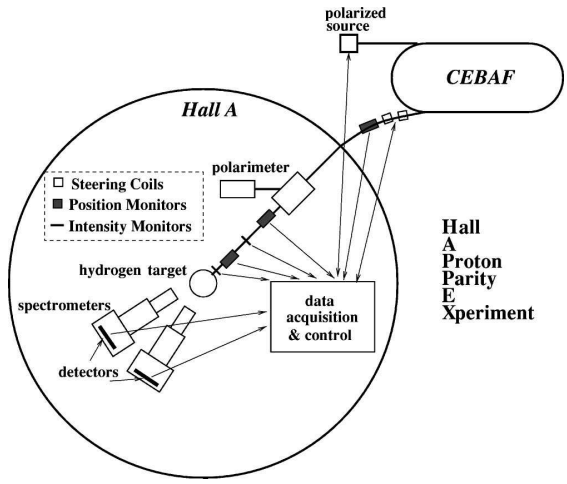

FIG. 3.5: *A schematic overview of the HAPPEX experiment in Hall A at Jefferson Lab. Figure taken from [183].*

1. HAPPEx-H-I with a LH_2 target at $Q^2 = 0.477$ (GeV/c)^2 [181–183],
2. HAPPEx-H-II with a LH_2 target at $Q^2 = 0.1$ (GeV/c)^2 [184, 186], and
3. HAPPEx-He with a ^{4}He target at $Q^2 = 0.1$ (GeV/c)^2 [185, 186].

The first HAPPEX measurement obtained data in two separate data-taking runs in 1998 and 1999, using a 3.2 GeV polarized electron beam on a 15 cm unpolarized liquid hydrogen target. For the 1998 run, a bulk GaAs photocathode was used in the polarized source to deliver 100 μA of beam with a polarization of about 38%, but for the 1999 run the experiment used a strained GaAs photocathode which produced a beam of about 40 μA at a polarization of about 70%, as measured with a laser-Compton polarimeter and a Møller polarimeter, as well as a Mott polarimeter located near the source. This marked the first use of a strained GaAs photocathode and a Compton polarimeter in a fixed target parity-violation experiment [183].

The elastically-scattered electrons from the hydrogen target at $\theta_{lab} = 12.3°$ were focused by the two high-resolution spectrometers (HRS) onto calorimeter detectors consisting of alternating layers of lead and Lucite sandwiched together. The Čerenkov light from the scattered electrons were collected by a photomultiplier tube, integrated over the duration of the helicity window (1/30 s), and digitized by analog to digital converters (ADCs). Since the HRS pair has high

enough resolution to spatially separate the elastic electrons from the inelastic electrons at the π^0 threshold, the amount of background events was small, and only resulted in a small correction.

As the measurement is at a forward angle, the measured asymmetry is sensitive to the linear combination of G_E^s and G_M^s. The measurement yielded an asymmetry of

$$A_p(Q^2 = 0.477) = -15.05 \pm 0.98_{stat} \pm 0.56_{sys} \text{ ppm}, \tag{3.10}$$

which gives an extraction for the linear combination of

$$(G_E^s + 0.392 G_M^s)(Q^2 = 0.477) = 0.014 \pm 0.020 \pm 0.010, \tag{3.11}$$

where the first error quoted is from the experiment and the second is from the electromagnetic form factor data [183]. Although consistent with zero, the measurement does not rule out the possibility that G_E^s and G_M^s are of opposite sign and cancel each other out, so a back-angle measurement at this kinematic point is necessary to separate them.

The HAPPEX collaboration carried out two other measurements on liquid hydrogen and on cryogenic high-pressure ^{4}He gas targets in two separate data-taking runs in 2004 and 2005. These measurements used a 3.3 GeV polarized electron beam on the 20 cm unpolarized cryogenic targets.

For these runs, an engineered superlattice of doped GaAs semiconductor layers was used as the photocathode in the polarized source, which yielded an electron beam intensity of 35 to 55 μA with a polarization of about 85%. As with the previous HAPPEX measurement, elastically-scattered electrons from the hydrogen target were focused by the two identical high-resolution spectrometers onto total-absorption calorimeter detectors, but this time at $\theta_{lab} \approx 6°$, which was achieved by using superconducting septum magnets. In these measurements, the detectors were made of alternating layers of brass and quartz, positioned so the Čerenkov light from the scattered electrons were collected by the phototube at the end of the detector. The phototube signals were integrated over the duration of the helicity window (1/30 s), and read out by the DAQ.

Results from these measurements were published in 2005 after the first data-collection period had ended [184, 185], and the final results of the complete data set have been recently published in

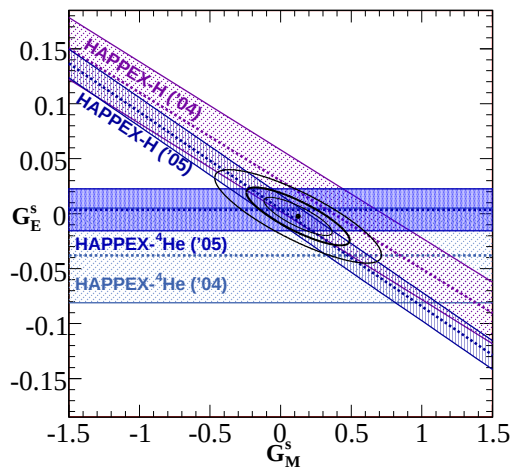

FIG. 3.6: *The recent HAPPEX results plotted in the G_E^s versus G_M^s plane. The ellipses indicate the 68% and 95% confidence levels. Data taken from [184–186].*

2006 [186]. The hydrogen measurement at this forward angle is sensitive to the linear combination of G_E^s and G_M^s. However, since ^{4}He is a spin = 0, isospin = 0, target, there are no contributions from the magnetic or axial vector currents, and the measured asymmetry can be directly related to G_E^s with some knowledge of the ^{4}He nucleus.

The measurement on hydrogen yielded an asymmetry of

$$A_p(Q^2 = 0.109) = -1.58 \pm 0.12_{stat} \pm 0.04_{sys} \text{ ppm}, \tag{3.12}$$

which gives an extraction for the linear combination of

$$(G_E^s + 0.09 G_M^s)(Q^2 = 0.109) = 0.007 \pm 0.011 \pm 0.006, \tag{3.13}$$

where the first error quoted is from the experiment and the second is from the electromagnetic form factor data [186].

For the measurement on helium, an asymmetry of

$$A_{^4He}(Q^2 = 0.077) = +6.40 \pm 0.23_{stat} \pm 0.12_{sys} \text{ ppm}, \tag{3.14}$$

was measured. This gives an extraction for the strange electric form factor of

$$G_E^s(Q^2 = 0.077) = 0.002 \pm 0.014 \pm 0.007, \tag{3.15}$$

where the first error quoted is statistical and the second is systematic, including those from radiative corrections and electromagnetic form factors [186]. The HAPPEX results are shown in Figure 3.6 in the G_E^s versus G_M^s plane. Because the measurements were done on both hydrogen and ^{4}He, a complete separation of G_E^s and G_M^s is possible, and the values of

$$G_E^s = -0.005 \pm 0.019 \quad \text{and} \quad \mathrm{G_M^s} = 0.18 \pm 0.27 \tag{3.16}$$

were obtained for $Q^2 = 0.1$ (GeV/c)^2. Both are consistent with zero at this Q^2.

The HAPPEX collaboration is preparing for another measurement at a higher Q^2 of ~ 0.6 (GeV/c)^2 in the future, which will be discussed in Section 7.1.

3.3.3 PVA4 at MAMI

Another experimental program to measure parity-violating asymmetries with the goal of determining the strange quark contribution to the magnetic and electric form factors is the PVA4 experiment that is being carried out at the Mainzer Mikrotron accelerator facility (MAMI) in Mainz, Germany. As with the previous experiments, there are several measurements that make up the experimental program for PVA4. The experiment has completed two measurements of the parity-violating asymmetry at forward electron scattering angles between $30° < \theta_e < 40°$ on liquid hydrogen targets. The collaboration is currently taking data for a backward-angle measurement at about 145°, which will be discussed later in this section and in Section 7.1.

The experiment uses a somewhat different approach to the previous experiments, in that the experiment utilized a counting technique to collect the data from the scattered particles, which is feasible in spite of the very high scattered electron rates because of the segmented detectors and specialized electronics. The custom-built detector system is azimuthally symmetric around the beam axis, and has no magnetic field. A schematic of the experimental configuration for the forward-angle measurement is shown in Figure 3.7. The forward-scattered electrons from the liquid hydrogen target were detected by a lead fluoride (PbF_2) Čerenkov total-absorption calorimeter, which consisted of 1022 PbF_2 crystals arranged in seven rings. The calorimeter accepted elastically

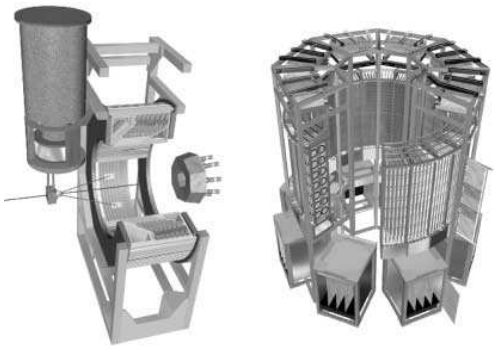

FIG. 3.7: *A schematic of the PVA4 experimental apparatus. The left side is a schematic of the lead fluoride calorimeter with the electron beam coming in from the left at about 2.2 m from the floor. The secondary ring of detectors are eight water-Čerenkov luminosity monitors. The right side is a schematic of the readout electronics, which stands about 3 m high. Figure taken from [187].*

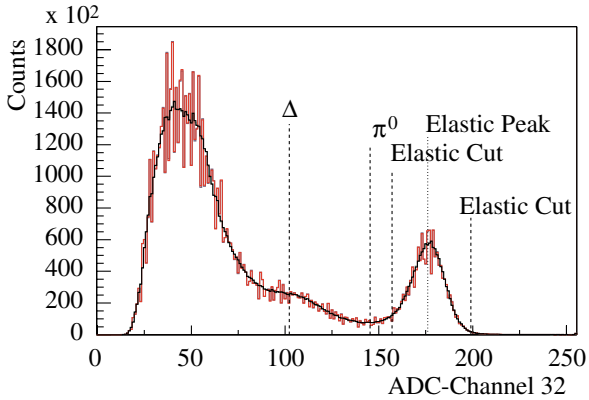

FIG. 3.8: *A histogram showing the energy spectrum of accepted particles from the hydrogen target into the PVA4 lead fluoride calorimeter. The dashed red histogram is the raw energy spectrum, and the solid black is the spectrum corrected for the differential non-linearity of the ADC. The position of the elastic scattering peak, the threshold for π^0 production, the position of the Δ resonance, and the position of the cuts used for the experiment are all indicated. Figure taken from [188].*

scattered electrons from $30° < \theta_e < 40°$ as well as inelastic electrons and photons from π^0 decays. The Čerenkov photons from the particles that were detected in the PbF_2 crystals were collected by phototubes. An energy deposition by the particles above a specified threshold triggered the digitization of the summed output of the signals from clusters of nine crystals, in which the charge was integrated over 20 ns and histogrammed to produce an energy spectrum of the scattered particles. The separation of the signal of the elastic electron scattering events from the inelastic background events was done based on their different deposits of energy in the PbF_2 crystals of the calorimeter. A typical energy spectrum is shown in Figure 3.8. The experiment used a 20 μA beam of electrons at about 80% polarization from a strained GaAs source, as measured by a Møller polarimeter in another experimental hall. The electron helicity was flipped every 20 ms for both measurements. The experiment also had eight water Čerenkov luminosity detectors placed symmetrically around the beamline at very small forward angles to monitor the target density.

As a forward-angle experiment, the measured asymmetry is sensitive to a linear combination of G_E^s and G_M^s. The first PVA4 forward-angle measurement was at a beam energy of 855 MeV,

at $Q^2 = 0.230$ (GeV/c)^2. For this measurement, only half (511 of 1022) of the channels for the detector and corresponding electronics were instrumented. They measured the asymmetry to be

$$A_p(Q^2 = 0.230) = -5.44 \pm 0.54_{stat} \pm 0.26_{sys} \text{ ppm}, \tag{3.17}$$

which gives the extracted value of

$$(G_E^s + 0.225 G_M^s)(Q^2 = 0.230) = 0.039 \pm 0.034 \tag{3.18}$$

for the linear combination [188]. The expectation from the standard model assuming no strangeness contribution to the vector current is $A_{nvs}(Q^2 = 0.230) = -6.30 \pm 0.43$ ppm. The experiment reported a linear combination at this Q^2 that is positive, and the result hints that either G_E^s and G_M^s are both small or have opposite signs and largely cancel each other.

The second PVA4 forward-angle measurement made use of the fully operational detector (all 1022 channels). The measurement was at a beam energy of 570.4 MeV, at $Q^2 = 0.108$ (GeV/c)^2, and yielded an asymmetry of

$$A_p(Q^2 = 0.108) = -1.36 \pm 0.29_{stat} \pm 0.13_{sys} \text{ ppm}, \tag{3.19}$$

which gives the extracted value of

$$(G_E^s + 0.106 G_M^s)(Q^2 = 0.108) = 0.071 \pm 0.036 \tag{3.20}$$

for the linear combination [189]. The prediction from the standard model assuming no strangeness contribution to the vector current is $A_{nvs}(Q^2 = 0.108) = -2.06 \pm 0.14$ ppm. Again, the experiment reported a value for the linear combination as positive, this time 2σ from zero.

After the completion of the forward-angle measurements of the experimental program, the PVA4 apparatus was turned around and modified for a series of backward-angle measurements. A double-ring of 72 scintillator counters that each cover 14 of the PbF_2 detectors were added to the detector system. These are used for electron tagging to differentiate the electrons from the photon background coming from π^0 decay at the measurement beam energy of 315 MeV [190]. The first back-angle measurement used a 20 μA of 315.1 MeV beam at a Q^2 of 0.230 (GeV/c)^2.

	Beam Energy	Q^2 $(\mathrm{GeV}/c)^2$	θ_{lab}	A_{phys} (ppm)	Target
SAMPLE-I	200 MeV	0.1	$\sim 145°$	$-5.61 \pm 0.67 \pm 0.88$	H
SAMPLE-II	200 MeV	0.1	$\sim 145°$	$-7.77 \pm 0.73 \pm 0.72$	D
SAMPLE-III	125 MeV	0.038	$\sim 145°$	$-3.51 \pm 0.57 \pm 0.58$	D
HAPPEX-H-I	3.2 GeV	0.477	$\sim 12.3°$	$-15.05 \pm 0.98 \pm 0.56$	H
HAPPEX-H-II	3.3 GeV	0.109	$\sim 6°$	$-1.58 \pm 0.12 \pm 0.04$	H
HAPPEX-He	3.3 GeV	0.077	$\sim 6°$	$+6.40 \pm 0.23 \pm 0.12$	^{4}He
A4	855 MeV	0.230	$\sim 35°$	$-5.44 \pm 0.54 \pm 0.26$	H
A4	570.4 MeV	0.108	$\sim 35°$	$-1.36 \pm 0.29 \pm 0.13$	H
A4*	315 MeV	0.230	145°	-17.1 ± 1.4	H

TABLE 3.1: *A summary of the measurements of parity-violating asymmetries from strange-quark contribution experiments prior to G^0. An asterisk (*) indicates a preliminary result. The data are taken from the publications, with the exception of the preliminary results, which are taken from presentations by the collaborations. The first and second error bars on the measured asymmetry $A_\perp$ designate statistical and systematic uncertainties, respectively.*

The collaboration has reported a very preliminary result of $A_{PV} = (-17.1 \pm 1.4)$ ppm, but the analysis and the data-taking are still ongoing at the time of this writing [191]. We are looking forward to these results in the near future.

The PVA4 collaboration has other backward-angle measurements with a deuterium target and at different beam energies planned, which will be discussed in Section 7.1.

3.3.4 Summary of Previous PV Experiments

A summary of the existing measurements of the asymmetries from related parity-violation experiments prior to or concurrent with the G^0 experiment is displayed in Table 3.1, from the published results of data taken from [180,183,186,188,189,191]. It is important to note that these data have been taken on different targets and at various kinematics, so not all of the asymmetries are sensitive to the same strange form factors. However, most of the measurements have been focused on measurements at lower Q^2 values, so it is evident that more investigation must be done at higher momentum transfer settings.

The extracted values for the linear combination of the strange electric and magnetic form factors $G_E^s + \eta G_M^s$ from the measured asymmetries in the forward-angle experiments are shown in

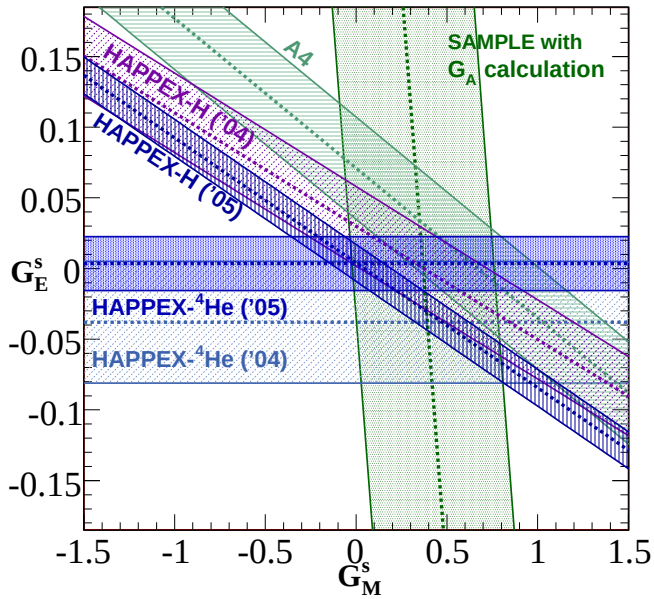

FIG. 3.9: *The results from other experiments plotted in the G_E^s versus G_M^s plane. The ellipses indicate the 68% and 95% confidence levels. Data taken from [180, 184–186, 189].*

Table 3.2 from the published results of data taken from [183, 186, 188, 189]. The published results from the measurements at $Q^2 = 0.1$ (GeV/c)^2 (where most of the data have been measured) are shown in the G_E^s versus G_M^s plane in Figure 3.9. Since these measurements have been done at different kinematics and on different targets, the intersection of the bands yields the values of G_E^s and G_M^s. These data give hints of possibly non-zero form factors, but nothing conclusive, making it clear that more data is necessary, especially at higher Q^2 values.

	Beam Energy	Q^2 (GeV/c)^2	θ_{lab}	η	$G_E^s + \eta G_M^s$
HAPPEX-H-I	3.2 GeV	0.477	12.3°	0.392	0.014 ± 0.022
HAPPEX-H-II	3.3 GeV	0.109	6°	0.09	0.007 ± 0.013
HAPPEX-He	3.3 GeV	0.077	6°	0 (G_E^s only)	0.002 ± 0.016
A4	855 MeV	0.230	35°	0.225	0.039 ± 0.034
A4	570.4 MeV	0.108	35°	0.106	0.071 ± 0.036

TABLE 3.2: *A summary of the extracted values for $G_E^s + \eta G_M^s$ and average kinematics from the indicated experiments at forward angles from the publications to date. The uncertainty for the linear combination is the reported statistical and systematic uncertainties combined in quadrature. Note that the extractions of $G_E^s + \eta G_M^s$ by the various experiments have used different parameterizations of the nucleon electromagnetic form factors in their published results.*

The values determined for G_M^s and $G_A^{e\,(T=1)}$ by the SAMPLE experiment from the measured asymmetries at a backward scattering angle were extracted from the data used two methods: using the first data set and the theoretical value from [85], and by using their two data sets alone [180]. As measurements at backward angles are necessary to disentangle the strange electric, magnetic, and axial form factors, it is clear that more measurements are needed to accomplish this.

The results of these experiments provide hints of possible non-zero strange form factors, but are not at all conclusive, especially at higher values of Q^2. As the G^0 experiment will measure the linear combination of G_E^s and G_M^s up to $Q^2 = 1$ (GeV/c)^2, and will perform a full separation at $Q^2 = 0.23$, 0.62 (GeV/c)^2, providing information at higher Q^2.

3.4 Previous Transverse Beam Spin Measurements

As parity-violating electron scattering experiments have achieved greater levels of precision due to improvements in experimental techniques, it has become increasingly more important for them to measure the parity-conserving transverse beam spin asymmetry as part of their systematics studies in order to provide a constraint on the contribution of any systematic false asymmetry in their measurement arising from any residual transversely-polarized beam component. However, these data are also of interest in their own right because they can be analyzed to study two-photon exchange processes. There are several experiments that have performed measurements of the transverse beam spin asymmetry in elastic electron-photon scattering in order to investigate two-photon exchange effects. This section discusses these experiments and their findings.

A key feature of most of these experiments is an azimuthally-symmetric detector in ϕ (around the beam axis) that can be divided into sections, since if averaged over ϕ, the measured transverse beam spin asymmetry averages to zero, but if divided into sections and plotted versus ϕ, the sinusoidal dependence of the transverse beam asymmetry can be easily seen.

3.4.1 SAMPLE at MIT-Bates

The SAMPLE Collaboration performed the first measurement of the transverse beam spin asymmetry in elastic *e*-*p* scattering using the SAMPLE apparatus discussed in Section 3.3.1. For the two data-taking periods of the measurement, the experiment used a 200 MeV transversely polarized electron beam of an average current of 40 μA incident on the liquid hydrogen target. To generate the transverse beam polarization required, the longitudinal electrons from the polarized source were oriented using a Wien filter and a set of beam solenoids to be transverse to the beam direction in the plane of the accelerator for one running period, and vertically polarized for the other. The polarization of the beam, measured by a Møller polarimeter on the beamline, averaged $36.3 \pm 1.8\%$ for the measurements. The rest of the experimental configuration was the same as for the primary SAMPLE parity-violation experiment, as described in Section 3.3.1. The data were corrected for effects including the beam polarization, background dilution, and radiative effects in the same manner as the other SAMPLE data. The transverse asymmetries were extracted for each of the ten mirrors positioned at varying azimuthal angles ϕ around the beamline, although the data for mirrors 4 and 5 and mirrors 6 and 7 were combined since they were positioned at the same azimuthal angle (but different polar angles).

The combined measured asymmetry results from both running periods are shown in Figure 3.10 as a function of the azimuthal scattering angle ϕ. The data show a sinusoidal trend as expected. From these measured asymmetries, the transverse beam spin asymmetry result was found to be

$$A_{\perp}(Q^2 = 0.1) = -16.4 \pm 5.9 \text{ ppm} \tag{3.21}$$

at an average electron laboratory scattering angle of 146.1°, which corresponds to a value of $Q^2 = 0.1$ (GeV/c)^2 [145, 180]. Figure 3.11 shows this result for $A_{\perp}$ plotted versus the center-of-mass angle along with a calculation by A. Afanasev for the collaboration for the transverse beam spin asymmetry for elastic electron-proton scattering. This measurement demonstrated that two-photon exchange observables were accessible by this technique, and were a possible systematic for

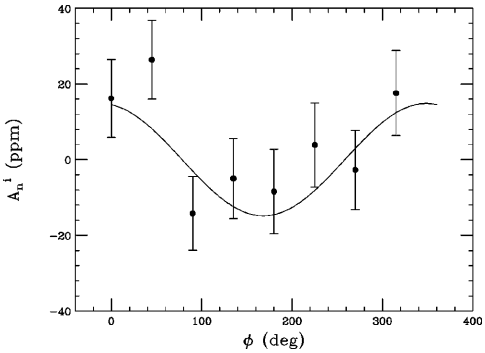

FIG. 3.10: *The combined measured transverse beam spin asymmetries for the SAMPLE experiment. The measured asymmetries are plotted as a function of the azimuthal scattering angle ϕ. Figure taken from [145].*

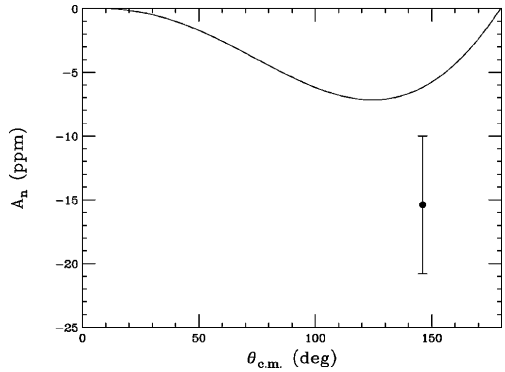

FIG. 3.11: *The SAMPLE extracted transverse beam spin asymmetry result as a function of center-of-mass angle compared to calculations by Afanasev. Figure taken from [145].*

parity-violation measurements.

3.4.2 PVA4 at MAMI

The PVA4 Collaboration also made measurements of the transverse beam asymmetry, both as part of their systematics studies for their forward-angle parity-violating asymmetries measurements, and in an effort to measure the imaginary part of the two-photon exchange amplitude. The measurements were at a higher beam energy than SAMPLE and at a forward angle, so, unlike the SAMPLE measurements, the PVA4 ones are sensitive to πN-intermediate states as well as the ground state.

The experiment performed two measurements at a forward angle of $\theta_e \sim 35°$ using the PVA4 apparatus (see Section 3.3.3). The experimental configuration was the same as for the primary forward-angle parity-violation experiment, except that the longitudinally polarized electrons in the beam from the source were rotated in the accelerator plane using a Wien filter, resulting in a transverse polarization of about 80% as measured by a Møller polarimeter in another experimental hall and by a transmission Compton polarimeter located in the hall between the liquid hydrogen target and the beam dump. Averaging the asymmetries from all the detectors would result in zero

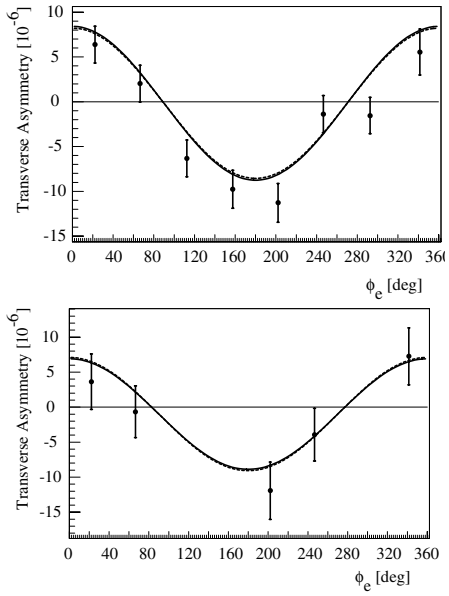

FIG. 3.12: *The measured transverse beam spin asymmetries for the forward-angle PVA4 experiment. The upper plot shows the data for a beam energy of 569.31 MeV, and the lower plot for the beam energy of 855.15 MeV. The measured asymmetries are plotted as a function of the laboratory angle ϕ_e. Figure taken from [156].*

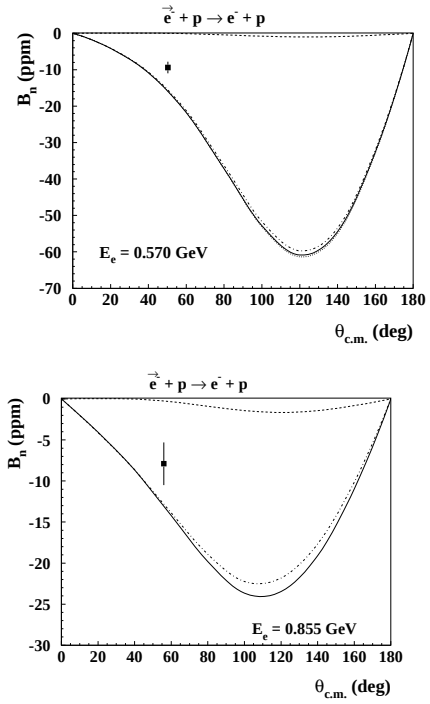

FIG. 3.13: *The PVA4 forward-angle transverse beam spin asymmetry results compared to calculations from [140]. Data taken from [156]. The dashed lines denote the elastic nucleon intermediate state contribution, the dashed-dotted lines the πN inelastic state contribution, and the solid lines the sum of both contributions.*

since the ϕ dependence of the transverse asymmetry results in a complete cancellation averaged over a ϕ-symmetric detector. Therefore, for these measurements the 1022 PbF_2 crystal detectors of the calorimeter were divided into eight sections (labeled 1 through 8) that each spanned a range of about 45° in ϕ. For the first measurement at 855.15 MeV however, only 756 channels had been installed, so data could only be taken for sectors 1, 2, 5, 6, and part of sector 8. The transverse beam spin asymmetry data were analyzed using the same analysis method as for the primary forward-angle parity-violation experiment described in [188], except that the data were divided into the sectors. The data for each of the sectors are shown in Figure 3.12, along with the sinusoidal fit to the data points.

The measurement at a $Q^2 = 0.106$ (GeV/c)^2 with a beam energy of 569.31 MeV yielded a

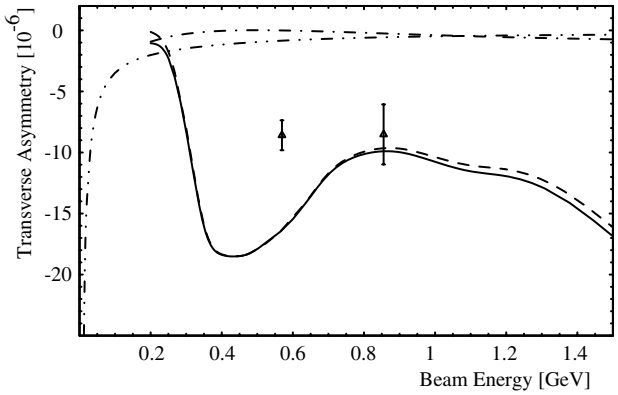

FIG. 3.14: *The PVA4 forward-angle transverse beam spin asymmetry results compared to predictions. In the calculations from [140], the elastic contribution is denoted by the dashed-dotted line, the πN-intermediate states (inelastic contribution) by the dashed line, and the full calculation by the solid line. The dashed-double dotted line shows the calculation from Reference [153] that uses an effective theory of electrons, protons, and photons. Figure taken from [156].*

result of

$$A_{\perp}(Q^2 = 0.106) = -8.59 \pm 0.89_{stat} \pm 0.75_{sys} \text{ ppm}, \tag{3.22}$$

and the second measurement at a $Q^2 = 0.230$ (GeV/c)^2 with a beam energy of 855.15 MeV yielded a result of

$$A_{\perp}(Q^2 = 0.230) = -8.52 \pm 2.31_{stat} \pm 0.87_{sys} \text{ ppm}, \tag{3.23}$$

where the two errors in both cases represent the statistical error and the systematic uncertainty respectively [156]. These results are shown in Figure 3.13 with the calculations by reference [140]. They are also shown in Figure 3.14, along with two model calculations from references [140] and [153]. The measurements show that the two-photon exchange contribution at these low-Q^2 kinematics of $Q^2 = 0.106$ and 0.230 (GeV/c)^2 is largely dominated by the inelastic πN-intermediate state of $\Delta(1232)$ resonance and higher resonances, as the contribution from the nucleon elastic state (the dotted-dashed curve) is very small and the inelastic contribution (the dashed curve) dominates the full calculation (the solid curve).

The PVA4 Collaboration also recently presented the preliminary results of their backward-angle measurement of the transverse spin asymmetry using the PVA4 apparatus in its backward-

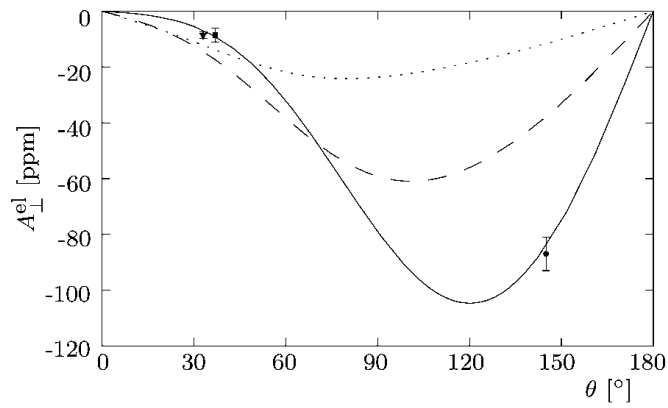

FIG. 3.15: *The PVA4 backward-angle transverse beam spin asymmetry preliminary results versus scattering angle compared to calculations of [140], where the dotted line is for a beam energy of $E = 855$ MeV, corresponding to the square data point from the forward-angle measurement, the dashed line and triangular data point are for $E = 570$ MeV, and the solid line is for $E = 300$ MeV with the circle for the preliminary backward-angle point. Data points taken from [156] and [157]; figure from [157].*

angle configuration from transverse beam spin data taken in March of 2006. With a 315 MeV beam at a lab angle of $\theta_e = 145°$ at $Q^2 = 0.23$ (GeV/c)^2, the measurement yielded a preliminary result of

$$A_\perp^{el} = -87 \pm 6_{stat} \text{ ppm}, \tag{3.24}$$

where the error bar is statistical [157]. These preliminary results seem to be in agreement with theoretical predications at $Q^2 = 0.23$ and a beam energy of 315 MeV, as shown in Figure 3.15. We look forward to their final results.

The PVA4 collaboration is presently taking more backward-angle data, and plan on conducting transverse beam spin measurements at different Q^2 values on liquid hydrogen and deuterium targets (see Section 7.1).

3.4.3 HAPPEX at Jefferson Lab

Recently, the HAPPEX Collaboration showed preliminary results of a transverse beam spin measurement taken with a hydrogen target during their 2004 run and the first measurement of the transverse spin asymmetry on a nucleus, taken on a ^{4}He target during their 2005 run period.

Unlike the previously described experiments, HAPPEX does not have an azimuthally-symmetric detector array around the beam axis, but instead has two high-resolution spectrometers positioned with left-right symmetry. With the electron beam transversely polarized in the plane of the accelerator, the measured asymmetry in the spectrometers would be zero because the $\vec{P}_e \cdot \hat{n}$ term (defined in the Section 2.7.1) introduces a sine dependence of $A_\perp^m$ on the electron azimuthal angle ϕ_e, with a zero crossing for the case where the scattering plane contains the incident electron polarization vector $\vec{P}_e$. Because of this, the experiment required out-of-plane transverse polarization, which was achieved with a Wien filter and an unbalanced counter-wound solenoid. This vertical polarization was measured using the 5 MeV Mott polarimeter and the Hall A Møller polarimeter with a tilted target foil. The rest of the experiment was in the usual parity-violation data-taking configuration for HAPPEX (see section 3.3.2 and reference [186]).

From the measurement on a liquid hydrogen target with a beam energy of 3 GeV, at $\theta_{lab} \sim 6°$ and $Q^2 = 0.099$ (GeV/c)^2 HAPPEX reported a preliminary result of

$$A_\perp(Q^2 = 0.099) = -6.58 \pm 1.47_{stat} \pm 0.24_{sys} \text{ ppm}, \tag{3.25}$$

where the first error is statistical and the second uncertainty is the systematic error on the measurement. On the helium target, a preliminary measurement of

$$A_\perp(Q^2 = 0.077) = -13.51 \pm 1.34_{stat} \pm 0.37_{sys} \text{ ppm} \tag{3.26}$$

was reported for a beam energy of 2.75 GeV, with $\theta_{lab} \sim 6°$ and $Q^2 = 0.077$ (GeV/c)^2 [161].

The preliminary HAPPEX asymmetry result for hydrogen agree well with the calculations by Afanasev and Merenkov [148]. The transverse asymmetry calculation for ^{4}He by Cooper and Horowitz predicts a magnitude on order of 10^{-10} for the HAPPEX kinematics, assuming that the nucleus remains in the ground state at all times [192]. As the HAPPEX transverse asymmetry results for ^{4}He are 5 orders of magnitude larger than this, the excited states of the nucleus must have a significant contribution to the asymmetry. Another prediction using the optical theorem to relate the transverse asymmetry to the total photoabsorption cross-section was in reasonable agreement [193].

	Beam Energy	Q^2 (GeV/c)^2	θ_{lab}	$A_\perp$ (ppm)	Target
SAMPLE	200 MeV	0.1	146.1°	-15.4 ± 5.4	H
A4	569.31 MeV	0.106	$\sim 35°$	$-8.59 \pm 0.89 \pm 0.75$	H
A4	855.15 MeV	0.230	$\sim 35°$	$-8.52 \pm 2.31 \pm 0.87$	H
HAPPEX*	3 GeV	0.099	$\sim 16°$	$-6.58 \pm 1.47 \pm 0.24$	H
HAPPEX*	2.75 GeV	0.077	$\sim 6°$	$-13.51 \pm 1.34 \pm 0.37$	He
A4*	315 MeV	0.23	145°	-87 ± 6	H

TABLE 3.3: *A summary of the measurements of the transverse beam spin asymmetry prior to G^0. An asterisk (*) indicates a preliminary result. The data are taken from the publications, with the exception of the preliminary results, which are taken from presentations by the collaborations. The first and second error bars on the measured asymmetry $A_\perp$ designate statistical and systematic uncertainties, respectively.*

3.4.4 Summary of Previous Transverse Measurements

A summary of the existing world data from measurements of the transverse beam spin asymmetry by other experiments prior to the G^0 experiment is displayed in Table 3.3 (data taken from references [145, 156, 157, 161]). As with the data shown from the parity-violation experiments, it is important to note that these measurements have been done at both forward and backward angles, as well as on different targets. The data suggest that two-photon exchange processes could be a sizable contribution to the radiative corrections for measurements of the electric form factor using Rosenbluth separation. However, these data are insufficient to extract the real part of the two-photon exchange amplitude from the measurement of the imaginary part of the two-photon exchange amplitude in order to cross check with model calculations to resolve the discrepancy observed in measurements of the elastic form factors, so more investigations into two-photon exchange effects are clearly necessary. The results also suggest that the transverse asymmetry could be a potential systematic uncertainty for parity-violation experiments as these experiments reach new levels of precision, implying that A_n cannot be considered negligible in future experiments and that a good understanding of these effects is necessary.

3.5 Remarks on Previous Experiments

As can be seen in this chapter, there have been other contemporary experiments with the goal of measuring the strange-quark contributions to the vector structure of the nucleon. However, most of these experiments have been performed at lower Q^2 values. The results of these experiments provide hints of non-zero strange form factors, but are not at all conclusive. As was discussed in Section 2.10, the G^0 experimental program is unique in its ability to measure the linear combination of the strange electric and magnetic proton form factors for 18 Q^2 values over the range of $0.1 < Q^2 < 1.0$ (GeV/c)^2 simultaneously, allowing researchers to study the possible Q^2 evolution of the linear combination $G_E^s + \eta G_M^s$. Combined with the anticipated backward-angle measurements, the G^0 experiment will also be able to perform a complete separation of the strange electric (G_E^s), magnetic (G_M^s), and axial (G_A^e) form factors for two of these Q^2 points. Along with the complementary experimental programs discussed in this chapter, these measurements should help give a better understanding of nucleon structure. In the following chapters, a description of how the G^0 experiment achieved these challenging goals is discussed.

CHAPTER 4

The G^0 Experimental Apparatus

Designing an experiment that meets all the demands of both forward and backward-angle measurement configurations in addition to all the other demands of parity-violation experiments is quite challenging. This chapter discusses how these challenges were overcome and describes the equipment constructed to accomplish this (for the forward-angle phase of the experiment).

4.1 The G^0 Experiment

The G^0 experiment used the technique of parity-violating electron scattering to measure tiny parity-violating asymmetries to determine the strange quark contributions to the properties of the nucleon. For the G^0 forward-angle measurement, the polarized electrons from the accelerator were incident on a liquid hydrogen target located inside a superconducting magnet system (SMS), as shown in Figure 4.1. The trajectories of the recoiling protons from the target were bent by the toroidal field of the SMS and focused onto arrays of scintillating detectors (called focal plane detectors, or FPDs) placed on the focal plane of the spectrometer. In order to identify elastic proton events from the background of positively-charged pions (π^+) and inelastic protons, the time-of-flight (ToF) of the particles from the target to the detectors was used. From the rates

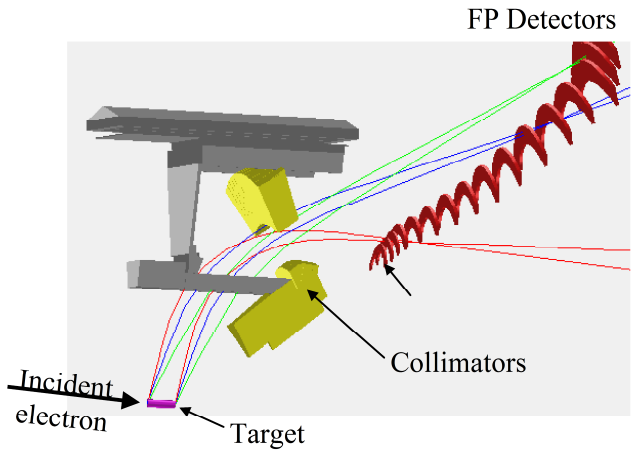

FIG. 4.1: *A schematic of the particle trajectories from the target to the detectors in the G^0 Spectrometer.*

measured in the detectors, the parity-violating asymmetry could be determined.

4.1.1 Experimental Technique

The principle of parity-violation in electron scattering is elegant and straightforward. The incident electron beam is polarized either parallel (referred to as right-handed or positive electron helicity) or anti-parallel (left-handed or negative electron helicity) to the beam momentum. The target for the experiment is unpolarized, and the outgoing particles from the interaction are detected at a particular scattering angle. The relative difference of the detected rates between the two electron helicity states is the parity-violating asymmetry, defined as

$$A = \frac{h^+ - h^-}{h^+ + h^-}, \tag{4.1}$$

where h^+ denotes the measured rate in the positive helicity state and h^- is the measured rate in the negative helicity state.

Due to the dominance of the parity-conserving electromagnetic interaction, the size of this parity-violating asymmetry is exceedingly small, only on the order of $10^{-4}Q^2$, where Q^2 is the four-momentum transfer in units of $(\mathrm{GeV}/c)^2$. Therefore, the asymmetries are usually measured in ppm, or parts-per-million.

4.1.2 Experimental Design

The concept of the parity-violation technique in electron scattering is very elegant, but it is also very difficult due to the minuscule size of the effects, only a few parts-per-million, that this technique is used to measure. All sources that could introduce a false asymmetry (an asymmetry other than the one desired to be measured) must be either eliminated, or failing that, minimized as much as possible and then thoroughly studied, understood, and corrected for through measurements of the false asymmetry.

The asymmetries were expected to range in size from about -2 ppm (at the lowest forward-angle Q^2) to about -70 ppm (the highest Q^2 in backward-angle). In order to measure these small asymmetries with a relative precision of a few percent, the statistical and systematic uncertainties needed to be very small, less than 10^{-7}. However, there were other aspects that had to be considered in the design. To accomplish the entire experimental program, the system had to be capable of both forward and backward angle measurements. As measurements on both liquid hydrogen (for forward and backward-angle measurements) and liquid deuterium (backward-angle only) were necessary, the cryogenic target had to be designed to handle both. The detector systems had to be capable of handling both configurations (forward and backward), as well as have a method for the rejection of background events.

Beamtime is a limited resource. The statistical uncertainty is $\Delta A = 1/\sqrt{N_{tot}}$, where N_{tot} is the total number of detected events, so a great many events are needed (10^{13} – 10^{14}!) to reach the desired statistical precision of about 5%. To measure each asymmetry at each momentum transfer Q^2 individually for the amount of time needed for a precise measurement of quantities of a few ppm is prohibitive. Therefore, the system needed to be able to measure the full range of Q^2 from 0.1 to 1.0 $(\mathrm{GeV}/c)^2$ simultaneously.

As the statistical uncertainty depends on the number of events, the more quickly the events are collected, the more quickly the desired statistical uncertainty is attained. This can be done by using a combination of high luminosity and large solid angle acceptance. To achieve a high

luminosity, G^0 used a relatively high beam current (intensity) of 40 μA, and a long target (20 cm) to achieve a luminosity of about 2×10^{38} cm^{-2} s^{-1} [194]. To achieve the second requirement, the experiment used a large-acceptance magnetic spectrometer that detects recoiling protons from the target in the forward-angle measurement, and backward-scattered electrons in the backward-angle measurement.

The spectrometer was designed to have a solid-angle acceptance of about 0.9 sr, which corresponds to an acceptance range of about 55° to 75° for forward-angle elastic scattering at a beam energy of 3 GeV. The acceptance is flat along the entire length of the target, with the optics of the spectrometer designed so that particles with the same momentum transfer are focused onto the same surface in the focal plane of the spectrometer, no matter where they originate from along the target length. This design allows the full range of momentum transfers in the forward-angle to be measured simultaneously, and corresponds to a single momentum transfer in the backward-angle measurements. However, even with this design, to reach the desired statistical precision, about 700 hours of total beamtime were needed.

By reversing the spectrometer with respect to the beam direction, the same spectrometer can be used for both forward and backward measurements. By detecting the recoiling protons at a lab scattering angle of about 70° in the forward angle measurement, and backscattered electrons at about 110° in the backward-angle measurement, the separation of the $G_E^\gamma G_E^Z$ and $G_M^\gamma G_M^Z$ terms can be done. In the forward-angle measurement, ToF was used to reject background particles. However, the background rejection must be done differently for the two measurements, since the time-of-flight technique will not work for the relativistic electrons. In addition, Q^2 varies slowly with angle in the backward direction, and so separate measurements with different beam energies are required to span the desired range of momentum transfer.

The success of attaining the desired small systematic uncertainties predominantly rests on the beam quality, and the ability to control and accurately monitor that quality is critical. Precision control of the intensity, alignment, and polarization of the laser used to drive the polarized beam

Parameter	Value
Beam energy E	3.0 GeV
Beam current I	40 μA
Target type	LH_2
Target length	20 cm
Proton momentum p	350 – 1130 MeV/c
Scattering angle $\theta^p_{elastic}$	$52.0° - 76.50°$
Momentum transfer Q^2	$0.12 - 1.0$ (GeV/c)^2
Azimuthal acceptance $\Delta\phi$	$0.44 \cdot 2\pi$
Solid angle$\Delta\Omega_{elastic}$	1.07 sr
Average field integral$\int \vec{B} \cdot \vec{dl}$	1.6 T.m

TABLE 4.1: *A summary of parameters for the forward-angle measurement, thus corresponding to elastic protons.*

source keeps the changes in the beam parameters associated with the helicity change of the beam electrons very small. In addition, the azimuthal symmetry (with each of the eight octants having an opposing octant) of the spectrometer allows the cancellation of any small helicity-correlated beam motion effects (to lowest-order) when the detected rates are summed over all the detectors.

Since the key to a parity-violation experiment is first doing the measurement, and then the "mirror-image" of the measurement, which for us is the flipping of the electron helicity, it is very important that this be accomplished without altering any other beam parameters. In the experiment, the electron helicity was flipped at 30 Hz (33.33 ms) in a pattern chosen pseudorandomly to avoid linear drifts over the timescale of the sequence and to cancel out any 60 Hz noise [195].

In order to separate the elastic protons from the background particles, time-of-flight is used (instead of explicitly measuring the trajectories) to determine particle momentum. However, the time-of-flight of the elastic protons from the passage of the beam through the target to the detectors is about 20 ns, much longer than the usual 2 ns spacing of the electron beam bunches at Jefferson Lab. Therefore, the experiment used a special 31.1875 MHz pulsed laser to drive the polarized source, which produced a beam with a spacing of 32 ns between the electron bunches. Because of the spectrometer optics and the kinematics of the experiment, the background particles in a given detector actually arrive earlier, pions at 7 ns and inelastic protons after the pions but before the elastic protons. As with all the other signals in the experiment, it is important that the start

signal for the ToF (which is generated by the passage of the beam through the target) be not only accurate, but also not correlated with the helicity-reversal of the beam.

The choice of having high luminosity to gain the needed statistics means that the rates will be relatively high, so the choices of detectors and electronics for the forward-angle measurement are driven by the need to handle these high rates. Because of this, the spectrometer is segmented into eight arrays, or octants, of detectors. The magnet focuses the protons of a particular Q^2 onto a particular area on the focal plane of the spectrometer, so by placing separate detectors in these areas on the focal plane, a separation by Q^2 can be achieved. The detectors are arc-shaped to follow a particular Q^2, with the widths chosen to give a good resolution in Q^2 but limiting the rate to about 2 MHz (half of which comes from the elastic protons of interest, and half from background pions and inelastic protons). The detectors are made up of pairs of plastic scintillators (pairs so as to reduce the background from neutrals by requiring a coincidence), with photomultiplier tubes at each end of the light guides from the detectors. A coincidence of the mean-timed signals from the scintillator pair in a detector defines an elastic proton event.

Since particle identification required time-of-flight, a system of electronics was used that counts the rates from the detectors instead of the charge-integrating systems usually used in parity-violation experiments. This meant that electronics deadtime introduced by the high rates would be an issue and would have to be corrected for carefully. The deadtime was corrected directly from singles measurements, and any helicity-correlated effects from it were corrected with other helicity-correlated parameters such as the beam position. The spectra containing the time-of-flight information were then read out for every beam pulse (33.33 ms) by the custom time-encoding electronics.

Each of the subsystems of the experiment were carefully designed and built to meet the stringent requirements of this measurement, as can be seen in the following sections.

4.2 Jefferson Lab Accelerator

The forward-angle measurement took place in Hall C at Thomas Jefferson National Accelerator Facility (TJNAF or Jefferson Lab) in Newport News, Virginia. The equipment was commissioned in dedicated commissioning runs, the first one beginning in October 2002 and the second in November of 2003. The forward-angle production data taking finally started in January 2004, ending in May 2004.

The G^0 experiment typically made use of 40 μA of a 3 GeV polarized electron beam delivered into experimental Hall C by the CEBAF (Continuous Electron Beam Accelerator Facility) accelerator at Jefferson Lab. The CEBAF accelerator has the ability to deliver continuous electron beams of different energies (from 1 to 6 GeV) simultaneously to three experimental endstations, Halls A, B, and C. The polarized electron beam available at Jefferson Lab is very clean, with little beam halo and small helicity-correlated differences in beam properties such as charge, position, and angle, making the lab the ideal place to conduct a precision parity-violation measurement like G^0. The beam is only approximately continuous, as in reality the beams are pulsed with a very high repetition rate, usually 499 MHz for normal running. However, for the G^0 experiment the Hall C beam had a repetition rate of 31.1875 MHz to allow for a good measurement of the particle flight time. The accelerator can be divided into several major components: the injector region, the recirculating arcs, the linear accelerators (LINACs), and the beam switchyard.

To generate the electron beams for each of the three halls, each hall has an individual laser that is pulsed at 499 MHz and offset in phase by 120° from each other. The circularly-polarized light from the lasers illuminate a common photo-cathode, where electrons are emitted by the photo-electric effect. The timing of the three beams is determined by the timing of the pulses of the three lasers for each of the halls. These electrons are then accelerated by a cathode gun to about 100 keV, where they then pass through a pre-buncher and a chopper cavity. These elements ensure the timing and the longitudinal spread of the three electron beams. The chopper operates at 499 MHz and provides three slits for the three individual beams destined for each of the

experimental halls. The electrons are then accelerated up to about 500 keV, before passing though two superconducting radio-frequency (SRF) cavities that provide more bunching and accelerate the beam to about 5 MeV. The electrons then pass through two more modules, each containing eight SRF cavities. They accelerate the beam to on average 45 MeV, before passing through a chicane and entering the main accelerator [196].

The CEBAF accelerator has a fundamental operation frequency of 1497 MHz and consists of two SRF LINACs joined by two 180° recirculating arcs. A diagram of the racetrack layout of the accelerator is shown in Figure 4.2. Each LINAC has 20 SRF cavities, and with each pass through a LINAC the electrons gain a maximal energy of 600 MeV, for a maximum of about 6 GeV in five passes through the entire machine. The beams at each pass have different energies, so at each recirculating arc they require different bending fields to make the turn. To account for this, the beam is split into several beams as it exits the LINAC by a series of magnets that deflects the beams of different energies into the different beamlines. At the end of each arc the reverse happens, and the beams are recombined vertically into one before entering the LINAC for further acceleration. The beams of various energies are extracted to be delivered to the three experimental halls by RF separators located at the exit of the south LINAC. The separator cavities operate at 499 MHz, and can be tuned to extract the beam bunches of the desired energy for any one hall without interfering with the acceleration of the remaining bunches [197]. The extracted beams then enter the beam switchyard, where they are deflected into Halls A, B, or C according to their different timing.

4.3 The Polarized Electron Beam for G^0

The rigid requirements of parity-violating electron scattering experiments, driven by the need for high statistical precision and low systematic uncertainties, demand an electron beam with three major characteristics: high intensity, high polarization, and stable high quality. As the asymmetries of interest are so small, false asymmetries introduced by properties of the beam that

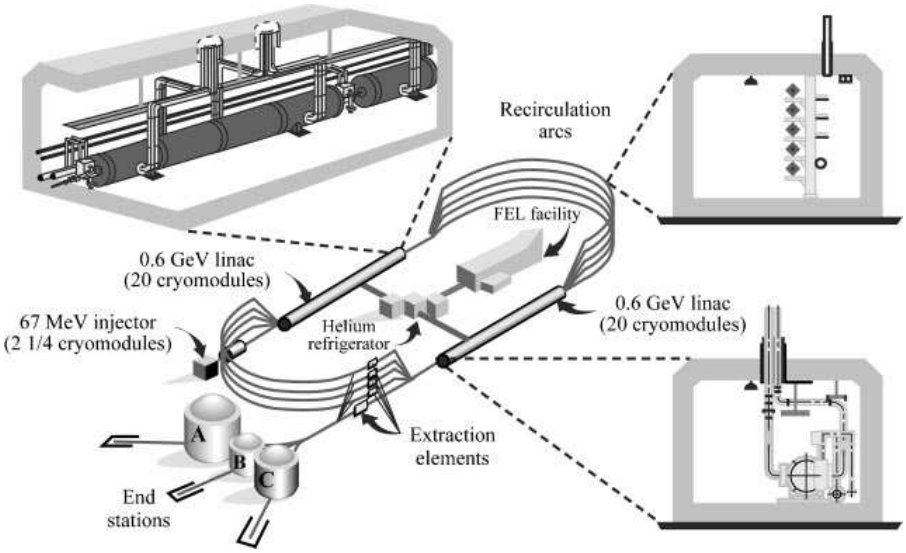

FIG. 4.2: *A diagram of the layout of the CEBAF accelerator. Figure from [196].*

change with the helicity change can easily skew the measurement. Ideally, only the helicity of the beam should change when the spin-flip occurs, but in reality, many things can change with the helicity change. Any asymmetry that comes from these other changes is in addition to the desired one, and is thus a helicity-correlated false asymmetry. These false asymmetries must be corrected for and removed. Therefore, the ability to control and accurately measure the beam properties is essential, as any false asymmetries arising from these properties must be minimized, and any corrections made because of the beam properties must be small and well understood. In addition to these requirements, the forward-angle G^0 measurement required a very different time structure than what is standard at Jefferson Lab, which created some unique challenges.

4.3.1 The Polarized Source

The highly polarized electron beam produced at Jefferson Lab is produced by shining circularly polarized laser light onto a strained gallium arsenide (GaAs) photocathode, where the polarized electrons are generated by photoemission. The linearly polarized light from the titanium(Ti)::sapphire G^0 laser is converted into circularly polarized light by a Pockels cell. A Pockels

cell is a birefringent crystal where the indices of refraction vary in direct proportion to the voltage applied to it. The voltage applied to it effectively makes the Pockels cell a $\lambda/4$ (quarter-wave) plate, which converts the linearly polarized laser light into left- or right- circularly polarized light. When the circularly-polarized laser light shines upon the GaAs crystal, electrons escape the crystal via the photoelectric effect, and have a net polarization due to the incident photon's polarization and the allowed transitions in the GaAs crystal. The choice of left- or right- circularly polarized light incident on the the GaAs crystal determines the helicity state, "h^+" or "h^-", of the emitted electrons [174]. At Jefferson Lab, the system is made up of three lasers (one for each experimental hall) and two identical 100 kV DC photoemission electron guns, although only one is used at any time (with the other held in readiness) [198, 199].

The strained-layer GaAs crystals used as photocathodes for the G^0 experiment are able to produce electron beam polarizations of about 75% at the beam current needed for the experiment (40 μA). Before being used, the cathodes are prepared by a brief atomic hydrogen cleaning in a dedicated chamber, transferred to the desired electron gun under nitrogen purge and bath, and then baked. To establish a negative electron affinity surface on the cathode, it is then heated and activated with cesium and nitrogen tri-fluoride. The laser light shines on the photocathode through a vacuum window, emitting radio-frequency electron pulses with widths of $\sim$ 100 ps that are synchronous to subharmonics of the CEBAF accelerating frequency of 1497 MHz. The polarized electrons from the cathode are then focused and accelerated by the electrode structure of the gun to a kinetic energy of about 100 keV.

The G^0 experiment required a spacing of 32 ns between the beam pulses (a frequency of 31.1875 MHz) in order to use ToF for particle identification. Two challenges immediately arose from this requirement. First, a new laser was needed to provide 31.1875 MHz, so a high-power Ti-Sapphire one was purchased from Time-Bandwidth Products, which could provide tunable wavelengths from 770 nm to 860 nm. For the forward angle measurement it was run at a wavelength of 840 nm, where it provided a power output of 300 mW. With a typical quantum efficiency of $\sim$ 0.15% for the

photocathode, the electron beam polarization was about 75%, with the required 40 μA of beam current.

The second challenge that arose came from space-charge effects. A high average current at a low repetition rate means that the peak current is large. With the beam current of 40 μA and the timing of 31 MHz required by the G^0 forward-angle measurement, the peak charge was 1.3 pC per micropulse, much higher than the more typical 0.2 pC of 100 μA at 499 MHz in the usual high-current operation at CEBAF. Due to this high peak charge, the resulting space-charge effects caused significant emittance growth in the beam pulses in the low energy (100 keV and 5 MeV) regions of the injector. This caused significant transmission losses and poor quality beam. However, the beam transport optics could not simply be re-optimized for 1.3 pC beam pulses, as the injector had to be capable of simultaneously delivering beam to three experimental halls, all of which have their own stringent demands that also depend on the injector tune. By modifying the injector hardware, tuning procedures, and typical laser parameters, and by stabilizing RF systems, an optics tune was developed was developed that satisfied both the requirements for G^0 and for other experiments running in the other experimental halls [194].

Because many of the potential sources of systematic false asymmetries originate in the polarized source, it is very important to carefully set up the optics on the laser table. It is also important that the random noise fluctuations in the intensity and direction of the emitted laser light be very small. The observations in Hall C at 30 Hz confirmed that the random noise was $< 0.1\%$ for intensity and < 10 μm for the centroid of the beam position, well below our specifications [194].

The polarization of the laser light, and thus the helicity of the beam electrons, was changed every 33.333 ms (30 Hz), which is called a macro-pulse (MPS). The MPS was the primary data-taking period for the experiment, and was chosen to be equivalent to twice the period of the power line voltage (60 Hz line frequency). This was done to reduce the possibility that slow drifts over time may affect the asymmetry measurement. By collecting signals from the experiment over this period, the dominant 60 Hz line noise present in the electron beam properties and in

electronic signals are effectively averaged out. Furthermore, to ensure the exact cancellation of linear drifts over the timescale of a sequence, the helicity signals are generated in quartets: $+--+$ or $-++-$, where the first member of the quartet is chosen pseudo-randomly (by a pseudorandom number generator) and the next member is the complement of the first. The change between the right and left-circularly polarized light is determined by the Pockels cell, which is driven by high voltage power supplies set to approximately ± 2.5 kV, corresponding to $\pm\lambda/4$ phase retardation at the wavelength for the experiment [194]. The switching itself was accomplished by sending the outputs of the HV supplies into a HV switcher that selects which supply output drives the Pockels cell depending on the state of a control signal, known as the helicity control signal. The helicity control signal and other important timing signals for the experimental electronics were generated by the helicity control electronics. At the transition, the Pockels cell is set to the new state, and then the helicity information signals "h^+" and "h^-" were sent to the G^0 electronics in the Hall C counting house from the polarized source helicity control box in "delayed reporting mode", where they were delayed by a preset number of 30 Hz pulses [195]. These signals are used to designate the helicity of a given MPS, although the labels "h^+" and "h^-" only describe the helicity state and its complement, respectively, and do not necessarily contain the state that the label implies, as will be discussed below. The initial helicity state is also accompanied by another signal, called the QRT signal. This QRT signal is what notifies the electronics that a new sequence of four MPS has begun. After each MPS, there is a wait period of approximately 500 μs to ensure that the Pockels cell has stabilized after a helicity change. During this wait period, no data is taken in the experiment, and all the scalers are read out. [194].

Cross-talk of the helicity signal with the other electronic signals in the experiment could lead to a false asymmetry, so all the signals from the helicity generation electronics were delivered by fiber optic cable from the injector, insuring complete ground isolation of these electronics from the remainder of the experimental electronics. Using the "delayed reporting mode" makes the possibility of cross-talk even more improbable, as in this mode the helicity signal reported to the

experimental electronics is delayed by eight MPS signals relative to the actual helicity signal sent to the Pockels cell HV switch. The true helicity is then reconstructed in the analysis software using knowledge of the pseudorandom pattern. [194].

As a systematics check, the G^0 experiment used an insertable half-wave plate (IHWP) on the laser table. The insertion of this IHWP reverses the helicity of the beam electrons with respect to the helicity signal reported to the G^0 electronics, so that the electrons labeled as "h^+" are flipped to the opposite helicity state than they were formerly. The parity-violating physics asymmetry reverses sign, but any electronics asymmetry does not under the insertion or removal of the IHWP. Since all other aspects of the experiment have remained the same, any helicity-correlated differences in the electronics become apparent when physics asymmetries from data taken with the IHWP in and out are summed together, and will tend to cancel when added with the proper correction for the true helicity state of the beam. If there are no helicity-correlated differences present in the electronics, the physics asymmetries summed over the two IHWP states will be zero. In addition, this helps to cancel the effects of helicity-correlated beam position effects. As the polarization reported by the Møller analyzer is calculated from the Møller asymmetry measured by the polarimeter, the sign of the Møller asymmetry also changes sign with the IHWP setting. This causes the polarization to be reported as positive or negative, depending on the actual helicity of the beam electrons in that IHWP setting. It is by this information that the actual helicity of the electrons is determined (see Section 5.2.2.3).

4.3.1.1 Beam Position and Intensity Feedback

As false asymmetries originating from the beam are a primary concern in this experiment, it is important to minimize the helicity-correlation in the beam properties. For G^0, active feedback systems were implemented in the polarized source to do this for the intensity (current), position, angle, and energy.

Helicity-correlated intensity and position differences in the beam originate with the Pockels cell that controls the helicity of the laser light as described earlier in Section 4.3.1. As with

most real-world objects, the Pockels cell does not provide perfectly circularly polarized light, but mostly circularly polarized light with a small residual bit of linearly-polarized light. The linearly-polarized components are transported differently by the optical elements depending on the polarization direction. As the polarization direction varies with the state of the Pockels cell, a helicity-correlated variation in the laser intensity results, which causes intensity variations in the electron beam produced by the laser light. Helicity-correlated position differences are caused in a similar manner, for example, from birefringence gradients in the Pockels cell [194].

Not all helicity-correlated effects are caused by the interaction of the laser light with the optical elements, though. Some are caused by the interaction of the laser light with the strained GaAs photocathode itself. For instance, an anisotropy has been observed in the quantum efficiency of the strained GaAs photocathode depending on the orientation of the linear polarization of light incident on it [200]. This can cause very large intensity asymmetries ($\sim$ 10,000 ppm) and position differences ($\sim$ 10,000 nm). Methods to control this were developed by the HAPPEX collaboration when they observed this effect [183], which were adopted for G^0.

The strategy is to use passive procedures to minimize the false asymmetries as much as possible, then to use active ones to further minimize to the desired requirements. For G^0, the passive measures consisted of careful alignment and configuration of the optical elements on the laser table in the polarized source, careful changes to the accelerator optics to achieve large adiabatic damping and the use of a rotatable $\lambda/2$ waveplate in the polarized source. Careful alignment ensures that the laser light takes a path that gives the least probability of the introduction of helicity-correlated effects as it passes through the optical elements. The natural adiabatic damping effects of the acceleration process can be used to help damp out position differences. In an ideally-tuned accelerator, the transverse beam size is reduced $\propto 1/\sqrt{p}$ where p is the beam momentum. In reality, imperfections in the electron beam transport prevent full suppression, but suppression factors between $10 - 25$ were observed between position differences measured in the low-energy injector region and in the experimental hall [201, 202]. By rotating the $\lambda/2$ waveplate (thereby adjusting the axis of

ellipticity of the laser beam polarization), minima in the intensity and position differences that arise from the anisotropic quantum efficiency of the strained GaAs can be found. After using these passive techniques, the intensity asymmetries were typically less than 100 ppm and the position differences were less than 300 nm at the G^0 target, but these fell far from the requirements of less than 1 ppm and less than 20 nm respectively. Therefore, an active feedback system was also implemented.

To reduce helicity-correlated beam intensity, a feedback system using an IA (intensity-attenuator) cell was used. The IA cell consists of a Pockels cell between two linear polarizers oriented parallel to each other. By varying the voltage on the Pockels cell, the intensity of the laser beam that generates the beam is also changed. During running, the Pockels cell in the IA cell is operated at low voltages, between 0 and 50 volts.

To calibrate the system, a helicity-correlated intensity asymmetry was produced by varying the voltage on the Pockels cell between two set points in a helicity-correlated way. By varying this voltage difference and measuring the corresponding helicity-correlated beam current (charge asymmetries) in the experimental hall, a calibration is made that is linear over the operating range. The slope of this calibration is then used in the feedback routine. During usual production running, the system is automatic. The measured helicity-correlated beam current is averaged over a period of about three minutes to a typical precision of $10 - 20$ ppm; that value and the calibration slope are then used to set the IA cell for the next three-minute running period.

Helicity-correlated beam position differences are minimized by feedback using a PZT mirror device. This device is made up of a mirror that is mounted on piezo-electric transducer mounts that allows motion in two orthogonal directions. The idea of the system is that the mount of the PZT mirror can be driven at the helicity-flip frequency, which induces helicity-correlated motion in the laser beam position, which is then used to compensate for other sources of helicity-correlated beam motion in the system.

In a somewhat similar manner to the IA, the PZT mirror feedback is calibrated by measuring

the helicity-correlated beam position differences in the experimental hall with the BPMs as a function of the two control voltages of the mirror (labeled PZTx and PZTy for the two orthogonal directions). As with the IA feedback, the system is automatic, and during normal running, the measured helicity-correlated beam positions are averaged over about 30 minutes, to a precision of 100 – 200 nm. The values are used to update the settings for the PZTx and PZTy values for the next 30-minute running period.

Ideally, the IA and PZT would be orthogonal devices, but in reality, this is not completely true. The IA cell induces some helicity-correlated position differences as well as the intensity asymmetry, and the PZT causes some helicity-correlated intensity variations in addition to the helicity-correlated beam positions. These cross-coupling terms are also measured as part of the calibrations, and the feedback algorithm uses a full 3x3 matrix to determine the new control voltages (IA, PZTx, and PZTy) for the updates [194].

4.3.1.2 Leakage Beam

As discussed previously, the G^0 experiment ran with a non-standard 31 MHz beam structure, achieved mostly by the G^0 source laser timing. However, the other experimental halls were using the standard 499 MHz beam generated using their lasers. During much of the data-taking period for G^0, the accelerator was simultaneously delivering the standard 499 MHz beam to one or both of the other halls. The timing of the three beams is determined by the timing of the pulses of the three lasers for each of the halls, so the beam into any one of the halls can have a small fraction of the beam from the other two lasers due to the fact that those lasers have a finite turn-off time and have not completely turned off when the laser for that hall fires. In addition, there is also a DC component of light caused by amplified spontaneous emission in the lasers. Due to these causes, a small amount of beam with 499 MHz structure could pass the chopper and be delivered to Hall C in addition to the desired 31 MHz beam. This small fraction of beam is referred to as “leakage beam”, and since it originates from different lasers, it can have very different characteristics from the primary desired beam. Because of the different time structure used for the G^0 forward-angle

running, this small fraction of leakage beam turned out to have a significant, but correctable, impact.

The intensity of this extra beam was very low compared to the primary 40 μA beam, about 50 nA, although this varied significantly depending on the current being delivered to the other experimental halls. Furthermore, the events caused by this beam were largely rejected by the ToF cuts, so the rates from this beam were not a significant background to the experiment. However, this beam carried a rather large charge asymmetry (of order 600 ppm), that differed from the charge asymmetry of the 31 MHz beam. Because the signals from the beam current monitors (BCMs) were digitized at 30 Hz, they recorded a charge asymmetry which was a combination of the charge asymmetry from the 31 MHz beam and from the leakage beam. The beam feedback system, which could only affect the 31 MHz beam, would then attempt to minimize the overall asymmetry reported by the BCMs, inadvertently creating an unmeasured charge asymmetry in the 31 MHz beam in order to counterbalance the charge asymmetry from the leakage beam. This meant the charge asymmetry measured by the BCMs was not the correct value needed to calculate the asymmetry in the elastic peak in the ToF spectrum, since the peak was almost entirely associated with the 31 MHz beam. This effect thus lead to a ToF-dependent false asymmetry.

Happily, this effect was correctable. The rate and the asymmetry of the leakage beam were measured by analyzing the regions of the ToF spectrum that could not contain physical processes caused by the 31 MHz beam, which meant that those regions were dominated by the leakage background events. The validity of this procedure was checked with dedicated measurements of the leakage beam using the luminosity monitors. In these measurements, the leakage beam was measured by leaving the lasers to the other halls on with the G^0 laser turned off. These studies and corrections are discussed in detail in Section 5.3.3.

4.3.2 Accelerator and Beam Transport

The electrons that are emitted from the GaAs crystal are longitudinally polarized. However, as the electron beam is transported through the accelerator to Hall C, the beam is bent by a series of dipole magnets that cause the beam polarization to precess relative to the momentum vector due to the anomalous magnetic moment of the electron. This rotation happens because the gyromagnetic ratio of the electron is 2.0023193, instead of precisely 2. For the four-pass, 747 MeV/pass beam, the total precession from the injector to Hall C was about 23π [203]. To compensate for the $g-2$ precession and ensure that the electrons that arrive at the G^0 target are longitudinally polarized, the beam passes through a Wien filter before the beam enters the accelerator. For the primary measurement, the beam polarization needed to be longitudinally polarized, but for the transverse systematic measurements, it had to be transversely polarized, and so the Wien was set accordingly.

The Wien filter consists of a pair of electrostatic plates and a magnetic dipole. The electric field from the plates is perpendicular to the magnetic field from the dipole, and both are perpendicular to the beam velocity. The electric and magnetic fields are set to cancel each other out, that is, the net Lorentz force on the electrons must be zero:

$$\mathbf{F} = q(\mathbf{E} + \vec{\beta} \times \mathbf{B}) = 0,$$

where $\vec{\beta} = \frac{\mathbf{v}}{c}$ is the electron velocity, and $\mathbf{E}$ and $\mathbf{B}$ are the electric and magnetic field vectors, respectively. Since there is no net force on the beam electrons, the trajectory of the beam is unchanged as it passes through the filter. However, the spin vector of the electron will precess about the magnetic field. The precession is given by [204–206]:

$$\frac{d\mathbf{s}}{dt} = \frac{e}{mc}\mathbf{s} \times \mathbf{B}\left[\frac{g}{2}(1+\beta^2) - 2\left(1 - \frac{1}{\gamma}\right)\right],$$

where m is the electron's mass, $\mathbf{s}$ is the electron's spin vector, $\frac{g}{2}$ is the magnetic moment of the electron in units of Bohr magnetons $\left(\mu_B = \frac{e\hbar}{2m_e}\right)$, and $\gamma = \frac{1}{\sqrt{1-\beta^2}}$. Assuming a perfect Wien filter

of length L, the total spin rotation angle is given by

$$\theta = \frac{L}{c\beta}\frac{eB}{mc}\left[\frac{g}{2}\left(1+\beta^2\right)-2\right].$$

The optimization of the Wien filter setting is done experimentally by using the Møller polarimeter to perform a "spin-dance" measurement, but it can be roughly set by using the knowledge of the beam energy and precession through the accelerator.

4.3.2.1 Precession through the Møller Solenoid

The transverse polarization component of the electrons in the beam also undergoes spin precession as they pass through the solenoid that polarizes the target for the Møller polarimeter. The interaction of the magnetic moment of the relativistic electrons with the electromagnetic fields it encounters on its journey to the hall causes the spin vector $\mathbf{s}$ to undergo rotations described by

$$\frac{d\mathbf{s}}{dt} = \mathbf{\Omega} \times \mathbf{s}, \tag{4.2}$$

where

$$\mathbf{\Omega} = \frac{e}{m}\left[\left(a+\frac{1}{\gamma}\right)\mathbf{B} - \frac{a\gamma}{\gamma+1}\vec{\beta}\left(\vec{\beta}\cdot\mathbf{B}\right) - \left(a+\frac{1}{\gamma+1}\right)\left(\vec{\beta}\times\mathbf{E}\right)\right] \tag{4.3}$$

where $\mathbf{\Omega}$ is the angular velocity of the spin precession and $\mathbf{s}$ is the spin vector, and $a = g/2 - 1$ [197, 204, 205].

The magnetic field generated by the Møller solenoid is along the beam axis ($B = B_z\hat{z}$). As the electron beam passes through the solenoid in the $\hat{z}$ direction, the transverse component of the polarization vector precesses around the velocity $\vec{v}$. The transverse polarization precession angle $\vec{\eta}$ is

$$\vec{\eta} = \frac{geB_z l}{2m\vec{v}\gamma}, \tag{4.4}$$

where $B_z l$ is the integral of the solenoid axial field $\int B_z \cdot dl$ [197, 206].

The direction of the rotation is given by the right hand rule. For example, for the polarization vector $\vec{P}$ passing through a solenoid with a magnetic field of $B\hat{z}$ as shown in Figure 4.3, the transverse polarization component will rotate from $\hat{x}$ to $\hat{y}$, changing in the azimuthal angle ϕ by the

amount η [206]. For the G^0 experiment, the solenoid was operated at 3 T, and so $\int B_z dl = 0.92925$ T·m, and therefore $\eta = 0.09246$ (5.30°).

This effect is really only of concern for the transverse beam polarization measurement. Interestingly, if $g = 2$, in a purely magnetic field the spin would precess in such a way that the longitudinal polarization would remain constant. For a relativistic particle, even the presence of an electric field would only cause the longitudinal polarization to change very slowly, at a rate proportional to γ^{-2} times the electric field component perpendicular to $\vec{v}$. However, the real world is more complicated, and g is not exactly 2, so the longitudinal polarization does change even in a pure B field [204, 205]. However, the longitudinal polarization still changes very slowly as the transversely-polarized beam traverses the solenoid, so we disregard it for this calculation.

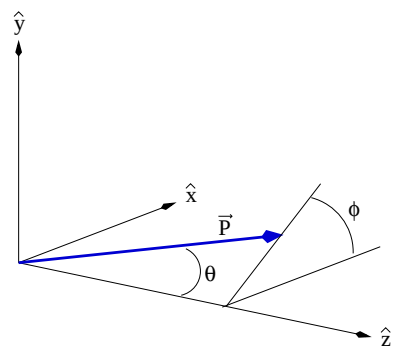

FIG. 4.3: *The coordinate system describing the beam polarization vector and the precession of the transverse component in ϕ.*

4.3.3 Electron Beam Polarimetry

Real-world electron beams are not polarized by 100%. Therefore, knowledge of the degree to which the beam is polarized is very important so that the correction for this can be made on the measured asymmetries. The accuracy and precision with which this measurement can be made is an overall systematic uncertainty for the experiment, so it is important that it is done well.

For the G^0 experiment, the polarization of the electron beam was periodically measured using the Hall C Møller polarimeter [207]. Møller polarimetry is an elegant experiment in itself, and so

the next sections are devoted to its description.

4.3.3.1 The Hall C Møller Polarimeter

The Møller polarimeter is used to measure the polarization of the electron beam entering Hall C. To accomplish this goal, the polarimeter measures the spin-dependent asymmetry in the cross section for the elastic scattering of polarized electrons from polarized electrons ($\vec{e} + \vec{e} \rightarrow e + e$), or Møller scattering. The cross section asymmetry for Møller scattering can be calculated exactly in quantum electrodynamics. For a longitudinally-polarized (in the z-direction) beam and target, the cross section in the center-of-mass (CM) reference frame is given by [208]:

$$\frac{d\sigma}{d\Omega} = \frac{d\sigma_\circ}{d\Omega} \left\{1 + P_z^B P_z^T A_{zz}(\theta)\right\},$$

where $\frac{d\sigma_\circ}{d\Omega}$ is the unpolarized cross section, $A_{zz}(\theta)$ is the analyzing power, and P_z^B and P_z^T are the beam and target foil longitudinal polarization, respectively.

The asymmetry for the cross-sectional difference between right-handed and left-handed incident beam electrons can be computed by the expression [208]

$$A_{Møller} = \frac{\left(\frac{d\sigma}{d\Omega}\right)^{\uparrow\uparrow} - \left(\frac{d\sigma}{d\Omega}\right)^{\downarrow\uparrow}}{\left(\frac{d\sigma}{d\Omega}\right)^{\uparrow\uparrow} + \left(\frac{d\sigma}{d\Omega}\right)^{\downarrow\uparrow}} = |P_z^B||P_z^T|A_{zz}(\theta),$$

At $\theta = 90°$ in the center-of-mass frame, the analyzing power is large ($A_{zz}(\theta) = -\frac{7}{9}$), and with a known target polarization P_z^T, a determination of the beam polarization can be made by measuring $A_{Møller}$.

The Hall C Møller polarimeter [209] measures the absolute polarization of the electron beam that arrives in Hall C with a statistical error of $< 1\%$ in about five minutes, and a systematic error which has been quoted to be below 0.5%. The polarimeter is located in the Hall C beam alcove, which is upstream of the entrance to Hall C, but downstream of the last dipole magnets that steer the electron beam into Hall C from the beam switchyard. This location ensures that there will be no further polarization changes due to spin precession caused by beam transport before the electron beam reaches the G^0 target in Hall C.

A schematic of the polarimeter apparatus is shown in Figure 4.4. For the typical polarization measurement in the experiment, a 4 μm thick iron foil target that was magnetized by a 3 T magnetic field produced by the superconducting Møller solenoid was used. The high magnetic field ensures a complete saturation, so the spin polarization of the outer shell target electrons in the target is well known ($8.036 \pm 0.015\%$). The target foil is mounted in a remotely controlled target ladder that is used to insert or retract the desired target into or out of the beam path. The Møller electrons that scatter at 90°_{CM} (1.06° in the lab frame at the 3 GeV beam energy for G^0) pass through a small quadrupole, a series of densimet (a tungsten alloy) collimators, and a large quadrupole magnet to achieve a satisfactory separation of the scattered Møller electrons and the beam line (a horizontal spread of 49 cm). The system of movable collimators and the pair of quadrupoles allows the system to be tuned for different beam energies from about 0.8 to 6 $(\mathrm{GeV}/c)^2$. In order to suppress the Mott background, the Møller polarimeter uses two symmetric lead glass total absorption detectors in coincidence. The narrow coincidence time gate (5 ns width) reduces the accidental background and the shower counters, which provide energy information, allow the suppression of any low-energy background. A Møller electron pair is defined as a coincidence between the left and the right lead-glass shower counters. Møller electrons separated 43 to 55 cm from the beam line (which corresponds to 83°_{CM} to 97°_{CM}) are accepted past the collimators that are placed directly in front of the lead-glass detectors [208]. A diagram of the position of the collimators and quadrupoles is shown in Figure 4.5.

4.3.3.2 Polarization Measurements

The majority of the measurements made with the Møller polarimeter were to determine the longitudinal polarization of the electron beam. However, the Møller was also used to determine the optimal Wien angle setting for the longitudinal running, as well as the optimal setting for the transverse polarized running. From this, the transverse polarization could be indirectly determined. Some polarization measurements of the leakage beam from the Hall A and B lasers were also performed.

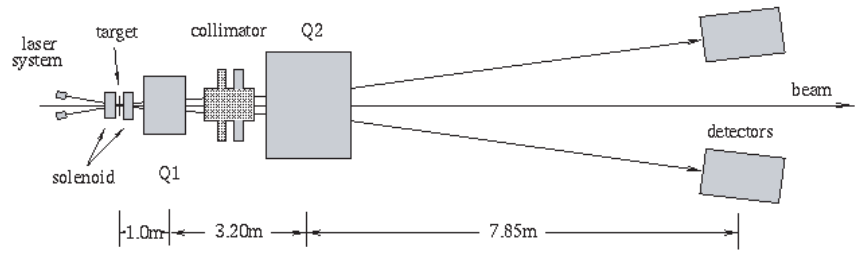

FIG. 4.4: *A diagram of the Hall C Møller polarimeter.*

4.3.3.2.1 Optimizing the Spin Direction Because of the spin precession that takes place during beam transport to Hall C, it is necessary to calibrate the Wien filter to the optimal setting that will maximize the desired polarization (longitudinal or transverse) at the G^0 target (see Section 4.3.2). As the Møller polarimeter is located after the last of the major bending magnets that steer the beam into Hall C, it is used to perform this calibration.

To perform the calibration, known as a spin dance, data were collected with the Møller polarimeter for several Wien angle setting spanning about 200°. The polarization of the beam at each Wien angle setting was determined from the measured data, and then plotted versus the Wien angles. The data showing the dependence of the measured polarization on the Wien angle were fitted using

$$P_{meas} = P_e \cos(\eta_{Wien} + \phi),$$

where P_e is the beam polarization amplitude, η_{Wien} is the Wien angle setting, and ϕ is the net spin rotation between the Wien filter and the Hall C polarimeter. From the fit, the net spin rotation ϕ at the maximum longitudinal polarization can be found, and the Wien filter can be set to the negative of this value to compensate for the spin rotation. An example of the data and the fit using the data from the February 10, 2004 spin dance is shown in Figure 4.6. After the spin dance, the Wien angle was set to $-12.62°$ to maximize the longitudinal polarization [210].

Ideally, the Wien filter setting should remain the same throughout an experiment if nothing

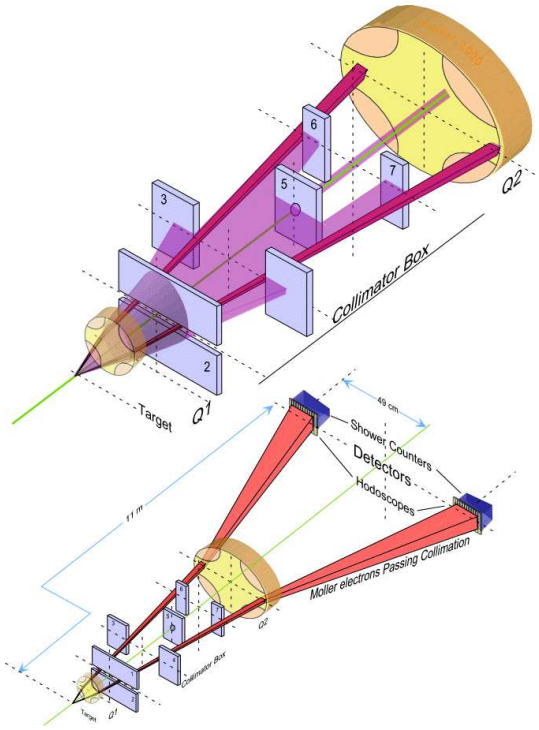

FIG. 4.5: *A diagram of the Møller lay-out and optics.*

else changes in the beam path. However, due to a pass/energy configuration change and the transverse data-taking, other spin-dance measurements were required through the span of the entire running period and the Wien angle settings were adjusted several times during the G^0 experiment, as noted in Ref. [207]; tables therein list all of the spin-dance polarization measurements performed.

4.3.3.2.2 Longitudinal Polarization Measurements Typically, polarization measurements were performed when the insertable half-wave plate setting was changed, or about every two or three days in the G^0 experiment. The procedure for taking data with the Møller polarimeter is simple, and was even more so for the G^0 experiment, since the experiment ran with the Møller quadrupoles on as part of the nominal beam optics. Directly before a measurement, while normal physics data-taking was proceeding, the injector parameters were recorded to verify that the Møller data were taken in a state as close to normal G^0 production data-taking conditions as possible. After recording the injector parameters and the state of the beam to the other two experimental halls, the G^0 target would be retracted and the accelerator operators would tune the beam for a

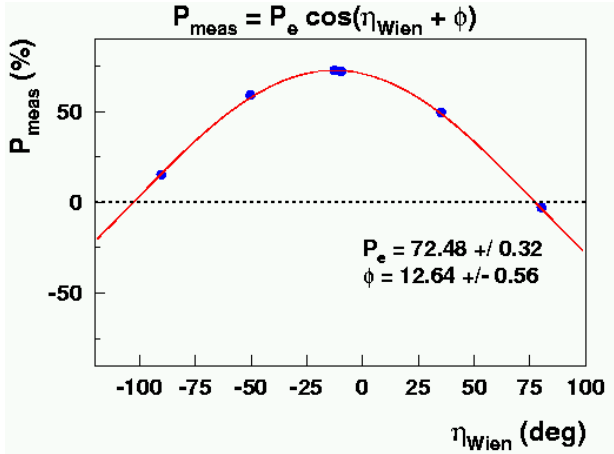

FIG. 4.6: *A fit of the form* $P_{meas} = P_e \cos(\eta_{Wien} + \phi)$ *to the polarization data from the February 10 spin dance.*

Møller measurement in Hall C. The Møller solenoid was usually left ramped up to the operating field of 3 T for most of the data run, but if necessary, the Møller solenoid was ramped up to the operating field at this point. In this interval, the high voltage to the G^0 main detectors and halo monitors would be turned off, the high voltage to the Møller detectors would be turned on, and the gain setting for BCM2 (a beam current monitor) would be switched up to gain setting 4 from 3. The beam would then be tuned and the beam position adjusted for the Møller measurement. After the beam positions were acceptable, the beam was turned off and Møller target 3 (the 4 μm thick iron foil target) was inserted into the beam path. The measurements were done with 2 μA of beam. For these measurements, the current was reduced using the chopper slit, so the leakage fraction remained the same at 2μA and 40 μA. After verifying that the Møller scalers were all counting at a coincidence rate of about 10 - 100 kHz, data would be taken with the Møller data acquisition system, with a typical Møller data run being about 5 minutes long and having at least 5 million coincidences. While the Møller data were being taken, the injector parameters were recorded again to compare to the usual G^0 running conditions. After taking two or three data runs, the half-wave plate setting would be changed, and then two or three more Møller data runs were taken. After each run finished, the Møller runs were replayed with the Møller analyzer to verify that the beam polarization and the sign of the beam polarization were as expected. After finishing

the measurement, the set-up steps were reversed to restore the normal running conditions and the results of the measurement were recorded in the G^0 electronic logbook, with the polarization typically about 74%.

Tables of the polarization measurements performed during the second engineering run and the forward-angle physics run of the G^0 experiment can be found in Ref. [207].

4.3.3.2.3 Transverse Polarization Measurements The Hall C Møller polarimeter is unable to directly measure the transverse polarization since it does not at present have the capacity to have a transversely-polarized target. However, an indirect determination of the transverse component of the polarization can be made using constraints set by a spin dance, by making the assumption that a measurement of zero longitudinal polarization means that the beam is purely transversely polarized.

By doing a sinusoidal fit to the measured polarization data at the different Wien angles and solving for the zero-crossings, the two Wien angles for purely transversely polarized beam were ascertained for the transverse running of G^0. To verify the Wien angle setting, polarization measurements were then taken. A longitudinal polarization measurement with the Hall C Møller polarimeter that is consistent with zero implies that the polarization is purely transverse. In the spin dance for the G^0 transverse running on March 22, the measurements gave an optimal longitudinal Wien angle of $+3.69°$ and two zero-crossings for the optimal transverse polarization at $-84.99°$ and $+93.90°$. The Wien was set to $-85.23°$, which yielded a longitudinal polarization measurement consistent with zero, as expected. However, it was found that in the four days of transverse running, the spin direction of the polarization relative to purely longitudinal had drifted $2.75° \pm 0.50_{stat} \pm 0.55_{sys}$, when the March 26 spin dance measured a zero crossing of $-87.98° \pm 0.71$ [211]. Therefore, we take the error in θ_{Wien} as $3°$.

Tables of the indirect transverse polarization measurements can be found in Ref. [207].

4.3.3.2.4 Leakage Polarization Measurements During the experiment, polarization data were taken to determine the effect of the leakage beam current from Halls A and B on the Hall C polarization. These data were were taken at different slit settings and different configurations of the other two halls, and were taken throughout the run.

One of the studies was performed to ascertain the worst-case scenario of the effect of the leakage current on the polarization in Hall C. To do this, the current was changed using the laser attenuator instead of the chopper slit, and the slit was set wide open. This gave the maximum sensitivity to the leakage current from halls A and B. It was determined that even with Hall A running at 120 μA and Hall B at 25 nA, the leakage current was quite small, about 50 nA. The effect of this leakage was to drop the measured polarization by about 3% at 2 μA with the Hall C slit wide open using the attenuator instead of the slit. From this information it can be determined that when taking data at 10 μA, the leakage current decreases the beam polarization by about 0.6%, at 20 μA by 0.3%, and at 40 μA it drops by about 0.15%, assuming the the current is changed using the attenuator [212]. Under normal data-taking conditions, using the slit instead of the attenuator to change the current, the maximum possible effect from the leakage was taken to be 0.2% (fractional) on the polarization.

Tables of the leakage beam polarization measurements can be found in Ref. [207].

4.3.4 Monitoring the Electron Beam Quality

As with all precision parity-violation experiments, it is essential for the beam properties to be continually monitored so that the quality will be consistently high and so that corrections for any residual helicity-correlated beam properties can be made to the measured asymmetries later. Although ideally no other property of the beam should change when the helicity of the beam electrons is reversed, many properties do change in practice. These changes that are correlated with the helicity-flipping cause a false asymmetry that is described by

$$A_{false} = \sum_{i=1}^{N} \frac{1}{2Y} \frac{\partial Y}{\partial P_i} \Delta P_i, \tag{4.5}$$

where Y is the detector yield (the number of detected scattering events), P_i represents the beam properties of interest, and $\Delta P_i = P_i^+ - P_i^-$ is the helicity correlation in those beam properties.

To keep the contributions of these false asymmetries small, active feedback systems are used, as discussed previously in Section 4.3.1.1, and then the beam properties are monitored and recorded throughout the injector, accelerator, and hall beamline. During the experiment, the beam current, position, angle, energy, and halo were continuously measured in the experimental hall and in other places around the accelerator. In this section, the beam monitoring systems required to accurately measure the properties of the beam are discussed. These systems measure these properties so that the ΔP_i values above can be determined continuously. This section also covers the beam control systems that are used to make deliberate variations in the beam properties in order to measure the yield slopes ($\partial Y/\partial P_i$) for corrections.

4.3.4.1 Beam Current Monitors

Experimental Hall C is equipped with two different types of monitors that allow for continuous and non-invasive measurements of the beam current (or intensity). In the G^0 experiment, the beam current was primarily measured with two microwave beam cavity monitors known as beam current monitors (BCM1 and BCM2) [213, 214]. These stainless steel, cylindrical cavities are resonant in the TM_{010} mode at 1497 MHz, so as the electron beam passes through the cavity, it resonates. This resonant mode was chosen because the spatial dependence of the electric field amplitude is nearly constant in the center of the cavity, making the response relatively insensitive to the beam position when the beam is in the center of the cavity [194]. The resonant frequencies of a cylindrical cavity are given by

$$f_{l,m,n} = \frac{\chi_{l,m} c}{2\pi R^2} \sqrt{1 + \frac{n\pi R^2}{L^2 \chi_{l,m}}}, \tag{4.6}$$

where l, m, n are integers, R and L are the radius and length of the cavity, and $\chi_{l,m}$ is the lth root of the mth order Bessel function. Because the resonant frequencies depend so much on the physical dimensions of the cavity, the cavities are thermally stabilized to reduce the temperature

dependence of the current measurement [215]. They were located in the Hall C beamline a few meters upstream of the G^0 target, mounted so that the beam travels through on the axis of the cavity.

The energy from the resonance of the excited modes is extracted from a wire loop antenna installed in the cavity, where the power picked up by the antenna is proportional to the beam current squared. This high frequency signal is then mixed down with downshifting electronics and converted to a DC level, which is then passed to a voltage-to-frequency converter and then to a scaler that is read out at the same rate as the rest of the data in the experiment [194].

These cavity BCMs only can give a relative measurement of the beam intensity because they measure a signal that is proportional to the beam intensity. Therefore, they must be calibrated using an absolute device. Once calibrated, they are very stable and linear. During the production data-taking of the G^0 experiment, the BCMs were calibrated about once a week.

Hall C is also equipped with a parametric current transformer (also known as the Unser monitor) [216], which is basically a toroidal sensor that fits around the beampipe. As the electron beam passes through, it induces a magnetic field in the toroid that is measured by a transformer. The total flux in the toroid is then driven to zero with a second transformer. The precise compensation of the magnetic field induced by the beam is used to determine the beam current passing through the toroid. Like the beam cavity monitors, the Unser is quite sensitive to temperature changes, so it is also thermally stabilized. The Unser has a very stable and well-understood gain, but it suffers from large, unstable drifts in the zero offset. Therefore, it is not used in the primary data-taking to measure the beam current. However, it is the only current monitor in the Hall C beamline that can be calibrated absolutely (since it measures the beam current passing through the toroids). Because it is an absolute measurement of the beam intensity, it is used to calibrate the other two BCMs which are more stable and linear, but are relative devices.

The Unser was calibrated before the experiment by running known currents of various magnitude from a very precise current source through a wire installed next to the beampipe that runs

through the toroid to determine the gain of the monitor. During the production data-taking of the G^0 experiment, the BCMs were calibrated about once a week. This was done by taking data with all the BCMs while alternately running with the beam on and the beam off in intervals of about two or three minutes, with each beam current period at a different magnitude (10 μA, 20 μA, etc.). The beam-off data were used to measure the zero offsets for the two types of monitors, and the data taken with the beam on were used to determine the gains of the beam cavity monitors by using the known Unser monitor gain.

For the G^0 experiment, it was important that the random noise level of these beam current monitors at the helicity-reversal rate of 30 Hz was small compared to the random fluctuations in the beam current in each MPS data acquisition interval of 33 ms used for the asymmetry computation. By comparing the measurements of the beam current by the two monitors, the upper limit on the random instrumental noise at 30 Hz was determined to be about 40 ppm, quite small compared to the usual random beam current fluctuations of about 500 - 1000 ppm [194].

4.3.4.2 Beam Position Monitors

Knowledge of where the beam actually is located is very important, so the beam positions were measured at many places along the Hall C beamline and throughout the accelerator. The stripline beam position monitors (BPMs) [217] continuously and non-invasively measure the position of the electron beam in the beam pipe.

These monitors consist of a set of four thin wire antennae that are placed symmetrically around the beam at 45 degree angles. Each of the wires has a length of one quarter wavelength at 1497 MHz. These four antennae inductively pick up the fundamental frequency of the beam as it passes through the device. The signals were then downconverted to about 1 MHz, filtered, and converted to DC voltage signals that were then sent through voltage-to-frequency converters and then recorded with scalers that are read out with the rest of the data from the experiment. The beam position can then be calculated from the linear combinations of the signals with the knowledge that the signals are proportional in strength to the distance from the antenna to the

beam. Since the position of the beam is determined from the ratio of the signals from opposing antennas, the measurement is essentially independent of the beam current (to first order).

The relative X' beam position can be calculated by using the equation

$$X' = k\frac{(X_+ - X_{\text{offset}+}) - \alpha_X(X_- - X_{\text{offset}-})}{(X_+ - X_{\text{offset}+}) + \alpha_X(X_- - X_{\text{offset}-})}, \tag{4.7}$$

where $X_{\text{offset}+(-)}$ is the offset for the $X_{+(-)}$ antenna, k is the sensitivity of the BPM at 1497 MHz, and α_X is a measure of the possibly different gain between the X_+ and X_- antennae [218]. The relative Y' beam position is computed in a like manner. The gain difference α_X is defined as

$$\alpha_X = \frac{X_+ - X_{\text{offset}+}}{X_- - X_{\text{offset}-}}, \tag{4.8}$$

and in a like manner for α_Y. The antennae within the BPMs are oriented at 45 degrees with respect to one another, so the position of the beam is given by [218]

$$\begin{pmatrix} X \\ Y \end{pmatrix} = \frac{1}{\sqrt{2}} \begin{pmatrix} 1 & -1 \\ 1 & 1 \end{pmatrix} \left[\begin{pmatrix} X' \\ Y' \end{pmatrix} - \begin{pmatrix} X'_{\text{offset}} \\ Y'_{\text{offset}} \end{pmatrix} \right]. \tag{4.9}$$

To find the position and angle of the beam on the G^0 target, two of the BPMs were used to project the beam path to the target. These monitors were separated by 2.5 m with a midpoint 4.8 m upstream of the target [194].

As with the beam current monitors, the random noise level in the calculated position (or position difference) due to both beam noise and electronic noise at 30 Hz was an important concern. The noise can be determined by using three different BPMs that have no magnetic elements between them. The first two BPMs are used to find the position of the beam in the third monitor, and then the predicted behaviour can be removed from the measured signal, leaving behind only the noise. By using this method, it was determined that the random noise fluctuations at the beam helicity reversal frequency was less than 3μm, which was below the typical normal random fluctuations of the beam position at that frequency, measured to be about 10μm [194].

As the BPMs are not intrusive to the beam, they are used to continuously monitor the beam position. However, they need to be calibrated, which is done by using the harps and super harps

installed on the beamline in Hall C [219, 220]. These devices pass a set of thin tungsten wires mounted in forks (looking rather like a harp or lyre) through the beam. The wires are attached so that the signal from the wires as they pass through the beam give x and y profiles of the beam. They give both beam profile and position information, and so are used to investigate the beam spot size and position. However, their use is disruptive to the beam, so they are used to calibrate the BPMs, which are used during normal running as they are non-invasive [215].

The BPMs were also used to measure the beam energy. To measure the electron beam energy, the beam position in the accelerator plane was measured by a BPM located at the center of the Hall C arc, where the beam dispersion was 40 mm/% [194]. The current of an arc dipole magnet is adjusted to center the beam at the end of the arc, where the beam position is measured. Using the dipole current, the beam energy can be calculated, assuming the beam follows the central path.

4.3.4.3 Beam Halo Monitoring System

The beam has yet another property that must be monitored carefully, the beam halo. The term beam halo refers to stray electrons that move along with the primary beam, but are sufficiently far from the beam center to be considered beam background. Beam halo can be generated by a variety of effects, including (but not limited to) space-charge effects from the electrons repulsing one another during bunching, scraping in the injector or accelerator, and poor vacuum in any region of the accelerator. Beam halo is a concern for G^0 because halo particles can interact with a 11mm diameter flange that is part of the G^0 target cell, causing background events and possibly a helicity-correlated false asymmetry in the G^0 detectors.

In an effort to prevent a contribution from halo, the beam specifications for G^0 required that less than 1×10^{-6} (or 1 ppm) of the electrons in the beam be located outside of a 3 mm radius from the center of the beam, a rather stringent requirement [221]. In addition, the halo needed to be monitored continuously, which meant that the measurement had to be non-invasive.

To accomplish this, a system was designed that continuously measured the amount of beam halo using an aluminum target with a circular hole in it and a series of detectors. This system was

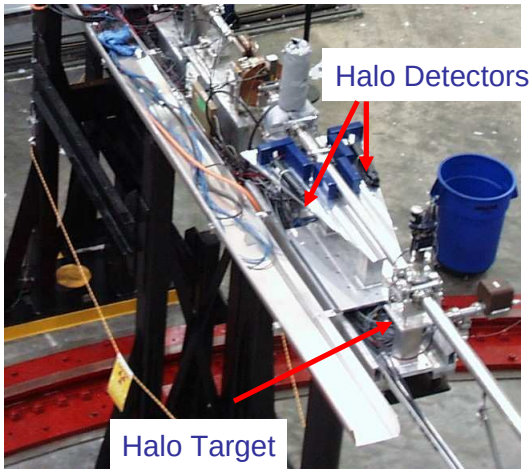

FIG. 4.7: *A photograph of the halo monitoring system on the halo girder.*

located on its own girder (called the Halo girder) on the beamline, about 8 m upstream of the G^0 target, as seen in Figure 4.7.

The target for the system was a 2 mm thick aluminum plate with a 6 mm diameter hole, which matched the specification. In addition, the plate also had an 11 mm diameter hole, which matched the size of the target cell flange, that could be used for studies. The target was mounted on a stepping motor (from a harp mechanism), so it could be inserted into the beam path in either target position, onto the frame (for calibration runs), or out of the beamline altogether. Although the beam was rastered in a square pattern, the areas of interest for halo interactions on the G^0 target were round, hence the halo target holes were also round. For normal running, the 6 mm halo target was used.

Particles scattered from the interaction of the beam halo electrons with the aluminum target were detected in a primary set of detectors placed at large ($\sim 15°$) and secondary sets placed at small ($\sim 3°$) angles. The primary detectors for the system were symmetrically placed in either side of the beamline about 1 m downstream of the halo target. These Čerenkov halo detectors were composed of 2 inch phototubes (identical to the ones in the G^0 detectors) attached to cylindrical pieces of Lucite. They were shielded from ambient radiation by lead bricks. Two secondary

scintillation halo detectors, located on either side of the beamline just before the G^0 target and just after the harps, were made of different phototubes attached to small pieces of scintillator. A third set of two halo monitors that consisted solely of phototubes were located with the secondary set. These were all unshielded.

The system could be used for relative measurements by comparing measurements taken with the halo target to measurements without the target. However, it could also be used for absolute measurements in the halo rate. To accomplish this, the system was calibrated by measuring the rate from 5 nA of beam on the 2 mm thick frame of the aluminum halo target in the halo detectors.

In addition to the halo monitoring system located in the hall on the halo girder, there were two halo detectors located upstream by the Møller polarimeter in the Hall C alcove. These alcove halos were used to monitor for poor beam quality as the beam entered Hall C from the beam swtich yard.

During the regular running of the experiment, the halo specifications were met as discussed in Section 5.4.3 [222, 223]. The halo monitor also served as a diagnostic of the general beam quality, for a sudden increase in the halo rates indicated changes in the beam tune that were causing a deterioration in the beam quality and thus needed to be corrected.

4.3.4.4 Luminosity Monitors

Another possible complication that could produce a systematic false asymmetry would be variations in the target fluid density caused by the beam, such as target boiling. Short-term fluctuations in the fluid density could cause nonstatistical fluctuations in the measured asymmetry, causing additional width in the distribution of the parity-violating asymmetry measurement. To prevent this, a raster system is used (see 4.3.4.7), and to monitor and study beam-induced variations in the fluid density in the target, a set of eight luminosity monitors are installed downstream of the G^0 target [194, 224].

The luminosity monitors are constructed of synthetic quartz cubes that are coupled to low-gain phototubes, except for Lumis 7 and 8, which were coupled to vacuum photodiodes (VPDs). The

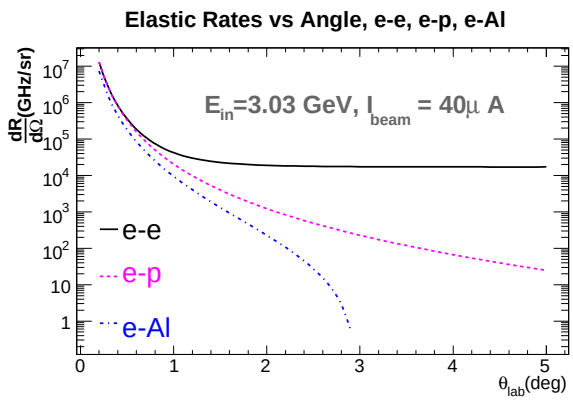

FIG. 4.8: *The electron rates per unit solid angle versus the electron lab angle for Møller, e-p, and e-Al scattering. Figure borrowed from [224].*

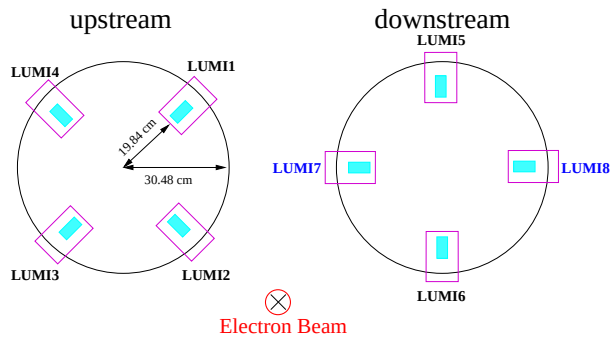

FIG. 4.9: *A diagram of the lumi positions as viewed looking downstream from the G^0 target. The upstream lumis are 699.7 cm downstream of the target, and the downstream lumis are 373.8 cm downstream from the upstream set. Figure borrowed from [224].*

eight monitors were placed symmetrically in two different rings in the beamline after the target, with Lumis 1 through 4 in the upstream ring (positioned 7.00 m after the target), and 5 through 8 in the downstream ring (1.074 m after the target), oriented as shown in Figure 4.9. They were positioned at very forward angles, $\theta_{lab} = 1.98°$ with respect to the incident beam for the upstream set, and $\theta_{lab} = 1.29°$ for the downstream set. At these angles, the dominant rate comes from Møller scattering in the target (as can be seen in Figure 4.8), but $e - p$ and $e-$Al scattering also have significant contributions [224]. Due to the very high rates from these Čerenkov detectors, the signals were integrated over the 30 Hz helicity window, converted to a voltage, passed through a voltage-to-frequency converter, and then counted with scalers, similarly to the electronics of many of the other beamline monitors.

The primary function of the luminosity monitors is to monitor the density fluctuations in the target, as these monitors are extremely sensitive to small changes in the asymmetry widths (each having a width of 200 ppm per quartet compared to the asymmetry width of each of the 15 rings of the G^0 FPDs of approximately 1200 ppm at 40 μA of beam current) [194].

In addition, the luminosity monitors are also sensitive to other small systematic effects such as small changes in beam halo or scraping of the beam upstream of the target, and so give com-

plementary information about the beam quality. The luminosity monitors were also used for measurements of the leakage beam from the other halls. The procedure developed to correct for this 499 MHz leakage beam made use of a region of the ToF spectra that was forbidden to processes caused by the 31 MHz beam of the experiment, but to double check the rates measured in this section of the ToF, the lumis were used to measure the leakage beam by turning off the G^0 laser and leaving the other lasers on.

4.3.4.5 Additional Beam Monitors

In addition to these monitors, a beam spill monitor lovingly referred to as "Herbert's Paddle" was used as a general beam quality monitor. It consisted of a paddle of scintillator coupled to a photomultiplier tube, with the signals displayed on a pico-ammeter. It was positioned on the hall floor under the Ferris wheel detector support structure, and was frequently used as a monitor of the general beam quality before any of the more sensitive detector systems were turned on.

4.3.4.6 Beam Position Modulation and Energy Modulation

Although it is very important to continuously monitor the beam properties during the data-taking, it is also very important to understand what effects changes in these beam parameters ($\partial Y/\partial P_i$) have on the detector yields, and thus the physics asymmetry. Therefore, systems were developed to vary the position, angle and energy at the target in a deliberate, controlled fashion to measure these effects.

The coil-modulation system (also called coil-pulsing or dithering) varies the beam positions and angles in a controlled manner using a set of six air-core steering coils that were positioned upstream of the Hall C dispersive arc. The coils were positioned by using beam transport simulations so that the modulation in x and y at the target adequately spanned the necessary positions and angles. The beam positions were modulated for a complete pattern at the beginning of each run while taking data, with occasional dedicated runs. The two modulation patterns used (a cross and a square grid) modulated over a range of about ± 0.5 mm in the position and ± 0.5 mr in the beam angle.

The beam energy is also modulated periodically as part of the coil modulation procedure. This is done using a vernier input on an accelerating cavity in the South Linac of the accelerator [194].

4.3.4.7 Beam Rastering System

At the usual running current of 40 μA for the G^0 experiment, the electron beam only has a diameter of about 200 μm, and deposits several hundred watts of power into the cryogenic target. This would result in density-fluctuations in the target fluid caused by the beam actually heating up and even boiling localized sections of the cryogenic target fluid, which would cause unwanted fluctuations in the measured yield in the detectors (see Section 4.4.2.1).

To reduce this effect, the beam was rastered in a 2 mm by 2 mm square pattern for the experiment, using two magnets located about 20 m upstream of the G^0 target. The two magnets of the fast raster system generate this pattern by sweeping the fields in x and y with triangular waveforms of 24.96 kHz and 25.08 kHz respectively, which gives a pattern that has a 95% uniformity in the beam density [194, 225, 226].

4.4 The G^0 Target

The target for the G^0 experiment is an unpolarized liquid hydrogen target. Due to the demands of precisely measuring parity-violating asymmetries of only a few ppm, the target system had to have a long target cell and be designed to handle large power depositions with the minimum possible systematic uncertainties due to density fluctuations. The target system also had to be designed to fit inside of the superconducting magnet system, not interfere with the magnet's toroidal field, and run reliably in continuous operation over the many months of the experiment since it could not be removed from the magnet easily for maintenance. It also had to be able to handle both liquid hydrogen and liquid deuterium, as the overall experimental program would make measurements on both cryogens [194]. This section discusses how these challenges were met.

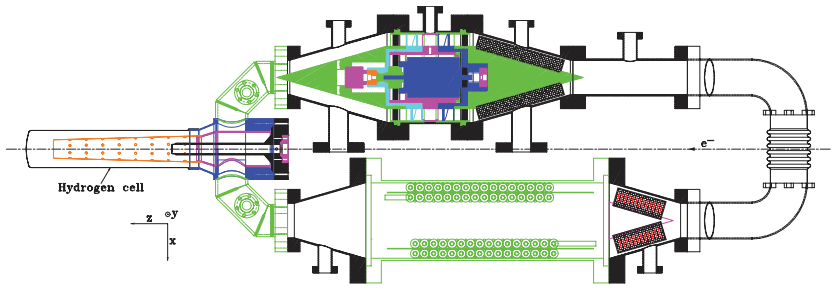

FIG. 4.10: *A schematic of the target loop. Figure from [227].*

4.4.1 The Target System

The G^0 cryogenic target is a closed loop recirculating system. The loop has a 20 cm long, thin-walled target cell that resides horizontally within the vacuum enclosure of the superconducting magnet. The target service module projects out of the magnet, holding all the lines and control features needed to communicate with the target from the outside world. Using actuators, the target type could be chosen: the hydrogen cell, one of the solid targets, or out of the beam path entirely. The target could also be warmed up independently of the rest of the spectrometer. This section describes the target system; for more detail, see References [194, 227, 228].

4.4.1.1 The Cryogenic Loop

During the normal running of the forward-angle configuration, the experiment ran with the liquid hydrogen at 19 K (2 degrees below the boiling point of the hydrogen) and a loop pressure of 1.7 atm. The temperature of the target loop is maintained by a proportional-integral-differential (PID) feedback system that used a resistive heater, located just downstream of the target manifold before the target fluid enters the circulating pump, to maintain a constant target temperature. A gas handling system supplied the cryogenic loop with gases and monitored the target pressure. The loop was connected to a 2500 gallon hydrogen ballast tank outside of Hall C that served as a pressure buffer to maintain a constant pressure. The liquid hydrogen is circulated at a high rate through the loop to facilitate mixing to dissipate the heat from the electron beam.

The primary aluminum hydrogen target cell was soldered to the target manifold with a secondary helium cell inside of it that served as the entrance window to the hydrogen cell. The 23 cm long primary cell was a thin-walled cylinder machined from one piece of Al-6061 T6, with an inner diameter of 5 cm and an outer shell thickness of 0.178 mm. The downstream exit window of the hydrogen cell was machined to a thickness of 0.076 mm over an 8 mm diameter nipple that was centered on the beam axis. Placed upstream of the primary hydrogen cell, the downstream window of the 16 cm long helium cell served as the entrance window to the hydrogen cell, machined to a thickness of 0.228 mm. On its upstream end, the He cell was protected from the vacuum by an 0.178 mm thick aluminum window. This cell has two purposes. Maintained at the same temperature and pressure as the primary hydrogen cell, it has the same shape and radius of curvature as the exit window of the hydrogen cell, reducing variations in the target length for different lateral beam positions on the target, and the systematic effects resulting from this. The design also provided azimuthal symmetry for particles scattered from the hydrogen target. The distance between the helium cell exit window and the hydrogen cell exit window defined the liquid hydrogen target length of 20 cm, or 1.44 g/cm^2 at the operating conditions of 19 K and 1.7 atm [227]. The total amount of aluminum in the three thin windows traversed by the beam was 0.130 g/cm^2 [194]. The target cells were all pressure tested to 85 psid for safety reasons.

The liquid hydrogen flowed longitudinally through the center of the target cell, guided by a thin-walled, perforated aluminum flow diverter that increased the flow speed as the liquid traveled down the length of the target, which encouraged the mixing and turbulence of the fluid. The holes in the diverter added even more turbulence and mixing to the longitudinal flow, enabled the heated fluid to exit the beam path more efficiently, and provided mechanical stress relief for the thin, conical flow-diverter. The holes lay in the shadows of the magnet coils, so they did not interfere with the experimental acceptance.

Upon leaving the manifold, the liquid hydrogen flowed to the leg of the cryogenic loop that housed both the cryogenic pump and the high-power heater (HPH). The target liquid was circulated

by a vane-axial pump with two impellers in series, powered by a Barber-Nichols custom DC brushless cryogenic motor. Just downstream of the pump was a conical aluminum flow diverter which housed the tachometer that gave a measurement of the motor's rotation. The motor is nominally operated at about 30 Hz, but the maximum available torque in the liquid hydrogen was found to be 23 oz·in at 42.7 Hz [227].

The high-power heater (HPH) is housed in a conical flow diverter located upstream of the pump, where it regulates the temperature of the target in a feedback loop during normal running conditions. It is a resistive heater made of three independent coils of Ni-Cr alloy ribbon wrapped on a G10 support. Each coil has a resistance of 3.5 ohms, wired in parallel to give a total resistance of 1.15 ohms, and is driven by a 40 V, 25 A DC power supply. The HPH is usually controlled through a Proportional-Integral-Differential (PID) feedback loop that tracks the beam current incident on the target, subtracts the deposited beam power from the total target power, and then sets the current on the heater to make up the deficit, thus keeping the temperature in the loop constant, as read out by one of the temperature sensors in the cryogenic loop. Six sensors made of Lakeshore Cernox CX-1070-AA resistors immersed in the cryogenic fluid monitored the temperature within the loop, along with two other sensors that monitored the helium coolant temperature on either end of the heat exchanger. Using this method, temperature excursions were smaller than 0.2 K during beam trips. During the normal G^0 running conditions, the heat load on the target was approximately 450 W, coming from the electron beam, the heater, or a combination of both.

In the other leg of the cryogenic loop (the lower one in the diagram) resided a double coil counterflow high-power heat exchanger that removed the heat from the beam from the liquid hydrogen. On the hydrogen side, the coils were made of finned copper tubing to increase the area for the heat exchange to occur; on the coolant side, cold helium gas from Jefferson Lab's End Station Refrigerator (ESR) at 15 K and 12 atm was used. Flow diverters were located along the loop to guide the target liquid smoothly around the loop and to assure a high Reynolds number in the target cell and heat exchanger, where turbulence facilitated heat transfer or removal and

mixing. After leaving the heat exchanger, the target liquid then re-enters the target manifold and then the cell again, restarting its endless journey.

During the G^0 experiment, the target loop was also filled with gaseous hydrogen (GH_2) in order to study the background contribution from the aluminum target cell windows. Measurements were made with the gaseous hydrogen target at two different temperatures, one at 28 K and one at 33 K, both with the pressure in the target loop at 2.2 atm. The G^0 target was also designed to be filled with liquid deuterium, a feature that will be used in the backward-angle measurements.

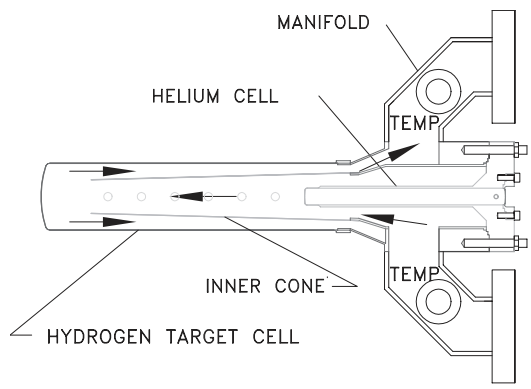

FIG. 4.11: *A schematic of the target manifold showing the hydrogen and helium cell. Figure from [227].*

4.4.1.2 Solid Targets

The target system also had solid targets, in addition to the cryogenic loop, that were designed to be used for various background, detector and beam studies. Several of these targets were mounted on an 0.125 inch-thick aluminum frame mounted on the target manifold, just above and 13.4 cm upstream of the center of the cryogenic target cell. At this position, the frame did not interfere with the trajectory of the particles scattered from the cryogenic target, but it also placed these solid targets on the upstream edge of the detector acceptance, allowing only the upper detector octants to have an unobstructed view of them [194]. On this frame resided a 5 mm thick Carbon target mounted over a 10 mm diameter hole, two hole targets used in beam halo studies, and a section of the frame itself that was used as an aluminum solid target. In addition, the

experiment made use of another Al solid target (see below) and a tungsten radiator that were not positioned on this frame.

The experiment used two aluminum dummy targets: the aluminum frame target and an aluminum foil target usually referred to as the "flyswatter", due to its similar shape to that household object. These two targets were used for studies of the contributions to the yield in the detectors from the entrance and exit windows of the target cell, respectively (see Section 5.3.5.1). The flyswatter consisted of a 0.76 mm thick aluminum foil on a supporting 20 cm long aluminum handle that was not attached to the target loop, but instead on the inside of the magnet. The handle was attached to beveled gears that acted like an elbow, allowing the target to be rotated through 90° either into the beam path or out of it as needed (and out of the particle trajectories from the cryogenic target). The beveled gears were attached to an approximately 6 m long rod that connected to a knob on the upstream flange of the target, where the flyswatter was inserted or retracted by hand. The flyswatter could be put in or out of the beam path independently of the other targets. When in position, the flyswatter was 10 mm downstream of the exit window of the liquid hydrogen target [194].

There were also two halo targets located on the solid target frame that were used for beam quality studies, known as the small and large hole targets. These were circular hole targets in the aluminum frame that were designed to study the beam halo at the helium cell inner diameter (12.5 mm), and at about half of that. The small hole target had a diameter of about 5.6 mm; the large hole target was about 11 mm across, and had a copper collar with the same inner diameter mounted behind it to match the radiation length of the aluminum flange that supported the vacuum window of the upstream helium cell [194, 228].

The carbon target was about 5 mm thick to match the radiation thickness of the liquid hydrogen target. This target was used during the first engineering run during the commissioning of the focal plane detectors. However, it was removed for the second commissioning run and the forward-angle measurement. The hole left from its removal allowed for the passage of a photon

flux produced by the electron beam on a tungsten (W) radiator target that was added for the second commissioning period. The tungsten radiator had a thickness of 0.0085 cm, chosen to match the radiation length of the liquid hydrogen target, but was located outside of the detector acceptance for elastic protons at 38.5 cm upstream of the flyswatter. The radiator was used in conjunction with the flyswatter to study the contribution of inelastic protons due to photo- or electro-production from the exit window.

4.4.1.3 Target Control and Instrumentation

The controls system monitored and recorded the target parameters, provided warnings of critical conditions to the target operator, moved the target when required, and controlled the PID feedback system to maintain target stability. The target electronics were based on a VME processor and Greenspring ADIO modules that sent data to a monitoring computer in the Hall C Counting House that was operated by a trained target operator whenever the target was operating. Target data were recorded using the EPICS slow controls system [229].

The target loop is rigidly supported inside the SMS vacuum system on a cantilevered platform connected to a service module, both of which were designed and constructed by Thermionics NW. The service module provides mechanical support for the loop, provides motion control for the target, and acts as the interface for gas lines for cryogens and electrical lines from vacuum to the outside world. The service module is connected to the upstream end of the magnet with the target cryogenic loop oriented so that the target manifold extends into the magnet cryostat and is the most downstream part of the target system. The position of the target with respect to the beam is controlled by four linear actuators, two vertical and two horizontal, placed in pairs in two vertical planes along the beam axis. These actuators move the cantilever through ball joints, providing pitch, yaw, and translation of the entire target loop vertically and horizontally. With this design, the target could be placed in position and aligned to the magnet-beam axis to better than 1 mm horizontally and vertically [194].

4.4.2 Target Performance and Systematics Studies

As hydrogen and deuterium are explosive gases, the target system was thoroughly tested to ensure safety. Tests were performed with cold helium gas to assess the performance of the cryogenic pump and the heat exchanger, and with liquid neon to test the safety of the gas handling system in the event of a catastrophic failure [194]. The details of these tests can be found in Refs. [227, 228].

The target operated at 19 K, 1.7 atm smoothly for the entirety of the G^0 forward angle data-taking with no major problems. The pump rotated at 31 Hz with speed fluctuations of less that 0.1 Hz over the months of continuous running. The speed was chosen to be slightly different than the 30 Hz of the data-taking helicity signals to avoid any possible source of systematic uncertainty in the asymmetry measurement due to the rotation of the pump. The hydrogen target cell vibrations were measured to be less than 0.01 mm at the pump's full rotation speed of 75 Hz, which was negligible for the experiment since it is about 10 times less than the natural motion of the beam. The liquid hydrogen relative density change due to beam trips is 0.3%, but the relative normalized yield change in the detectors is about 1% because of beam position drifts while ramping back to the nominal current. To avoid this problem, a beam trip cut was implemented to insure that data taken before the beam was stable on the target were excluded. With relatively stable beam (40 ± 0.5 μA), the PID loop maintained the target temperature to within 0.02 K [227].

4.4.2.1 Target Boiling Studies

To assess the contributions from target fluid density fluctuations from beam heating in the target, studies were performed by measuring the width of the asymmetry distribution in the focal-plane detectors and in the luminosity monitors as a function of beam current, target pump speed, beam raster setting and beam spot size. To improve the statistical precision, and thus the sensitivity, of these tests, groups of detectors were averaged together. Fast scalers were used to compute the detector yields (integrated over the ToF) to reduce the deadtime effects.

The results of the data analysis from these tests show that at the nominal running conditions for G^0 (40 μA of 3 GeV beam rastered over a square of 2×2 mm with the target circulating pump

operating at 30 Hz), the maximum contribution to the asymmetry widths coming from localized density fluctuations was 238 ± 65 ppm, which resulted in at most a 2% increase in the width of the asymmetry in a Q^2 bin of the G^0 FPDs. This was a negligible effect for the experiment. The investigations of global density reductions of the liquid hydrogen due to heat from the beam were found to be less than 1.5% at the nominal operating conditions. For details of these studies and the analysis of the data, see Refs. [227, 228]

4.5 The G^0 Spectrometer

The spectrometer used for the G^0 experiment consisted of a superconducting toroidal magnet (the SMS) and segmented scintillation detector arrays arranged symmetrically azimuthally around the beamline. For the forward-angle configuration, the detectors were located just downstream of the SMS, as can be seen in the photograph of the spectrometer in Hall C in Figure 4.12.

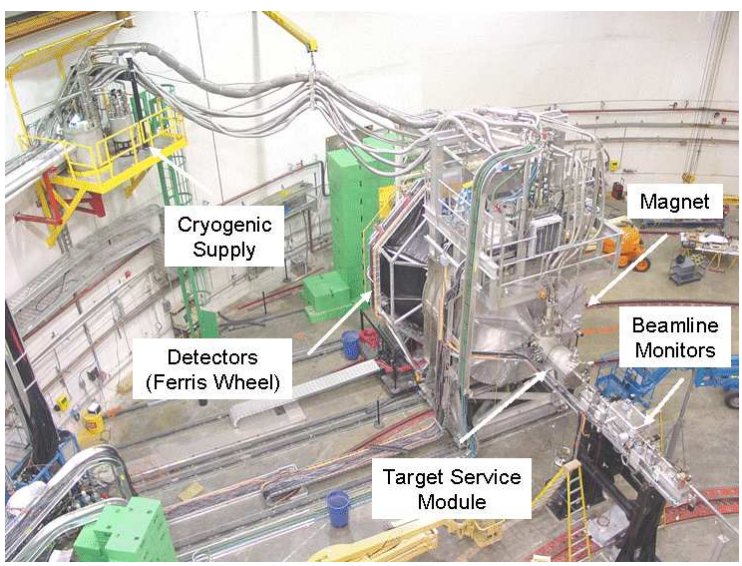

FIG. 4.12: *A photograph of the G^0 spectrometer in Hall C.*

The detectors were placed in the focal plane of the spectrometer, so as the particles traverse the magnet, the field focuses the protons of a particular range of Q^2 onto a detector. For the forward-angle measurement, the entire range of Q^2 was spread across the detectors, allowing a simultaneous measurement of the full range. As the momentum of a recoiling proton increased

(and its angle correspondingly decreased), its trajectory coincidenced with the focal surface further from the beam axis and the target, allowing a separation of Q^2 by segmenting each octant into a number of separate detectors that follow the curve of a particular Q^2 ring. Fifteen detectors per octant were chosen in order to limit the rate in each one while providing a reasonable Q^2 resolution. Because of the magnet optics, the proton trajectories turn around at the top of the focal surface, and the higher Q^2 protons start moving closer to the beam axis. Therefore, the top two detectors contained multiple Q^2 bins, which were obtained by separating the elastic protons by ToF. Finally, a sixteenth detector was located at the top of the focal surface, outside of the acceptance for elastic scattering, where it monitored backgrounds.

To separate the elastic protons from the background particles, time-of-flight is used to determine particle momentum. The time-of-flight of the elastic protons from the target to the detectors is about 20 ns. Because of the spectrometer optics and the kinematics of the experiment, the background particles in a given detector actually arrive earlier, pions at 7 ns after the beam passes through the target, and inelastic protons after the pions but before the elastic protons.

The spectrometer can be broken down into two parts: the magnet, and the detectors. Both of these systems were designed and built for the experiment, before being installed in Hall C.

4.5.1 The Superconducting Magnet System (SMS)

The first part of the the spectrometer is the superconducting magnet system (SMS) that does the actual focusing of the elastic protons. Built by BWXT, the SMS consists of eights coils that are arranged azimuthally around the beamline. The magnet was designed to be azimuthally symmetric, as unobstructing as possible, and iron-free to prevent any false asymmetry in the detectors from particles rescattering off magnetized iron. Since the target is so long, the SMS is designed so that particles from different z locations along the target with the same momentum and angle are focused onto the same location on the focal plane, thus allowing the magnet to sort the recoiling protons into the detectors. Since the magnet is a toroid, the field at the target is zero, which avoids any beam steering. The angular deflection of the elastic protons in the magnetic field ranges from 35°

to 87°, with an azimuthal acceptance of about $0.44 \cdot 2\pi$. The cryogenic target system and magnet share the same vacuum space (defined by gate valves on the beamline upstream and downstream of the magnet), which has a total volume of about 19.3 m^2 and a typical vacuum of 1.4×10^{-7} Torr. Overall, the magnet is 4 m in diameter and 2 m long. When cold, the axis of the magnet is centered on the beamline (4 m above the floor of Hall C). The SMS was tested and field mapped at UIUC, then shipped to JLab for installation in Hall C.

The complete initial cooldown of the magnet took about 21 days (from 300K to 4K). The superconducting coils of the SMS are wound from NbTi superconducting wires and are cooled with liquid helium delivered from the 4 K supply by the end station refrigerator (ESR) to a mean coil temperature of 4.5 K. The volume with the coils and liquid helium is surrounded by a shield filled with liquid nitrogen. Lead-alloy collimators placed in the space between the coils defined the acceptance of the particles and block the line-of-sight view from the target to the detectors, shielding against neutral particles. Scattered particles exit the magnet volume through eight thin titanium exit windows about 0.020 inches thick on their way to the detectors.

The usual operating conditions for the magnet in the forward-angle data production required a current of 5000 A. With this current, the magnetic field integral was $\int B \cdot dl = 1.6$ T·m, and the energy stored in the field when energized was 6.6 MJ [194]. The current to the SMS was supplied by a Dynapower 8000 A silicon-controlled-rectifier-based supply jumpered for 20 V output. The leads from the power supply to the magnet were water-cooled cables (low-conductivity water) until the transitions to the superconducting buss, where vapor cooled leads (VCLs) from the helium reservoir were used.

The magnet was controlled and monitored through a Programmable Logic Controller (PLC) located in a heavily shielded area of the experimental hall that communicated with a dedicated control console computer (running Windows) in the control center-counting house. Quench protection systems and other safety circuits could cause either a slow dump or a fast dump in the case of problems. In a slow dump, the current in the magnet was brought to zero in 900 s by a

powered discharge. This was used, for example, in a situation wherein the cooling cryogen levels were dropping, but there was still enough cryogen in the reservoir to allow a safe, slow discharge. In a fast dump, the magnet was disconnected from the power supply and the full energy of the magnet was dissipated by the high-power dump resistor in 10.4 s. This made a spectacular racket as the cryogens boiled off and whooshed out of the relief valves, but safely dissipated the stored energy.

The SMS was installed on a platform on rails, so that it could be pushed out of the beam path when not in use for G^0. The magnet is also being used for the backangle measurements, after having been turned around and set back onto its support structure. Overall, its performance has been excellent during the long periods of continuous running of the experiment.

4.5.2 The G^0 Focal Plane Detectors

The particle detectors for the experiment are contained in eight arrays, or octants, that are symmetrically arranged around the beamline. In the forward-angle measurement, they detect recoiling protons from small-angle elastic $e-p$ scattering. In each of these octants, sixteen detectors are placed in the focal plane of the spectrometer, and are thus called the focal plane detectors (FPDs). They consist of plastic scintillator pairs that curve in the azimuthal direction to follow a particular value of Q^2.

The first 14 detector pairs each measure a narrow range of Q^2 values from 0.12 to 0.55 $(\mathrm{GeV}/c)^2$. Detector 15 actually measures recoil protons with Q^2 values from about 0.55 to about 0.9 $(\mathrm{GeV}/c)^2$, so for this detector the ToF is a measurement of the momentum of the proton. Because of the spectrometer optics, the higher energy protons "fold over", and the elastically scattered protons with a Q^2 near to 1.0 $(\mathrm{GeV}/c)^2$ actually fall on FPD 14. However they are at a different location in the time spectrum, so are separate from the other elastic events. The last detector, number 16, was used to monitor backgrounds and the spectrometer field.

The shapes of the arc-shaped scintillators were determined by using the TOSCA program to trace the proton rays from elastic scattering through the SMS magnetic field. The detector sizes

were determined by simulation to provide elastic scattering Q^2 bins with decent resolution and roughly equal count rates up to about FPD 11. For higher detectors, the elastic rates are reduced, and the detector widths were chosen on the basis of momentum resolution.

Each octant has an azimuthal acceptance of $\phi = \pm 10°$, defined by the upstream collimators in the SMS magnet (with 0.5° added on to account for possible misalignment of the collimators). The scintillators range from 60 to 120 cm long, with widths of 5 to 10 cm. Detector 16 is identical in shape and size to detector 15, as it serves as a monitor for backgrounds.

Each FPD consists of two identical scintillators mounted as a pair to reduce background from neutral particles through the requirement of a coincidence between them. Each end of each scintillator is viewed with a photomultiplier tube (PMT or phototube), so there are four PMTs per FPD. As the low Q^2 FPDs were rather close to the magnet, long light guides were used to conduct the light from the scintillators to the PMTs, which were then mounted in a region of low magnetic field. These light guides were as much as 2 m long for those low Q^2 detectors, which caused concerns about too much material bulk for the available space. To cut down on the material on the sides of each detector, the light guides were designed to be relatively thin with rather complex shapes. Because of concern that the length and thinness of the scintillators and light guides would prevent the needed number of photons from reaching the PMTs, both simulations and experimental studies were carried out before the costly and time-consuming fabrication of the detectors [194].

Upon assembly of the octants, the FPDs were aligned to 2 mm, and then the octants were aligned relative to the magnet and electron beam when mounted around the beam line in Hall C. This was done using adjustment degrees of freedom provided by the detector octant support frame known imaginatively as the Ferris Wheel, because of its shape. Like the SMS, the Ferris Wheel is mounted on a platform on rails, so that it can be pushed to the side of the experimental hall when not in use by the experiment.

Because of budgetary constraints (among other things), the detectors and electronics were built by two different groups within the collaboration. Four octants (labeled 1, 3, 5 and 7) were

built by the North American (NA) part of collaboration (USA-Canada), and the other four (2, 4, 6 and 8) by the French part of the collaboration (IPN-Orsay and LPSC-Grenoble). They are based on the same concept, but have differing design details. The octants were mounted into the Ferris Wheel support structure in staggered fashion, with octants from the same group opposing each other (i.e. 1 and 5) to reduce possible systematic errors.

4.5.2.1 North American Detectors

The scintillation detectors for the North American octants were fashioned from sheets of Bicron BC-408. The scintillators were rough-cut by water jet, using sheets 1 cm thick for detectors 5–16, and 5 mm thick for the low Q^2 detectors 1–3. FPD 4 had a 1 cm front layer and a 5 mm back layer. Groups of five were stacked and milled with a CNC (computer numerical control) machine on their curved sides, and then polished by hand on these machined edges using gradually finer grades of very fine sandpaper. The hand-polished surfaces were then quality tested using an automated laser reflection technique. Any scintillators that did not pass the tests were re-polished to improve their performance. The individual scintillators were then wrapped in strips of aluminized mylar and mounted onto the octant support structure designed by the JLab design group and then aligned by teams working in the Jefferson Lab cleanroom, as seen in Figure 4.13. The complexly-shaped light guides were fabricated from UVT transmitting Lucite (Bicron BC-800) at Carnegie-Mellon University using a series of jigs and bending techniques that were developed for this purpose. The lightguides were then mounted onto the octant support structure and the ends were glued with a UV-curing epoxy to the scintillators. On the far end, silicone cookies were used to couple the light guides to the phototubes. The detectors were mounted with a 3 mm layer of black plastic (polycarbonate) between the scintillator pair as an absorber to reduce any low-energy charged-particle background entering the back scintillator created by neutrals in the front scintillator of the pair.

After the assembly and alignment, the performance of each detector was measured by positioning a ^{155}Ru β source at several locations along the length of the detectors and measuring the

FIG. 4.13: *A photograph of the the assembly of a NA octant in the cleanroom at Jefferson Lab. The arc-shaped scintillators are clearly visible in the octant.*

light output. The detectors were designed to yield greater than 100 photoelectrons for proton detection and greater than 50 for electron detection in the worst case when the source was on the far end of the scintillator away from the phototube. The results exceeded the design goal by at least a factor of two in all cases. Other tests were also performed to monitor for possible deterioration of the scintillators, light guides, and phototubes over time by taking cosmic ray data. After the completion of the tests, the entire octant support was lined with Tedlar to minimize the reflection of light within the octant and covered by a Herculite cover to make the octants light-tight [230, 231].

The photomultiplier tubes (PMTs) chosen by the NA collaboration were 12-stage Philips XP-2262B phototubes (now Photonis). The phototubes were all tested for non-linearity and their gains characterized, and then assigned an identifying bar code along with the bases. The passive-design bases and plastic housings were designed and built by the TRIUMF/University of Manitoba members of the collaboration. Made of resistors and Zener diodes, they include a Zener-assisted front stage designed to maintain collection efficiency of the primary photoelectrons independently of the PMT HV setting and are designed to handle the large dynamical range required by the experiment. When mounted onto the octant support frame, the phototubes were surrounded with μ-metal magnetic shields to prevent ambient magnetic fields from interfering with their performance [194, 232].

The signals from the phototubes in the experimental hall have to travel through approximately 150 m of coaxial cable to reach the electronics in the counting house. This results in a tremendous attenuation of the signals, so to ensure the signals arrived in a usable form either an extra stage of amplification was needed or the PMTs had to be operated at a rather high gain. Raising the gain of the PMTs would reduce their lifetimes due to high anode currents, and given the long running time of the experiment, this idea was discarded in favor of adding extra amplification. Modified Phillips model 776 amplifiers, used to increase the signals by a factor of about 20, were added in the experimental hall, which kept the PMT anode currents at an acceptable level.

4.5.2.2 French Detectors

The detectors manufactured by the French collaborators were cut from scintillator BC-408 purchased from Eurisys, a European subsidiary of Bicron. The scintillators were cut and polished to shape, using 1 cm thick scintillator for FPDs 4 – 16 and 5 mm thick for FPDs 1 – 3. The long PMMA light guides were machined in straight sections by a contractor and then bent into shape on the octant support structure directly. Other parts of the light guide system (such as PMT adaptors) were fabricated separately and later glued to the light guides. After gluing, the scintillators, light guides, and joints were wrapped in aluminum foil. Like the NA detectors, the detectors were mounted with an absorber between the scintillator pair, in this case 3 mm thick aluminum plates [233]. After the assembly test at LPSC Grenoble, France, measurements of the photon yield were also performed for these detectors. These measurements were done at three positions on the scintillators using light produced by cosmic rays. A light-emitting diode (LED) was used for the absolute calibration of the signal, allowing the conversion into the number of photo-electrons. The French detector design has comparable photoelectron yields for proton and electron detection as the NA detectors (approximately 100 and 50 respectively) [194, 234–237]. The octants were then shipped across the Atlantic to Jefferson Lab, where the final gluing of the delicate joints was done in the cleanroom, and the PMTs were attached to the light guides with optical grease.

The French detector arrays make use of lower gain, 8-dynode XP2282B phototubes, that were specified to have small gain dispersion to simplify the gain adjustment through variation of the high voltage. As with the NA PMTs, the characteristics of each PMT were recorded in a database. The bases for these PMTs included a built-in amplifier of gain 20, so the anode currents could be kept low enough to allow long-term operation, as well as a base-line restorer to avoid baseline shifts from counting rate variations. The amplifier design used Zener diodes, chosen after a series of irradiation tests showed they were more hardy than transistors. The phototubes were shielded by both μ-metal and an electromagnetic shield made of a copper sheet wrapped around the plastic housing to decrease the PMT signal noise.

The mechanical octant structure was designed in Orsay using finite element analysis to ensure a strong, yet light design that met the specifications. As the weight was a consideration, the octant support structure is constructed of welded aluminum tubes, with a backplane made of two 20 mm thick beams that form a V-shape. It was designed to support the focal plane detectors and align them to better than 2 mm. The octant structures were made light-tight by a Tedlar cover mounted onto a dedicated aluminum structure [194].

4.5.2.3 Detector Protection Systems

As the lifetimes of the PMTs were a concern, the anode currents were measured continuously to prevent unnecessary PMT aging. In the event of a sudden increase in anode current due to events in the hall (for example, if the SMS current suddenly goes down), to protect the phototubes from damage an electronic high-voltage shutdown circuit was designed and built. The "high-voltage sniper" as it was known, took signals from eight of the PMTs, as well as signals from the SMS and Møller polarimeter magnets. The threshold for the PMTs was set at about twice the desired maximum anode current. Upon any of the input signals showing a bad condition, the shutdown circuit shut off all the detector high-voltage power supplies [194].

Herbert's paddle (see Section 4.3.4.5) and the beam halo monitoring system (see Section 4.3.4.3), were also used to monitor the impact of poor beam quality on the rates in the detector

phototubes before turning them on.

4.5.2.4 The Gain Monitoring System

Due to the length of the data-collection period and the high rates involved, concerns were raised about the long-term health of the scintillator-based detector system. Therefore, a Gain Monitoring System (GMS) was devised to track changes in the pulse-height and time response of the detectors. The basic concept is simple: a short photon burst is distributed to the scintillation detectors by optical fibers and their response is measured.

Originally the system used a fast nitrogen laser, but the reliability was poor and short pulses unnecessary, so a nitrogen gas plasma flashlamp was used instead. The light produced by the flashlamp had a maximum intensity in the UV range near 350 nm, with wavelengths below 200 nm cut off by the exit window of the lamp. UV light was chosen because the conversion into blue light by the fluorescence effect when shining the light directly to the scintillator is similar to the process of scintillation, and provides uniform illumination of the detector that is similar to the passage of a charged particle through the detector. The distribution of light is done by a continuously rotating mask that permits the light to fall upon 1 of 15 clusters of optical fibers that contained 19 fibers each. A set of switches gives the mask location and the electronics control a signal to ensure that the lamp only fired when the mask was in a valid position. The optical fibers were comprised of pure silica in order to transmit the UV light over a long distance and to be resistant to the high radiation in the hall.

The fibers were arranged so that either the left or the right end of each FPD scintillator fired at a time. By comparing the response of the scintillators and PMTs for these left and right pulses, changes in the scintillator condition could be determined separately from changes in the individual PMT gains. However, the flash lamp varied significantly from pulse to pulse, so a reference system of small scintillators that were illuminated with each flash were used as well. One scintillator in the reference system used an source of about 0.6 nCi of ^{241}Am to monitor the drift in the gain of the reference system using the signals from the alpha decay of the source.

The GMS provided a relative gain reference, so once the relationship between the GMS and the detector responses were established in the commissioning, the GMS provided a way of monitoring the state of the scintillator transmission length and PMT gains. It was also used for checks of configuration changes to the detectors and DAQ during beam down periods [194, 238].

4.6 The Electronics and Data Acquisition System

The electronics take the signals from the phototubes and process them to reconstruct and record the time-of-flight information used to distinguish the elastic recoil proton events from the background events. They also record the data from all the various subsystems and monitoring systems. The data acquisition system (DAQ) controls the processing and acquisition of these signals, recording them for later analysis. This section discusses the electronics and DAQ for the G^0 experiment; the curious can find many more details in Refs. [194, 239].

4.6.1 The G^0 Electronics

Due to the high counting rates of the experiment, event-by-event recording with conventional electronics could not be done, so custom-built time-encoding electronics were used to store histograms of the particle ToF spectra for each MPS (1/30s). A diagram of the G^0 forward-angle electronics is shown in Figure 4.14. The French and North-American octants had different sets of time-encoding electronics; the electronics for the NA detectors, in octants 1, 3, 5 and 7, were built by a NA group (based at CMU); the ones for the French detectors, in 2, 4, 6, and 8, were built by a French group in (based in IPN-Orsay, France). The two groups developed the two independent systems based on completely different approaches, so the systems provide a powerful cross-check between the two subsets of data to look for false asymmetries. As the results of the forward-angle experiment from both sets were entirely consistent, which strongly suggests that no false asymmetries were introduced from the electronics.

The signals from the detectors in Hall C are routed upstairs to be processed by the G^0 electronics. Despite their differing designs, they both have the same overall concept and consist

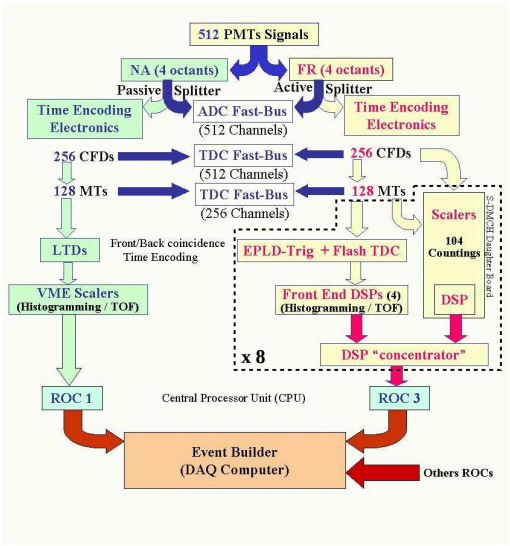

FIG. 4.14: *A flowchart of the electronics for the forward-angle G^0 measurement. Figure taken from [194]*

of two subsystems: time-encoding electronics and monitoring Fastbus electronics. The signals from the phototubes at the ends of each detector travel to a patch panel in Hall C through 36 m RG58 cables, and then to the G^0 electronics counting room through 107 m RG8 cables chosen for low attenuation (due to the great length of cable the signals had to traverse). Upon reaching the counting house, the signals were split into two independent copies: one that was sent to the Fastbus monitoring electronics and the other to the time-encoding electronics that record the primary data for the experiment.

The Fastbus data were taken by both the NA and French designs for the monitoring and calibrating the detector system. They were based on commercial ADC and TDC units in Fastbus crates and provided event-by-event information information on the pulse height and time response of the detectors. However, these electronics were highly prescaled to reduce the rate to one that the DAQ can handle (less than 1 kHz).

The time-encoding electronics (TEE) built the ToF spectra of the detected particles, enabling the separation of the elastic protons of interest from various backgrounds. When an event occurred,

the front-end electronics (consisting of constant fraction discriminators (CFDs), meantimers (MT), and a coincidence unit) of the TEE only kept events from coincidences between front and back scintillators to remove low-energy background. The two CFD output signals corresponding to the left and right PMTs of a scintillator were mean-timed, which ensured that the timing of an event delivered by the MT was independent of the hit location on the scintillator paddle's length. An event was accepted when a coincidence between the front and back MT is obtained; the event timing was encoded and the corresponding bin of the ToF was incremented.

Of course, to measure the time-of-flight, there must be a start signal. The beam structure for the experiment (forward-angle) was chosen to be 31.1875 MHz (499/16) to allow for the time-of-flight of the particles, which corresponds to one beam pulse every 32 ns (micropulse). The start of the ToF measurement was generated by the Y_0 signal. This signal was synchronous with RF picked up directly from the electron beam passing through a microwave cavity just upstream of the target [240].

As discussed in Section 4.3.1, the helicity of the beam electrons was flipped at 30 Hz, so the duration of one helicity state was 33 ms. These 33 ms periods were called macropulses MPS, and were grouped into quartets of $+--+$ or $-++-$ for the asymmetry computation. The readout of the ToF spectra from the time-encoding electronics takes place that the end of each MPS during the 500 μs time period for the helicity flip and settling. The selection of the elastic events to compute the asymmetries was done in the off-line analysis.

There was concern that possible 60 Hz noise could cause false asymmetries in the measurement. To detect this, dedicated runs where the DAQ over-sampled the data at 120 Hz instead of 30 Hz were taken occasionally. Analysis of these runs over the G0 production period showed negligible 60 Hz contributions [194].

The sustained rates in the detectors were several MHz, coming from elastic and inelastic protons and pion. In addition, there was a large low-energy background from (mostly neutral) particles that fired fewer than 4 phototubes and caused a large deadtime, which was comparable

to (or larger than) the deadtime due to true events. As deadtime was such an important concern, both designs included methods to reduce the helicity-dependent effects related to it: next-pulse neutralization (NPN) and the buddy method. In the NPN method, after an event is detected in an MPS, the encoding is disabled for the following micropulse (32 ns later). This ensures that the signals completely clear the MT. Although this increases the deadtime by a few percent, the introduced deadtime is well-known and precisely correctable. In the "buddy" method, the frequency that each detector recorded a hit when its buddy (the same detector located in an opposing octant of the array) was dead was recorded. These data were then studied for indications of helicity-dependent structure in the beam intensity, which would be seen as a helicity-correlation variation in the buddy rates. This method was used to monitor for helicity-correlated deadtime losses that could introduce a false asymmetry. The French electronics had the capability to do this for each ToF bin in the spectrum [194, 239].

4.6.1.1 North American Electronics

The electronics used to process the signals from the NA detectors are primarily designed to be be robust and modular, primarily composed of commercially available modules, using separate modules to perform the needed tasks of discrimination, meantiming, time encoding, ToF accumulation, and generation of the clocking signals used by the time-encoding boards.

First, the phototube signals from the hall are split by a passive splitter, with $\frac{1}{3}$ of the signal going to the Fastbus monitoring electronics, and $\frac{2}{3}$ going to the constant fraction discriminators (CFDs) that are the first stage of the time-encoding electronics (TEE). The TEE used commercial CFDs (LeCroy 3420) to make the timing independent of the PMT signal amplitude.The CFDs also have a threshold on the signal amplitude to reject low-level noise, set to about 50 mV. From the CFDs, the signals go to the mean timers (MT). The signals from the PMTs at the opposite ends of each scintillator arrive at different times depending on where along the length of the detector the particle passed; the signals are meantimed to make the timing independent of where along the detector the particle passed through. The custom MTs were built by CMU and based on ASICs

developed at LPSC-Grenoble. Copies of the CFD and MT outputs are also sent to the monitoring electronics.

The MT produces a signal when a coincidence is detected between the two PMTs on a scintillator, which then is sent to the time-encoding boards (TE), known as the latching time digitizers (LTDs). To count as an event, a coincidence is required between each front and back scintillator in the FPD pair, which is then encoded by its arrival time. To do this, a timing reference signal is necessary. The NA electronics used two timing signals: the Y_0, the 31 MHz start signal for the ToF, and the CLK, the 499 MHz signal used to run the shift registers. They are both synchronized the the passage of the beam through the G^0 target, instead of the RF of the accelerator, in order to prevent any helicity-correlated dependencies in transit time from the injector to the experimental hall. To accomplish this, these signals were produced using feedback loops stabilized with respect to a 1497 MHz RF cavity driven by the beam located upstream of the target [240].

The signals arriving at the LTDs are time-encoded using a gated clock signal generated by turning off the 499 MHz clock signal for 8 ns. When a coincidence occurs between the front and back scintillators, the shift register's input is latched-on. The shift register then recorded this data in its lowest bit, shifting the previous data to the next higher bits. The depth of the signal thus depends on the time of the coincidence within the 32 ns ToF, encoding the time of the coincidence. However, this only yielded a 2 ns timing resolution. To obtain a 1 ns timing resolution, the latch input signal was sent to two 16-bit shift registers, one of which was clocked by the leading edges of the clock train and one of which is clocked by the trailing edges. By taking the interleaved differences between the scaler channels on the two shift registers, a 1 ns resolution was obtained. Each LTD encodes times from two front scintillators (buddy pairs).

At the end of the gated clock train, the shift registers send their data to registers that are read out by individual scalers that record the time spectrum. They are custom-built VME 32-bit latching scalers that were designed by LPSC-Grenoble, based on a scaler ASIC developed there. The scalers collect data for the 33 ms macropulse, and then the data is latched into on-board

memory and the scaler channels cleared in the break between macropulses. The DAQ system read out these latched data during the next macropulse while the scalers accumulate the next spectra. At the end of the clock train, the latches are cleared and disabled for the duration of the next clock train (NPN). This added deadtime improves the accuracy of the deadtime corrections by reducing the dependence on the deadtime properties of the PMTs, CFDs, and MTs, which are less well defined [194]. The NA electronics have a differential non-linearity, where the widths of the timebins fluctuate slightly, but this was correctable.

4.6.1.2 French Electronics

The French took a different strategy and designed the system to be entirely custom-made with a higher resolution of 250 ps. Unlike the NA design, everything was essentially on one board. The French electronics design was fully integrated and therefore very compact, with all the electronics for the four French octants fitting into a single VXI crate.

The entire system consists of a CPU board holding the read-out controller (ROC), a Trigger Interface board connected to the Trigger Supervisor, and 8 custom mother boards that are controlled by an interface box that provided signals such as the Y_0 and MPS to the mother boards. These mother boards were called DMCH-16X (discrimination, Mean-timing, time enCoder, Histogramming, 16 mean timer channels with the VXI standard). Each of these DMCH-16X processed 32 phototube signals (half of an octant or 8 detectors). Each DMCH-16X board held all the electronics needed to process the signals from the phototubes.

The signals from the French detectors in the hall first are split by an active splitter that sent exact copies of the original signals (at full gain) to the Fastbus monitoring electronics and to the CFDs for the time-encoding electronics. Once the signal was received in a CFD, it was disabled for the remainder of the meantiming sequence to prevent confusion. If the CFD for the other end of the scintillator also received a signal, the signal was meantimed and sent to the EPLD-Trig (electrically programmable logic device for triggering) chips. Otherwise, the MT reset and waited for another signal. The deadtime from this was general about 37 ns. Like the NA CFDs, the

thresholds for the CFDs were controlled by software, generally set to about 50 mV.

Once the EPLD-Trig received the signal, it generated a 7 ns coincidence window and looked for a coincidence between the front and the back scintillator pair. Upon detecting a coincidence, the time of the event was encoded by a custom numerical time encoder called the ASIC (Application Specific Integrated Circuit) designed by the electronics department of IPN Orsay. The 128 bin flash TDC TE had a 250 ps time resolution and was locked onto the Y_0 reference signal for the timing. The TE had nine independent channels: eight used for the MT signals, and a ninth was used when running with either the internal signal generator (GDMCH) for testing the CFDs and MTs or the with GMS, where it was used for an extra signal that controls the laser firing. The data from the TE then went to the DSPs (Digital Signal Processors) that accumulated the ToF spectra for each detector.

There was an additional daughter board (SDMCH) in each DMCH that was independent of the time-encoding data system. It provided individual scalers for CFD and MT events, designed to provide information about the deadtime from incomplete events (such as single CFDs) in addition to that provided from the Fastbus monitoring data.

At the end of an MPS, the data from the DSPs and the SDMCH were transferred in 29 μs to the DSP concentrator through link ports (40 MB/s) during the 500 μs for the helicity flip and settle time. During the next MPS, the data (5 kB) was transfered from the DSP concentrator to the ROC, and from there all the data from the DMCH-16X boards were gathered up with the data from all the other ROCs into the CODA event builder for recording. The French data took a lot of resources; the total flow was about 1.4 MB/s, which was about 2/3 of the total G0 data transfer [194, 239–241].

In addition to the system for the coincidence logic, the system had other modes for testing purposes. These modes allow configurations where spectra only contained signals from the front or the back signals, signals from both, and the NPN and buddy schemes. The system also had the capability of a differential buddy system, where the buddy scheme could be done timebin-by-

timebin in a ToF spectrum. The TE had an inherent differential non-linearity (DNL), but this is corrected for in the off-line analysis.

There were nine DMCH boards in all; eight that processed the signals from the French Detectors, and one that was used for the Franco-American Hybrid Electronics (see Section 4.6.1.3).

4.6.1.3 Franco-American Hybrid Electronics

In addition to the above, there was another, rather curious electronics arrangement. In an effort to gain resolution in the higher-numbered NA detectors to make the background subtraction easier, and as an additional cross-check of the two systems, copies of the signals from detectors 14 and 15 in the NA octants were processed by the French electronics in precisely the same manner as the French TEE above (with no Fastbus). This gave ToF spectra from the NA detectors 14 and 15 with the French resolution of 250 ps. These electronics were referred to as the Franco-American Hybrid Electronics (FrAm), and these spectra were used in the background correction studies described in Section 5.4.5.

4.6.2 The Data Acquisition System

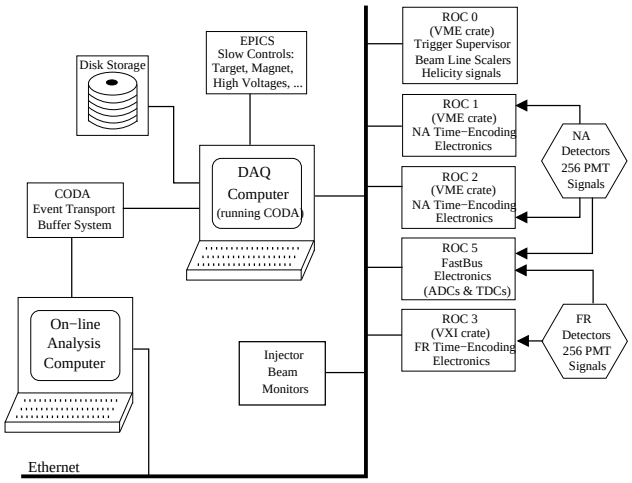

FIG. 4.15: *A flowchart of the data-acquisition system for the forward-angle G^0 measurement. Figure from [239].*

The data acquisition (DAQ) for the experiment used CODA (CEBAF Online Data Acquisition system), which was developed and is used extensively at Jefferson Lab [242,243]. The CODA DAQ

ran on a Linux computer in the Hall C counting house, and communicated with the electronics for all the G^0 subsystems, which were housed in crates in the electronics cage on the second floor of the counting house. Each crate housed the modules forming a subsystem or a part of a subsystem, along with triggering control and event readout boards. A conceptual flowchart of the system can be seen in Figure 4.15.

The DAQ computer communicates with each of the electronic crates by sending the trigger signals to a command module called the trigger supervisor (TS), which in turn passes the signal to the readout controllers (ROC) that are located in each crate. The data acquisition software on each ROC read out the data from the modules in the crate according to the trigger types and parameters, and then shipped the data to the DAQ via ethernet.

For the forward-angle measurement, the experiment used five crates. The first crate contained ROC0, along with the trigger supervisor (TS0), the scalers for the beamline monitors and the VME TDC module that sampled the Y_0 signals. The beam helicity information for the run was stored in the input register of the trigger supervisor as well. The VME crates that housed the scalers for the NA detectors (32 channels/module) also housed ROCs 1, 2, and 4. ROC3 was located in the French VXI crates that read the data from the nine DMCH boards, and ROC5 was located in the Fastbus crate that housed all the monitoring ADC and TDC modules.

The different trigger sources are passed to the trigger supervisor. If it is not busy upon receiving the trigger signal, it registers the arrival of the signal and begins to process the event. The trigger supervisor passes the information about the trigger type to the trigger interface module in each of the other crates. The DAQ software on the ROC in each crate reads out the individual front-end modules depending on the trigger type.

The experiment used three primary trigger types: 30Hz, 120 Hz, and Fastbus. The standard 30 Hz trigger (trigger type 1) was the one used for the primary production mode to take the data needed to form the parity-violating asymmetry. For this trigger, the time-encoding scaler data from ROCs 0,1,2,3 and 4 (the NA scalers, DMCH modules, and beamline instrumentation; no

Fastbus crates) were read out at the end of each MPS, during the 500 μs window for the Pockels cell to settle after flipping the helicity state.

The experiment also used a special trigger (type 2) where the DAQ over-sampled the data at 120 Hz to measure possible 60 Hz noise present in the electronics that could cause false asymmetries. Two trigger types were used for this mode: one where the DMCH were read out at 30 Hz, and one where the NA and beam scalers were read out for the three intermediate 120 Hz phases between each MPS trigger [194]. (no Fastbus for any of these events) The analysis of the 120 Hz data showed that the contribution of 60 Hz noise was negligible over the running period.

The monitoring Fastbus triggers (trigger type 4) used a hardware-prescaled copy of the Y_0 signal to ensure only a small sample of the beam pulses were taken, giving a trigger input rate of about 500 kHz. Additional prescaling was done in the trigger supervisor software, which gave a trigger rate between 120-500 Hz for usual operating conditions. For these triggers, ROCs 1-4 and the beamline scalers are not read out (only the Fastbus crate). During typical data-taking, the time required to read out the Fastbus data was about 1 ms, which limited the trigger rate to only a few hundred Hz.

To improve the trigger efficiency, some data-taking required a second level of triggering for the readout of the monitoring electronics. In this case, a fast clear cleared all the channels unless there was at least one good front-back coincidence hit from a particle during the ADC gate in one detector pair in either the NA or French readout. If cleared, the triggering components were ready for another gate in about ~ 2 μs.

In addition to these primary three trigger types, there were triggers for GMS lamp events (type 5) and GMS source events (type 6), in which the Fastbus crates were read out, but ROCs 1-4 and the beamline scalers were not.

In addition to these data, slow controls data (detector high voltages, beamline parameters, target and magnet conditions, etc.) were monitored by the Experimental Physics and Industrial Control System (EPICS) [229], written to the G^0 data stream, and archived in the CEBAF EPICS

database.

The data were collected in runs of about one hour in length. As the data were collected for each run, the data were written into a shared memory buffer by the DAQ called the event-transfer buffer, which was read by the G0RealTimeMonitor, a program written in C++/ROOT to produce realtime diagnostic plots of beam quality parameters, detector rates, and so forth. At the end of a run, the CODA datafiles were copied onto a disk drive and to the JLab tape silo storage system. After being written to the disk drive, the G0Analysis replay engine running on a dedicated analysis computer in the counting house analyzed the datafile, producing ntuples and histograms in files to be read by ROOT by the online analysis scripts written in C++/ROOT, and writing the data into a MySQL database for later offline analysis. More details about the G0Analysis program will be discussed in Section 5.1

4.7 Summary

Overall, the performance of the complex G^0 apparatus was excellent, allowing the collection of parity-violating asymmetry data over the span of several months. In this time, slightly more than 700 hours of production data were taken, amounting to about 10 TBytes of data recorded as CODA files. These data could be used to form a raw asymmetry directly. However, the road from a raw measured asymmetry to the final physics asymmetry result is a long one, as will be discussed in the next chapter on the data analysis.

CHAPTER 5

From Raw Asymmetries to Physics Asymmetries

Once the data have been taken, there is a lot of work to be done before the measured raw asymmetries become the final physics results. The raw asymmetries must be corrected for a variety of systematic effects before they can be used to calculated the linear combination of the strange electric and magnetic form factors. In particular, they must be corrected for electronics deadtime, "leakage" beam, helicity-correlated beam properties, the asymmetry from background events, beam polarization, and electromagnetic radiative corrections. In addition, the four-momentum transfer Q^2 of each of the detectors must be determined. This chapter summarizes how these corrections were done.

5.1 Overview

The raw data is analyzed using the G^0 analysis software (G0Analysis), which was developed using C++ and ROOT, an object-oriented analysis toolkit developed at CERN. The analysis software processes the raw data using the calibration values stored in a MySQL database, and

then writes all of the results of the analysis into the database.

Cuts are applied on an MPS-by-MPS basis (see Section 4.3.1) to ensure that only high-quality data are used for the physics results. Events with a beam current below 4 μA are removed, along with the next 500 MPSs after a beam trip recovery to allow the beam and the target to stabilize. Cuts are done to ensure that the data were taken at the proper magnet current and target temperature; that there were no electronics malfunctions; and to ensure that the beam parameters were all within the tolerances of the measurement (see Table 5.4). If any MPS in a quartet fails a cut, the entire quartet is removed. Over 900 hours of data were taken in the experiment; a quarter of it did not pass the cuts, leaving a dataset of 100.88 C of integrated beam current for the physics asymmetry analysis.

The data that pass the cuts then moves on for further analysis. Any slight differential non-linearity (DNL) in the timebin widths in the ToF spectra are corrected using measured calibration files [244]. The deadtime corrections (see Section 5.2.1) are applied to the rates bin-by-bin for each detector. These rates are then normalized by the beam current to obtain the yields as

$$Y(t) = \frac{R(t)}{I}, \tag{5.1}$$

where $Y(t)$ denotes the yield in a given timebin t, $R(t)$ is the rate in that timebin, and I is the beam current. The asymmetry in each timebin is then computed by

$$A(t) = h\,\frac{Y_1 + Y_4 - (Y_2 + Y_3)}{Y_1 + Y_4 + Y_2 + Y_3}, \tag{5.2}$$

where Y_i represents the yield measured in the ith MPS in the quartet, where the quartets have the pattern $+--+$ or $-++-$. The variable h takes a value of 1 or -1, which is determined by the helicity bit that sets the polarity of the helicity Pockels cell. The determination of the true sign of the asymmetry is discussed in Section 5.2.2.3. Other asymmetries in the experiment are calculated in the same manner. For the beam position, beam angle, and energy differences, the helicity-correlated difference is used instead:

$$\Delta p = h\,\frac{p_1 + p_4 - (p_2 + p_3)}{2}, \tag{5.3}$$

where p_i is that parameter in an MPS. The running averages of these values over an entire run are also computed and written to the database. The correlation slopes for the beam parameters are calculated (see Section 5.3.2), and then the means and uncertainties of the yields and asymmetries for the detectors and beam parameters are written into the MySQL database.

To remove the possibility of the introduction of human bias during the analysis of the data, what is known as a blind analysis was done. The analysis code was designed to apply a multiplicative blinding factor ($f_{blinding} \equiv 0.805619$), which was not known by any of the analysis team until the end of the analysis. At the end of the analysis, this global blinding factor was removed.

This chapter describes the analysis of both the parity-violating asymmetry data taken with a longitudinally polarized electron beam and the analysis of the transverse asymmetry data taken with a transversely polarized beam. First, elements of the analysis common to both data sets are covered, then the parity-violation data, and finally, the transverse asymmetry data set.

5.2 Analysis Common to Both Datasets

The result of the processing by the analysis software is a time-of-flight spectrum of the yield and the asymmetry for each data run. An example spectrum can be seen in Figure 5.1. The spectrum shows a pion peak at about 8 ns, a proton peak at 20 ns, and an inelastic peak in between. The inelastic peak extends underneath the elastic peak of interest, and so the contribution of these events must be removed from the elastic asymmetry.

Cuts were made for particle identification along the ToF spectrum, which were different for the parity-violation and transverse datasets. In addition, the French and NA electronics have different timing resolutions, so the cuts are not exactly the same width for each. An example of the elastic proton cut is shown in Figure 5.1; for the cuts used the analysis of each dataset, see Sections 5.3.1 and 5.4.1.

The asymmetry reported for a run is the asymmetry integrated over the cut, weighted by the

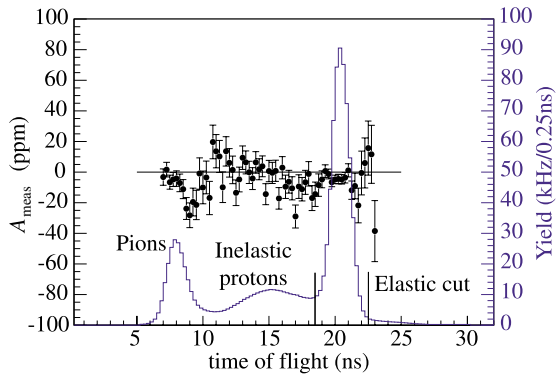

FIG. 5.1: *Spectrum from the G^0 forward-angle measurement showing the measured yield (histogram) and raw asymmetry (data points) as a function of ToF for Detector 8. Figure from [245].*

measured yield. The statistical asymmetry is calculated by counting statistics:

$$\sigma_{A_{elas}} = \frac{\sigma_{A_{qrt}}}{\sqrt{N_{qrt}}} \simeq \frac{1}{\sqrt{N_{elas}}}, \tag{5.4}$$

where $\sigma_{A_{elas}}$ is the statistical width of the asymmetry distribution, N_{qrt} is the number of quartets, and N_{elas} is the number of elastic proton events. The asymmetry distribution should have a perfect Gaussian shape, and the NA G^0 data behave in this manner, following counting statistics as expected.

However, a problem was discovered for the French dataset. The French proton cut contains 17 timebins. There are two ways to calculated the mean and width of the asymmetry in the proton cut. In the first, the yield can be integrated over all 17 bins to obtain the proton yield, which is then used to calculate the asymmetry and its width. In the second case, the asymmetry and its width can be calculated bin-by-bin, and then a weighted average can be done to get the proton asymmetry and width. If the measurement of each timebin is independent, both methods should be equivalent. However, in the French dataset the methods differed by about 20%, due to an intrinsic jitter in the TDCs that introduced correlations between the timebins [228]. As the first method is insensitive to this effect, this method was used to calculate the uncertainty.

Finally, the data were studied to investigate if there were any long term systematic drifts or electronics false asymmetries by studying the behaviour under half-wave plate reversal. The

asymmetry flipped sign with each half-wave plate state change, and averaged to zero as expected.

5.2.1 Deadtime Corrections

Deadtime in the electronics is an unavoidable systematic in a counting experiment [246]. The electronics for the G^0 experiment count the signals from the passage of particles through each of the FPDs at a rate of about 2 MHz [239]. The electronics require a finite amount of time to process the detection of a particle, which means that the electronics cannot process any other events that take place during this period. This time period τ is the deadtime, and is a characteristic of those electronics. Since protons that pass through the detectors are unrecorded, this deadtime affects the measured counting rate, and thus the measured parity-violating asymmetry, and so must be corrected for carefully.

The deadtime fraction f_{dt} is the probability that a channel is dead upon the arrival of the next event, and is proportional to the event rate, given by

$$f_{dt} = \tau R_{meas}, \tag{5.5}$$

where R_{meas} is the measured detector rate, τ is the deadtime, which when using the NPN method is the time-length of a 32 ns beam pulse. The measured rate will then by related to the actual rate by f_{dt} (to first order):

$$R_{meas} = (1 - f_{dt})R_{true}, \tag{5.6}$$

where R_{true} is the true rate. In the same manner, the measured charge normalized yield Y_{meas} is also related to the true yield Y_{true}:

$$Y_{meas} = (1 - f_{dt})Y_{true}, \tag{5.7}$$

where $Y_{meas} = \frac{R_{meas}}{I}$ is the normalized raw yield and $Y_{true} = \frac{R_{true}}{I}$ is the normalized true yield. The rate is proportional to the beam current I, so a charge asymmetry present in the beam coupled with deadtime effects can introduce sizable false asymmetries. The true asymmetry is related to

the measured asymmetry through the deadtime fraction:

$$A_{meas} = A_{phys} - \frac{f_{dt}}{1 - f_{dt}} \left(A_{phys} + A_Q \right), \tag{5.8}$$

where f_{dt} is the deadtime fraction, A_{meas} is the measured asymmetry, A_Q is the charge asymmetry, and A_{phys} is the true asymmetry without deadtime effects.

In the G^0 experiment, two different approaches were used to reduce helicity-dependent deadtime effects [194,239], as discussed in more detail in Section 4.6.1. In the Next-Pulse-Neutralization (NPN) method, if an event triggers the electronics, any events in the following beam pulse 32 ns later in the same channel are ignored. This introduces a deadtime of known length that is well understood. The other system to monitor and study deadtime effects is called the "buddy" system, where a comparison of the deadtime in a detector is compared to the deadtime in the same Q^2 detector in a diametrically-opposed octant (the detector's buddy), as discussed in Section 4.6.1. Both sets of electronics use these methods. In the G^0 experiment, the correction for deadtime is made MPS by MPS.

The true scattering rate is proportional to the beam current, so deadtime effects can be determined from the correlation of the measured, normalized yield and the beam current. The deadtime fraction is then the slope of the normalized yield versus beam current. In addition, Equation 5.8 shows that f_{dt} can be measured by artificially inducing a known charge asymmetry and then observing the correlation between A_{meas} and A_Q:

$$\frac{\partial A_{meas}}{\partial A_Q} = -\frac{f_{dt}}{1 - f_{dt}}. \tag{5.9}$$

The deadtime fraction determined by both methods were in good agreement. The deadtime fraction at the standard beam current was about 10% for the NA electronics and 15% in the French electronics. After the correction, the remaining asymmetry slope for the NA detectors was negligible, but the French detectors had a slight residual slope of about $\sim -2.5\%$. The remaining false asymmetry after the deadtime corrections are estimated from a knowledge of the electronics themselves. The correction for any residual false asymmetry is made after the background correc-

tion. A point-to-point systematic error bar of 100% of the correction was assigned to this final correction.

5.2.2 Beam Polarization Correction

The correction to the raw asymmetry for the beam polarization is simply

$$A_{corr} = \frac{A_{raw}}{P_b}, \tag{5.10}$$

where P_b is the polarization of the beam, and A_{raw} and A_{corr} are the raw and corrected asymmetries. In addition to this correction, however, the uncertainty in the measurement of the polarization is a global systematic uncertainty for the experiment, which makes a careful measurement and understanding of the polarization measurements necessary [207].

5.2.2.1 Longitudinal Polarization Analysis

The beam polarization measurements for the experiment, as measured with the Hall C Møller polarimeter as described in Section 4.3.3, are shown by IHWP state in Figure 5.2 for the production running period. The measurements are shown grouped according to the configuration of the polarized source and injector, with a constant fit shown for each grouping. The closed points denote longitudinal polarization measurements; the open points represent the transverse polarization values. The polarization was quite stable, on average about 74%. The polarization for each configuration was used for the corresponding range of G^0 data runs, with the asymmetries and their uncertainties corrected on a run-by-run basis. The average polarization for the entire experimental run, weighted by the physics production data, was 73.73%.

The statistical error for each polarization measurement is typically around 0.3%, which is quite small compared to the systematic uncertainty. The systematic uncertainty of the polarization measurement has contributions from the foil polarization, target heating and warping, and various other errors in the set-up and tuning of the equipment. The contributions to the systematic uncertainties are summarized in Table 5.1. The systematic errors due to potential mis-tuning

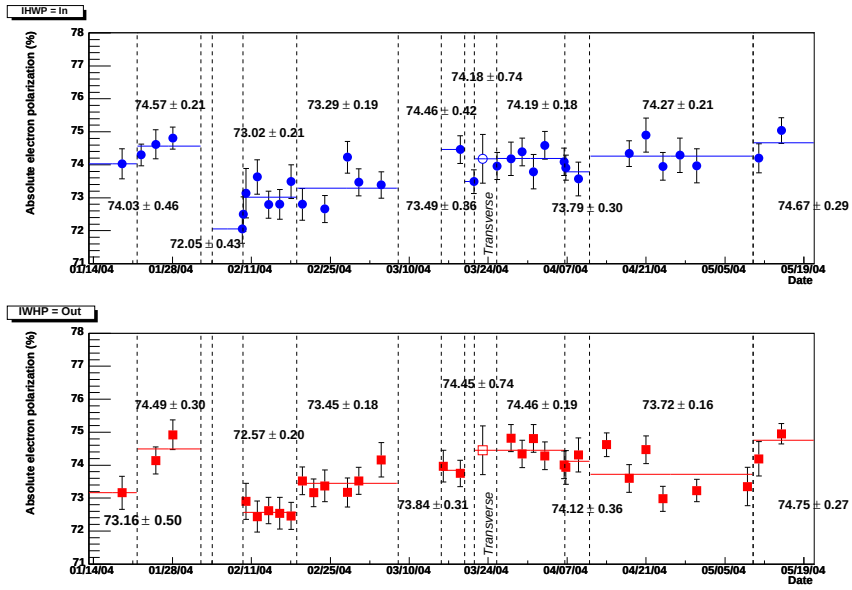

FIG. 5.2: *The beam polarization versus date for the forward-angle running period of the G^0 experiment, shown by insertable half-wave plate (IHWP) state. The measurements are grouped according to the configuration of the polarized source, with a constant fit for each group. The closed points denote longitudinal polarization measurements; the open points represent the transverse polarization values. Error bars are statistical. Figure from [207].*

or misalignment of the various parts of the polarimeter have been well studied before, as have the contributions of the uncertainty of the beam position measurement, the corrections for the Levchuk effect (the motion of the atomic electrons in the iron target), and the contribution of multiple scattering [209, 247].

For the G^0 run, the Møller solenoid field was set to 3T instead of 4T, due to historical reasons. This field setting gave a target polarization of 0.08036 ± 0.00015, so there is a $+0.1\%$ correction to the beam polarization numbers, and a contribution of 0.19% to the uncertainty.[1] At 3T, 2° of target warping yields an uncertainty of 0.37%. For the measurement current of 2 μA, and a beam spot size of 100 μm, the effect on the polarization of target heating from the beam on the iron foil is 0.2%, with a random uncertainty of 0.1%.

Leakage beam from the other halls gives a contribution of 0.2% fractional error on the polarization in the worst case scenario. The correction for the charge measurement is very small, at most $Q_+/Q_- \sim 1.008$, and usually smaller. The charge asymmetry is even smaller. The gain of

[1] For a 4T field, the target foil polarization is $8.043 \pm 0.015\%$.

Source	Uncertainty	Effect on A (%)
Beam position x	0.5 mm	0.15
Beam position y	0.5 mm	0.03
Beam angle x	0.15 mr	0.04
Beam angle y	0.15 mr	0.04
Current Q1	2 %	0.10
Current Q2	1 %	0.07
Position Q2	1 mm	0.02
Multiple Scattering	10 %	0.12
Levchuk Effect	10 %	0.30
Collimator Position	0.5 mm	0.06
Target Temperature	5°	0.2
Direction B-field	2°	0.06
Value B-field	5 %	0.03
Spin Polarization in Fe	0.19%	0.1
Target Warping	2°	0.37
Leakage		0.2
High-Current		1.0
Solenoid Monte-Carlo		0.1
Electronic Deadtime		0.04
Charge Measurement		0.02
Monte Carlo Statistics		0.28
Accelerator Configuration		0.5
Total Uncertainty		1.32

TABLE 5.1: *Sources of error in the determination of the beam polarization (solenoid at 3T). The percentages are fractional.*

the BCMs is nonlinear at the 0.2–0.3% level, which is negligible for these measurements. Assuming the offset is uncertain at the 10 kHz level (0.25 counts/MHz versus 0.24), this leads to a 0.02% effect. For a typical Møller run, the rates are $\sim$ 25 kHz, and so the effect on the Møller asymmetry of the electronic deadtime is 0.04%.

To be conservative, we have added two more sources of error: one for the high-current extrapolation, and another for accelerator configuration changes. Recall that the polarization measurements are made at a beam current of 2 μA instead of the nominal 40 μA. Although the mechanism is not known, it is conceivable that the polarization could change over this span. There is no current dependence of the polarization measurement at the 1 % level up to 10 μA, verified by tests with the Møller raster in 2003, and there is no convincing argument for a change in beam polarization at higher currents. However, there have been no good measurements of the beam polarization in

Hall C in this current range. Tests with the Møller kicker in 2004 suggest the extrapolation is valid at the 1–2% level at 40 μA, but the polarized source was too unstable for a precise measurement. In the interest of being conservative, a 1% fractional uncertainty is assumed for the extrapolation from 2 μA to 40 μA. The 0.5% designated for accelerator configuration changes is meant to account for any laser spot moves, quantum efficiency changes, or other accelerator configuration changes that affected the polarization. This number was determined by observing the spread caused by these changes.

The conservative number for the total systematic uncertainty, including the contributions from the high-current extrapolation and the accelerator ambiguities, is 1.32% (fractional). This number is assigned as a global systematic uncertainty for the physics asymmetry measurement. Tables of the polarization measurements performed during the second engineering run and the forward-angle physics run of the G^0 experiment can be found in Ref. [207].

5.2.2.2 Transverse Polarization Analysis

The determination of the transverse polarization was done by assuming that the longitudinal polarization measured for the spin dance on March 26 was the value of the polarization during the transverse running. The transverse running was very short, and there was only one data set for each IHWP setting. In addition, the stability of polarization during the months of longitudinal running indicates that the polarization should remain stable over the few days of the transverse measurement. The statistical error bars were assigned based on the interpolation between the two spin dances on March 22 and 26, with some inflation due to the indirect nature of the determination and the drift of 2.75 degrees that occurred during that period. The systematic error uncertainty of 1.66% (fractional) comes from the reported conservative systematic uncertainty of 1.32% for all the forward-angle polarization measurements (see Ref. [207, 248]) with an additional 1.0% systematic uncertainty combined in quadrature due to the indirect nature of the measurement. Based on the constraints from the spin dance, the interpolated polarization values for the transverse running are shown in Table 5.2. The data for the transverse running were corrected for the polarization using

the average value for the period, which comes to 74.32 ± 1.34 (or a 1.80% fractional error bar).

Run Range	Polarization (%)	IHWP	Time Period
20791 – 20819 20877 – 20900	$74.18 \pm 0.74_{stat} \pm 1.23_{syst}$	In	3/22 – 3/23 3/25 – 3/26
20820 – 20876	$74.45 \pm 0.74_{stat} \pm 1.24_{syst}$	Out	3/23 – 3/25
20791 – 20900 (All runs)	$74.32 \pm 0.52_{stat} \pm 1.23_{syst}$	Average	3/22 - 3/26

TABLE 5.2: *The polarization for the transverse running period. The statistical error bars are quasi-statistical with some interpolation error folded in, and the systematic error bars are from the systematic study for the longitudinal polarization measurements for the G^0 experiment inflated by another 1.0%.*

5.2.2.3 Determination of Physics Asymmetry Sign

An insertable half-wave plate (IHWP) on the laser table is used as a systematics check in the G^0 experiment. The insertion of the IHWP reverses the helicity of the beam pulse electrons with respect to the helicity signal sent to the electronics so that the electrons labeled as "h^+" are now actually in the opposite helicity state than they were formerly. The parity-violating physics asymmetry reverses sign, but any electronics-related false asymmetry present does not. Since all other aspects of the experiment have remained the same, any helicity-correlated differences in the electronics become apparent when the physics asymmetry data from both IHWP states ("in" or "out") are summed together, as ideally they should sum to zero.

The physics asymmetries are calculated in the analysis assuming that the electron pulses labeled as "h^+" and "h^-" contain positive and negative helicity electrons, respectively. However, this is only true for one of the IHWP states, in or out, and the actual helicity is the opposite of the designated helicity in the other IHWP state. The question then is this: how can the true electron helicity designation be determined? There is no unbiased way to determine the correct helicity designation for the calculation of the actual physics asymmetry from the physics data itself.

The polarization reported by the Møller analyzer is calculated from the Møller asymmetry measured by the polarimeter, so the sign of the Møller asymmetry also changes with the IHWP setting, causing the polarization to be reported as positive or negative. An understanding of the

measured Møller asymmetry and the Møller polarimeter can therefore be used to determine the actual electron helicity throughout the experiment by knowing the sign of the measured polarization [249].

As mentioned before, the theoretical Møller asymmetry is defined as the cross-section asymmetry

$$A_{Møller} = \frac{\sigma^{\uparrow\uparrow} - \sigma^{\downarrow\uparrow}}{\sigma^{\uparrow\uparrow} + \sigma^{\downarrow\uparrow}} = |P_b||P_t|A_{zz}(\theta), \tag{5.11}$$

where $\sigma^{\uparrow\uparrow}$ denotes that the electron spins of the beam and the Møller target are aligned, $\sigma^{\downarrow\uparrow}$ denotes that the electron spins of the beam and the Møller target are anti-aligned, P_b is the polarization of the beam, P_t is the polarization of the Møller target electrons, and $A_{zz}(\theta) = -\sin^2\theta\frac{(8-\sin^2\theta)}{(4-\sin^2\theta)^2}$ is the analyzing power [209]. At 90°_{cm}, $A_{zz}(\theta) = -\frac{7}{9}$. Note that the defined Møller asymmetry is negative.

The Møller solenoid generates a $\vec{B}$-field in the direction of the beam momentum (downstream). However, even though the target magnetization is with the direction of the beam momentum, the spins of the target electrons are anti-aligned with the magnetization. The magnetic moment of the electron is defined as

$$\vec{\mu} = \frac{ge}{2m_e c}\vec{s}, \tag{5.12}$$

where $\vec{s}$ is the spin angular momentum, m_e is the electron mass, g is the electron anomalous magnetic moment, e is the electron charge, and c is the speed of light [205]. Since the electron charge is negative, the Møller target foil electron spins are pointing *upstream*.

The Møller analyzer calculated the measured Møller asymmetry by using the equation

$$A_{meas} = \frac{\text{“}h^+\text{”} - \text{“}h^-\text{”}}{\text{“}h^+\text{”} + \text{“}h^-\text{”}}, \tag{5.13}$$

where “h^+” and “h^-” are the helicity states of the beam electrons labeled as positive and negative from the Pockels cell. When the measured Møller asymmetry is negative, the beam electrons are aligned parallel with the Møller target foil electron spins, which are pointing opposite to the beam momentum. Therefore, when $A_{meas} < 0$, “h^+” contains a true negative electron helicity state,

h^-, and when $A_{meas} > 0$, "h^+" contains a true positive electron helicity state, h^+. The beam polarization is calculated using the equation

$$P_b = A_{meas} \times \text{beam polarization factor}, \tag{5.14}$$

where the beam polarization factor is defined as the inverse of the analyzing power of the system and is positive by definition. Since the beam polarization factor is positive, a negative beam polarization value implies a negative Møller asymmetry. Therefore, if the analyzer calculated a negative polarization, the helicity state labeled as "h^+" actually contains a true negative electron helicity state (and "h^-" a true positive helicity state). If the analyzer computes a positive polarization, the opposite is true. When the IHWP is placed into or retracted from the laser beam path on the laser table, the sign of the polarization that the Møller analyzer computes should clearly change since the electron helicity states labeled "h^+" and "h^-" by the Pockels cell have been switched.

Since the physics asymmetry measured by G^0 is defined as

$$A_{phys} = \frac{h^+ - h^-}{h^+ + h^-}, \tag{5.15}$$

the physics asymmetry over the entire running period should be the difference of the physics asymmetries calculated for the two different IHWP states:

$$A_{physicsoverall} = \left\{\frac{h^+ - h^-}{h^+ + h^-}\right\}_{\text{IHWP state 1}} - \left\{\frac{h^- - h^+}{h^+ + h^-}\right\}_{\text{IHWP state 2}} \tag{5.16}$$

We know that the IHWP setting that has the state labeled "h^+" containing the actual electron helicity state h^+ is the IHWP setting that has the positive measured polarization. Therefore,

$$A_{physicsoverall} = \{A_{phys}\}_+ - \{A_{phys}\}_-, \tag{5.17}$$

where $\{A_{phys}\}_+$ is the asymmetry from the data taken in the IHWP with positive polarization, and $\{A_{phys}\}_-$ is the asymmetry from the data taken in the IHWP with negative polarization.

The determination of the actual beam electron helicity must be redone each time that there is any change on the laser table that might reset the Pockels cell, possibly swapping the way it labels the helicity states. Such occurrences are usually obvious, since the sign of the measured

Start Date	End Date	Run Range	Physics Asymmetry
October 15, 2002	January 27, 2003	14152–16140	$A_{phys} = A_{out} - A_{in}$
November 17, 2003	December 9, 2003 (7:00)	17260–18090	$A_{phys} = A_{out} - A_{in}$
December 9, 2003 (16:00)	March 8, 2004	18091–20568	$A_{phys} = A_{in} - A_{out}$
March 15, 2004	May 18, 2004	20589–22186	$A_{phys} = A_{out} - A_{in}$

TABLE 5.3: *The actual beam electron helicity for the determination of the physics asymmetry sign for the G^0 experiment.*

polarization in that half-wave plate setting should change, indicating that a swap has occurred. However, as long as nothing on the laser table is disturbed and the beam itself is unchanged, the polarization should keep the same respective sign in each of the two half-wave plate settings.

The determination for the G^0 experiment is shown in Table 5.3. The helicity changed between the polarization measurements in December, 2003 due to work on the laser table involving the Pockels cell. It changed again in March 2004 when the accelerator changed configuration from 3-pass, 990 MeV/pass beam to 4-pass, 747 MeV/pass beam. As the total spin precession from the injector to Hall C had changed by an odd multiple of π, the electron helicity was flipped and the physics asymmetry changed sign.

5.3 Longitudinal Data Set

The raw asymmetries are corrected for electronics deadtime effects, the leakage beam asymmetry from the other halls, any false asymmetry introduced by helicity-correlated beam properties, and the beam polarization. Corrections are made to remove the contribution of background events to the elastic proton asymmetry of interest. Radiative corrections are then done to account for higher-order processes. Finally, the corrected final asymmetries are unblinded, and then used to compute the strange form factors, which will be discussed in the next chapter. As a note, in this chapter the asymmetries are usually blinded, unless indicated as otherwise.

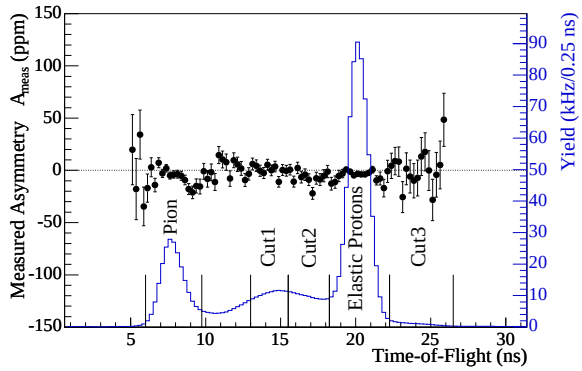

FIG. 5.3: *Spectrum from the G^0 forward-angle measurement showing the measured yield (histogram) and raw asymmetry (data points) as a function of ToF for Detector 8.*

5.3.1 Time-of-Flight Particle Identification Cuts

The result of the processing by the analysis software is a time-of-flight spectrum of the yield and the asymmetry for each data run. An example spectrum can be seen in Figure 5.3. The spectrum shows a pion peak at about 8 ns, a proton peak at 21 ns, and an inelastic peak in between. The inelastic peak extends underneath the elastic peak of interest, and so the contribution of these events must be removed from the elastic asymmetry.

Cuts were made for particle identification along the ToF spectrum. As the French and NA electronics have different timing resolutions, the cuts are not exactly the same width for each. The main ToF cuts used for the analysis were:

- pion cut: pion peak window,
- cut1: first window within the inelastic peak,
- cut2: second window within the inelastic peak,
- proton cut: the elastic proton peak window of interest,
- cut3: a window directly after the proton cut,
- total: the entire 32 ns spectrum.

These cuts are shown in the figure, and are mentioned to make later discussions simpler.

5.3.2 Corrections for Helicity-Correlated Beam Properties

One of the primary possible sources of false asymmetries comes from helicity correlation in the beam properties. The cross section depends on the beam energy, the detector sensitivities vary with the beam position and angle, and the background levels can vary with the beam position and halo, which makes careful monitoring and study of the beam quality important.

5.3.2.1 Helicity-Correlated Beam Parameters

The yield measured in the detectors is proportional to the scattering cross section and the acceptance; both have dependence on the beam properties such as the incident beam positions, angles, and energy. Because of this, helicity-correlated changes in these beam parameters will cause a change in the yield δY that can be written in terms of the change in each of the beam parameters δP_i and the correlation slope $\frac{\partial Y}{\partial P_i}$ that describes the response of the measured detector yield to the changes in the beam parameters:

$$\delta Y = \sum_{i=1}^{N} \frac{\partial Y}{\partial P_i} \Delta P_i, \tag{5.18}$$

where $\delta Y \equiv Y - \langle Y \rangle$ is the change in the yield and $\Delta P_i \equiv P_i - \langle P_i \rangle$ is the helicity-correlation in the beam parameter P_i. Changes in the yield in turn affect the asymmetry, so any helicity-correlated differences in the beam parameters will cause a false asymmetry described by [194]

$$A_{false} = \sum_{i=1}^{N} \frac{1}{2Y} \frac{\partial Y}{\partial P_i} \Delta P_i \tag{5.19}$$

in the measured asymmetry, which must be corrected for.

Thus, it is important to monitor the beam parameters for quality and measure them for corrections for residual effects in the physics asymmetry. To remove the false asymmetry, the ΔP_i and the correlation slopes $\frac{\partial Y}{\partial P_i}$ must be determined. The ΔP_i were monitored continuously with the beam monitors during the measurement and their asymmetries calculated. To determine the slopes, a standard multi-dimensional linear regression technique was used. A given beam parameter may be correlated with the others; this technique takes into account these correlations and

accurately corrects for effects where the spectrometer sensitivity couples to the helicity-correlated beam properties. The G^0 experiment monitored six beam parameters for helicity-correlation and recorded data for the physics asymmetry correction: the beam charge, the x and y positions, x and y beam angles, and the beam energy.

Helicity-correlation in the beam originates in the polarized source at the helicity Pockels cell, the optical element that determines the polarization state of the beam, and can be generated in a variety of ways. One way that the Pockels cell can cause helicity-correlated effects is through steering the beam. Crystalline materials that exhibit a Pockels effect are also piezoelectric, so the application of a voltage across the crystal can cause a distortion of its shape, which in turn can cause the laser to refract off of the beam axis by slightly different amounts for the two polarization states. As the laser beam is then steered differently for the two helicity states, the beam will illuminate the cathode in two different locations, causing the generated electron beam to have two originating positions. This creates helicity-correlated position differences. These helicity-correlated steering effects can also cause a charge asymmetry if the cathode has a significant quantum-efficiency (QE) gradient across the surface. As the laser is incident on the cathode surface in two locations, different amounts of charge will be photoemitted depending on this gradient, which creates a helicity-correlated charge asymmetry. Charge asymmetries can also arise from the fact that the Pockels cell does not create a perfectly circularly polarized light, and that the cathode has some analyzing power. As the light has a small residual component of linearly polarized light, this light will rotate when the handedness of the circularly polarized light is flipped, causing a helicity-correlated photo-emission difference. A RHWP is used in the injector to minimize this effect, and the IA and PZT feedback systems are used to minimize all these effects (see Section 4.3.1.1). Helicity-correlated beam effects are further complicated by the transport of the beam (adiabatic damping, beam scraping, betatron mismatch) [250].

The beam charge was measured using the two RF cavity BCMs (see Section 4.3.4) in Hall C. The x- and y-positions and angles at the target were determined using stripline BPMs IPM3HG0

Helicity-Correlated Beam Parameter	Measured Value	Specification
Charge Asymmetry A_q (ppm)	-0.14 ± 0.32	< 1
x-position difference Δx (nm)	3 ± 4	< 20
y-position difference Δy (nm)	4 ± 4	< 20
x-angle difference $\Delta\theta_x$ (nrad)	1 ± 1	< 2
y-angle difference $\Delta\theta_y$ (nrad)	1.5 ± 1	< 2
Energy Difference ΔE (eV)	29 ± 4	< 75

TABLE 5.4: *The measured helicity-correlated beam parameters during the G^0 forward-angle production running, along with the desired beam quality specifications [250].*

and IPM3HG0B (G0 and G0B), which were located about 5 meters upstream of the G^0 target, separated from each other by about 2.5 meters, in the hall. As the two BPMs measured both the x and y positions and had no steering or focusing magnets between them and the target, the positions and angles at the target were extrapolated from these measurements (see Section 4.3.4). The beam energy was determined using the measured x position of the beam from a BPM (IPM3HC12, called 3C12) located in a dispersive section in the Hall C arc (see Section 4.3.4). The helicity-correlated differences in the beam parameters averaged over the entire experiment can be seen in Table 5.4.

The other contribution to the false asymmetry in Eq. 5.19 comes from the slopes. Two methods were used to determine the slopes $\frac{\partial Y}{\partial P_i}$ during the experiment. The first method used the natural beam motion (NBM) to observe how the detector rates varied as a function of the beam parameters. This method yields a realtime measurement of detector response to changes in the beam parameters; however, the NBM does not have a large dynamic range (a good thing, actually, as it indicated a stable beam position), the typical range of motion being about 0.1 mm. To study the detector responses over a larger dynamic range, a second method was also used. This method uses a set of steering coils (see Section 4.3.4.6) upstream of the target to artificially dither the beam position by about 1 mm in a grid or cross pattern to increase the dynamic range of the parameters. This was called coil pulsing (CP) or beam modulation, and these data were taken automatically for a short period (about a minute) at the beginning of most of the data runs. The slopes for the experiment were then calculated three ways: two calculations based on

measurements of the yield using NBM and CP, and a calculation of the position slopes using a G0GEANT simulation [251, 252]. The yield slopes calculated from the NBM data were used to determine the false asymmetry contribution for the experiment; the CP data were used as a cross-check for the slopes from the NBM, as were the ones from the simulation.

Standard multiple linear regression techniques were used to calculate the slopes from the measured data [250, 253]. This method takes into account the correlations between the beam parameters and the yields as well as the beam parameters themselves:

$$\langle \delta P_j \delta Y \rangle = \sum_i \frac{\partial Y}{\partial P_i} \langle \delta P_j \delta P_i \rangle, \tag{5.20}$$

where $\langle \delta P_j \delta Y \rangle$ is the vector representing the covariance between the yields and the beam parameters, and $\langle \delta P_j \delta P_i \rangle$ is the 6×6 matrix representing the correlation between the six monitored beam parameters. If the beam parameters were 100% correlated, the matrix would become a singular matrix, and could not be inverted; but in reality, due to noise in the devices, this is never the case. The linear regression is done for each of the PID cuts (i.e. proton cut, etc.) for each FPD, and the slopes and the uncertainties are calculated and written to the database. The yields can be then corrected MPS-by-MPS during a second-pass replay with the analysis engine following

$$Y^m_{corr} = Y^m_{meas} - \sum_i \frac{\partial Y}{\partial P_i} (P^m_i - \langle P_i \rangle), \tag{5.21}$$

where the m superscript denotes the MPS, Y^m_{corr} and Y^m_{meas} are the corrected and measured yields of each MPS, ∂P_i represents the six beam parameters, and $\frac{\partial Y}{\partial P_i}$ denotes the six calculated slopes [250, 253].

The linear regression analysis determined the slopes quite accurately, and the dependence of the corrected yield on the beam parameters are largely removed. Figures 5.4 and 5.5 show the data before and after the linear regression correction, and how well the corrections remove the beam position sensitivity for these detectors. Because of the azimuthal symmetry of the spectrometer, octants that are diametrically opposed have sensitivities to the beam position that are equal in magnitude, but opposite in sign, with those placed horizontally (3 and 7) having

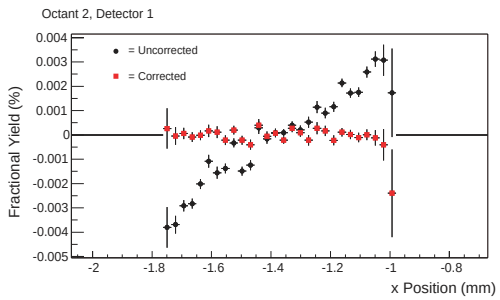

FIG. 5.4: *The fractional yield versus beam position in the x-axis for Octant 2, Detector 1, with the yield shown uncorrected and corrected for the sensitivity to the beam position. Octants 2 and 6 are diametrically opposed, and thus this shows an oppositely signed sensitivity compared to Octant 6. Figure from [250].*

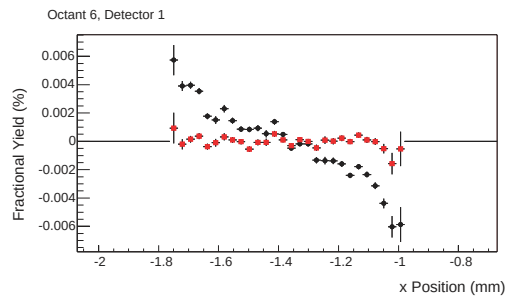

FIG. 5.5: *The fractional yield versus beam position in the x-axis for Octant 6, Detector 1, with the yield shown uncorrected and corrected for the sensitivity to the beam position. Octants 2 and 6 are diametrically opposed, and thus this shows an oppositely signed sensitivity compared to Octant 2. Figure from [250].*

the most sensitivity in x and those placed vertically (1 and 5) having the most sensitivity to y. This geometrical sensitivity can be seen in Figure 5.6, which shows the linear regression slopes from both the NBM and the CP calculations during the production run period versus each octant. The data are in excellent agreement with the beam position sensitivity study results [252] done using the G0GEANT simulation. The slopes follow a sinusoidal curve. The advantage of having an azimuthally symmetric spectrometer becomes obvious in this case, as the false asymmetry contribution to the physics asymmetry largely cancels out when the slopes are summed over all the octants. This is true for all the position and angle slopes. The charge slopes have a NA versus French detector dependence due to the differing electronics deadtimes in the two sets of octants. The yield slopes for all the octants and other information on the helicity-correlated beam parameters can be found in [250, 253].

By using the octant-summed slopes and the measured beam parameter differences, the false asymmetry caused by the helicity-correlated beam parameters can be determined using Equation 5.19. The total helicity-correlated false asymmetries for each of the detectors over the G^0 forward-angle measurement are shown in Table 5.5. As can be seen, the linear regression correc-

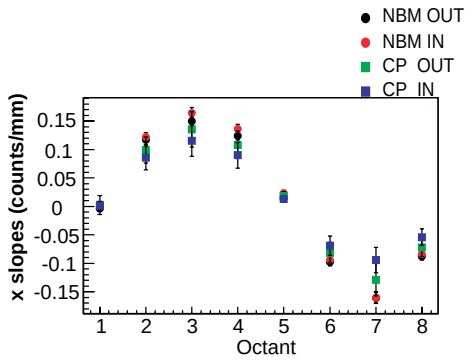

FIG. 5.6: *The linear regression slopes in x versus Octant for Detector 1. The slopes are calculated from NBM and CP. Figure from [250].*

tions give an average false asymmetry over all detectors of about -20 ppb, with an error of less than 10 ppb for each detector. These corrections and their contributions to the overall uncertainty of the measured asymmetry are negligible.

The statistical uncertainty in the slopes can be calculated in quadrature from the covariance terms, but due to the high rates in the G^0 detectors, the statistical uncertainty is very small compared to the slopes themselves. However, the run-by-run fluctuations of the slopes are significantly larger than their corresponding statistical uncertainties. This implies that the uncertainty in the slopes is dominated by systematic effects that may come from beam instabilities (such as beam halo) as well as the apparatus. When averaged over a time frame long enough to suppress short-term systematic fluctuations, the slopes display the expected spectrometer sensitivity and seem reasonably stable. Therefore, the standard deviation of the slopes over the entire production run is taken as the uncertainty.

For more details about this procedure that in this summary, the reader is directed to the dedicated analysis in Refs. [250, 253] by another G0 student.

5.3.2.2 Helicity-Correlated Beam Background Asymmetry

The beam halo can carry a helicity-correlated asymmetry, and was therefore monitored carefully by a beam halo monitoring system built for that purpose (see Section 4.3.4.3). The helicity-correlated beam background asymmetry, or halo asymmetry over the production period was gen-

Detector	False Asymmetry (ppm)	Detector	False Asymmetry (ppm)
1	-0.017 ± 0.004	9	-0.029 ± 0.008
2	-0.019 ± 0.004	10	-0.026 ± 0.007
3	-0.018 ± 0.004	11	-0.032 ± 0.009
4	-0.021 ± 0.004	12	-0.013 ± 0.004
5	-0.026 ± 0.006	13	-0.027 ± 0.007
6	-0.024 ± 0.005	14	-0.022 ± 0.007
7	-0.028 ± 0.007	15	-0.006 ± 0.006
8	-0.024 ± 0.006		

TABLE 5.5: *The total false asymmetries from helicity-correlated beam parameters for each detector calculated from multiple linear regression.*

erally consistent with zero for the IHWP In state, within the rather large error bars (about 20 ppm) due to the relatively low rate in the halo detectors. However, it was observed that the halo asymmetry for the IHWP Out state could become somewhat large, about -30 to -40 ppm for extended periods. The origin of this halo asymmetry is unknown. Because of the concern that this halo asymmetry could contribute a false asymmetry to the primary physics measurement, studies were done to estimate the possible contribution.

Data were taken with the 5 mm hole target on the G^0 target ladder with the beam at the nominal halo conditions as measured with the 6 mm halo target by the halo monitoring system. This set up reflects a conservative estimate of the halo effects, as the beam halo was generally within the nominal specifications for the 6 mm halo target, and the 5 mm hole would certainly yield higher halo rates in the detectors than the specifications at 6 mm or the aperture of the helium cell (at 11 mm diameter). The rates from solely the beam halo in the G^0 detectors using the 5 mm hole target were then measured, and compared to the rates using the LH_2 target in normal running conditions. This gave a fractional contribution of the halo to the usual detector rates of ~ 0.0002, which is clearly an upper bound. Assuming the halo asymmetry to be the upper measured value of -40 ppm, the upper limit of the halo asymmetry contribution to the measured elastic asymmetry is only 0.008 ppm, which is negligible for this measurement. In addition, no correlation was observed between the halo monitor signals and the yield in the primary G^0 detectors during usual running.

5.3.3 Corrections for Leakage Beam

The G^0 beam is structured so that the beam bunches are separated by 32 ns to allow the ToF measurements to be done; however, Halls A and B were not running with this structure, but with the standard CEBAF beam structure with 2 ns between beam bunches. The accelerator delivers beam to all three halls simultaneously by alternating the beam pulses to the halls at 499 MHz ($3 \times 499 = 1497$ MHz fundamental frequency). Each hall has its own laser to generate its beam; each laser turns off after a beam pulse to prevent it from interfering with the lasers for the other halls. However, in reality the laser takes a finite amount of time to turn off, so some of the light from a laser leaks into the pulses for the other halls, causing "leakage" beam with the time structure of that laser. In addition, the lasers all have a DC component caused by amplified spontaneous emission (ASE). This component does not modulate at 31 or 499 MHz, and creates a DC component for all three halls.

Even though this is a problem that is common to all three halls, it is of particular concern for the G^0 experiment because of the unique beam structure needed for the ToF technique. As the pulse frequency for G^0 at 31 MHz is 1/16 of the usual 499 MHz, there should be no beam at all for 15 of the 16 beam bunches. Leakage beam current at 499 MHz and the DC component violated this and shows up as a global background underneath the 32 ns ToF spectra. During the experiment, the leakage contamination of 499 MHz beam from Halls A and B was found to be about 50 nA (compared to the nominal 40 μA Hall C beam). Although very small in current and only about 0.1% of the total rate, the charge asymmetry of this leakage current turned out to be quite large, about +600 ppm, and even more troublesome, not constant in time. The beam charge monitors in Hall C were set up to measure the integrated beam charge every 1/30 s (i.e., at 30 Hz), which made them only sensitive to the combined average current of the G^0 and the leakage beam. The beam feedback system would attempt to minimize the large charge asymmetry from the leakage beam, but as the system could only affect the G^0 beam, not beam from other halls, it inadvertantly caused a large charge asymmetry in the G^0 beam to counterbalance the one from the

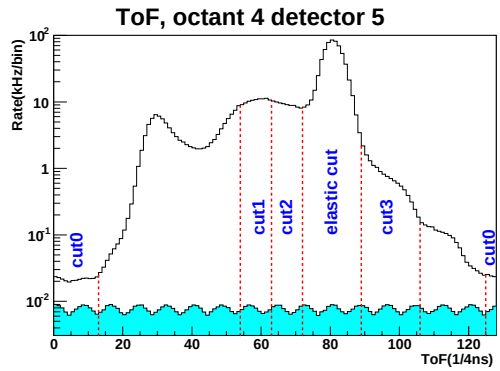

FIG. 5.7: *A G^0 spectrum showing the cuts and the leakage beam spectrum. Figure from [254].*

leakage beam [194]. This resulted in a significant ToF dependent false asymmetry, which clearly had to be corrected for.

To correct for this leakage effect, the rate and the asymmetries from areas of the ToF spectrum forbidden to physics events from the target were used. These regions, designated as "cut0", occurred very early and very late in the ToF spectrum, as can be seen in Figure 5.7.

To determine the beam leakage contribution to the measured asymmetry, the leakage current and the charge asymmetry must both be taken into account. The measured yield is a combination of both the G^0 beam and the leakage current

$$Y_{meas}(t) = \frac{R_m(t)}{I_m} = \frac{Y_{G^0}(t)I_{G^0} + Y_L(t)I_L}{I_{G^0} + I_L}, \tag{5.22}$$

where $R_m(t)$ is the rate, $Y_{G^0}(t)$ and $Y_L(t)$ are the yields from the primary beam and the leakage beam, and I_{G^0} and I_L are the currents of the respective beams [224,254]. The measured asymmetry can be written in terms of the G^0 beam and the leakage beam:

$$\begin{aligned} A_{meas}(t) &= \frac{R_{G^0}(t)}{R_{meas}(t)} A_{Y_{G^0}}(t) + \frac{R_L(t)}{R_{meas}(t)} A_{Y_L}(t) \\ &\quad + \left(\frac{R_{G^0}(t)}{R_{meas}(t)} - \frac{I_{G^0}}{I_{meas}} \right) A_{I_{G^0}} + \left(\frac{R_L(t)}{R_{meas}(t)} - \frac{I_L}{I_{meas}} \right) A_{I_L}, \end{aligned} \tag{5.23}$$

where $R_{G^0}(t)$ and $R_L(t)$ are the rates from the G^0 and leakage beams, $A_{Y_{G^0}}(t)$ and $A_{Y_L}(t)$ are the asymmetries from these beams (in the detectors), and $A_{I_{G^0}}$ and A_{I_L} are the charge asymmetries from these beams. The charge asymmetry measured by the BCMs is a weighted average of $A_{I_{G^0}}$

and A_{I_L},

$$A_{I_{meas}} = \frac{I_{G^0}}{I_{meas}} A_{I_L} + \frac{I_L}{I_{meas}} A_{I_L}, \tag{5.24}$$

so the measured asymmetry may be written as

$$\begin{aligned} A_{meas}(t) &= \frac{R_{G^0}(t)}{R_{meas}(t)} A_{Y_{G^0}}(t) + \frac{R_L(t)}{R_{meas}(t)} A_{Y_L}(t) \\ &\quad + \left(\frac{R_{G^0}(t)}{R_{meas}(t)} \frac{I_{meas}}{I_{G^0}} - 1 \right) A_{I_{G^0}} - \frac{\frac{I_L}{I_{G^0}} - \frac{R_L(t)}{R_{G^0}(t)}}{1 + \frac{R_L(t)}{R_{G^0}(t)}} A_{I_L}. \end{aligned} \tag{5.25}$$

As the leakage current (and thus the detector rate) is orders of magnitude smaller than the contribution from the main beam, it is valid to approximate $R_{G^0} \approx R_{meas}$, $R_L \ll R_{G^0}$, and $R_L \ll R_{meas}$. With these approximations, $\frac{R_{G^0}}{R_{meas}} \frac{I_{meas}}{I_{G^0}} - 1 \approx 0$, and $\frac{R_L}{R_{meas}} \approx 0$, so our equation simplifies to

$$A_{meas}(t) \approx A_{Y_{G^0}}(t) - \frac{I_L}{I_{G^0}} \left(1 - \frac{Y_L(t)}{Y_{G^0}(t)} \right) A_{I_L} = A_{Y_{G^0}}(t) - \left(\frac{I_L}{I_{G^0}} - \frac{R_L}{R_{G^0}} \right) A_{I_L}. \tag{5.26}$$

The false asymmetry contribution caused by the charge asymmetry of the leakage beam can then be written in terms of the leakage (I_L) and G^0 (I_{G^0}) beam currents:

$$A_{false}(t) = A_m(t) - A_{Y_{G^0}}(t) \simeq -\frac{I_L}{I_{G^0}} \left(1 - \frac{Y_L(t)}{Y_{G^0}(t)} \right) A_{I_L}. \tag{5.27}$$

The leakage currents and asymmetries from the A and B lasers were directly measured by turning off the G^0 laser and leaving the Hall C slit open, making the leakage beam the only beam in Hall C. The current was then computed from the rates in the FPDs, and the luminosity monitors were used to measure the charge asymmetry (as the statistical precision was higher due to the higher rates). To measure the leakage beam due to the G^0 laser itself (from ASE)), the G^0 beam was diverted to the A or B slit, and the leakage beam in Hall C was studied as before. These studies were used to characterize the leakage beam and its properties. However, these dedicated runs are not enough to determine the contribution of the leakage beam over the entire period of the measurement, due to the unstable nature of the leakage beam.

To have a run-by-run measurement of the leakage beam contributions, the leakage beam asymmetry was measured in areas of the ToF spectra that do not contain any physics events from the primary beam, and thus are predominantly from the leakage beam. These areas are defined

by cuts and designated as cut0. Figure 5.7 displays a ToF spectrum taken at the nominal 40 μA and showing the locations of several of the typical cuts for the experiment, including the cuts for the proton peak, three cuts to study inelastic background events, and the location of the cut0 regions (note the log scale). Two values are extracted from the information in cut0: the current of the leakage beam and its associated asymmetry (monitored on a run-by-run basis). The rate measured in cut0 is a combination of the leakage and G^0 background components, $R_{meas,cut0} = R_{l,cut0} + R_{G^0,bkg}$, where $R_{meas,cut0}$ and $R_{l,cut0}$ are the measured and leakage rates in cut0 and $R_{G^0,bkg}$ is the background rate from the main G^0 beam. These contributions can be measured by turning off the G^0 laser and observing the rates coming from the Halls A and B lasers; the DC component was determined as described above. From these measurements, the total G^0 background rate of 3.5 ± 0.17 kHz at 40 μA was determined.

With the determination of $R_{G^0,bkg}$, the leakage rate can be determined on a run-by-run basis from cut0. The leakage current is then described by

$$I_{L,deduced} = \frac{\frac{R_{L,cut0}}{w_{cut0}}}{Y_{G^0}} = \frac{\frac{R_{meas,cut0}-3.5kHz}{w_{cut0}}}{Y_{G^0}}, \tag{5.28}$$

where w_{cut0} is the total width of cut0 and Y_{G^0} is the ToF-averaged G^0 yield. The charge asymmetry in cut0 due to the leakage beam is then

$$A_{I_L} = \frac{R_{meas,cut0}}{R_{L,cut0}} A_{cut0} = \frac{R_{meas,cut0}}{R_{meas,cut0} - 3.5kHz} A_{cut0}, \tag{5.29}$$

where A_{cut0} is the measured cut0 asymmetry and A_{I_L} is the leakage charge asymmetry. On average, $I_L \sim 50$ nA and $A_{I_L} \sim +570$ ppm, with a statistical uncertainty of $\sim 5\%$ of A_{I_L} (after correcting for the beam polarization and the blinding factor) for the production period [224, 254].

The leakage correction is additive,

$$\begin{aligned} A_{Y_{G^0}}(t) &= A_m(t) + \Delta \\ \Delta &\equiv -A_{false} \simeq \frac{I_L}{I_{G^0}} \left(1 - \frac{Y_L(t)}{Y_{G^0}(t)}\right) A_{I_L}, \end{aligned} \tag{5.30}$$

where Δ is the correction. The correction was done on a run-by-run basis, using the values computed from the cut0 measurements from that run. Clearly, the size of the correction varies

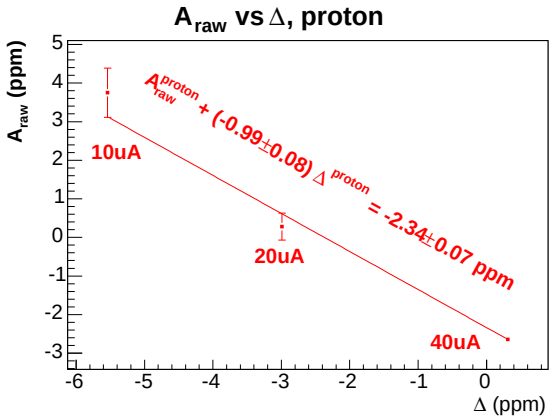

FIG. 5.8: *Raw Asymmetries versus the leakage correction. (Proton cut, A_{raw} versus Δ) Figure from [254].*

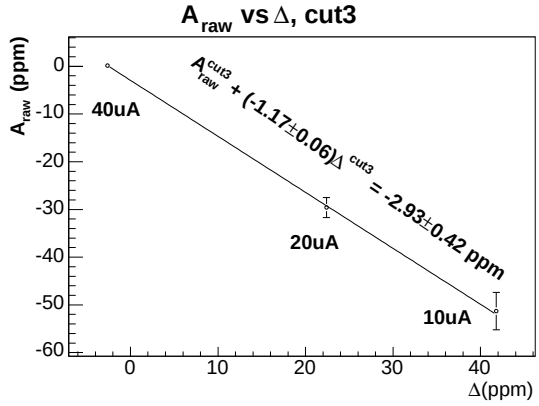

FIG. 5.9: *Raw Asymmetries versus the leakage correction. (Cut3, A_{raw} versus Δ) Figure from [254].*

with the beam current, with the smallest correction being at the largest beam current. However, if the corrections are ideal, the corrected asymmetries at all beam currents should converge to a constant physics asymmetry. In this ideal case, a plot of the raw asymmetry versus the correction at various beam currents should show the data following a straight line of slope -1 (a perfect correlation). A more positive slope would indicate over-correction; a more negative one, under-correction. Figures 5.8 and 5.9 show these plots for the proton cut and cut3, respectively. A linear fit to the proton cut data agrees very well with -1, and the linear fit to the cut3 data agree to within 20%, although with a suggestion of undercorrecting for the effect.

The systematic uncertainty of the correction was determined in several methods. A comparison of the calculated I_L and A_{I_L} from cut0 and those directly measured in the beam leakage tests shows an agreement of 22%, which is an estimate of the fractional uncertainty of the correction. The second evaluation method makes use of the fact that cut3 is the most sensitive to the leakage, other than cut0. After the correction, the statistical properties of the asymmetry data for cut3 were significantly improved, but the reduced χ^2 after the correction was still about 2, which indicates that there is a residual systematic fluctuation in the data samples roughly the same size as the statistical uncertainty of $\sim$ 0.6 ppm (in one half-wave plate state). By assuming

a systematic error of 0.6 ppm, we have a corresponding fractional error of 23%. In the third approach, the leakage correction technique was applied to data taken at different beam currents (10, 20, and 40 μA). As the leakage contribution is fractionally smaller at 40 μA than at lower beam currents, the correction is also the smallest at the nominal current. The assumption is made that at 40 μA the corrected asymmetry approaches the physics asymmetry. For the lower beam currents, the correction is calculated that is needed to bring the measured asymmetry to the physics asymmetry. The difference between this quantity and the calculated correction gives an evaluation of the systematic uncertainty of the correction, about 17%. The calculations agree to within 20% in all cases, so an uncertainty of 20% was assigned to the false asymmetries for the leakage corrections.

The final correction to the elastic asymmetries for all the Q^2 bins was 0.71 ± 0.14 ppm, corrected for the beam polarization and the blinding factor [224, 254]. The correction and the systematic uncertainty are global (for all rings). The leakage beam also had the undesirable property of large position differences amounting to hundreds of nm, but even with the assumption of position differences of 1 μm from the leakage beam, the false asymmetry is about 1 ppb, which can be safely ignored [254].

For more information on the beam leakage corrections for the G^0 experiment than is included in this summary, see the dedicated analysis in Refs. [224, 254].

5.3.4 Transverse Systematic Uncertainty

Even with the Wien filter calibrations (see Section 4.3.3.2.1), the beam may not be perfectly longitudinally polarized. The predicted size of the transverse asymmetry for the forward-angle kinematics is not enormous, ~ 5 ppm (see Section 2.8.3), but as it is on the order of the parity-violating asymmetry, it is an issue that must be addressed. This is a possible source of systematic error for the experiment, as a false asymmetry can be introduced from the parity-conserving asymmetry that arises from the interference of the single- and two-photon exchange amplitudes in the scattering of transversely polarized electrons from nucleons [255, 256]. More about this

particular bit of physics is discussed in Sections 2.7 and 5.4.

The transverse asymmetry contribution to the measured asymmetry in a parity-violation experiment can be expressed by

$$A_{meas}(\theta,\phi) = P_b \cos(\theta_{spin}) A_{PV}(\theta) + P_b \sin(\theta_{spin}) \sin(\phi - \phi_{spin}) A_n(\theta), \tag{5.31}$$

where P is the polarization of the beam, A_{PV} is the parity-violating asymmetry, $A_n(\theta)$ is the transverse asymmetry, and θ_{spin} and ϕ_{spin} are the polar and azimuthal polarization angles [257]. The value of $\theta_{spin} = 3°$ is the conservative estimate of the accuracy of the Wien filter calibration to deliver longitudinal beam. For the G^0 experiment, ϕ_{spin} does not need to be known because of the azimuthal symmetry of the G^0 spectrometer. Therefore, to estimate the effects of residual transverse polarization in the beam, measurements of $A_n(\theta)$ must be done.

In order to minimize the effect of the transverse spin asymmetry on the parity-violating asymmetry, the polarization was set to be longitudinal, verified by a spin-dance, for the G^0 measurements (Section 4.3.3.2.1). To put a constraint on the possible contribution of the transverse spin asymmetry due to any residual transversely polarized beam, measurements of $A_\perp$ were conducted with a transversely polarized beam as well. About 30 hours of data were taken with a transversely polarized beam. The asymmetry data were blinded in the same method as the longitudinal forward-angle data. The proton asymmetries measured in each octant were summed over detectors 1–4, 5–8, 9–12, and 13–14, and then plotted versus octant. The amplitude of the resulting sinusoidal dependence in ϕ was then determined via a fit of the form

$$A_\perp^{meas}(\theta) = A_n(\theta) \sin(\phi + \phi_0). \tag{5.32}$$

The average amplitude over all the detectors was $A_n \simeq 2$ ppm (blinded). For more details of this analysis technique, see Section 5.4.

Assuming the maximum 3° mis-alignment of the Wien filter, the false asymmetry coming from a residual transverse component of the beam is

$$A_{trans}^{false}(\theta,\phi) = P_z \sin(3°) \sin(\phi - \phi_{spin}) A_n(\theta), \tag{5.33}$$

where $P_z \simeq 0.74$, and $A_n(\theta) \simeq 2$ ppm was determined from the transverse asymmetry data. Unblinded, this yields an amplitude of $A_{trans}^{false}(\theta) = 0.096$ ppm, which oscillates sinusoidally in ϕ. This is a conservative estimate based on the maximum mis-alignment of the Wien; assuming a 1° misalignment yields a value of 0.032 ppm (unblinded). The azimuthal symmetry of the detectors greatly suppresses any contribution when the results from each detector in a ring are averaged together, much like the corrections for beam position fluctuations. Taking the symmetry of the spectrometer into account, the estimate for the false asymmetry contribution from residual transverse polarization is of order 0.01 ppm.

The vertical polarization component is suppressed by the transport through the accelerator. Furthermore, the vertically transverse component bounds were estimated to be $\leq P_z \sin(11^\circ)$ using the transverse asymmetry data, where P_z is the longitudinal polarization. In addition, dedicated studies were performed for HAPPEX, and the vertical transverse component was found to be very small [258].

5.3.5 Physics Backgrounds

A cursory inspection reveals that the peak associated with the inelastic protons extends underneath the proton elastic peak that the experiment is interested in. These are largely inelastically scattered protons from the hydrogen target, and quasielastic and inelastic protons from the aluminum entrance and exit windows of the target cell. Clearly, this background must be corrected for, both for its dilution of the elastic yield and for any false asymmetry that it introduces to the elastic physics asymmetry. Studies were conducted to understand the source of these background events and gain insight about its behavior. The elastic asymmetries were then corrected using the measured background yields and asymmetries in the ToF spectra. A summary is presented here; for extensive details, see the dedicated analysis in Refs. [224, 259]

5.3.5.1 Background Decomposition

The background is mostly made up of inelastic protons that come from the target (the aluminum windows and the helium in the upstream cell) and from processes in the hydrogen itself.

As it is important to understand both separately, several methods were used. After determining the sources of the background yields, the background asymmetries arising from them were studied.

Both empirical methods and simulations were used to study the background yields. Unfortunately, the inelastic contribution from the target windows cannot be determined solely from empty target measurements because the "empty" target has gaseous hydrogen (GH_2) in it and because the contribution from the aluminum windows is enhanced by additional photon radiation in the LH_2 in the full target. Therefore, a combination of measurements was used to determine the inelastic contributions of the target windows and the helium cell. In addition to the measurements taken with target full of LH_2 and "empty" (filled with GH_2), the tungsten (W) radiator and aluminum dummy targets were used. The tungsten radiator was used to enhance the photon flux, and was used with the aluminum flyswatter target to study the effect of the additional photon radiation in the full LH_2 target on the background yields (see Section 4.4.1.2). The aluminum dummy targets were used to investigate the yield and asymmetry contributions from aluminum, as can be seen in Figure 5.10. Another method used to empirically determine the contribution of the three target windows was the comparison of empty target measurements taken at different temperatures (and thus, different gas densities). The difference between the measurements gives the combined contribution from the gaseous H_2 and the gaseous helium in the upstream windows, allowing the calculation of the contributions from the target windows [260].

Simulations were also used to study the composition of the yields. The G0GEANT simulation [251] implements G^0's spectrometer geometry and field map and the target design into the GEANT simulation program. The inelastic proton yields from the aluminum, hydrogen, and helium gas in the upstream cell come from photo- and electro-production processes. To simulate the inelastic protons and pions from the hydrogen, three different models of inelastic generators were used [261]. The first is a model by Lightbody and O'Connell [262], which is used to calculate the photoproduction cross-section from the aluminum windows and the helium. The inelastic protons and pions coming from the hydrogen are simulated using MAID (the 2003 version) [155], Δ-resonance in

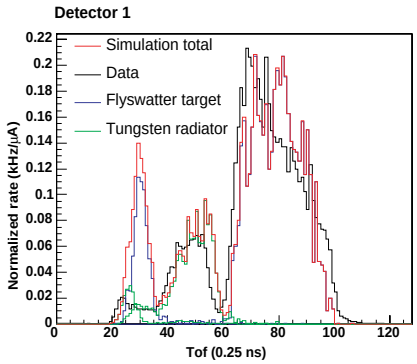

FIG. 5.10: *The measured yield from the flyswatter and tungsten radiator, compared to simulations of the individual and total contributions from each. Figure from [250]*

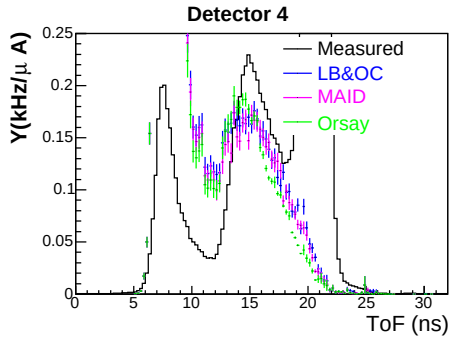

FIG. 5.11: *Background yield simulations compared to the hydrogen data (in black) for Detector 4. The simulations are Lightbody and O'Connell (blue), MAID (pink) and the Orsay Generator (green). Figure from [224]*

the Lightbody and O'Connell model [262], and a generator that was developed at Orsay [263, 264]. MAID, a unitary isobar model for pion photo- and electroproduction on the nucleon (developed at Mainz), can be used for photon energies below 1 GeV. This corresponds to a maximum invariant mass of ~ 1.7 GeV; however, the acceptance favors inelastic protons with $W > 2$ GeV, especially in the higher-numbered detectors, making any predictions by MAID in the region unreliable. The Orsay model was based on a photo-production generator for the GRAAL experiment, and models the pion photo-production up to 4 GeV.

An example can be seen in Figure 5.11. The three models are in good agreement for the lower-numbered detectors; above Detector 6, the Lightbody and O'Connell and MAID generators over-predict the yield in the inelastic region. All three models underpredict the yield in the cut3 (superelastic ToF) region. However, the models suggest a smooth falling off of the background yield under the elastic peak.

The studies, both by empirical measurements and Monte Carlo simulations, led to a reasonable understanding of the background yields from the target windows and the helium. However, neither set of studies clearly showed how to separate the elastic and inelastic yields from the hydrogen.

The dilution of the elastic yields by the inelastic yields is not the only concern; the inelastic

background events were also shown to have a significant asymmetry that extended underneath the elastic peak. This can be seen in Figure 5.12. The background asymmetries are negative in the ToF regions associated with the pions. A positive asymmetry peak is apparent in the inelastic region of the ToF, located after the pion peak in the lowest-numbered detectors and that moves to longer times-of-flight with increasing detector number, until it is beneath the elastic peak in the highest-numbered detectors (12–15). However, the evolution of the background asymmetry in the inelastic regions is smooth in a given detector, allowing the evaluation of the background asymmetry contribution underneath the elastic peak using fits. Furthermore, the progressive change of the background asymmetry with increasing detector number indicates that the underlying physics varies smoothly. This positive background asymmetry is not significant for the lower-numbered detectors, as it does not affect the elastic peak for these detectors, but it is very significant in the higher-numbered detectors 12 and above, where it does overlap with the elastic peak.

Studies were then undertaken to understand the source of the positive asymmetry background. Inelastic protons from the aluminum target cell and windows were at first suspected to be the source of this asymmetry; however, the measured asymmetries from the "empty" (gaseous hydrogen) target and aluminum dummy target data sets are negative in the inelastic cut. The background asymmetry did not show a sinusoidal azimuthal dependence, and the measured asymmetry in the inelastic cut in the transverse data set also failed to show a large positive asymmetry, ruling out the possibility that the source was from single-spin asymmetries from a residual transverse component of the beam. The measured asymmetries from both the NA and French data sets agree overall, although there is some variation from octant to octant, and the asymmetries exhibit the expected sign change with insertable half-wave plate reversal, which indicates the asymmetries are not due to some electronic artifact. This all indicates that the background asymmetry arises from a parity-violating process in the LH_2 itself.

The positive background asymmetries in the inelastic regions of the ToF spectra (and the variation seen in the background from octant-to-octant) can be explained by the production of

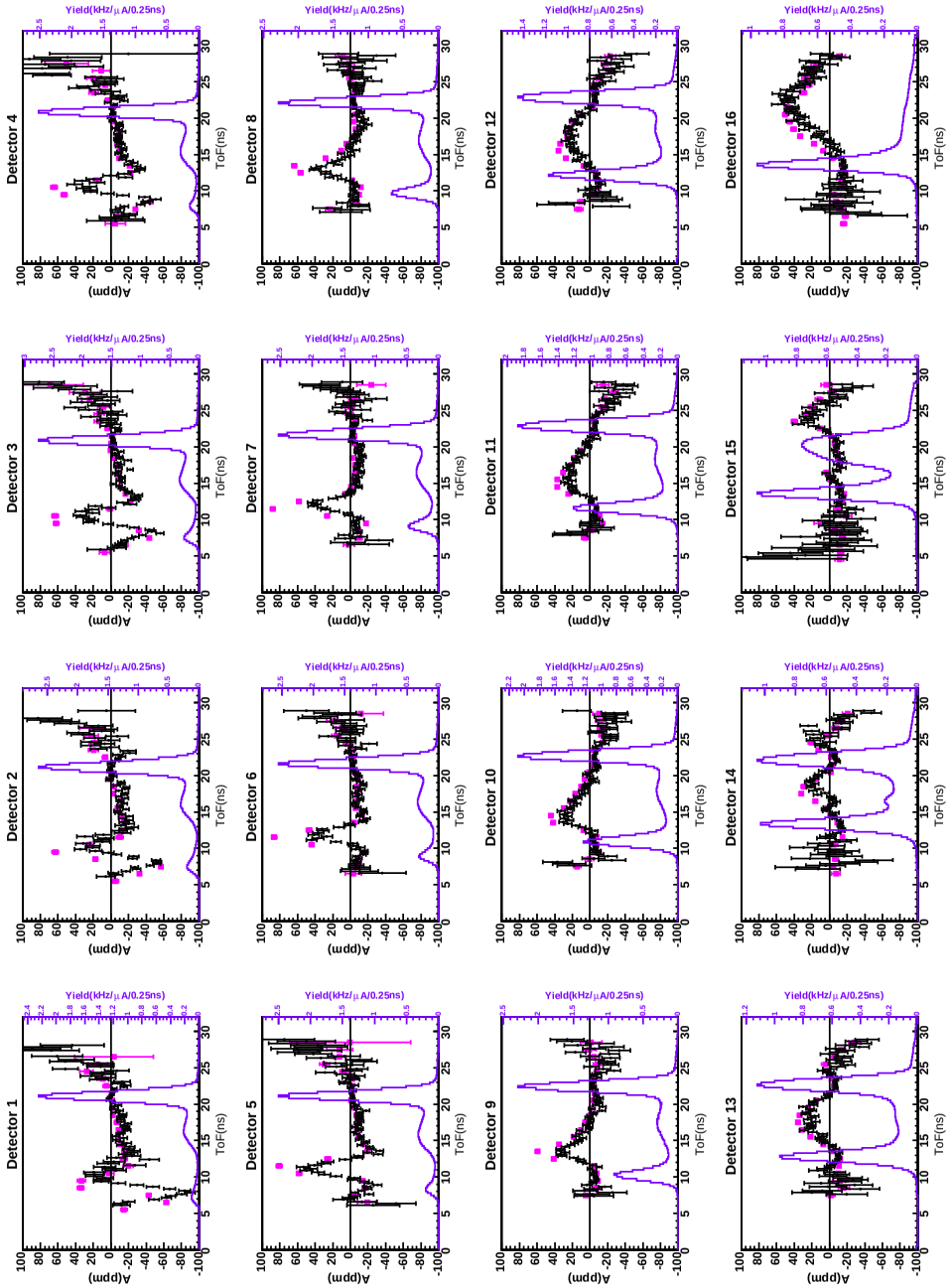

FIG. 5.12: *Average asymmetry versus time-of-flight for the NA (pink) and French (black) datasets, displayed by detector to show the evolution of the background asymmetries across TOF. The yield histogram from the French data is overlaid. Figure from [224].*

hyperons (Λ, Σ^+, and Σ^0) in the hydrogen and their subsequent decay. Hyperons are baryons containing strange quarks, and can be produced in electron-proton scattering by photo- or electro-production, where a large fraction of the incident beam polarization is transferred to them [265]. For the forward-angle phase of the G^0 experiment, the dominant hyperon channels are [266]

$$\begin{aligned} \gamma^* + p &\rightarrow \Lambda + K^+, \\ \gamma^* + p &\rightarrow \Sigma^+ + K^0, \\ \gamma^* + p &\rightarrow \Sigma^0 + K^+, \end{aligned} \tag{5.34}$$

where the γ^* can be either a real or a virtual photon. The Λ and Σ^+ hyperons decay through a weak interaction process into protons and neutrons and pions; the Σ^0 decays into a Λ, which then also decays. These decay particles carry a large parity-violating asymmetry, and thus could be a significant source of background for the experiment if these particles are seen by the detectors.

A detailed Monte Carlo study was done to understand the contribution from the weak decay of hyperons produced in the hydrogen [224, 266]. To simulate the hyperon production yields, the KAON-MAID model [267], an effective Lagrangian model for Kaon photo- and electro-production on the nucleon, is implemented into the G0GEANT simulation to calculate the differential cross-section of the photo-production of hyperons. The calculations from KAON-MAID agree fairly well with data from SAPHIR [268, 269], as can be seen in Figure 5.13.

The G0GEANT simulation of the detector rate is done by combining the differential cross section with the detector acceptance. The simulation of the hyperon asymmetry is done by considering the electron plane, which contains the incident and scattered electron, the hyperon production plane, which contains the virtual photon and the hyperon, and the hyperon decay plane, which contains the nucleon and pion decay particles. The simulation estimates that about 100% of the polarization of the photon gets transferred to the Λ [265]. The transferred polarizations for the Σ^0 and Σ^+ have not yet been measured, so it was assumed that the Σ^+ shares roughly the same polarization as the Λ and that the Σ^0 shares roughly the same polarization as the Λ with an

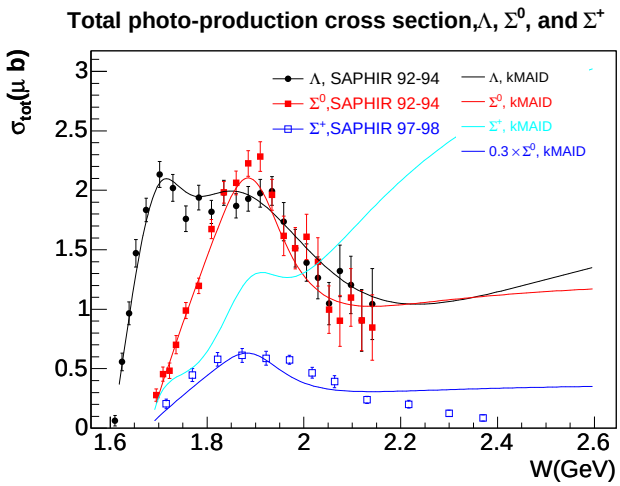

FIG. 5.13: *A comparison of the measured total photo-absorption cross section σ_{total} from SAPHIR [268, 269] with KAON-MAID [267] calculations as a function of invariant mass W. Figure from [266].*

opposite sign, which fit the data rather well. The asymmetry can then be written as

$$A = \alpha P_b P'_z \cos\left(\theta^{RF}_{\hat{z},\vec{k}_N}\right), \tag{5.35}$$

where α characterizes the parity-violating nature of the decay, P_b is the beam polarization, P'_z is the polarization transferred, and $\theta^{RF}_{\hat{z},\vec{k}_N}$ is the angle between the decay-nucleon and the direction of the photon ($\hat{z}$ in the reference frame of the hyperon).

Rescattering from the lower primary collimator allows the particles from the decays to be detected by the higher-numbered detectors. The simulated hyperon rate for the G^0 kinematics is very low, four orders of magnitudes smaller than the total rate in each detector; however, as a small fraction of the particles make it to the detectors through rescattering, and these particles have a large asymmetry, they cause a large background asymmetry. An example of the simulated hyperon contribution from each of the three production channels to the background asymmetry for Detector 14 is shown in Figure 5.14, where the solid black circles denote the contribution from Λ, the solid red squares Σ^+, and the open blue circles Σ^0. The dashed histogram is the measured yield spectrum. The total background asymmetry coming from hyperon production simulation, which is obtained by summing the three production channels, is shown in Figure 5.15 compared to

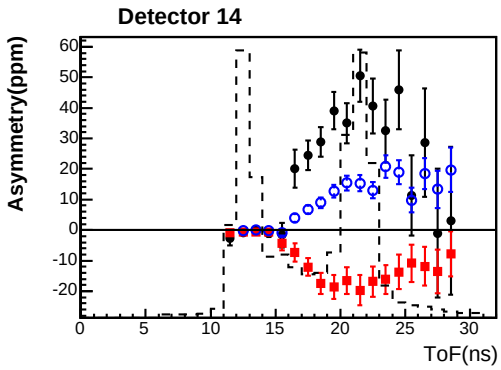

FIG. 5.14: *The hyperon contribution to the background asymmetry for Detector 14. The solid black circles denote the contribution from* Λ*, the solid red squares* Σ^+*, and the open blue circles* Σ^0*. The dashed histogram is the measured yield spectrum. Figure from [266].*

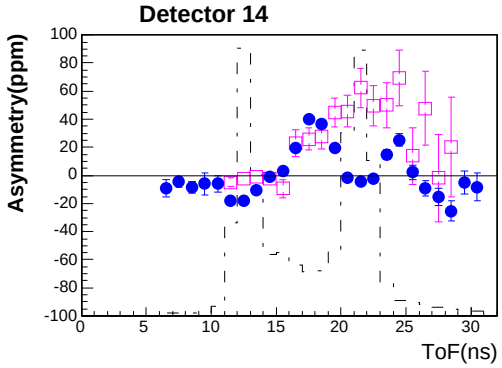

FIG. 5.15: *The total background asymmetry coming from hyperon production from summing the three production channels from the simulation (open pink squares) compared to the measured asymmetry in detector 14 (solid blue circles). The dashed histogram is the measured yield spectrum. Figure from [266].*

the measured asymmetry in Detector 14. These asymmetry spectra clearly show the large positive contribution of the hyperon asymmetry in the region of the elastic asymmetry, ~ 50 ppm, a clear background to the small negative elastic asymmetry.

This study does reproduce the measured positive background asymmetry in the G^0 data. However, due to the limited accuracy of the simulation because of the lack of knowledge of the transferred polarization of the Σ^+ and Σ^0 and the cross sections of these hyperon productions with high invariant mass, these results were only used to understand the origin of the positive background asymmetry and were not used to correct the measured data. The data were corrected for the background by fitting/interpolating the measured data themselves.

5.3.5.2 Background Correction

The studies of the background yield and asymmetries were done to gain an understanding of the source and behavior of the background that extends underneath the elastic peak. However, the background correction itself was made only using the data measured in the experiment.

In any timebin t, the measured yield $Y_m(t)$ consists of both the elastic yield of interest, $Y_{elas}(t)$,

and the yield of the background, $Y_{bkg}(t)$:

$$Y_m(t) = Y_{elas}(t) + Y_{bkg}(t). \tag{5.36}$$

The measured asymmetry, $A_m(t)$, can be expressed in terms of the elastic asymmetry, $A_{elas}(t)$, and the background asymmetry, $A_{bkg}(t)$, as

$$A_m(t) = \big(1 - f_b(t)\big)A_{elas}(t) + f_b(t)A_{bkg}(t), \tag{5.37}$$

where $f_b(t) = \dfrac{Y_{bkg}(t)}{Y_m(t)}$ is the background fraction (or dilution factor) of the background yield in the measured yield. The goal of the background correction is to determine $Y_{bkg}(t)$ and $A_{bkg}(t)$, and then use Eq. 5.37 to determine the elastic asymmetry.

5.3.5.2.1 Detectors 1 through 14

In Detectors 1 – 14, the correction for the background was done using a two-step elastic sideband fitting procedure. In this procedure, the elastic peak is fitted with a Gaussian, with the background modeled with a polynomial function. With this information, the background fraction $f_b(t)$ is determined. This background fraction is then used to do the fit to the measured asymmetry. In this step, the measured asymmetry is fitted assuming a constant asymmetry over t and a polynomial background asymmetry, which gives a simultaneous determination of the elastic and background asymmetry. Examples of these fits are shown in Figures 5.16 and 5.17, where the yield fit is on the left and the asymmetry fit is on the right.

Because of the high rate in the detectors, the uncertainty of the yield in each timebin is dominated by systematics. The uncertainty is estimated by the variation in the yields over time and in the different octants. This gives an uncertainty of 2% (fractional) for the bins inside of the elastic peak, which is scaled in a statistical manner for timebins away from the elastic peak.

The yield is then fitted with the Gaussian for the elastic peak and the background function (usually a quadratic), as can be seen in the example in Figure 5.16. The yields are fitted for several nanoseconds on either side of the elastic peak in order to obtain a good characterization

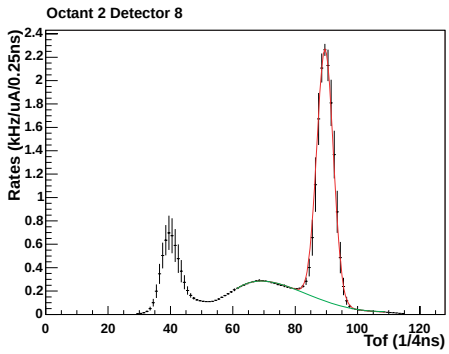

FIG. 5.16: *The yield fit for Octant 2, Detector 8, showing the combined fit (red) of a Gaussian for the elastic peak and the fourth-order polynomial fit to the background, which is shown individually in green. Figure from [250].*

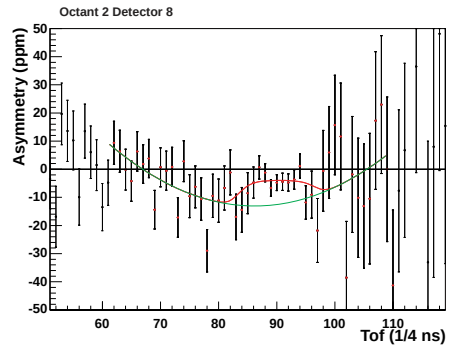

FIG. 5.17: *The asymmetry fit for Octant 2, Detector 8, showing the quadratic fit to the background asymmetry (green) and the combined fit of the constant elastic asymmetry and the quadratic background (red). Figure from [250].*

of the background shape. The background fraction $f_b(t)$ under the elastic peak is then calculated by taking the extracted value of the background yield $Y_{bkg}(t)$ from the fit and dividing it by the measured yield $Y_m(t)$. Once $f_b(t)$ is determined, the measured asymmetry can be fitted to extract $A_{elas}(t)$ and $A_{bkg}(t)$ simultaneously using Eq. 5.37. An example fit is shown in Figure 5.17. In the asymmetry fit, the elastic asymmetry is assumed to be a constant, and the form of the background is chosen based on the behavior of the background asymmetry, usually a quadratic.

The functional forms used for the background yield are chosen as the lowest-order polynomial that gives a reasonable χ^2. The asymmetry fits were less sensitive to the functional form chosen for the background asymmetry; these fits were performed with various polynomials as the background and the extracted elastic asymmetries for each were compared. The result in the center of the spread was chosen as the best fit. The background was treated as being different for the different octants, but as the elastic asymmetry should be the same in all eight octants for a given detectors, this assumption was used as a constraint. However, relaxing this constraint and allowing the elastic asymmetry to differ from octant to octant had little effect.

The value of the extracted asymmetries are shown with the final asymmetries in Table 5.8. The results obtained by this method are in good agreement with those found in an independent

analysis method using a simultaneous fit to both the yield and the asymmetry spectra [270].

The uncertainty in the elastic asymmetry can be written as [224, 259]

$$\sigma^2(A_{elas}) = \sigma^2(A_1) + \sigma^2(A_2) + \sigma^2(A_3) + \Delta, \tag{5.38}$$

$$\sigma(A_1) = \frac{\sigma(A_{meas})}{1 - f_b}, \tag{5.39}$$

$$\sigma(A_2) = \frac{|A_{meas} - A_{bkg}|}{(1 - f_b)^2}\,\sigma(f_b), \tag{5.40}$$

$$\sigma(A_3) = \frac{f_b}{1 - f_b}\,\sigma(A_{bkg}), \tag{5.41}$$

$$\begin{aligned}\Delta &= 2\,\frac{\partial A_{elas}}{\partial f_b}\frac{\partial A_{elas}}{\partial A_{bkg}}\,\mathrm{cov}(f_b, A_{bkg}) \\ &= -2\,\frac{f_b(A_{meas} - A_{bkg})}{(1 - f_b)^3}\,\mathrm{cov}(f_b, A_{bkg}),\end{aligned} \tag{5.42}$$

where f_b, A_{meas}, and A_{bkg} are the averages of $f_b(t)$, $A_m(t)$, and $A_{bkg}(t)$ over the elastic proton cut; and $\sigma(A_{meas})$, $\sigma(f_b)$, and $\sigma(A_{bkg})$ are the uncertainties on the measured asymmetry, the background fraction, and the background asymmetry. The correlation term Δ [271] takes into account that the uncertainties in values of f_b and A_{bkg} are not independent, as a change in the determination of f_b will lead to a correlated change in the value of A_{bkg}. The term $\mathrm{cov}(f_b, A_{bkg})$ is the covariance between f_b and A_{bkg}. This is evaluated using a Monte Carlo simulation.

$\sigma(A_1)$ is a purely statistical uncertainty resulting from the measured uncertainty in A_{meas}; $\sigma(f_b)$ is a purely systematic error because the uncertainty in $\sigma(f_b)$ is dominated by the systematic (model) uncertainty. However, the background uncertainty $\sigma(A_{bkg})$ contains both statistical and systematic components. Thus, $\sigma^2(A_3) = \sigma^2_{stat}(A_3) + \sigma^2_{syst}(A_3)$, where σ^2_{stat} is the statistical piece that arises from the counting precision of the background events beneath the elastic peak as $\sigma_{stat}(A_3) = \frac{f_b}{1-f_b}\sigma_{stat}(A_{bkg}) = \frac{f_b}{1-f_b}\frac{1}{\sqrt{f_b}}\sigma(A_{meas})$, and $\sigma_{syst}(A_3)$ is the systematic piece that comes from the choice of the model for the background asymmetry. Δ is a systematic uncertainty. Using this, $\sigma(A_{elas})$ can then be expressed in terms of the statistical and systematic components

as [224, 259]

$$\sigma^2(A_{elas}) = \sigma^2_{stat}(A_{elas}) + \sigma^2_{syst}(A_{elas}), \tag{5.43}$$

$$\sigma_{stat}(A_{elas}) = \frac{\sqrt{1+f_b}}{1-f_b}\sigma(A_{meas}), \tag{5.44}$$

$$\sigma_{syst}(A_{elas}) = \sqrt{\sigma^2(A_2) + \sigma^2_{syst}(A_3) + \Delta}. \tag{5.45}$$

The statistical uncertainty $\sigma_{stat}(A_{elas})$ is evaluated in this manner because the error given by the asymmetry fit depends on the precision of the asymmetry in the side bands of the fit as well as on the measured asymmetry in the elastic peak itself.

The estimates of $\sigma(A_2)$ and Δ were determined using a Monte Carlo simulation. The background yield $Y_{bkg}(t)$ was varied, which resulted in varying values of $f_b(t)$. The measured asymmetry was then fitted with Eq. 5.37 using the values of $f_b(t)$ and assuming a quadratic background asymmetry $A_{bkg}(t)$. Then the variance in the extracted values of A_{elas} was studied to determine the covariance between f_b and A_{bkg}. The allowable range for $Y_{bkg}(t)$ was constrained by a parallelogram (or lozenge) with a flat top and bottom, with the two slopes starting from the mid-point of the elastic proton cut, and the ends fixed at the measured background yields at the end of the elastic window, as seen in Figure 5.18. Large numbers of random points lying within the parallelogram were chosen by the simulation; each point connected by straight line to the ends of the parallelogram. The area beneath these lines was then used as the model of the background yield.

The term $\sigma_{syst}(A_3)$, the systematic uncertainty associated with the systematic uncertainty in the background uncertainty, is estimated by studying the effects on the extracted elastic asymmetries of making variations in the background asymmetry $A_{bkg}(t)$, both by using different functional forms for $A_{bkg}(t)$ and by varying the range over t of the fits. For this study, the background yield is fixed at its best fit value. The upper bound is formed by taking two lines that are tangential to the background asymmetry fit in the sidebands, which defines a kink, as seen in Figure 5.19. The lower bound is defined as the straight line that connects the the background asymmetry values from the second-order polynomial fit ± 3 ns from the elastic peak. The distribution of the elastic asymmetries for each of the background asymmetry models, including the upper and lower bounds,

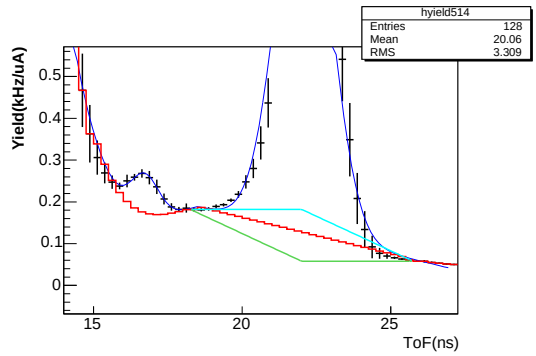

FIG. 5.18: *The lozenge shape chosen as the upper and lower bounds of $Y_{bkg}(t)$. Figure from [259].*

are then studied to estimate $\sigma_{syst}(A_3)$, as the variation is an indication of the model-dependency of the uncertainty. The choice of the function forms used to model $A_{bkg}(t)$ is somewhat arbitrary, however, which would make the simple option of using the half-spread as the uncertainty too model-dependent. Therefore, the spread is calculated by weighting the extracted values of A_{elas} by the χ^2 of the fit. The results of this procedure are significantly smaller than the half-spreads, and so the average of the two procedures is used as the estimate for $\sigma_{syst}(A_3)$ for each detector. The systematic uncertainty for A_{elas} can then be computed using Eq. 5.45.

The systematic uncertainties for A_{elas} contain components that are independent for each individual detector, called point-to-point uncertainties, and uncertainties that globally affect all the detectors in a correlated manner, or global uncertainties. An example of this would be if the function form assumed for $Y_{bkg}(t)$ or $A_{bkg}(t)$ had a common bias that makes the uncertainty correlated across the detectors. The estimate for this is done by changing the functional form for $Y_{bkg}(t)$ or $A_{bkg}(t)$ globally, then studying whether there is a resulting global change in the extracted elastic asymmetries. To study $\sigma(A_2)$, the polynomial used for $Y_{bkg}(t)$ was varied globally from first to third-order polynomials. In all detectors, the first and third polynomials give the least and most negative values of the elastic asymmetry, respectively, which gives the global change expected if the background model where globally changed. The ratio of this separation and the total width of

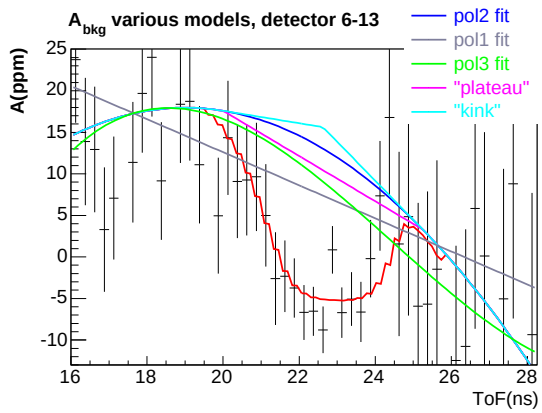

FIG. 5.19: *The asymmetry data for Octant 6, detector 13, showing the fit to the data (red) and various background models. Figure from [259].*

the distribution of all three background models is 0.58, which is the estimate of ratio of the global component of $\sigma(A_2)$ [224, 259].

A very similar study was done to ascertain $\sigma_{syst}(A_3)$. Again, the first and third-order polynomial fits of $A_{bkg}(t)$ yielded the most and least negative values of the elastic asymmetry. Using the elastic asymmetry extracted with the second-order polynomial as the reference point, the relative differences $\frac{|A_{pol3}-A_{pol2}|}{|A_{pol2}|}$ and $\frac{|A_{pol1}-A_{pol2}|}{|A_{pol2}|}$ were computed, where A_{poln} denotes the background model used to extract that particular elastic asymmetry. The correlation coefficient between these relative differences was 0.45, based on fourteen detectors. The global uncertainty estimate is then $0.45 \times \sigma_{syst}(A_3)$ [271].

Given that the ratio of the global to overall systematic uncertainty is about 0.50 for both $\sigma(A_2)$ and $\sigma_{syst}(A_3)$, the systematic uncertainty for all detectors was determined to be

$$\sigma_{syst}^{global}(A_{elas}) = 0.50 \times \sigma_{syst}(A_{elas}), \tag{5.46}$$

with a corresponding point-to-point systematic uncertainty of [224, 259]

$$\sigma_{syst}^{pt-pt}(A_{elas}) = \sqrt{1-0.50^2}\,\sigma_{syst}(A_{elas}) = 0.87 \times \sigma_{syst}(A_{elas}). \tag{5.47}$$

The background-corrected elastic asymmetries and their uncertainties are listed in Table 5.8.

5.3.5.2.2 Treatment of Detector 15

Unlike the previously discussed detectors, Detector 15 has a very wide elastic peak corresponding to a wider Q^2 range from $0.41 < Q^2 < 0.9$ (GeV/c)^2 due to the optics of the spectrometer. This makes the extraction of the elastic and background yields and asymmetries more difficult because simple fits can no longer be used effectively. Instead, to determine the background contribution, the information about the background yields and asymmetries in Detectors 12, 13, 14, and 16 are used to interpolate these values in Detector 15. These values are then used to obtain the elastic asymmetries from the Q^2 bins in Detector 15.

The resolution of the NA electronics is only 1 ns, which makes the Q^2 separation in Detector 15 very difficult. For this detector, the data from the hybrid Franco-American system was used, as these data had the finer resolution of 0.25 ns (signals from NA Detectors 14 and 15 were routed though the French electronics). However, Detector 16 was not measured by the FrAm electronics, so the 1 ns spectra were rebinned into 0.25 ns bins by assuming linearly varying yield in each 1 ns bin. This approximation worked very well for the simple spectra from Detector 16.

The background yield in Detector 15 was determined from studying the behaviour of the fitted background yields in Detectors 12, 13, and 14 and the measured background yield in Detector 16. The background spectra from these detectors are shown in Figure 5.20, where the time-of-flight spectra have been shifted relative to that of Detector 15 to align the spectra to a continuous band in proton (p, θ) phase space and have been corrected for the varying acceptance of each detector. The hierarchy of the background yield with detector number is obvious. The value of the background in a particular timebin can be parameterized as a linear function across this group of detectors. Figure 5.21 shows the fits of the background contributions in a given timebin versus detector number. The linearly interpolated value can then be used for the value of the background for those timebins in Detector 15. Other procedures were also used to study the background yield in Detector 15. One approach determined the value of the background yield in a given timebin in Detector 15 by averaging the background yield in that timebin in Detectors 14 and 16. A third

approach used an interpolation in (p, θ) space to determine the differential cross section in (p, θ) across the acceptance of Detector 15, which was then used as an event generator in G0GEANT to calculated the background yield [224, 259]. All these approaches were in good agreement, as can be seen in Figure 5.22. A simple parameterization of the background yield in detector 15 can be obtained by scaling the measured yield in detector 16 by 1.3, which only has background events. This is the method that was finally used to model the background yield.

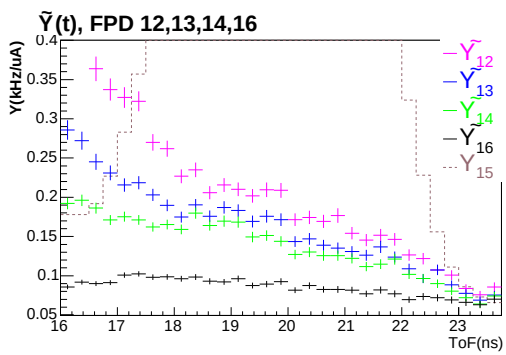

FIG. 5.20: *Background yield spectra for Detectors 12, 13, 14, and 16, showing the trend by detector. Figure from [259].*

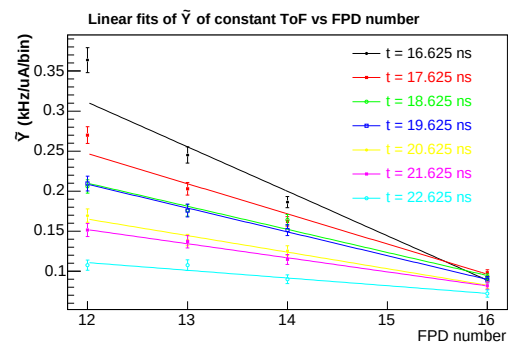

FIG. 5.21: *Linear fits to the background for given timebins versus detector number, used to interpolate the background in Detector 15. Figure from [259].*

The systematic uncertainty for the interpolated background yield in Detector 15 $Y_{bkg}(15, t)$ is done by calculating the upper and lower bounds from the yields in Detectors 14 and 16:

$$Y_{bkg}^{upper} = 0.75 \times Y_{bkg}(14, t) + 0.25 \times Y_{bkg}(16, t), \tag{5.48}$$

$$Y_{bkg}^{lower} = 0.25 \times Y_{bkg}(14, t) + 0.75 \times Y_{bkg}(16, t), \tag{5.49}$$

where $Y_{bkg}^{upper(lower)}$ denotes the upper (lower) bounds and $Y_{bkg}(14(16), t)$ represents the background yields from Detectors 14 and 16. These $\pm 1\sigma$ bounds (similar to using $\pm\frac{1}{2}$ detector as the uncertainty), are shown in Figure 5.22.

The elastic peak in Detector 15 was divided into three Q^2 bins along the time-of-flight spectrum, corresponding to $Q^2 = 0.511$ (20.0 to 22.75 ns), $Q^2 = 0.631$ (18.5 to 20.0 ns), and $Q^2 = 0.788$ $(\text{GeV}/c)^2$ (16.5 to 28.5 ns). The determination of the background asymmetry $A_{bkg}(t)$ in the three

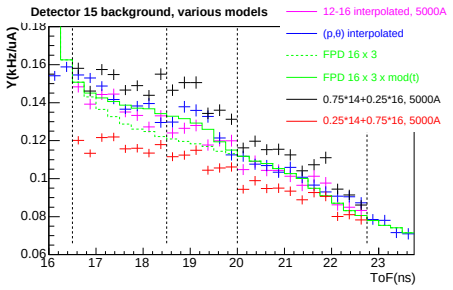

FIG. 5.22: *Comparison of the methods used to determine the background yield in Detector 15. Figure from [259].*

Q^2 bins of Detector 15 was done in a similar manner to the background yield determination, by studying the evolution of the background asymmetry across the higher-numbered detectors and interpolating the value in Detector 15. The background asymmetries in Detectors 12, 13, and 14 were obtained as described in Section 5.3.5.2.1; the measured background asymmetry in Detector 16 was fitted with a fourth-order polynomial.

The background asymmetries from octants 2, 6, and 8 were combined to improve the statistical precision; octant 4 was was fitted separately as the background asymmetry was somewhat different from the others. These asymmetries are shown as a function of time-of-flight in Figure 5.23, where the progression with detector number can again be observed. As with the background yields, a linear interpolation is done for each timebin versus the detector number, with the interpolated value taken as the background asymmetry for Detector 15.[2] An example is shown in Figure 5.24, where the measured asymmetries for octant 3 are shown with the best fits of the background asymmetries.

A second method was done, where the background asymmetry was fitted in the same manner as the second step of the two-step fitting procedure done for the lower-numbered detectors (see Section 5.3.5.2.1), except that the interpolated background yield for detector 15 was used. The background yield was modeled as a third-degree polynomial. The fit for octant 3 using this method

[2]This was done in all cases except for octant 4, where this value did not accurately reproduce the measured asymmetry in the pure background region above 23 ns; the fit for 13 was used as the best fit instead.

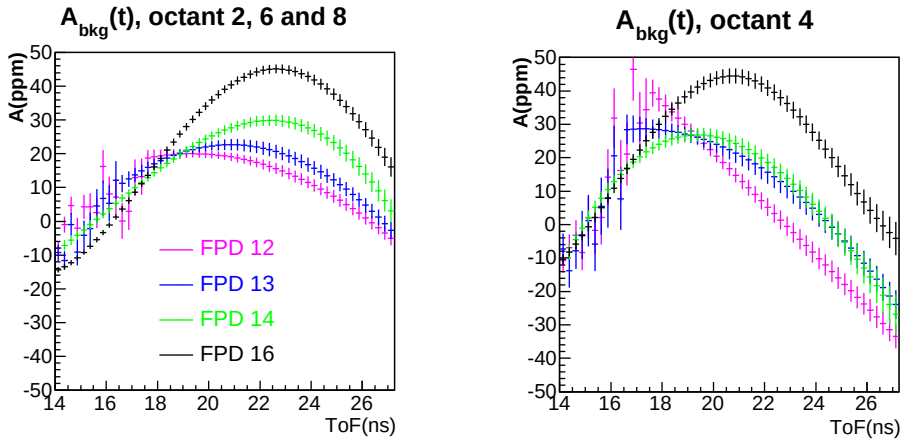

FIG. 5.23: *The fitted background asymmetries for Detectors 12, 13, 14, and 16, showing the trend by detector. Octants 2, 6, and 8 are combined; octant 4 is done separately. Figure from [259].*

is shown as the dashed curve in Figure 5.24.

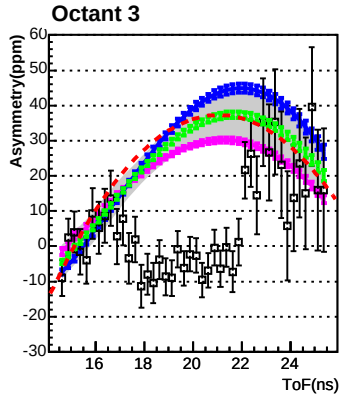

FIG. 5.24: *The best fit to the interpolated background asymmetries for Octant 3, Detector 15, shown with the measured asymmetries (black points) and the background asymmetry obtained from the two-step fit method (dashed line). Figure from [224].*

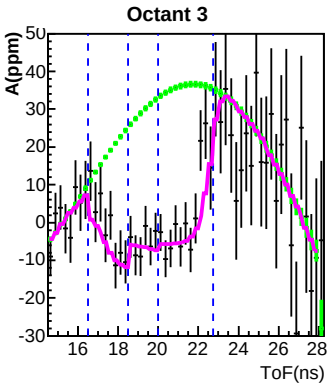

FIG. 5.25: *The fit to the measured asymmetries for Octant 3, Detector 15, using the interpolated background asymmetries. The vertical lines delineate the three Q^2 bins. Figure from [224].*

With the values of the background yields and asymmetries, the elastic asymmetry can be found for each octant by fitting the measured asymmetry bin by bin according to Eq. 5.37, assuming that the elastic asymmetry in each of the three Q^2 bins is a constant for all eight octants. An example of this fit, the fit for Octant 3, is shown in Figure 5.25. Allowing the elastic asymmetry

to float for individual octants had a negligible impact on the extracted elastic asymmetry. The elastic asymmetries were also extracted using the two-step method as a check, which were in good agreement. Although the two-step method allows more flexibility to optimize the agreement between the data and the fit, the interpolation method uses physical constraints from the other detectors, and thus these are the results that are used for this detector.

As with the background yield, the systematic uncertainty for the background asymmetry is done in what was called the "±1 detector" uncertainty, where the interpolated asymmetries at detectors 14 and 16 were assigned as the upper and lower bounds. The uncertainty is then enlarged so that it covers the variation when the background asymmetry is shifted in time by ±0.5 ns to ensure a good match with the sideband asymmetries. The resulting $\pm 1\sigma$ error band was shown in Figure 5.24 as a gray band.

The systematic uncertainty for the elastic asymmetry can be divided into the contributions from the background yield ($\sigma(A_2)$) and the contributions from the background asymmetry ($\sigma_{syst}(A_3)$). Since the background yields and asymmetries are determined independently, the correlation term Δ is no longer a concern. A Monte Carlo simulation was used to vary the background yield with a random scaling variable (common to all eight octants) between the upper and lower bounds and the background asymmetry with a random scaling variable (common for 7 octants, independent for octant 4) within the upper and lower bounds. A global random timing jitter of 0.5 ns was also introduced octant by octant to account for any possible effects coming from misalignment of $Y_{bkg}(t)$ relative to $Y_{meas}(t)$. The spread of the resulting elastic asymmetries gives the overall systematic uncertainties, which are shown in Table 5.6. These uncertainties in the three Q^2 bins are almost 100% correlated.

To separate the point-to-point and global uncertainties, more variations are introduced in the Monte Carlo simulation. The uncertainty due to the background asymmetry was estimated by using a quadratic background asymmetry function with randomly varying curvature, where the allowable range was determined by the curvatures from the two-step fits to the background

$\langle Q^2 \rangle (\mathrm{GeV}/c)^2$	$\sigma(A_2)$ (ppm)	$\sigma_{syst}(A_3)$ (ppm)
0.788	1.79	2.30
0.631	0.88	1.15
0.511	0.87	1.44

TABLE 5.6: *The overall systematic uncertainties for the three Q^2 bins in Detector 15 (blinded) [224, 259].*

asymmetry, and varying endpoints, which are randomly chosen within the width of the error band. The correlation coefficients between the elastic asymmetry in each Q^2 bin and the average of the other two were then calculated. The coefficients were found to be about 0.7. The value for the middle Q^2 bin was somewhat higher than the two other bins, which was expected since it is directly adjacent to them both. This suggests that an equal division in quadrature of the point-to-point and the global systematic uncertainties would be appropriate for $\sigma_{syst}(A_3)$ [224, 259]. A similar technique is used for the background yield, where the values of the background yield at the edges of each Q^2 bin were chosen randomly within the error band and connected with straight lines. The calculated correlation coefficients of the elastic asymmetries between the bins was about 0.5, somewhat less than the background asymmetry; however, an equal division in quadrature of the point-to-point and the global systematic uncertainties for $\sigma(A_2)$ was also adopted to be conservative [224, 259]. It is expected that the systematic uncertainties for Detector 15 are more globally correlated than the lower-numbered detectors because the three Q^2 bins are taken from the same time-of-flight spectrum and because the use of interpolation depends on the fits in the lower-numbered detectors.

The elastic peak in Detector 15 has been divided into three Q^2 bins along the time-of-flight spectrum. However, this choice is somewhat arbitrary, as the peak could have been divided into more bins or fewer. To study the sensitivity of the extracted results on the choice of how the time-of-flight spectrum was divided into Q^2 bins, the elastic peak was divided into 1, 2, 3, 4, and 5 bins, and the background correction procedure was repeated for each division scheme. Linear fits were made for the elastic asymmetries extracted for each division set. The division sets with

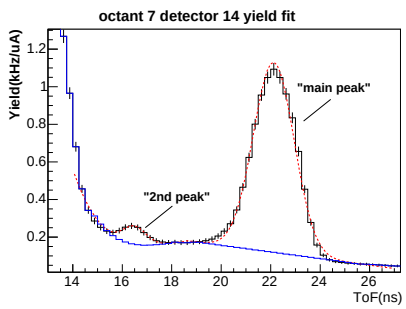

FIG. 5.26: *Yield fit for the high Q^2 peak of Octant 7, Detector 14. The two elastic peaks are fitted with Gaussians (red fits) with a fifth-order polynomial background from 14 to 19 ns and a linear background from 19 to 27 ns (blue curve). Figure taken from [224].*

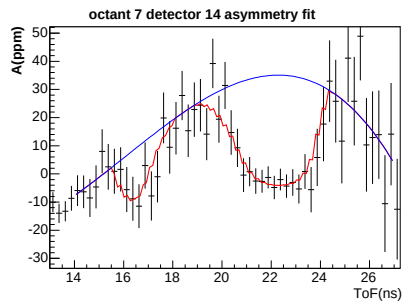

FIG. 5.27: *Asymmetry fit for the high Q^2 peak of Octant 7, Detector 14. The elastic asymmetry in each peak is assumed to be constant, while the background asymmetry is modeled with a third-degree polynomial over the entire range. The red line is the fit to the measured asymmetries; the blue curve is the fit to the background asymmetries. Figure taken from [224].*

only one and two Q^2 bins did not have sufficient resolution to accurately reflect the variation of the elastic asymmetry. However, the results for the sets with three, four, and five bins were in excellent agreement, indicating that the choice of three bins accurately shows the evolution of the elastic asymmetry in Q^2 [224, 259].

5.3.5.2.3 High Q^2 Peak of Detector 14

Because of the optics of the spectrometer (see Section 4.5.2) and the resulting "fold-over" of the higher Q^2 points, Detector 14 actually has two elastic peaks: a primary peak at a time-of-flight of about 23 ns corresponding to $Q^2 = 0.41$ (GeV/c)^2 that was discussed earlier in Section 5.3.5.2.1, and a smaller, secondary peak at about 17 ns corresponding to $Q^2 = 0.997$ (GeV/c)^2. The second peak can be viewed in Figure 5.26, where it is located just after the pion peak in the ToF spectrum.

As with Detector 15, the data from the NA electronics do not have the resolution needed for this analysis, so the data from the French detectors and the FrAm hybrid detectors was used instead. The secondary peak was treated in much the same manner as detectors 1–14 (main peak), this time with the background modeled as a 5th-order polynomial and the elastic peak as a Gaussian for the yield fits. The primary elastic peak (at $\sim$ 23 ns) was fitted simultaneously with a

Gaussian as the elastic peak with a linear background function in order to gain an understanding of any correlation between the two peaks.

The asymmetry fit was done by assuming a constant elastic asymmetry in each Q^2 bin and using a polynomial for the background asymmetry $A_b(t)$, which was fitted over the entire ToF, as shown in Figure 5.27. The fit quality was not very sensitive to the polynomial function chosen for $A_b(t)$, so the results for the elastic asymmetry obtained from the fits using second, third, fourth and fifth-order polynomials were combined in a straight average to obtain as result of $A_{elas} = -30.56$ (still blinded) [224].

As with the other Q^2 bins, the statistical uncertainty of the elastic asymmetry was evaluated based on counting statistics, with the background dilation ($\sim 78\%$), deadtime effects ($\sim 20\%$) and beam polarization accounted for, giving a value of $\sigma_{stat}(A_{elas}) = 5.83$ ppm (still blinded).

To determine the systematic uncertainty arising from the uncertainty of f_b, $\sigma(A_2)$, and Δ (the correlation term), the Monte Carlo was used. First, the uncertainty of f_b was estimated. The octant to octant fitted elastic yield varied by about 12%, which gives an estimate of the fractional uncertainty in Y_{elas}. However, the fitted elastic yield is only about 54% of the yield predicted by the simulation, probably due to the acceptance. This can also be expressed as $\frac{\text{G0Geant}-\text{Fit}}{\text{Fit}} = 84\%$, which gives an estimate of about 42% for the uncertainty. An average of these estimates has been used as the fractional uncertainty for Y_{elas}, 27%, giving $f_b = 78 \pm 6\%$. In the Monte Carlo, f_b was varied from the best fit with a single random scaling variable within $\pm 6\%$ (stat). The values of σA_2 and Δ were then calculated, which resulted in a (blinded) value of $\sqrt{\sigma^2(A_{elas}) + \Delta} = 5.72$ ppm.

To evaluate the model uncertainty due to the background asymmetry, $\sigma_{syst}(A_3)$, a ± 1 detector error band was put around A_{bkg}, which was scaled randomly and then fitted with the two-step procedure. This procedure over-estimated the uncertainty of the background asymmetry in the primary peak by a factor of 3, so the uncertainty obtained for the secondary peak was reduced by a factor of three. This yields a total systematic uncertainty of $\sigma_{syst}(A_{elas}) =$

$\sqrt{\sigma^2(A_2) + \Delta + \sigma^2_{syst}(A_3)} = 7.28$ ppm. The secondary elastic peak is located at the pion peak tail, outside of the fit range of the other detectors, so this systematic uncertainty is not correlated with those from other Q^2 bins, nor is it strongly correlated to the main peak in detector 14 (based on the values), so this is regarded as a point-to-point systematic uncertainty [224, 259].

5.3.6 Electromagnetic Radiative Corrections

There is another category of corrections that are required in elastic electron scattering experiments: radiative corrections. Radiative corrections are required in these experiments because the electron can radiate photons through various mechanisms. This causes a loss of energy in the incident and scattered electrons, which affects the kinematics of the scattered particle. In this measurement, the recoiling protons are detected from the interaction. Electromagnetic radiative emission from the recoiling, non-relativistic proton is negligible due to its large mass, but the kinematics (e.g. the angle, energy, Q^2) of the proton are affected by the radiative emission from the electron. As the radiative emission from the incident electron changes the kinematics of the elastic reaction, this changes the measured elastic asymmetry from that of the tree-level Born asymmetry without photon radiation.

The radiative corrections must correct for changes in proton rate and asymmetry, as well as the Q^2. The electromagnetic radiative emission gives rise to a tail that extends to very low energy. For G^0, this emission is manifested in the yield spectrum as a tail toward the earlier ToF of the elastic peak, increasing the average Q^2 in each bin. This has the consequence of increasing the magnitude of the measured elastic asymmetry from the anticipated Born asymmetry. A dedicated GEANT simulation was developed to treat the radiative corrections for G^0 [81, 272, 273]. Four types of radiative corrections were considered for the measurement: ionization, external, internal real and internal virtual radiative corrections.

The first type of correction, ionization, refers to electron energy losses in the beam line and target material. Studies using G0GEANT to model this showed that the average energy loss at the target mid-point was on the order of 5 MeV, although it could be as much as 15 MeV [272].

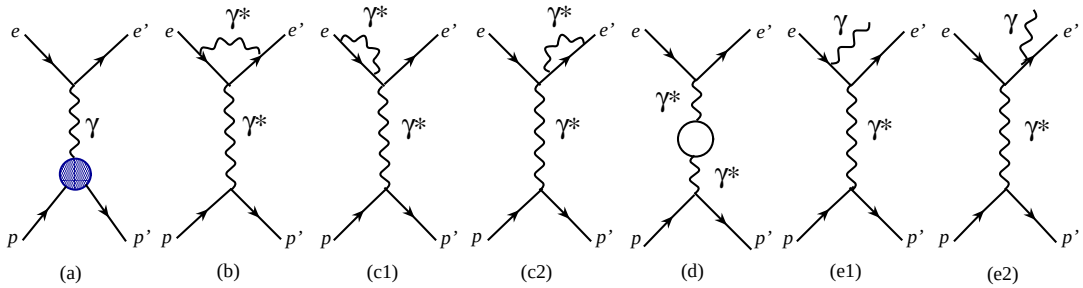

FIG. 5.28: *Feynman diagrams representing the amplitudes of various radiative corrections. Diagrams a shows the tree-level (Born) term. Diagrams b through d represent the amplitudes for virtual internal radiative corrections. The electrons emit and then reabsorb the virtual photons. The diagrams in e show the amplitudes for real internal radiative corrections. In these, the emission of the real photon results in a three-body final state that changes the kinematics of the recoiling proton. [272]*

The second type, external radiative corrections, describes the energy loss from the emission of Bremsstrahlung photons by incident beam electrons decelerated by nuclear interactions in the ionization process. This results in a broad energy spectrum, with an average energy loss of 40 MeV, but which can reach a maximum of 3 GeV (the total beam energy) [272]. These effects from external Bremsstrahlung radiation were also characterized using G0GEANT.

The last two types are internal radiative corrections, which correspond to the emission of photons before or after the interaction between the electron and the proton in the target. The first of these two types, virtual internal radiative corrections, deal with the case when a photon is emitted, and then reabsorbed, leaving the final state similar to that from elastic scattering. This does not modify the proton kinematics; however, it can affect the momentum transfer as well as the polarization of the electron at the scattering vertex.

The last type, real internal radiative corrections, involve the emission of a real photon, resulting in a three-body final state (e, p, and γ). This effect also takes place in the diagrams with the Z^0, which adds to the complication. This effect changes the momentum transfer, and in the case where the photon is emitted prior to the scattering, can change the electron polarization at the scattering vertex. The calculation of corrections from these internal radiative effects are done following the framework of Mo and Tsai [46, 274].

The calculations are done via simulation. Using the G0Geant simulation, the incident energy of the electron was varied and the overall effect of energy loss on the elastic rate was observed. In principle, the electrons in the beam can lose all their energy through radiation. However, the probability that they lose 500 MeV or less is about 96%, and only about 60% of the electrons lose 1 keV or less [81]. The 4% of electrons that lose more than 500 MeV correspond to protons that have times-of-flight outside of the G^0 experimental cuts, and are therefore ignored. Therefore, the simulations were done for incident beam energies that varied between 2.5 and 3.0 GeV. The parity-violating asymmetry was calculated based on the kinematics at the reaction vertex after the radiative emission and assuming that $G_E^s = G_M^s = 0$. The elastic asymmetry was then calculated without the energy losses, under the same assumption. The calculated radiated asymmetries, A_{el}, corresponding the elastic asymmetry from the measurement, and the Born asymmetries, A_{RC}, corresponding to the radiatively corrected asymmetries (no energy losses) were averaged over the elastic proton cut. The ratio $R = \frac{A_{el}}{A_{RC}}$ for 17 of the detector bins is shown versus Q^2 (the average Q^2 is computed based on the Born scattering cross section) in Figure 5.29. In general the ratio R, which shows the effect of the correction on the asymmetries, is slightly less than 1. The radiative effects for the highest Q^2 point from detector 14 are insignificant compared to its statistical error bar, and is thus ignored. Following the increase in Q^2, the effect is that the radiative corrections increase the average asymmetry. The increase is of order 0.5 – 3.0% over the range of the detectors [81].

The estimate of the uncertainty in the correction is based on the assumption that the elastic cuts have a 10% uncertainty, which represents an upper limit on the uncertainty since the elastic cuts are known to better than that. The corrections are then calculated using cuts that are 5% larger and then 5% smaller than the standard elastic cut. In addition, another estimate of the uncertainty was done by making a global fit of the ratio A_{el}/A_{RC} with a polynomial and assuming that the difference with the actual RC correction is due to systematics. The uncertainty varies slowly and is of the order 0.1–0.3%, about 10% of the actual correction, depending on the detector

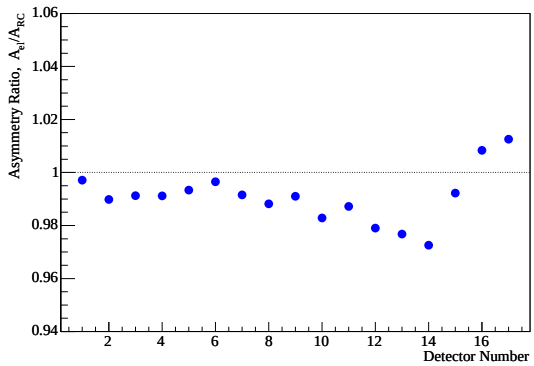

FIG. 5.29: *The ratio of asymmetries A_{el}/A_{RC} versus detector number where A_{el} is the elastic asymmetry and A_{RC} is the asymmetry corrected for radiative emission. Data points from [81].*

bin [81, 272]. The correction was applied as an overall multiplicative factor, $A_{phys}(Q^2) = R \times A_e$, which gives back the Born asymmetry to be compared to theory.

5.3.7 Determination of Q^2

An important part of the analysis is to determine the average four-momentum transfer (Q^2) value of the elastic protons measured in each of the detectors, as well as the uncertainty in this value. For the G^0 experiment, a 1% precision on Q^2 for a relative contribution of 5% statistical error was desired. In order to do this, the precise magnetic field produced by the SMS must be determined very accurately, as the $\vec{B}$-field dictates the particle trajectories, and thus the time-of-flight and Q^2 in each FPD at the chosen kinematics. However, the direct readout of the SMS current (4991 A) is not precise enough to attain the desired precision. Thus, two methods to accomplish this goal were developed, both requiring the comparison of the experimental data with a simulation of the G0 spectrometer. The first method was used to obtain the magnitude of the magnetic field generated by the spectrometer magnet; the second method was used both to determine the magnetic field and the average Q^2 value per detector [233, 275–277].

In the first method, the property that the absolute elastic proton rates in detectors 15 and 16 have a high sensitivity to the actual $\vec{B}$-field strength is used to determine the magnetic field. At the nominal magnetic field (i.e., at the nominal magnet current of 5000 A), there is no elastic rate

in detector 16; however, the elastic protons lie at the very edge of Detector 16's acceptance. By varying the magnetic field (by varying the SMS current), the focusing of the spectrometer magnet changes, changing the elastic Q^2 of the detectors, most significantly for this, in Detectors 15 and 16. At fields lower than the nominal value, Detector 16 is in the acceptance region for elastic protons. As the absolute rates in detectors 15 and 16 are the ones most sensitive to the SMS field variations, one can fit these values as a function of the current and extract the value of the field by a comparison to a simulation of the experimental apparatus. Of course, the quality of the simulation then becomes very important.

Figure 5.30 shows the elastic proton rate as a function of the magnet current (which is essentially the field strength as there are no ferromagnetic elements present) for Detectors 15 and 16 (French octants), along with the simulation (black curve). For detector 16, elastic protons are detected at field values lower than the nominal, but as the current increases to about 4900 A, the elastic protons are focused outside of the acceptance, leaving only the lower rates from background particles. An increase in the magnetic field leads to an increase of the elastic Q^2 and the elastic acceptance in Detector 15, but a decrease in the cross section. The combination of these effects causes the bump in the elastic rate in detector 15 at about 4880 A. The fits to the measured data points (after the background correction) were compared to the fits to the simulation to extract the field value. The actual magnet current was determined by this method to be 5003.5 ± 5 A [276] for the first engineering run and 4985 ± 10 A for the production run [275, 276]. However, as this method does not provide enough constraints to take into account any detector position offsets from possible misalignment that would cause an effective variation in Q^2, another method was also developed.

The second method was used to determine both the magnetic field of the spectrometer and the average Q^2 value for each detector. In this method, the measured differences in the ToF between the elastic proton and pion peaks $\Delta t_{\pi p}$ in the data from each detector were compared with the differences obtained from the simulation ($\Delta t^{sim}_{\pi p}$) at the nominal field at 5000 A. From

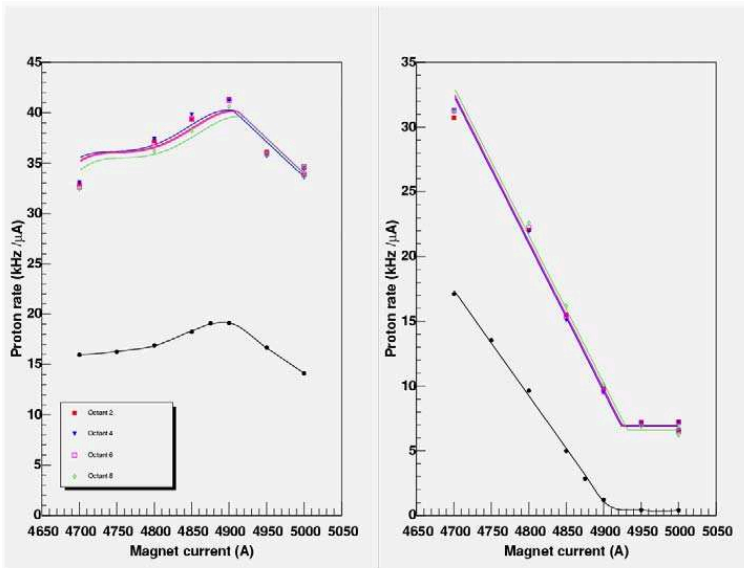

FIG. 5.30: *The elastic proton rates in Detectors 15 and 16 as a function of the SMS current. The colored curves are fits to measured data; the black curve is from the simulation. Figure from [275].*

this comparison, the actual $\vec{B}$-field was determined. This magnetic field value is then used in the simulation to determine the average Q^2, $\langle Q^2 \rangle$, of the detectors. This method is relatively precise; a measurement of $\Delta t_{\pi p}$ to a precision of ~ 50 ps allows a determination of the magnetic field to $< 0.2\%$ and of the four-momentum transfer for each Q^2 bin to $< 1\%$ [233, 277]. By using the ToF separation $\Delta t_{\pi p}$, an absolute calibration of timing offsets in the electronics was unnessary. In addition, $\Delta t_{\pi p}$ is also sensitive to the potential longitudinal and radial offsets of the detetctors as well as the magnetic field strength, so it also accounts for uncertainties coming from misalignments in the detectors.

The ToF separation for each detector can be written to first order as [275]

$$\Delta t = \Delta t_{nominal} + \alpha^B_{\Delta t} \left(\frac{B}{B_{nominal}} - 1 \right) + \alpha^X_{\Delta t} \Delta X + \alpha^Z_{\Delta t} \Delta Z, \tag{5.50}$$

where $\Delta t_{nominal}$ and $B_{nominal}$ are the ToF separation and magnetic field at the nominal field of 5000A, Δt denotes the measured time separation, B is the true field value, ΔX and ΔZ are the radial and longitudinal positions of the detectors, and $\alpha^B_{\Delta t}$, $\alpha^X_{\Delta t}$, $\alpha^Z_{\Delta t}$ are coefficients associated

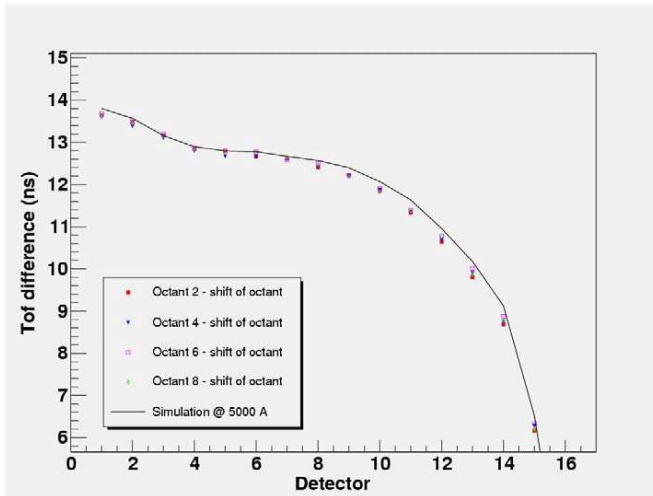

FIG. 5.31: *The difference between the measured elastic proton ToF and pion ToF for each detector (colored points), compared to the result from the simulation (black curve). Figure from [275].*

with the expansion. Similarly, the difference in the Q^2 can be expanded as

$$\frac{\Delta Q^2}{Q^2_{nominal}} = \alpha^B_{Q^2}\left(\frac{B}{B_{nominal}} - 1\right) + \alpha^X_{Q^2}\Delta X + \alpha^Z_{Q^2}\Delta Z, \tag{5.51}$$

where ΔQ^2 is the difference in the Q^2, and $Q^2_{nominal}$ is the Q^2 of the detector at the nominal 5000A. To reduce the number of unknowns so that the system of linear equations can be solved, constraints were imposed, including a common ΔZ for all detectors, and that the longitudinal and radial shifts average to zero.

Figure 5.31 shows the difference between the measured elastic proton ToF and pion ToF for each detector, compared to the result from the simulation. By using this method, the magnet current was found to be 5015 A for the first engineering run and 5025 A for the production run [276]. The position offsets of the FPDs were determined to range from a few mm to about 1.5 cm detector by detector, within a precision of about 3 mm [233, 277] The extracted $\vec{B}$-field value was then used in the simulation to determine the average $\langle Q^2 \rangle$ of each the FPDs. The position offsets that were determined from the fits had little impact on the average Q^2 of the bins, $\sim< 1\%$. This value was used as a conservative estimate of the uncertainty of the Q^2 [276].

By using the extracted $\vec{B}$ value in the simulation, a spectrum of $Q^2(t)$ was determined for

each detector. This was integrated over the elastic proton peak, weighted by the yield:

$$\langle Q^2 \rangle_{det} = \frac{\int Q^2(t) Y_{meas}(t)}{\int Y_{meas}(t)}, \tag{5.52}$$

where $\langle Q^2 \rangle_{det}$ is the central value of Q^2 for the elastic peak for a particular detector. The resulting values of the Q^2 for each detector can be seen in the Table 5.8 in Section 5.3.8.

The elastic asymmetry measured in each Q^2 bin is an average asymmetry weighted by the yield. The form factors do have a Q^2 dependence; however, because $A(Q^2)$ is approximately linear in Q^2 to leading order, the approximation $\langle A(Q^2) \rangle = A(\langle Q^2 \rangle)$ is valid, with a small width of the Q^2 distribution in each Q^2 bin, ranging from 5% (for Detector 1) to 10% (the three Q^2 bins in detector 15) of $\langle Q^2 \rangle$. Because of this, it is valid to interpret the measured elastic asymmetry of each bin as the elastic asymmetry at the average 4-momentum transfer.

The magnetic field values that are determined by the two methods do not perfectly agree, but have a reasonable agreement considering that the first method does not take into account any offsets in the detector position (misalignments). For this reason, the results for the $\langle Q^2 \rangle$ and its uncertainty of 1% from the second method of the $\vec{B}$-field determination were used. The 1% uncertainty is uncorrelated with the uncertainty of the measured asymmetry, but can be expressed as an effective uncertainty of the asymmetry as

$$\sigma_{eff}(A_{Q^2}) = \frac{\partial A}{\partial Q^2} \sigma(Q^2). \tag{5.53}$$

This 1% uncertainty in Q^2 becomes a 1% uncertainty in the measured asymmetry.

5.3.8 The Physics Asymmetry

After all corrections to the measured asymmetries were performed, the blinding factor of 0.8056 was removed. The final physics asymmetries for the 18 Q^2 bins are are shown in Table 5.8 as published in [245]. The asymmetries are shown with the statistical errors and the point-to-point and global systematic uncertainties. The systematic corrections and the uncertainty associated with them are shown in Table 5.7. The background corrections and uncertainties are given as a range. The uncertainties associated with the deadtime, helicity-correlated beam parameters, and radiative

Source	Correction	Uncertainty
Deadtime	0.2 ppm	0.05 ppm
Helicity-correlated beam parameters	0.01 ppm	0.01 ppm
Ordinary radiative corrections	1% (fractional)	0.3%
Background correction	0.1–40 ppm	0.2 – 9 ppm
Beam polarization	$\frac{1}{73.7\%}$(factor)	1.3% (fractional)
Leakage beam	0.71 ppm	0.14 ppm
Transverse polarization	0	0.01 ppm
Q^2	0	1%

TABLE 5.7: *Systematic uncertainties for the measured asymmetries.*

corrections are average values, as the actual corrections were done detector by detector. These uncertainties, along with the point-to-point component of the background correction, are treated as point-to-point uncertainties. The systematic uncertainties arising from the beam polarization, beam leakage correction, transverse polarization, the global component of the background, and the Q^2 are treated as global uncertainties. The uncertainties from the background correction dominate both the global and point-to-point uncertainties, except for in detectors 1 through 4, where the beam leakage uncertainty dominates the global systematic uncertainty. For comparison, the measured (uncorrected) asymmetry and the extracted background asymmetry are also shown in Table 5.8, along with the dilution factor.

These asymmetries can now be used to extract the linear combination of the electric and magnetic strange form factors, $G_E^s + \eta G_M^s$. How this is done will be discussed in the next chapter.

5.4 Transverse Data Set

The transverse data collection took place from March 22 through March 26, 2006. After setting up the beam tune to deliver transversely-polarized beam into Hall C, about 30 hours of data were taken with the transversely polarized beam on the liquid hydrogen target. The experimental configuration for the transverse measurement was identical to the usual G^0 forward-angle running, except that the electron beam was transversely polarized in the plane of the accelerator. For the

Q^2 (GeV/c)^2	A_{phys} (ppm)	ΔA_{stat} (ppm)	ΔA_{pt-pt} (ppm)	ΔA_{glob} (ppm)	A_{meas} (ppm)	A_{bkg} (ppm)	f
0.122	-1.51	0.44	0.22	0.18	-1.38 ± 0.40	-3.69 ± 2.51	0.061
0.128	-0.97	0.41	0.20	0.17	-1.07 ± 0.36	-4.36 ± 0.78	0.084
0.136	-1.30	0.42	0.17	0.17	-1.34 ± 0.37	-5.49 ± 0.90	0.085
0.144	-2.71	0.43	0.18	0.18	-2.67 ± 0.38	-4.05 ± 2.81	0.077
0.153	-2.22	0.43	0.28	0.21	-2.46 ± 0.37	-6.13 ± 2.46	0.096
0.164	-2.88	0.43	0.32	0.23	-3.13 ± 0.37	-7.94 ± 2.82	0.100
0.177	-3.95	0.43	0.25	0.20	-4.47 ± 0.36	-9.76 ± 1.91	0.110
0.192	-3.85	0.48	0.22	0.19	-5.01 ± 0.41	-15.39± 1.66	0.110
0.210	-4.68	0.47	0.26	0.21	-5.73 ± 0.40	-13.53± 1.99	0.116
0.232	-5.27	0.51	0.30	0.23	-6.08 ± 0.41	-9.73 ± 2.06	0.136
0.262	-5.26	0.52	0.11	0.17	-5.55 ± 0.41	-5.35 ± 0.99	0.154
0.299	-7.72	0.60	0.53	0.35	-5.40 ± 0.46	8.33 ± 2.25	0.174
0.344	-8.40	0.68	0.85	0.52	-3.65 ± 0.51	18.37 ± 3.11	0.182
0.410	-10.25	0.67	0.89	0.55	-1.70 ± 0.51	36.49 ± 2.80	0.180
0.511	-16.81	0.89	1.48	1.50	-5.80 ± 0.79	40.86 ± 8.16	0.190
0.631	-19.96	1.11	1.28	1.31	-9.74 ± 0.94	31.54 ± 5.97	0.200
0.788	-30.83	1.86	2.56	2.59	-12.66± 1.01	15.65 ± 5.83	0.400
0.997	-37.93	7.24	9.00	0.52	4.21 ± 1.19	16.08 ± 2.22	0.780

TABLE 5.8: *The asymmetries and uncertainties measured in the G^0 experiment (forward-angle phase).*

measurement, the experiment typically made use of 40 μA of a 3 GeV polarized electron beam delivered into experimental Hall C by the accelerator at Jefferson Lab. This section describes the analysis of these data looking for evidence of two-photon exchange effects.

The asymmetry data were blinded in the same method as the longitudinal forward-angle data [224]. As the measurement has a much lower statistical precision than the primary longitudinal measurement, a similar, but slightly different analysis method was employed. However, corrections such as the ones due to leakage beam, deadtime effects, DNL, etc. were treated in an identical manner to the primary longitudinal data set. The North American (NA) and French data sets were treated in a similar manner, and in a similar analysis path as the longitudinal data. For more information, see References [248, 278]

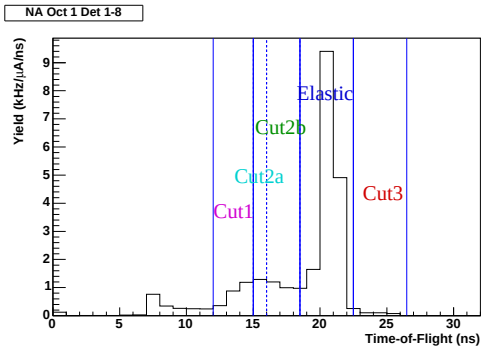

FIG. 5.32: *The ToF spectrum for Octant 1 Detector 1–8, showing the five PID cuts for the NA spectra.*

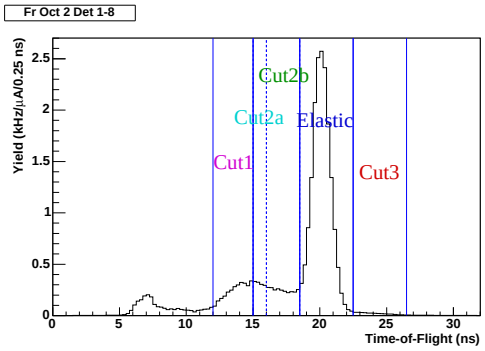

FIG. 5.33: *A picture showing the ToF spectrum and the five defined PID cuts for Octant 2, Detectors 1–8.*

5.4.1 Time-of-Flight Spectra and PID Cuts

Because of the low statistics of this measurement and because the data could not be summed over the detector rings, many of the analysis techniques as the forward-angle data could not be used effectively. In an effort to gain some statistical precision, the detectors in each octant were binned into three Q^2 bins: detectors 1 through 8, 9 through 12, and 13 and 14. Detector 15 was left to itself, and will be discussed further later in Section 5.4.1.2 with Detector 16. Table 5.9 shows the average Q^2 and center-of-mass angle θ_{CM} coverage for each of the bins, and with the first fourteen detectors combined into one Q^2 bin. After being summed, PID cuts were defined to study both the elastic proton and the background asymmetries.

Detector Bin	Q^2 (GeV/c)^2	θ_{CM}
1 - 8	0.15 ± 0.02	20.22°
9 - 12	0.25 ± 0.03	25.91°
13 - 14	0.38 ± 0.03	32.11°
15	~ 0.6	37.4°
1 - 14	0.20 ± 0.09	23.08°

TABLE 5.9: *Elastic proton kinematic coverage for the transverse data.*

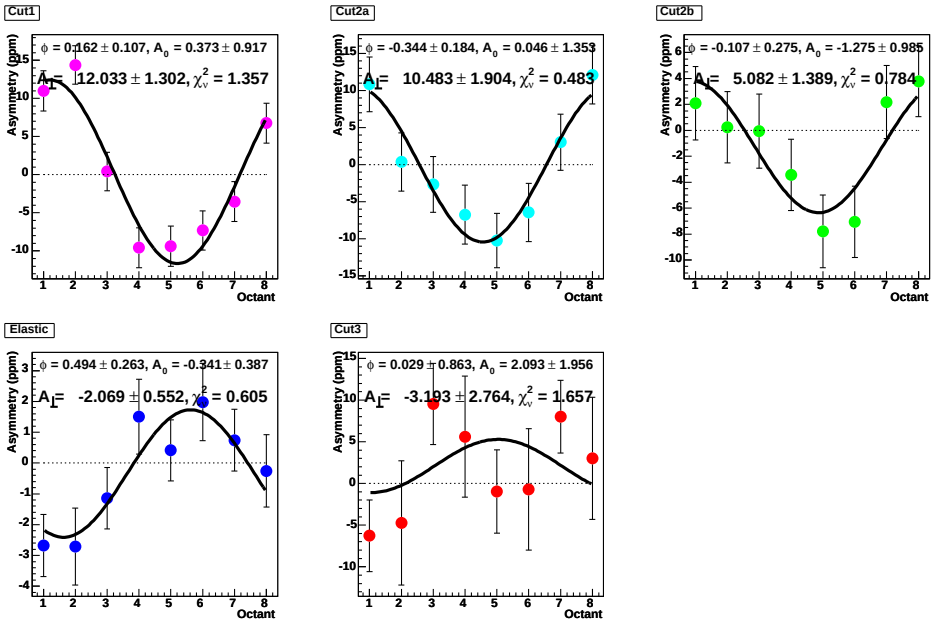

FIG. 5.34: *Raw Asymmetries versus Octant for the five PID cuts for Detectors 1–8 [note: asymmetries are blinded].*

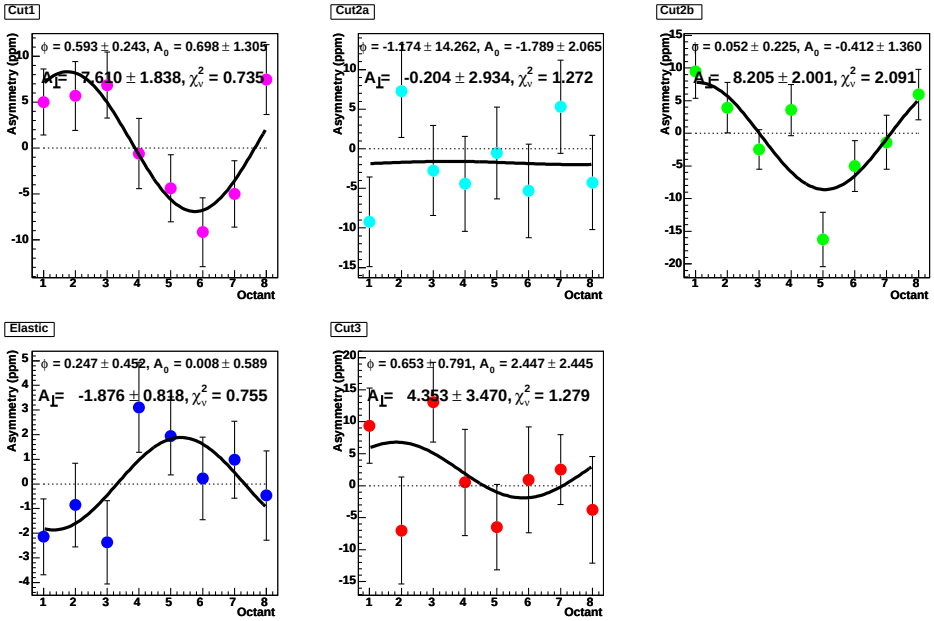

FIG. 5.35: *Raw Asymmetries versus Octant for the five PID cuts for Detectors 9–12 [note: asymmetries are blinded].*

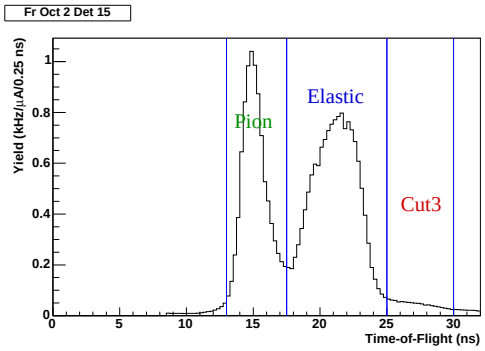

FIG. 5.36: *The ToF spectrum for Octant 2 Detector 15, showing the three PID cuts for the French spectra.*

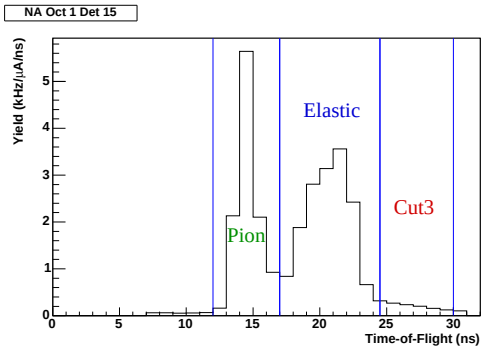

FIG. 5.37: *A picture showing the ToF spectrum and three defined cuts for Octant 1, Detector 15 for the NA spectra.*

5.4.1.1 Detectors 1 – 14

After the deadtime, DNL, and beam leakage corrections were applied to each detector as in the longitudinal case (see Sections 5.2.1 and 5.3.3), the first fourteen detectors were binned into three Q^2 groups by shifting the time-of-flight spectra for each detector to align the elastic peaks. Five time-of-flight cuts were defined for these summed spectra, as shown in Figures 5.32 and 5.33: cut1, cut2a, cut2b, the elastic proton cut, and cut3. The asymmetries for each of the five cuts in each detector bin are shown plotted versus the azimuthal angle of the octants in Figures 5.34, 5.35, and 5.40 for detectors 1–8, 9–12, and 13–14 respectively. The asymmetries in these plots have been corrected for deadtime, DNL (differential non-linearity), and beam leakage (see Section 5.4.3), but have not yet been corrected for the background events (see Section 5.4.5). The asymmetries for each cut are shown fitted with a sinusoidal fit, along with the reduced χ^2 for the fit, the phase of the fit ϕ_0, the ϕ-independent global offset of the fit A_0, and the transverse asymmetry amplitude $A_\perp$. For detectors 1–8, and to a somewhat lesser extent detectors 9–12, a smooth evolution of the fits to the asymmetries for the background cuts (cut1, cut2a, cut2b, and cut3) can be seen, but the poor statistical precision of the data for detectors 13 and 14 can be clearly seen.

5.4.1.2 Detectors 15 and 16

For detector 15, because of the very wide Q^2 acceptance and timing distribution, it is not clear how a reliable background subtraction can be done, so a very basic analysis of the raw asymmetries has been done and some limits have been determined. Detector 15 was divided into three broad cuts: a pion cut, an elastic proton cut, and cut3. Detector 16 was treated in the same fashion. Figures 5.36 and 5.37 show the yield ToF spectra with the defined cuts for detectors 15 for both the NA and French detectors, and Figures 5.38 and 5.39 show the yield ToF spectra with the defined cuts for the French and NA detectors 16. It is worth noting that the "elastic" cut for detector 16 has no actual elastic events since detector 16 is outside of the elastic proton acceptance. The cut defined as "elastic" for this detector simply corresponds to the elastic proton cut for detector 15. The raw asymmetries versus azimuthal angle for detectors 15 and 16 for each of the three cuts are shown in Figure 5.41. The asymmetries for each cuts are shown fitted with both a sinusoidal fit (the solid black line) and a constant fit (the dashed black line), along with the corresponding reduced χ^2 values and values of interest such as the phase ϕ_0, A_0 (the ϕ-independent offset in the fit from zero), and the transverse asymmetry $A_\perp$. The plots also show a straight-line fit to the data points for comparison (the dashed line). The data in these plots are corrected for beam leakage and deadtime, but have not had the background subtracted. There is a sinusoidal shape to the data for the elastic proton cut for detector 15, but the error bars are so large it is difficult to infer much from the data. From the fits, it can be inferred that $A_\perp$ is not large, probably between -11 and +2 ppm in magnitude for these kinematics. It seems that it might admit a change in sign, but this is of somewhat marginal significance.

5.4.2 Insertable Half-Wave Plate Reversal

The In+Out half-wave plate plots for the hydrogen data taken during the transverse running period are consistent with zero within statistics, with no compelling azimuthal effect or other indication of a systematic false asymmetry. The summed In+Out half-wave plate reversal plots for Detectors 1–8 for all five cuts are shown in Figure 5.42 as a typical example. The data also showed

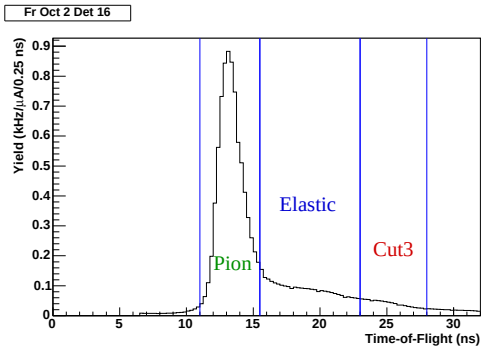

FIG. 5.38: *The ToF spectrum for Octant 2 Detector 16, showing the three PID cuts for the French spectra.*

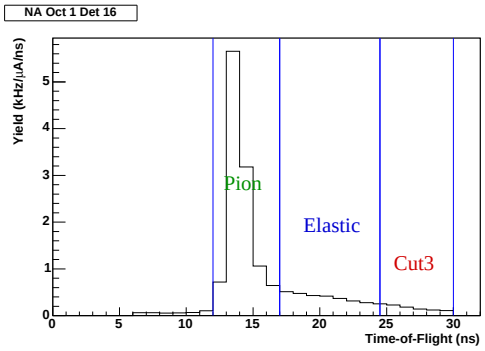

FIG. 5.39: *A picture showing the ToF spectrum and three defined PID cuts for Octant 1, detector 16.*

the predicted behaviour that averaging together the asymmetries from each of the eight octants for a detector bin gave an average asymmetry value consistent with zero, since the sinusoidal trend cancels itself out over the full 2π range.

5.4.3 Corrections for Helicity-Correlated Beam Properties: Beam Leakage, Beam Parameters and Linear Regression

The sinusoidal fits to the asymmetry data showed that there was a significant global ϕ-independent offset A_0 to the asymmetry data for the elastic cut, about -1.4 ppm over all (blinded and not corrected for the beam polarization). An example of this can be seen in the fit to the elastic asymmetries for detectors 1–8, shown in Figure 5.43, where there is clearly a global negative ϕ-independent offset of about -1 ppm (blinded, not corrected for beam polarization). The correction for the beam leakage corrected this ϕ-independent offset, as can be seen in the fit to the asymmetries for detectors 1–8 with the leakage correction applied shown in Figure 5.44. The correction due to the beam leakage was performed identically to the primary forward-angle data set as described in Reference [224], and resulted in a correction of $+1.27$ ppm to each of the asymmetries for detectors 1–8 and $+1.46$ ppm for the asymmetries of detectors 9–12, where these values are blinded (0.805619) and not corrected for the beam polarization (0.7432). Over the two detector bins, the average correction was $+1.37$. Interestingly, the leakage beam does not have much of an

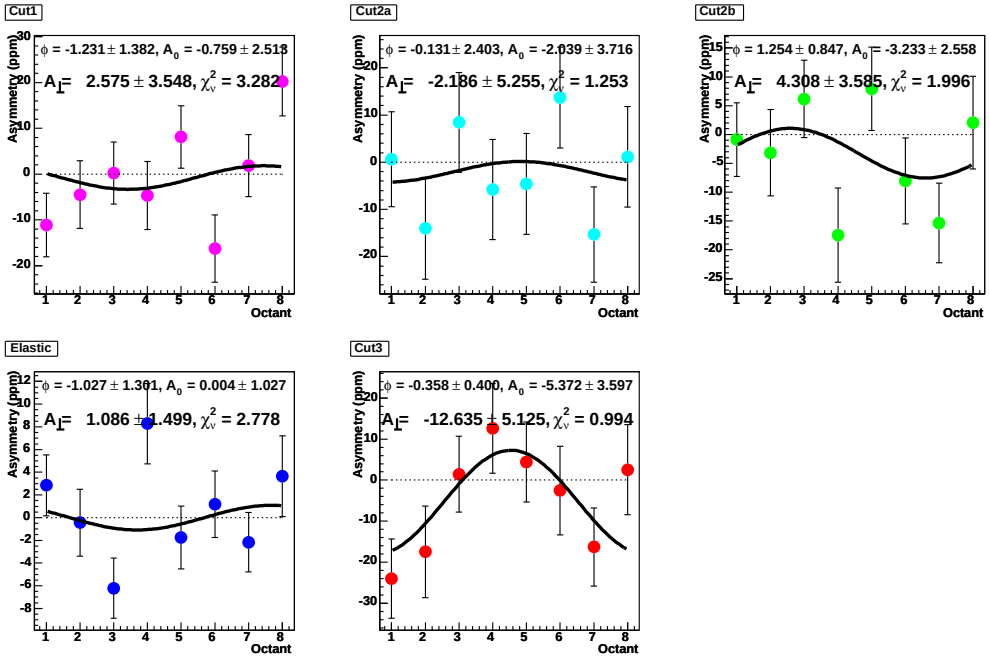

FIG. 5.40: *Raw Asymmetries versus Octant for the five PID cuts for Detectors 13–14 [note: asymmetries are blinded].*

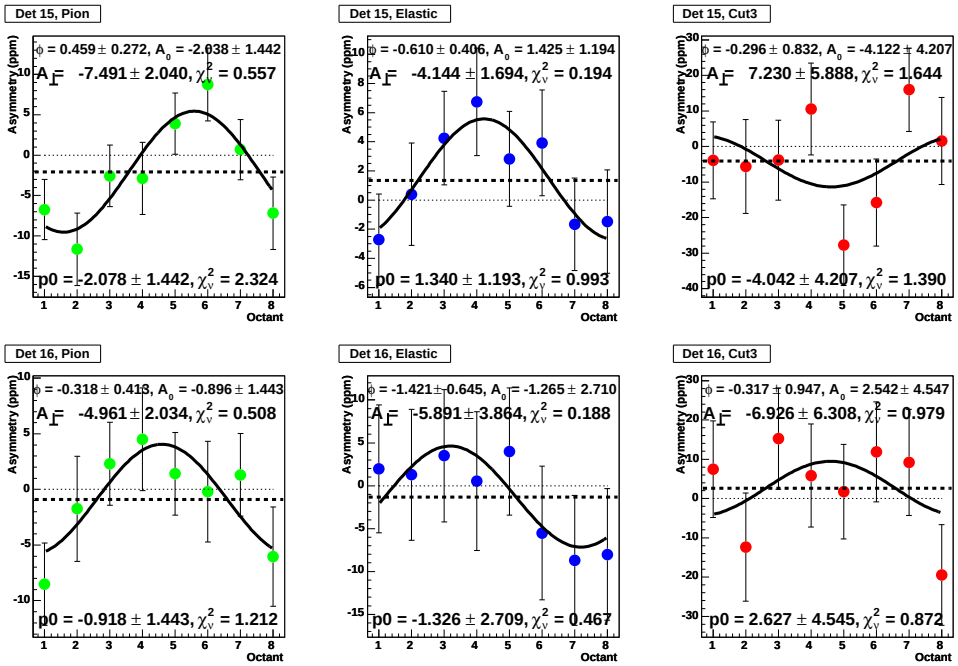

FIG. 5.41: *Raw Asymmetries versus Octant for the five PID cuts for Detectors 15 and 16 [note: asymmetries are blinded].*

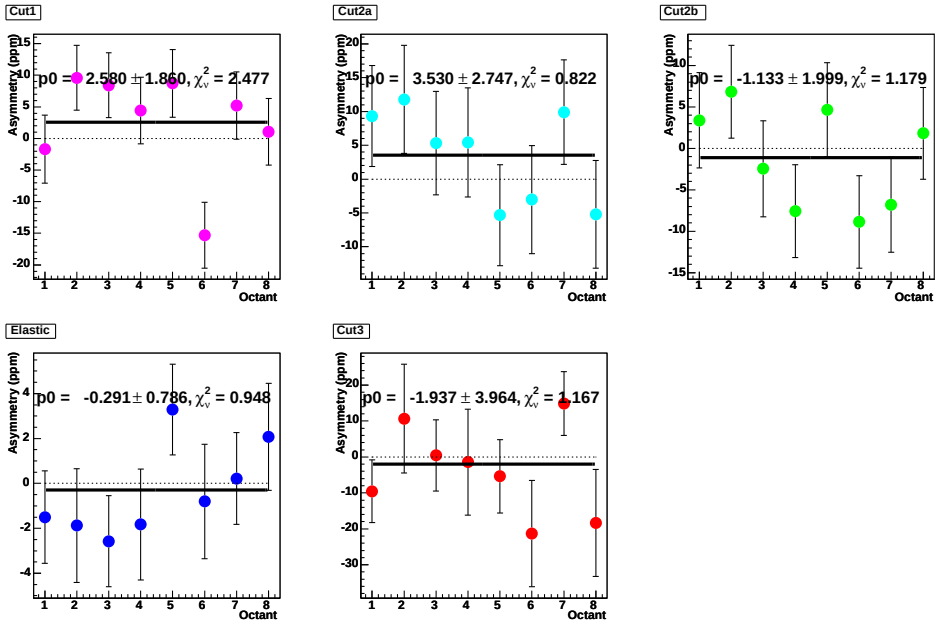

FIG. 5.42: *Linear fits to the summed in+out raw asymmetries versus octant for the transverse data set on hydrogen in each of the five PID cuts for Detectors 1–8 [note: asymmetries are blinded].*

effect on the amplitude of the azimuthal fits since it is a global, ϕ-independent effect, as can be seen by the comparison of the A_n values in Figures 5.43 and 5.44.

Plots of the beam parameter asymmetries and the halo asymmetries from the transverse data-taking period are shown in Figures 5.45 and 5.46. In general, the helicity-correlated beam parameters were not as lovely as they were in the primary longitudinal forward-angle data-taking, probably due to the very different optics for the transport of the transverse beam and the lack of the time required to diagnose and resolve these issues. The charge asymmetry and the halo asymmetries were the most significantly increased during this period. However, both were deemed to be acceptable given the statistical precision of the transverse asymmetry measurement. In the analysis, reasonable cuts were applied to exclude any runs with particularly poor-quality beam.

The regression correction for the helicity-correlated beam parameters cannot be directly applied trivially since the slopes were calculated for the cuts defined in the database for the longitudinal forward-angle data set, not for the modified, detector-summed cuts we have defined for the

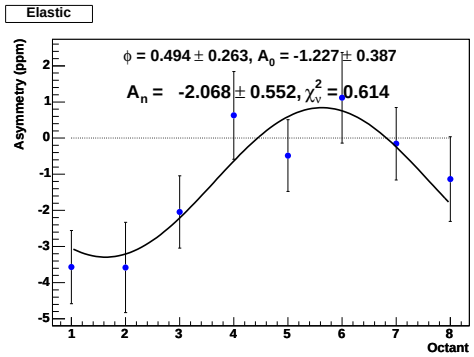

FIG. 5.43: *Raw Asymmetries versus Octant for the elastic cut for Detectors 1–8 without the beam leakage correction applied.*

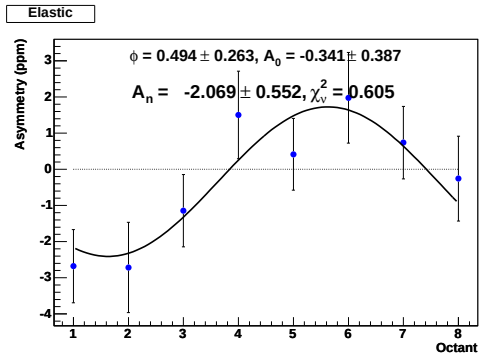

FIG. 5.44: *Raw Asymmetries versus Octant for the elastic cut for Detectors 1–8 with the beam leakage correction applied.*

Detector Bin (DB Cuts)	Unregressed $A_\perp$	Unregressed A_0	Regressed $A_\perp$	Regressed A_0
1-8	-2.25 ± 0.52	-1.19 ± 0.37	-2.18 ± 0.53	-0.91 ± 0.38
9-12	-1.67 ± 0.79	-0.69 ± 0.55	-1.63 ± 0.80	-0.46 ± 0.56
13-14	-1.32 ± 1.43	-0.55 ± 0.97	-1.57 ± 1.44	-0.30 ± 0.98

TABLE 5.10: *The regressed and unregressed values for the database cuts.*

transverse data set. However, as can be seen in Table 5.10, the effect on the extracted value for $A_\perp$ is less than 0.1 ppm for detectors 1 through 12, and 0.25 ppm for 13 and 14, so this discrepancy has been adopted as the systematic uncertainty in for $A_\perp$ due to the helicity-correlated beam parameters.

5.4.4 Luminosity Monitors

The luminosity monitors are also sensitive to the transverse beam asymmetry. These eight quartz Čerenkov detectors are positioned at small angles where the dominant rate comes from Møller scattering (as can be seen in Figure 5.47), but where $e - p$ and $e -$ Al scattering also have significant contributions in order to make things more complicated to interpret [224]. Even so, the azimuthal dependence of the lumi asymmetries gives a valuable cross-check as to the spin-direction of the beam electrons.

The luminosity detectors are actually positioned in two different rings in the beamline after

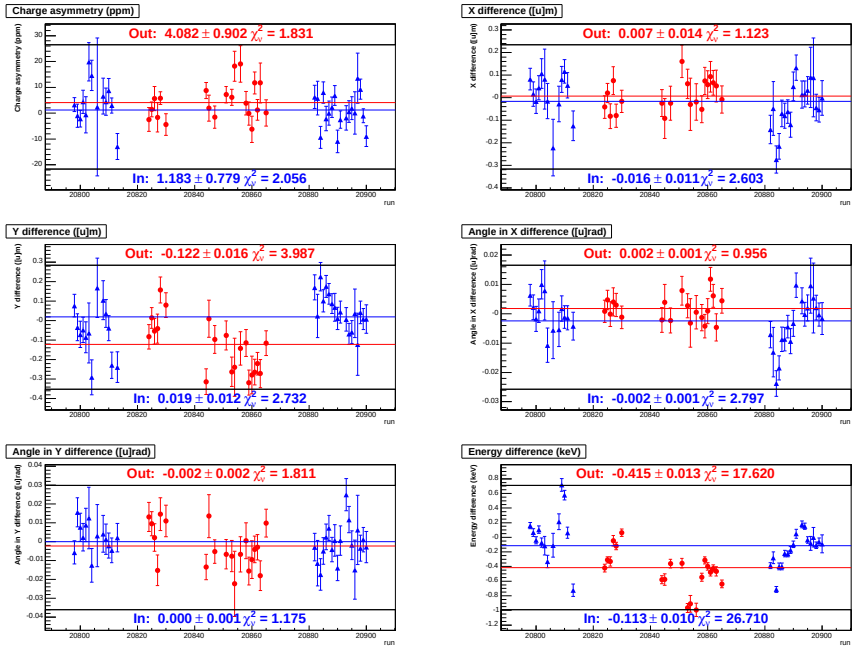

FIG. 5.45: *The helicity-correlated beam parameter asymmetries during the transverse data-taking.*

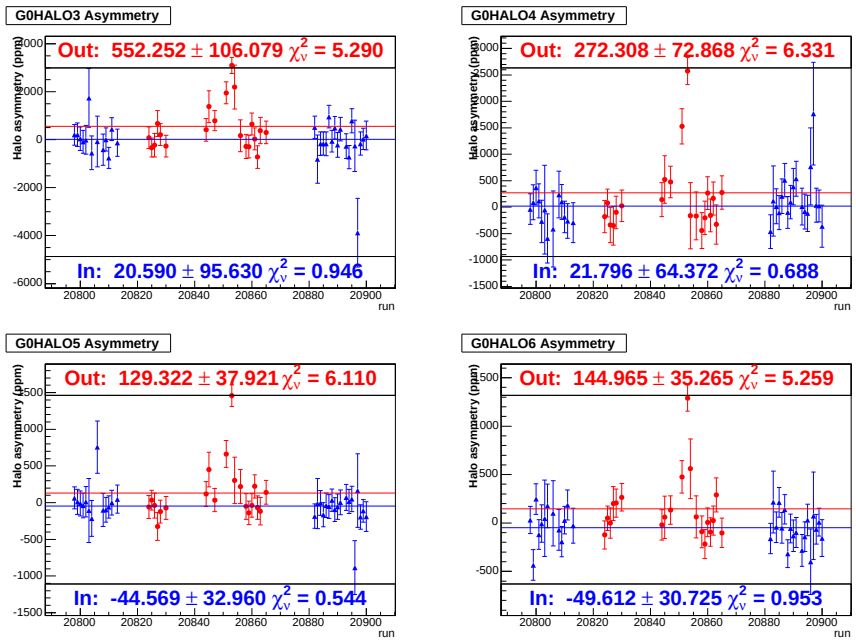

FIG. 5.46: *The asymmetries measured by the girder halo monitors during the transverse data-taking.*

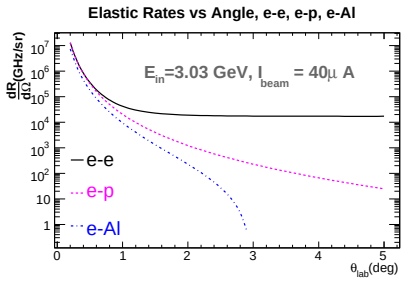

FIG. 5.47: *The electron rates per unit solid angle versus the electron lab angle for Møller, e-p, and e-Al scattering. Figure borrowed from [224].*

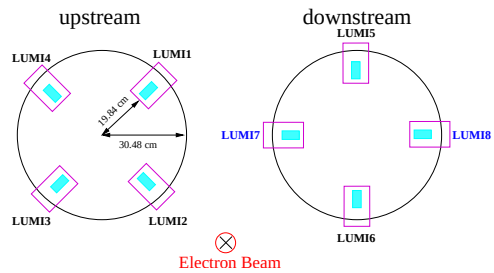

FIG. 5.48: *A diagram of the lumi positions as viewed looking downstream from the G^0 target. The upstream lumis are 699.7 cm downstream of the target, and the downstream lumis are 373.8 cm downstream from the upstream set. Figure borrowed from [224].*

the target, with lumis 1 through 4 in the upstream ring, and 5 through 8 in the downstream ring, oriented as shown in Figure 5.48. Because of this, the lumis in principle are making slightly different measurements due to their locations at slightly different scattering angles ($\theta_{lab} = 1.98°$ for the upstream set, and $\theta_{lab} = 1.29°$ for the downstream set), but this is neglected in this study. Another consideration is that lumis 1 through 6 used photomultiplier tubes (two different models), while 7 and 8 were equipped with vacuum photodiodes, but again, this is neglected, as the asymmetries should be independent of the measurement devices.

The asymmetries measured by the luminosity monitors are shown for each lumi throughout the transverse run period in Figure 5.49 by insertable half-wave plate state. Figures 5.50 through 5.53 show the asymmetries from the luminosity monitors plotted versus the ϕ position of the monitors and fitted for their azimuthal dependence with a sine function. The azimuthal angle ϕ is defined as before, with $\phi = 0°$ at beam left looking downstream, at the position of Lumi7, proceeding clockwise from there. The lumi asymmetries in these plots are from the runs that have passed the parity cut requirements, and have had the regression corrections applied. Figure 5.50 shows the fit to the data points with all the fit parameters allowed to float. The phase from this fit gives us a check of our calculated phase from the spin precession due to the field of the Møller solenoid. From this fit, we find that the phase is $\phi_0 = 0.062 \pm 0.028$ ($3.55° \pm 1.60°$), which agrees fairly well with

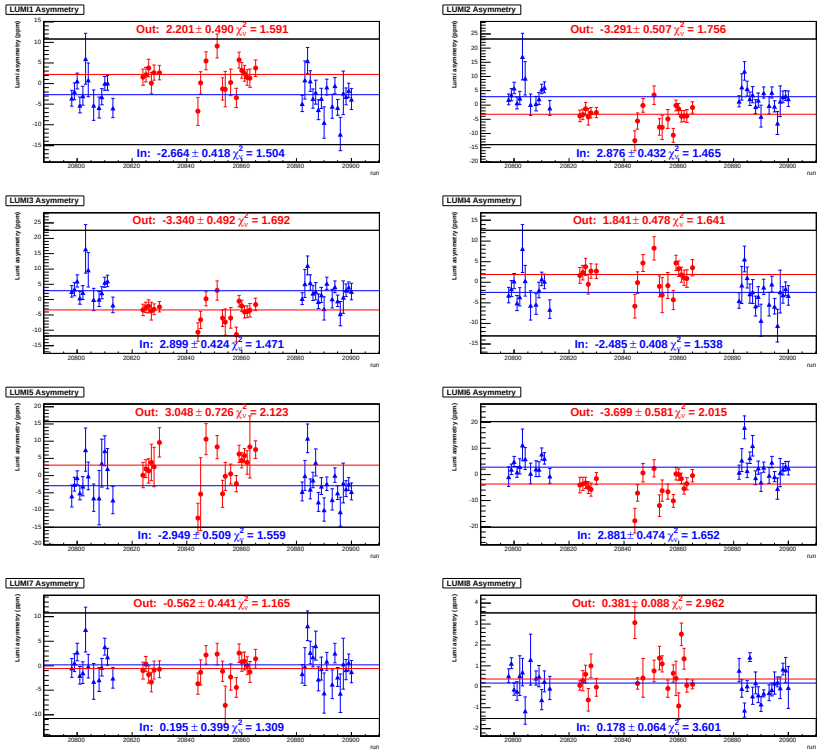

FIG. 5.49: *The helicity-correlated lumi asymmetries for the transverse running period (with regression and parity cuts).*

the calculated value of 0.092 radians, about 5.3 degrees. From this fit, we obtain an amplitude $A_n = -3.53 \pm 0.17$ ppm with $\chi^2_\nu = 1.140$. Forcing the offset A_0 to zero effectively forces the phase ϕ_0 to zero ($\phi_0 = 0.008 \pm 0.014$) with a small increase in the χ^2_ν of the azimuthal fit to 1.800 and a slight decrease of the amplitude, as can be seen in Figure 5.51. Constraining the phase to the calculated Møller precession improves the χ^2_ν to 1.156, although the amplitude decreases a small amount, as shown in Figure 5.52. Finally, constraining both the offset to zero and the phase to the calculated precession of the beam electrons through the Møller solenoid causes the χ^2_ν of the azimuthal fit to deteriorate to 6.196, with a further small decrease in the amplitude. Figure 5.53 displays the fit and the extracted amplitude of the sinusoidal dependence with these constraints. These plots are shown with a straight-line fit for comparison.

For further comparison, the lumi data for the longitudinal running show no clear azimuthal dependence, which tells us that the spin direction of the electrons in the beam for these data was

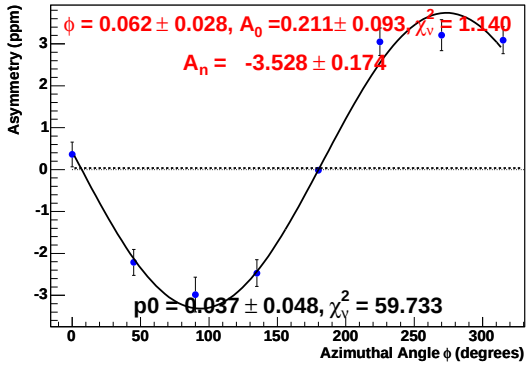

FIG. 5.50: *A plot of the regression-corrected lumi asymmetries versus the phi position of the luminosity monitors with the best sinusoidal fit to the data points. All fit parameters are allowed to float in this fit.*

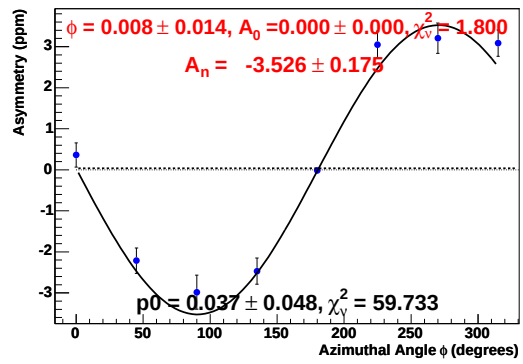

FIG. 5.51: *A plot of the regression-corrected lumi asymmetries versus the phi position of the luminosity monitors with the best sinusoidal fit to the data points. The fit has been constrained to zero vertical offset.*

mostly longitudinal. For an unconstrained azimuthal fit to the lumi asymmetries, an amplitude of $A_n = 0.25 \pm 0.03$ ($\chi^2 = 7.37$) was observed, and by using the same constraints as Figure 5.51, the extracted amplitude becomes $A_n = 0.00 \pm 0.04$ ($\chi^2 = 32.22$). The straight-line fit in these cases was -0.164 ± 0.016 ($\chi^2 = 17.21$).

The rates in the lumis are predominantly from Møller scattering, and the amplitude of the transverse asymmetry from Møller scattering in interesting in its own right. However, the contributions from other scattering processes to the lumi rates make the interpretation of the transverse lumi asymmetry somewhat difficult. The lumi asymmetries for the transverse running of the backward-angle measurements are almost entirely from Møller scattering, and should contain interesting physics.

5.4.5 Corrections for Physics Backgrounds

Because of the poor statistics of this measurement, the same background-correction method used for the forward-angle longitudinal polarization data set described in [224] was unable to be applied. However, simpler methods were used to great success.

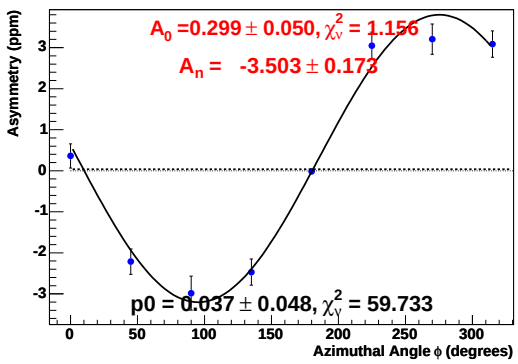

FIG. 5.52: *A plot of the regression-corrected lumi asymmetries versus the phi position of the luminosity monitors with the best sinusoidal fit to the data points. The fit has been constrained to the calculated precession of the spin of the beam electrons through the Møller solenoid.*

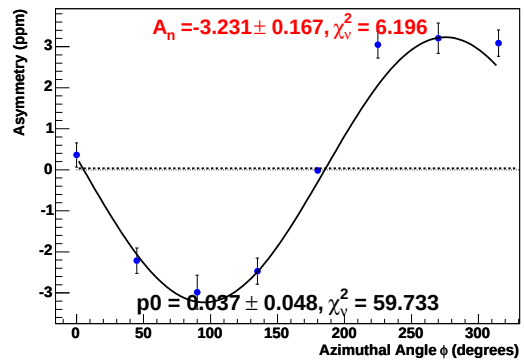

FIG. 5.53: *A plot of the regression-corrected lumi asymmetries versus phi with the best sinusoidal fit to the data points. The fit has been constrained to both the calculated precession of the spin of the beam electrons through the Møller solenoid and to zero vertical offset.*

5.4.5.1 Dilution Factors

In each timebin of the ToF histogram, the measured yield $Y_m(t)$ in it is a combination of the yield from the elastic proton events we are looking for $Y_{elas}(t)$ and some unwanted background events $Y_{bkg}(t)$. So, the measured asymmetry $A_{\perp}^{meas}(t)$ is also a combination of the sought-after elastic asymmetry A_{elas} and the asymmetry due to the background events $A_{bkg}(t)$. The measured asymmetry can be expressed as

$$A_{\perp}^{meas}(t) = f(t)A_{elas}(t) + (1 - f(t))\, A_{bkg}(t), \tag{5.54}$$

where $f(t) = \frac{Y_{elas}(t)}{Y_m(t)}$ is the fraction of the elastic yield in the measured yield.

Fits to the yield spectra for each of the Q^2 bins were then used to determine the dilution factor $f(t)$ for each of the timebins, using the same technique as the forward-angle longitudinal analysis. The elastic peaks of the ToF spectra were fitted with a Gaussian, and the background yields were fitted with a fourth-order polynomial. From these two fits the fraction $f(t)$ was determined for each timebin. An example of this fit for octant 8, detector bin 1–8 is shown in Figure 5.54. The dilution values averaged over the timebins in the elastic cut for each of the detector bins in each octant are shown in Table 5.11.

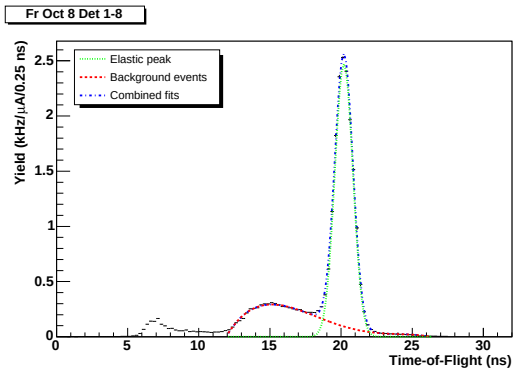

FIG. 5.54: *The fit to extract the dilution factors for octant 8, detectors 1–8.*

The timebin-by-timebin dilution factors were determined for each of the detector groups; however, only the average dilution factor over a PID cut was used to correct the asymmetry for that cut since the statistical precision of the bin-by-bin asymmetries was so poor that a bin-by-bin fit to the asymmetries could not be done satisfactorily.

Octant	Dilution Factors f		
	Detectors 1–8	Detectors 9–12	Det 13–14
1	0.861	0.805	0.897
2	0.916	0.854	0.841
3	0.875	0.763	0.875
4	0.917	0.860	0.837
5	0.862	0.794	0.767
6	0.909	0.863	0.840
7	0.862	0.647	0.867
8	0.916	0.864	0.840

TABLE 5.11: *Elastic cut dilution factors (signal/measured yield).*

5.4.5.2 The Two-Step Method

To estimate the asymmetry contribution of the background underneath the elastic peak, the asymmetries for cut1, cut2a, cut2b, and cut3 for each octant and detector bin were corrected for the dilution of the asymmetry by the elastic events by using the formula

$$A_{bkg} = \frac{1}{1-f}\left(A_{\perp}^{meas} - f A_{elas}\right), \tag{5.55}$$

since we know that the measured asymmetry $A_{\perp}^{meas}$ is a combination of the elastic and background asymmetries (i.e. $A_{\perp}^{meas} = fA_{elas} + (1-f)A_{bkg}$, where f is the dilution fraction of the elastic signal yield divided by the total measured yield). Since we do not actually know the precise elastic asymmetry, for this we used the measured elastic asymmetry, since the dilution of the elastic peak into the other cuts was in general very small. The background asymmetries were then fitted with a background function that was linear in ToF. The background function was then evaluated at the elastic peak to determine the background asymmetry. The fits to the background asymmetries for the NA and French detectors can be viewed in Figures 5.55 and 5.56 respectively. In the plots, the open blue circles are the original data points (shown for comparison only), the filled blue circles are the points after the dilution correction for the elastic contamination that were fitted to determine the background asymmetry, and the red square is the extracted background underneath the elastic peak. The error bar on these estimated background values were determined by defining the intercept to be at the elastic peak and then using the usual weighted error bars for the intercept on a linear fit. For fits where the reduced χ^2 was greater than 1, the error bars for the estimated background under the elastic peak were inflated by multiplying them by the $\sqrt{\chi^2_\nu}$ to account for any unknown systematic driving the poor fit. The elastic asymmetry was then corrected for the estimated background asymmetry using the equation

$$A_{elas} = \frac{1}{f}\left(A_{\perp}^{meas} - (1-f)A_{bkg}\right). \tag{5.56}$$

It is hard to tell if the background varies smoothly with detector number, since there are only three points for each octant. The background asymmetries do not really display a particularly nice sinusoidal shape, but interpretation is difficult due to the really poor statistics involved. These plots can be viewed in Figures 5.57 and 5.58.

The contamination of the elastic events into the cuts defined for the background events was very small due to the rather large width of the elastic cut. To better understand the effect of these elastic events in the background cuts, the background fit was done and the background asymmetry extracted both with and without applying the dilution correction for the elastic contamination

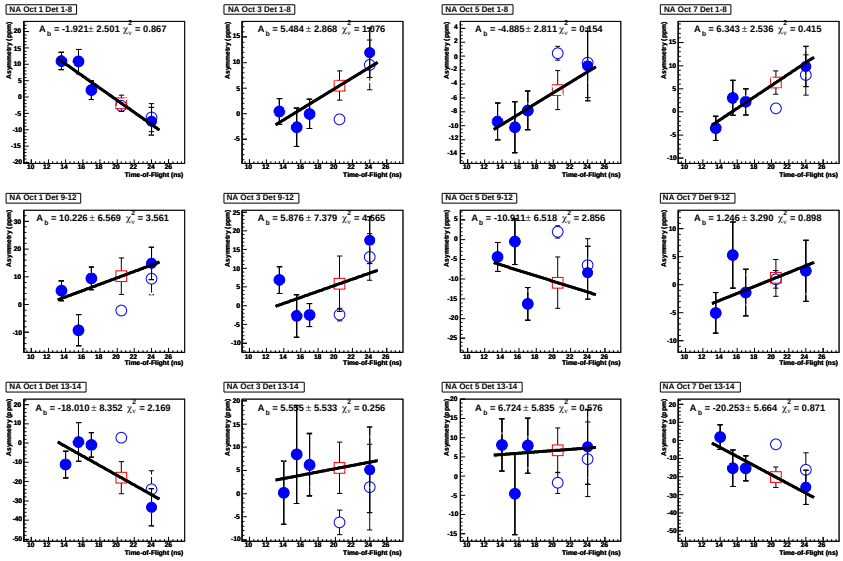

FIG. 5.55: *The Two-Step Method – The linear fit to estimate the background asymmetry for the NA detectors. The estimated background asymmetry and the reduced χ^2 of the fit are shown. The red square is the estimated background asymmetry under the elastic peak, and the blue circles are the data points for each of the five cuts (open circles are original data points; filled are dilution-corrected used in the fits).*

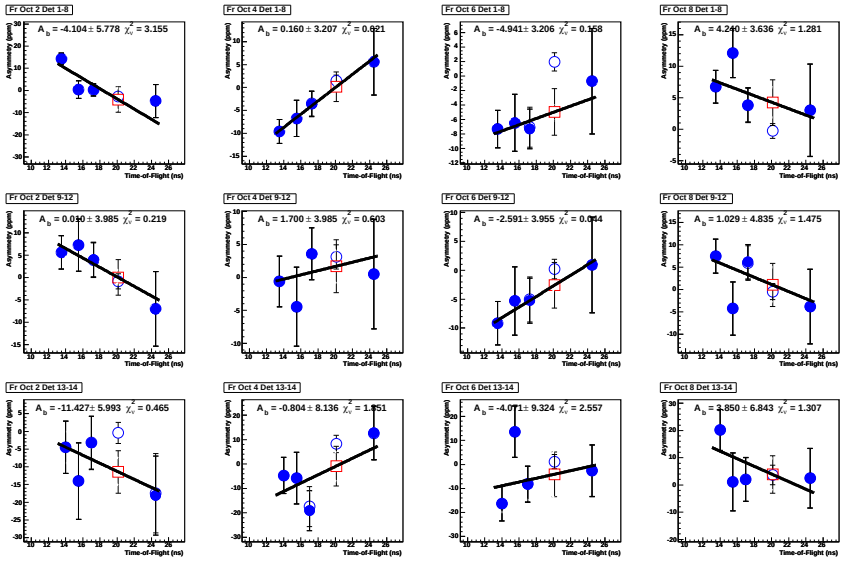

FIG. 5.56: *The Two-Step Method – The linear fit to estimate the background asymmetry for the French detectors. The estimated background asymmetry and the reduced χ^2 of the fit are shown. The red square is the estimated background asymmetry under the elastic peak, and the blue circles are the data points for each of the five cuts (open circles are original data points; filled are dilution-corrected used in the fits).*

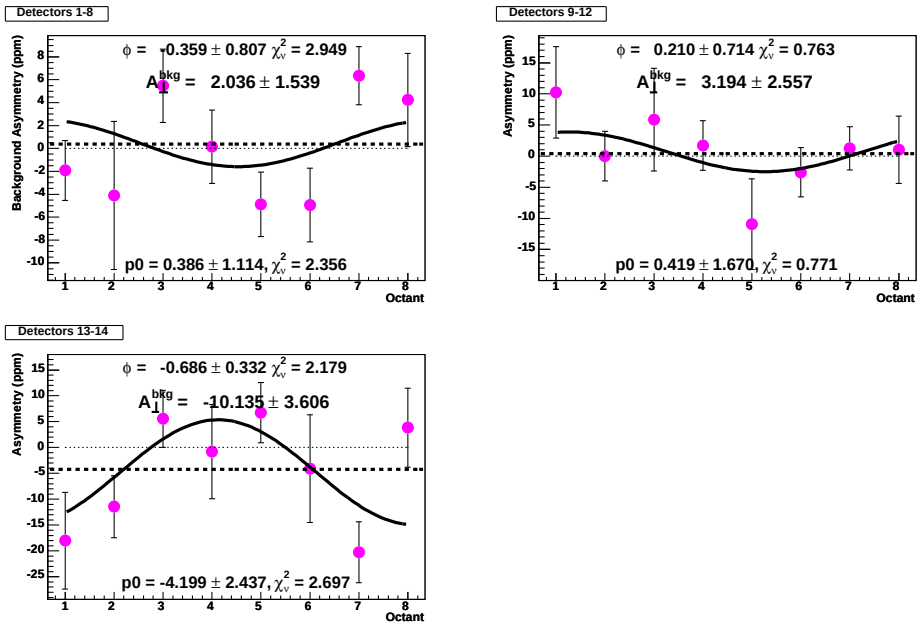

FIG. 5.57: *The Two-Step Method – Azimuthal fits of the extracted background asymmetries for each detector bin.*

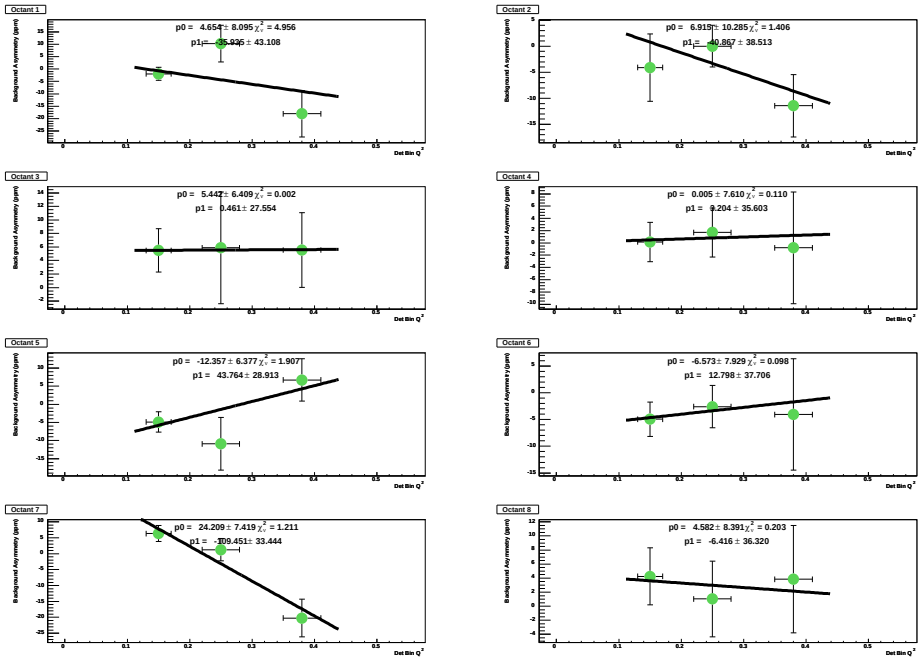

FIG. 5.58: *The Two-Step Method – Linear fits to the extracted background asymmetries for each octant.*

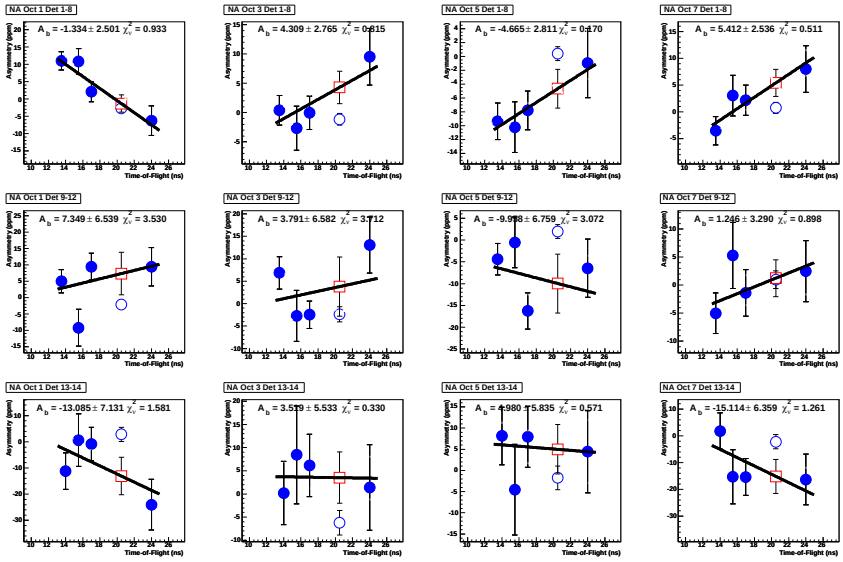

FIG. 5.59: *The Two-Step Method,* No Dilution Correction – *The linear fit to estimate the background asymmetry for the NA detectors without using the dilution correction. The estimated background asymmetry and the reduced χ^2 of the fit are shown. The red square is the estimated background asymmetry under the elastic peak, and the blue circles are the data points for each of the five cuts.*

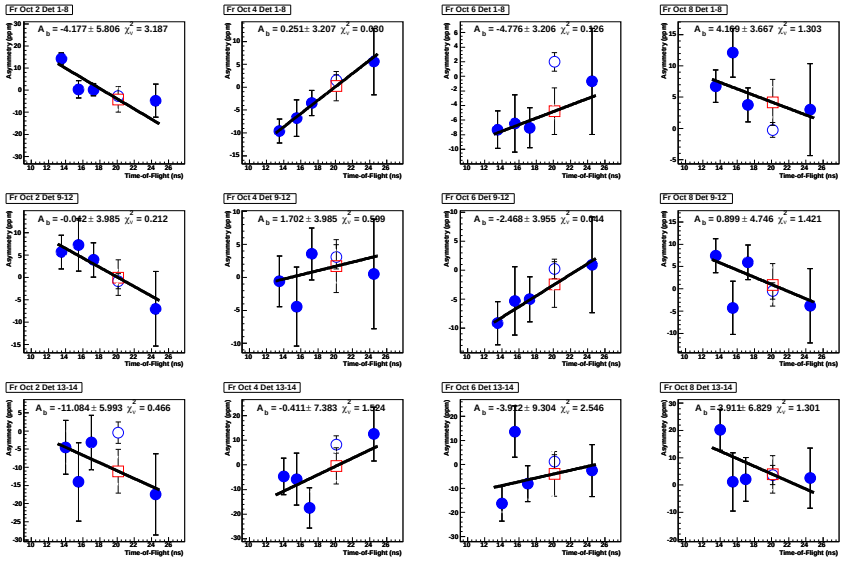

FIG. 5.60: *The Two-Step Method,* No Dilution Correction – *The linear fit to estimate the background asymmetry for the French detectors without using the dilution correction. The estimated background asymmetry and the reduced χ^2 of the fit are shown. The red square is the estimated background asymmetry under the elastic peak, and the blue circles are the data points for each of the five cuts.*

Octant	Extracted Background Asymmetry A_{bkg} (ppm)		
	Detectors 1–8	Detectors 9–12	Detectors 13–14
1	-1.92 ± 2.60	10.23 ± 7.34	-18.01 ± 9.34
2	-4.10 ± 6.46	0.01 ± 3.99	-11.43 ± 5.99
3	5.48 ± 3.21	5.88 ± 8.25	5.56 ± 5.53
4	0.16 ± 3.21	1.70 ± 3.99	-0.80 ± 9.10
5	-4.89 ± 2.81	-10.91 ± 7.29	6.72 ± 5.84
6	-4.94 ± 3.21	-2.59 ± 3.96	-4.07 ± 10.43
7	6.34 ± 2.54	1.25 ± 3.49	-20.25 ± 5.91
8	4.24 ± 4.07	1.03 ± 5.41	3.85 ± 7.65

TABLE 5.12: *The extracted background asymmetries under the elastic peak for each detector bin and octant using the two-step correction method.*

into the other cuts. Cut3 had the most contamination from the elastic peak, so the effect of the dilution correction is most evident for those asymmetries. In general, the cut3 asymmetries only shifted a few ppm, although the largest shift in NA detector bin 13–14 was approximately 8 ppm (although the error bars on these asymmetries are approximately 10 ppm, so they only weakly constrain the fits). Linear fits to the asymmetries in the background cuts without the dilution correction applied as shown for comparison in Figures 5.59 and 5.60.

5.4.5.3 Simultaneous Fit Method

Another method used to extract the elastic proton asymmetry and the background asymmetry from the measured asymmetry was by fitting the asymmetries for all five cuts assuming a linear background function in τ and a constant elastic asymmetry using the equation

$$A_{\perp}^{meas} = f A_{elas} + (1 - f) A_{bkg}(\tau), \tag{5.57}$$

where f is the dilution factor, A_{elas} is constant over τ, $A_{bkg}(\tau)$ is linear with τ, and τ is the average time-of-flight for a particular cut, not the ToF for each bin as in the analysis for the longitudinal forward-angle dataset. By doing this fit to the measured asymmetry, a simultaneous determination of the elastic and background asymmetries can be made. The value of the pure elastic asymmetry is then directly obtained from the constant function A_{elas}, and the value of the background asymmetry under the elastic peak is obtained by evaluating the linear background function $A_{bkg}(\tau)$ at

the elastic time-of-flight. The linear background fits are shown in Figures 5.61 and 5.62 for the NA and French detectors, respectively. In the plots, the filled blue circles are the data points for the five cuts that were fitted to obtain the elastic and background asymmetries, and the red square is the extracted background underneath the elastic peak. As with the previous method, the error bar on this estimated background values were determined by defining the intercept to be at the elastic peak and then using the usual weighted error bars for the intercept on a linear fit. Background fits that had a reduced $\chi^2 > 1$ were again inflated by the $\sqrt{\chi^2_\nu}$. This method yields comparable results to the first method for the extracted background under the elastic peak, shown in Table 5.13.

As with the previous method, it is difficult to infer much about the behaviour of the extracted background asymmetry across the detectors since there are only three detector bins. Again, the background asymmetry does not show a clear sinusoidal shape with the octants, but the precision of the points is also rather poor. Both of these plots can be seen in Figures 5.64 and 5.63, respectively.

Octant	Extracted Background Asymmetry A_{bkg} (ppm)		
	Detectors 1–8	Detectors 9–12	Det 13–14
1	-2.27 ± 3.25	10.50 ± 10.41	-15.85 ± 11.67
2	-4.02 ± 6.55	-0.01 ± 4.03	-11.60 ± 6.26
3	4.90 ± 3.67	3.37 ± 9.68	7.03 ± 7.88
4	0.14 ± 3.26	1.59 ± 4.08	-0.66 ± 9.28
5	-5.30 ± 3.52	-12.57 ± 8.38	7.13 ± 8.84
6	-4.92 ± 3.25	-2.60 ± 4.04	-3.98 ± 10.80
7	6.69 ± 3.06	1.25 ± 3.49	-24.23 ± 8.94
8	4.31 ± 4.10	0.90 ± 5.54	3.80 ± 8.04

TABLE 5.13: *The extracted background asymmetries under the elastic peak for each detector bin and octant using the simultaneous fit method.*

5.4.5.4 Simple Monte Carlo

As a sanity check for the error bars for the background fits, a simple Monte Carlo was developed. In this Monte Carlo, the two-step fitting method was used. A point was randomly generated for each of the four background cuts according to a Gaussian distribution centered at the measured asymmetry value for that cut and with a sigma equivalent to the error bar for that measured

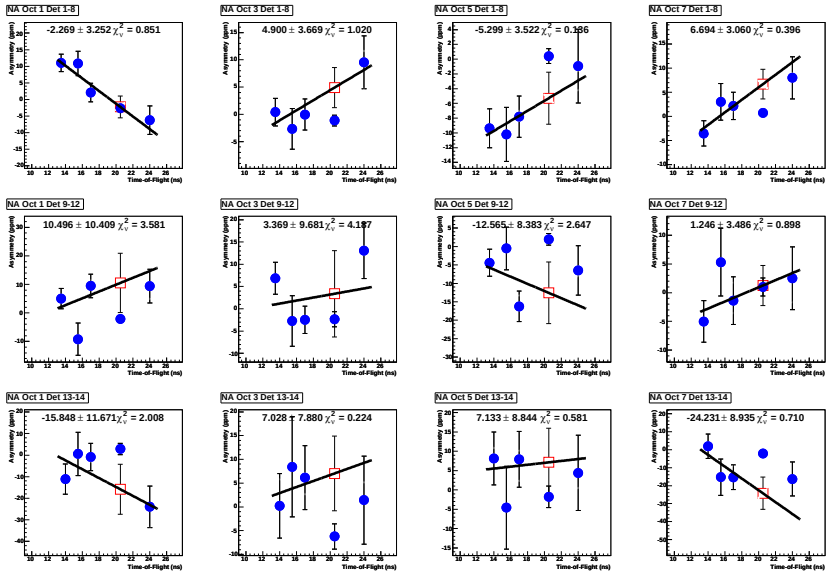

FIG. 5.61: *Simultaneous Fit Method – The linear fit to estimate the background asymmetry for the NA detectors using the simultaneous fit method. The estimated background asymmetry and the reduced χ^2 of the fit are shown. The red square is the estimated background asymmetry under the elastic peak, and the blue circles are the data points for each of the five cuts.*

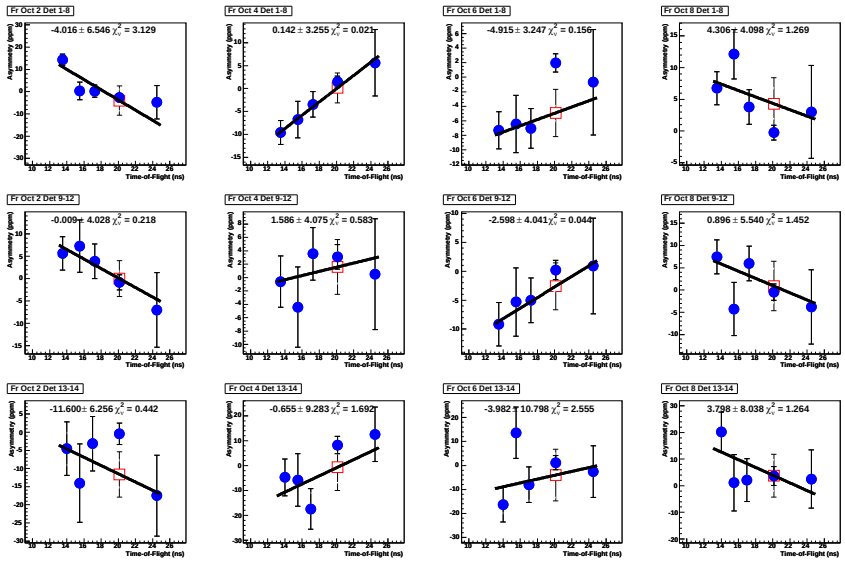

FIG. 5.62: *Simultaneous Fit Method – The linear fit to estimate the background asymmetry for the French detectors using the simultaneous fit method. The estimated background asymmetry and the reduced χ^2 of the fit are shown. The red square is the estimated background asymmetry under the elastic peak, and the blue circles are the data points for each of the five cuts.*

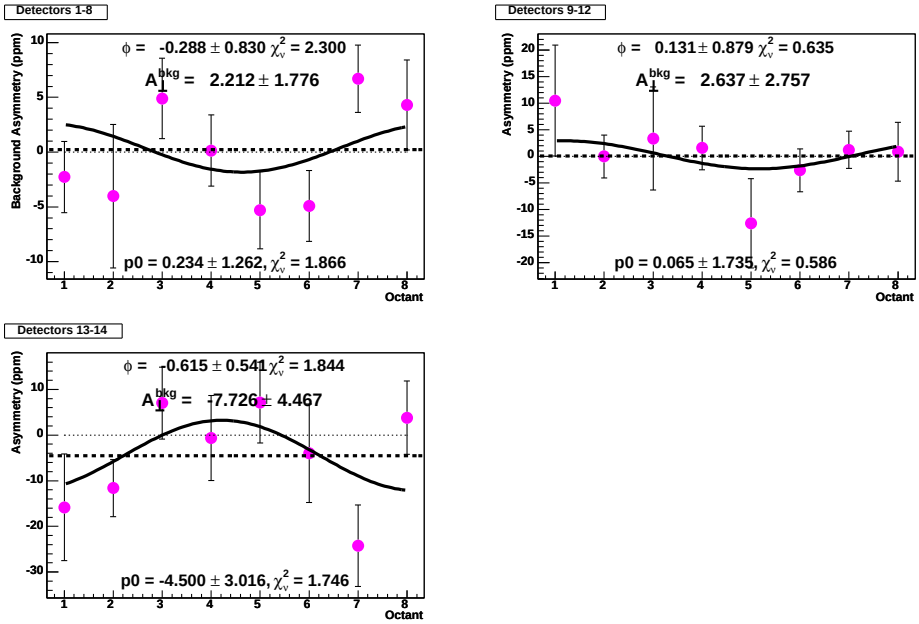

FIG. 5.63: *Simultaneous Fit Method – Azimuthal fits of the extracted background asymmetries for each detector bin.*

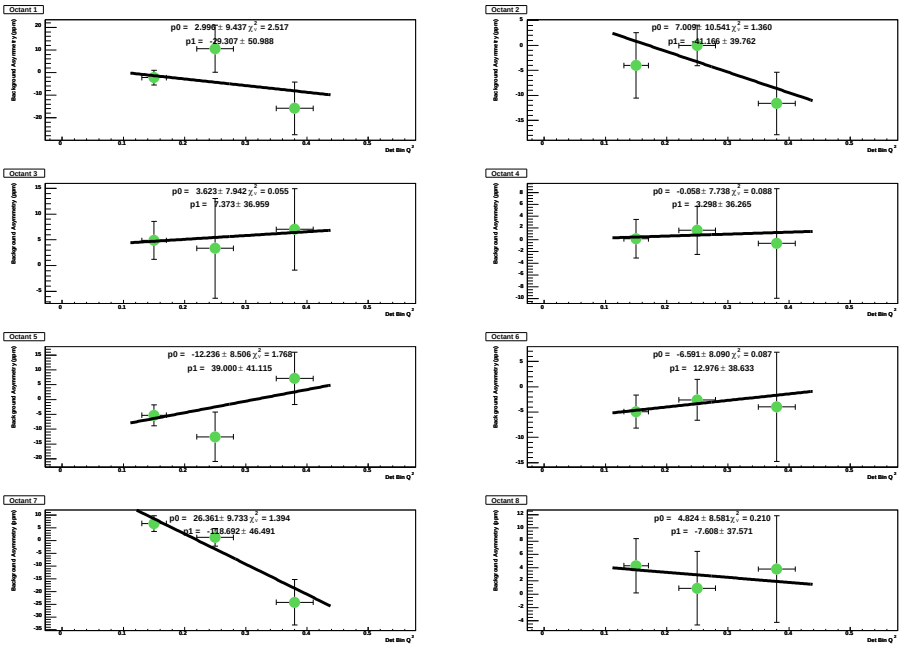

FIG. 5.64: *Simultaneous Fit Method – Linear fits to the extracted background asymmetries for each octant.*

asymmetry. After the four background points had been generated, a linear fit was performed and the value of the linear background fit at the proton peak ToF was evaluated and dumped into a histogram. This process was repeated a few thousand times and then the resulting Gaussian peak was fitted to obtain the mean and the sigma values. This was done for each of the detectors bins for each octant. The results of the Monte Carlo simulation are displayed in Table 5.14. The Monte Carlo gives very similar results and error bars to the background fits in the other methods (before the inflation by the $\sqrt{\chi^2}$ for the poorer fits).

Octant	Estimated Background Asymmetry (Monte Carlo)		
	Detectors 1–8	Detectors 9–12	Detectors 13–14
1	-2.1 ± 2.6	10.4 ± 3.4	-18.0 ± 5.5
2	-4.2 ± 3.2	0.01 ± 4.0	-11.5 ± 5.8
3	5.5 ± 2.7	6.1 ± 3.2	5.6 ± 5.4
4	0.3 ± 3.3	1.8 ± 3.8	-0.7 ± 5.8
5	-5.0 ± 2.7	-10.7 ± 3.6	6.7 ± 5.8
6	-4.8 ± 3.2	-2.6 ± 4.1	-4.3 ± 5.8
7	6.5 ± 2.6	1.2 ± 3.4	-20.6 ± 5.4
8	4.2 ± 3.0	1.3 ± 4.0	3.6 ± 6.0

TABLE 5.14: *The Monte Carlo results based on the two-step method. Asymmetries are in ppm.*

5.4.5.5 Comparison of Extracted Background Asymmetries

The extracted background asymmetries for the events that reside underneath the elastic peak that have been determined by these two analysis methods are summarized in Table 5.15. The results from the two-step Monte Carlo are also shown for ease of comparison. The extracted background asymmetries are very consistent between the two analysis methods. The Monte Carlo also gives similar results, and error bars that are comparable (before the inflation of the fitted results by $\sqrt{\chi^2_\nu}$ for the poorer fits).

For the purposes of publications and presentations of these data, the simultaneous fit method was chosen due to its generally somewhat more conservative error bars. However, the good agreement between the two methods is a good cross-check and implies that there are no dominant unknown systematic errors in the background correction technique.

Octant	Detectors 1–8		
	A_{bkg}^{2step} (ppm)	A_{bkg}^{simul} (ppm)	A_{bkg}^{MC} (ppm)
1	-1.92 ± 2.60	-2.27 ± 3.25	-2.1 ± 2.6
2	-4.10 ± 6.46	-4.02 ± 6.55	-4.2 ± 3.2
3	5.48 ± 3.21	4.90 ± 3.67	5.5 ± 2.7
4	0.16 ± 3.21	0.14 ± 3.26	0.3 ± 3.3
5	-4.89 ± 2.81	-5.30 ± 3.52	-5.0 ± 2.7
6	-4.94 ± 3.21	-4.92 ± 3.25	-4.8 ± 3.2
7	6.34 ± 2.54	6.69 ± 3.06	6.5 ± 2.6
8	4.24 ± 4.07	4.31 ± 4.10	4.2 ± 3.0
Octant	Detectors 9–12		
	A_{bkg}^{2step}	A_{bkg}^{simul}	A_{bkg}^{MC}
1	10.23 ± 7.34	10.50 ± 10.41	10.4 ± 3.4
2	0.01 ± 3.99	-0.01 ± 4.03	0.01 ± 4.0
3	5.88 ± 8.25	3.37 ± 9.68	6.1 ± 3.2
4	1.70 ± 3.99	1.59 ± 4.08	1.8 ± 3.8
5	-10.91 ± 7.29	-12.57 ± 8.38	-10.7 ± 3.6
6	-2.59 ± 3.96	-2.60 ± 4.04	-2.6 ± 4.1
7	1.25 ± 3.49	1.25 ± 3.49	1.2 ± 3.4
8	1.03 ± 5.41	0.90 ± 5.54	1.3 ± 4.0
Octant	Detectors 13–14		
	A_{bkg}^{2step}	A_{bkg}^{simul}	A_{bkg}^{MC}
1	-18.01 ± 9.34	-15.85 ± 11.67	-18.0 ± 5.5
2	-11.43 ± 5.99	-11.60 ± 6.26	-11.5 ± 5.8
3	5.56 ± 5.53	7.03 ± 7.88	5.6 ± 5.4
4	-0.80 ± 9.10	-0.66 ± 9.28	-0.7 ± 5.8
5	6.72 ± 5.84	7.13 ± 8.84	6.7 ± 5.8
6	-4.07 ± 10.43	-3.98 ± 10.80	-4.3 ± 5.8
7	-20.25 ± 5.91	-24.23 ± 8.94	-20.6 ± 5.4
8	3.85 ± 7.65	3.80 ± 8.04	3.6 ± 6.0

TABLE 5.15: *The extracted background asymmetries under the elastic peak for each detector bin and octant using the two-step method and the simultaneous fit method, as well as the results of the simple Monte Carlo. The errors are the errors from the fits (all asymmetries are blinded).*

5.4.6 Corrected Asymmetries

The background-corrected, but still blinded elastic asymmetries for both analysis methods with the errors from the fits are listed in Table 5.16, along with the uncorrected measured asymmetries for comparison. The two methods yield results in excellent agreement.

The corrected elastic asymmetries for the two analysis methods are shown in Figures 5.65 and 5.66 plotted versus octant and fitted with the form

$$A_{\perp}^{meas} = |A_{\perp}| \sin(\phi + \phi_0), \tag{5.58}$$

where ϕ is the azimuthal angle (following our defined coordinates where octant 7 is at 0°, octant 1 is at 90°, etc.), ϕ_0 is the phase, and A_0 is the offset. Both the phase ϕ_0 and the ϕ-independent offset A_0 are allowed to be free in these fits. A constant fit is also shown in each plot for comparison. The asymmetries in detector bins 1–8 and 9–12 show a distinct sinusoidal trend. The value of $A_{\perp}$ from the fits for each of the detector groups is shown on the plots.

The azimuthal fits for detectors 13 and 14 are poor in both analysis methods. The wretched statistical precision of these data prevents the detailed study of the background asymmetries needed for these higher-numbered detectors, where the backgrounds from processes such as hyperon decay became an issue in the primary forward-angle longitudinal analysis. Extensive investigation has not revealed any problems with these data due to hardware, software, or beam issues, but the statistics are so poor that it was not possible to pinpoint a particular set of runs or period of time where the data might indicate that a problem arose. As with many measurements, more data would have been useful. It is worth noting that although these data may show some evidence of a sinusoidal trend, the constant fit also shown in the plots is somewhat better.

5.4.7 Aluminum Frame Data

There were a few hours (∼5) of data taken on the aluminum frame target. The data do not indicate a significant transverse beam asymmetry contribution from the aluminum of the target within the very poor statistics of these data. The "raw" asymmetries (corrected for deadtime,

Octant	Detectors 1-8		
	$A_{\perp}^{meas}$ (ppm)	A_{elas}^{2step} (ppm)	A_{elas}^{simul} (ppm)
1	-2.68 ± 1.01	-2.80 ± 1.25	-2.72 ± 1.61
2	-2.72 ± 1.25	-2.59 ± 1.49	-2.61 ± 1.64
3	-1.14 ± 1.00	-2.09 ± 1.23	-1.97 ± 1.52
4	1.50 ± 1.21	1.63 ± 1.36	1.63 ± 1.51
5	0.41 ± 0.99	1.26 ± 1.24	1.34 ± 1.61
6	1.98 ± 1.25	2.67 ± 1.42	2.66 ± 1.60
7	0.74 ± 1.00	-0.16 ± 1.23	-0.23 ± 1.56
8	-0.26 ± 1.17	-0.67 ± 1.33	-0.68 ± 1.49
Octant	Detectors 9-12		
	$A_{\perp}^{meas}$	A_{elas}^{2step}	A_{elas}^{simul}
1	-2.15 ± 1.54	-5.15 ± 2.62	-5.18 ± 3.85
2	-0.85 ± 1.70	-1.00 ± 2.10	-0.99 ± 2.56
3	-2.37 ± 1.69	-4.94 ± 3.39	-3.86 ± 4.59
4	3.11 ± 1.83	3.33 ± 2.22	3.38 ± 2.68
5	1.95 ± 1.58	5.28 ± 2.74	5.80 ± 3.69
6	0.22 ± 1.68	0.67 ± 2.04	0.67 ± 2.47
7	0.98 ± 1.56	0.83 ± 3.07	0.83 ± 5.01
8	-0.47 ± 1.81	-0.70 ± 2.26	-0.65 ± 2.70
Octant	Detectors 13-14		
	$A_{\perp}^{meas}$	A_{elas}^{2step}	A_{elas}^{simul}
1	2.85 ± 2.68	5.25 ± 3.18	4.83 ± 3.78
2	-0.44 ± 2.95	1.64 ± 3.68	1.71 ± 4.58
3	-6.21 ± 2.66	-7.90 ± 3.14	-8.18 ± 3.98
4	8.28 ± 3.53	10.06 ± 4.58	9.87 ± 5.60
5	-1.76 ± 2.77	-4.34 ± 4.02	-4.43 ± 6.72
6	1.17 ± 2.93	2.17 ± 4.01	2.13 ± 4.84
7	-2.16 ± 2.62	0.60 ± 3.15	1.39 ± 4.19
8	3.65 ± 3.56	3.61 ± 4.47	3.58 ± 5.50

TABLE 5.16: *The corrected measured elastic transverse asymmetries for each detector bin and octant using both the two-step method and the simultaneous fit method. The measured asymmetries before the correction for the background are shown for comparison. Errors come from the fits (all asymmetries are blinded and are not corrected for the beam polarization).*

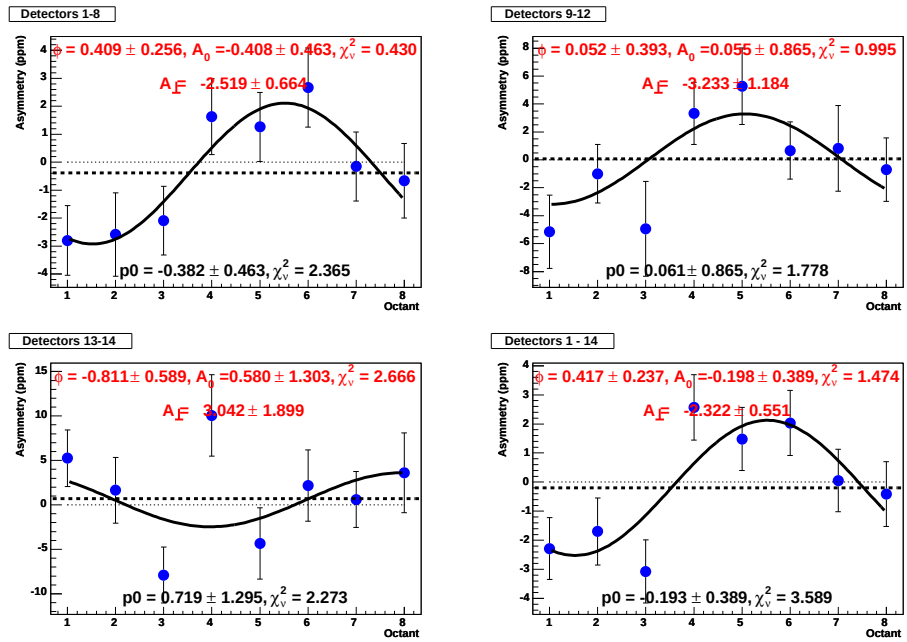

FIG. 5.65: *The Two-Step Method – Azimuthal fits to the corrected elastic asymmetries versus octant for each of the detector groups using the two-step analysis method. A linear fit is also shown for comparison [note: asymmetries are still blinded].*

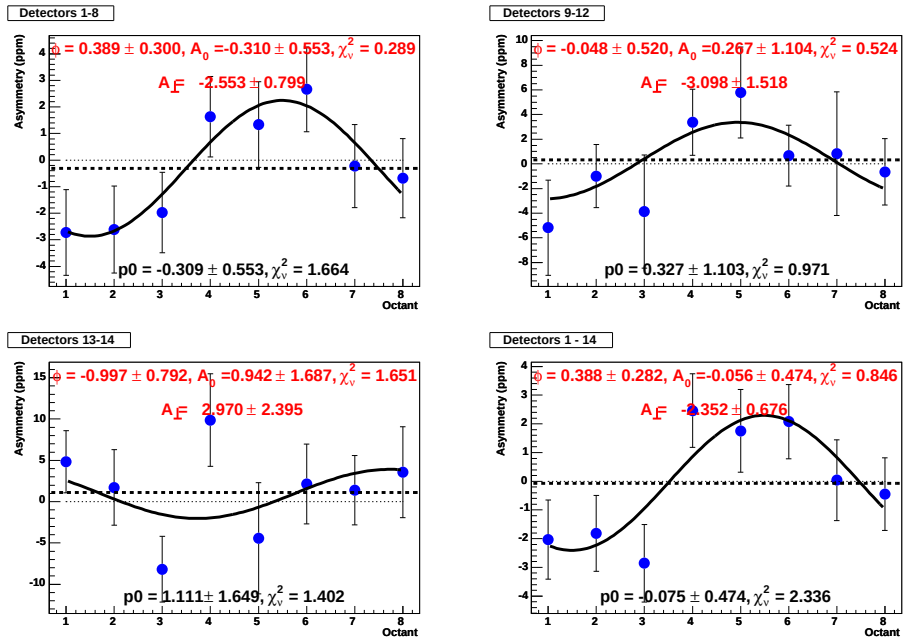

FIG. 5.66: *Simultaneous Fit Method – Azimuthal fits to the corrected elastic asymmetries versus octant for each of the detector groups using the simultaneous fit analysis method. A linear fit is also shown for comparison [note: asymmetries are still blinded].*

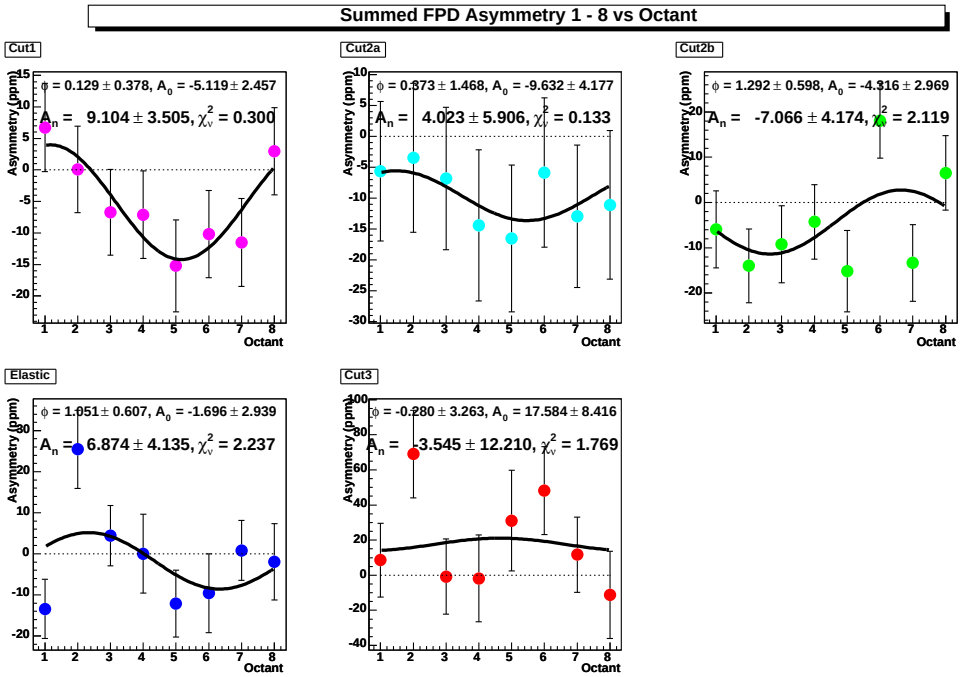

FIG. 5.67: *Azimuthal fits to the raw asymmetries versus octant for the aluminum data in each of the five PID cuts for Detectors 1–8 [note: asymmetries are blinded].*

DNL, etc., but not for background) for the five PID cuts for detectors $1-8$ are shown in Figure 5.67. These data are also shown without any beam leakage corrections or parity-quality beam cuts. The ϕ-independent offset A_0 that is caused largely by the beam leakage is readily apparent. The data are shown with a sinusoidal fit that is unconstrained in the phase and global offset A_0.

Table 5.17 shows the results of the sinusoidal fit and measured linear fit to the measured aluminum elastic asymmetries for the three detector bins. Within the pathetic statistics of the measurement, the aluminum of the target cell does not appear to contribute a significant azimuthal component to the measured elastic asymmetry from the hydrogen target, although the measurement is not very precise.

Detector Bin	Aluminum Elastic Asymmetry A^{Al}_{elas}			
	$A_\perp$ (ppm)	χ^2_ν	constant fit (ppm)	χ^2_ν
1–8	6.87 ± 4.14	2.237	-1.59 ± 2.93	1.993
9–12	-5.85 ± 6.15	0.855	-9.08 ± 4.34	0.740
13–14	-12.41 ± 10.53	1.065	-3.27 ± 7.50	0.959

TABLE 5.17: *The comparison of the results from the sinusoidal and constant fits of the raw asymmetries for the elastic cut of the aluminum transverse data.*

5.4.8 Discussion of Systematic Uncertainties

The sources of systematic errors and their uncertainty for this measurement are summarized in Table 5.18. All of the yield rates were corrected for electronics deadtimes of 10–15%, determined by measurements of the yield dependence on the beam current, exactly as it was done for the analysis of the longitudinal data set [194, 245]. The corresponding uncertainty in the asymmetry is ~ 0.05 ppm. The error bars on the dilution factors have been neglected because they were insignificant compared to the statistical error bars. Likewise, the precision of the Q^2 centroids for each detector is washed out by the width of the present Q^2 bins.

The effect of the linear regression correction for the helicity-correlated beam parameters on the extracted $A_\perp$ is small, less than 0.1 ppm for the first two Q^2 bins, but it is ~ 0.25 for the third bin. These values were determined using the cuts defined in the database, as described in Section 5.4.3. As these cuts are somewhat different than those used for the actual analysis of these data, and because the effects are so small, no correction was done, and the magnitude of the correction was used as the systematic error only.

The beam leakage introduced a global negative offset to the asymmetries, about -1.3 ppm overall, that was corrected when the beam leakage correction was applied. The uncertainty in the elastic asymmetry due to the beam leakage correction is 0.33 ppm for detectors $1 - 8$ and 0.38 ppm for detectors $9 - 12$. These uncertainties were found following one of the methods used for the forward-angle longitudinal data set [224]. Of all the ToF regions other than the cut0 one, cut3 is the most sensitive to the beam leakage. Figures 5.68 and 5.69 show the asymmetries for cut3

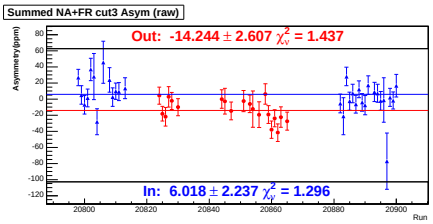

FIG. 5.68: *Raw cut3 asymmetries versus run for all the detectors and octants without the beam leakage correction applied.*

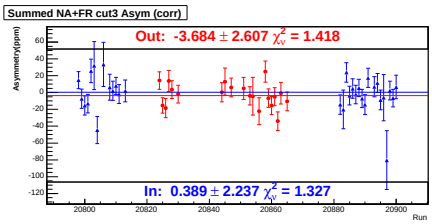

FIG. 5.69: *Raw cut3 asymmetries versus run for all the detectors and octants with the beam leakage correction applied.*

by half-wave plate both uncorrected and corrected for the beam leakage, respectively. Although the correction is significant, the reduced χ^2 after the correction is still ~ 1.4, which points to some residual systematic fluctuation in the data. If we assume that the residual systematic uncertainty is about the same size as the statistical uncertainty, about 2.607 ppm (a conservative estimate since the reduced χ^2 is less than 2 and is only for one half-wave plate state), which corresponds to a fractional uncertainty of 25% relative to the size of the correction (-10.56 ppm for the out state). This is similar to the 23% found by this method for the longitudinal case. To find the uncertainty in the elastic asymmetry due to the leakage, we find the difference between the leakage corrected and uncorrected elastic asymmetries , and multiply by our fractional uncertainty:

$$\delta = A_{e,corr} - A_{e,raw} \sim 1.3 \text{ ppm}, \tag{5.59}$$

$$\sigma(\delta) = \delta \times 25\% = 0.33 \text{ ppm}, \tag{5.60}$$

where +1.3 ppm was the average correction for the asymmetries for detectors 1–8. For detectors 9–12, the average correction was +1.5, and so the uncertainty due to the leakage correction is 0.38 ppm. This is a global systematic uncertainty.

The analysis of the transverse beam polarization data and the determination of the systematic error bar of 1.7% on the polarization (1.8% total error for the measurement) was described in Section 5.2.2.2. The large uncertainty in the beam polarization is largely due to the interpolation necessary because of the indirectness of the measurement and the 3° shift in the zero-crossing.

There is the possibility of a small amount of residual longitudinal polarization, since there

Source	Uncertainty
Deadtime	0.05 ppm (not blinded)
Helicity-correlated beam parameters	< 0.1 ppm for 1-12; 0.25 ppm for 13-14
Background correction	0.3 - 3.11 ppm
Leakage beam	0.33, 0.38 ppm
Beam polarization	1.8% (fractional)
Longitudinal polarization	0.002, 0.017, 0.166 ppm
Finite Q^2 binning	0.03 ppm (not blinded)

TABLE 5.18: *Systematic uncertainties for the measured asymmetries. The first three are point-to-point systematic uncertainties; the last three are global systematic uncertainties. [Still blinded.]*

was the shift in the zero-crossing of about 3°; however, we are confident that the spin angle was at 90° for the measurement, so we do not perform a correction for it, but do have an uncertainty assigned for it. In assigning the uncertainty, we have assumed the maximum possible residual longitudinal polarization. Any residual longitudinal polarization would manifest as a vertical offset in the plots of A_m versus ϕ. The amount that A_0 would shift with the maximum amount of residual longitudinal polarization was found by summing the elastic longitudinal asymmetries into the appropriate detector bins, and then multiplying the summed asymmetries by sin 3° (about 5% of $A_{\parallel}$). These values were found to be 0.12 ppm for detectors 1–8, 0.28 ppm for detectors 9–12, and 0.49 ppm in detectors 13–14. To find out how much these offsets could affect the extracted asymmetry amplitude $A_{\perp}$, the fits to the measured asymmetry data were performed with the offset constrained to the maximum, minimum, and zero offsets (i.e. fits with $A_0 = +0.12$, -0.12, and 0.0 for detectors 1–8), and the values of the extracted $A_{\perp}$ were compared to obtain the dispersion of the values. For detectors 1–8, the dispersion was found to be 0.002 ppm; for detectors 9–12, 0.017 ppm; and for detectors 13–14, 0.166 ppm. We then took this to be the systematic uncertainty associated with any residual longitudinal polarization component in the beam.

For the systematic error on the extracted background asymmetries, the two independent analysis methods were used as a measure of the systematic uncertainty. The dispersion between the two methods was calculated for each octant and detector bin, which was added in quadrature to the error bar obtained for the extracted background asymmetry from the simultaneous fit.

The error on the elastic asymmetry can be written as

$$\sigma(A_{elas}) = \sqrt{\sigma^2_{stat}(A_{elas}) + \sigma^2_{sys}(A_{elas})}, \tag{5.61}$$

$$\sigma_{sys}(A_{elas}) = \frac{1-f}{f}\,\sigma(A_b), \tag{5.62}$$

$$\sigma(A_b) = \sqrt{\sigma^2(A_{bkg}) + \delta^2}, \tag{5.63}$$

where the statistical error $\sigma_{stat}(A_{elas})$ comes from the fits, $\sigma(A_{bkg})$ comes from the background fits, and δ is the dispersion between the two methods. The elastic asymmetries and the systematic uncertainties on the elastic asymmetries are found in Table 5.19. The table shows the statistical uncertainty, the point-to-point systematic uncertainty, and the global systematic uncertainty. In addition, the table also displays the systematic uncertainty contribution from the background correction. Unsurprisingly, the background correction clearly dominates the point-to-point systematic uncertainties for the data points.

A conservative model-dependent systematic error due to finite Q^2 bin size is also indicated in Table 5.18.

As a final note, because the octants are not exactly at a particular angle in ϕ but in actuality cover a range of about 21° (±10.5° from their designated azimuthal position), the measured asymmetries are in essence the average of the sinusoidal shape over that range. Therefore, the asymmetries at the peak are slightly shifted down toward zero, and the sinusoidal effect is somewhat washed out. To determine if a correction should be done for this effect, the values over an ideal sine curve with an amplitude of 1 ppm over eight 21° bins were averaged. The largest variation between the ideal curve's value and the average across an azimuthal bin was at the peak (as predicted), and for an amplitude of 1 ppm, the value was shifted from an absolute value of 1 to 0.9941 ppm. The shift of 0.00585 multiplied by the extracted $A_\perp$ amplitudes (unblinded) in this data set yields that the data points at the maxima and minima of the sinusoidal shape have

Octant	Detectors 1 – 8				
	A_{elas}(ppm)	σ_{stat} (ppm)	$\sigma_{sys_{pt-pt}}$ (ppm)	$\sigma_{sys_{global}}$ (ppm)	$\sigma_{sys_{bkg}}$ (ppm)
1	-2.72	1.61	0.54	0.44	0.53
2	-2.61	1.64	0.61	0.44	0.60
3	-1.97	1.52	0.54	0.44	0.53
4	1.63	1.51	0.32	0.44	0.30
5	1.34	1.61	0.58	0.44	0.57
6	2.66	1.60	0.34	0.44	0.32
7	-0.23	1.56	0.50	0.44	0.49
8	-0.68	1.49	0.39	0.44	0.38
Octant	Detectors 9 – 12				
	A_{elas}(ppm)	σ_{stat} (ppm)	$\sigma_{sys_{pt-pt}}$ (ppm)	$\sigma_{sys_{global}}$ (ppm)	$\sigma_{sys_{bkg}}$ (ppm)
1	-5.18	3.85	2.530	0.51	2.528
2	-0.99	2.56	0.70	0.51	0.69
3	-3.86	4.59	3.112	0.51	3.111
4	3.38	2.68	0.67	0.51	0.66
5	5.80	3.69	2.22	0.51	2.21
6	0.67	2.47	0.65	0.51	0.64
7	0.83	5.01	1.901	0.51	1.898
8	-0.65	2.70	0.88	0.51	0.87
Octant	Detectors 13 – 14				
	A_{elas}(ppm)	σ_{stat} (ppm)	$\sigma_{sys_{pt-pt}}$ (ppm)	$\sigma_{sys_{global}}$ (ppm)	$\sigma_{sys_{bkg}}$ (ppm)
1	4.83	3.78	1.39	0.54	1.36
2	1.71	4.58	1.21	0.54	1.18
3	-8.18	3.98	1.18	0.54	1.15
4	9.87	5.60	1.83	0.54	1.81
5	-4.43	6.72	2.71	0.54	2.69
6	2.13	4.84	2.06	0.54	2.05
7	1.39	4.19	1.52	0.54	1.50
8	3.58	5.50	1.55	0.54	1.53

TABLE 5.19: *Uncertainties for the extracted elastic asymmetries.* A_{elas} *is the elastic asymmetry,* σ_{stat} *is the statistical uncertainty,* $\sigma_{sys_{pt-pt}}$ *is the point-to-point systematic uncertainty,* $\sigma_{sys_{global}}$ *is the global systematic uncertainty, and* $\sigma_{sys_{bkg}}$ *is the contribution of the background systematic error to the point-to-point uncertainty. [Everything is still blinded.]*

shifted about 0.024 ppm toward zero for detectors 1–8 and 0.028 ppm for 9–12, so the absolute value of A_n for each should be increased by that amount. This 0.59% correction is pretty negligible for this measurement given our statistical error bars; however, for the sake of completeness this has been corrected for. The correction was actually applied multiplicatively (except for on the points where the zero-crossing should occur, to prevent accidental forcing of the point to zero), although the results were the same whether applied additively or multiplicatively. The corrections calculated for each point have been applied to each point individually and then fitted, although in principle one could just do the correction on the amplitude curve itself. This was done so that the asymmetries listed in tables would already have the correction, avoiding confusion as to why a fit to the listed points for detectors 1–8 differs from the reported fit by -0.024 ppm. Finally, this effect is determined by how large a slice of the sine curve is accepted (i.e. an octant covering a full 45° would require a larger correction), so assuming that the backangle measurements have the same detector acceptance since they do make use of the same focal plane detectors (among other things), the correction needed for the backward angle transverse measurements should be about -0.59 ppm for an A_n of about -100 ppm.

5.4.8.1 Phase Sensitivity Study

The phase ϕ_0 in Equation 5.58 depends on the direction of the beam polarization and determines the overall sign of the asymmetry amplitude A_n. For this measurement, ϕ_0 should be equivalent to the calculated precession of the polarization as it traverses the magnetic field of the Møller solenoid, but it is important to have a good understanding of the phase and the impact of different phases on the extracted transverse asymmetry A_n.

As the phase takes into account the direction of the transverse polarization relative to the orientation of the spectrometer, the possibility that the Ferris wheel is tilted with respect to the plane of the accelerator (and to the transverse polarization of the beam) must be considered. A back-of-the-envelope calculation shows that the Ferris wheel would have to be rotated by about 11 inches with respect to the plane of the accelerator and our polarization for the effect on the phase

to be as large as the contribution from the Møller solenoid, about 5.3°. Due to the unlikeliness of this being unnoticed by the surveys, it was decided that this scenario probably would not be a significant source of uncertainty in the phase ϕ_0.

A study was conducted to ascertain any systematic effects due to the knowledge (or lack thereof) of the phase ϕ_0 that the sinusoidal fits are constrained to. To do the study, the final corrected elastic asymmetries for each Q^2 detector bin were plotted versus the azimuthal position of each octant and fitted for their sinusoidal dependence as described in Section 5.4.6. However, the fits were performed with the phase ϕ_0 constrained to values from $-90°$ to $90°$, in one-degree-per-step intervals, with the reduced χ^2 and the amplitude A_n recorded for each value of ϕ_0.

The results are shown plotted in Figure 5.70. As expected, the blue curve of the reduced χ^2 versus the constrained phase ϕ_0 shows the value of χ^2 reaching a minimum at the value of the phase obtained in a free fit where all the parameters are allowed to float, about 22.1° for detectors 1–8, $-5.8°$ for detectors 9–12, and $-58.3°$ for 13 and 14. The same is true for the value of the extracted asymmetry amplitude A_n, shown in the green curves, which attains a largest absolute value at these values of ϕ_0. The three-dimensional plot shows the relationship between all three values: the phase ϕ_0, the asymmetry amplitude A_n, and the reduced χ^2. As a consequence of the sinusoidal fit shape, the relationship of the three values forms a saddle shape, with the χ^2 minima and the A_n absolute maxima occurring at 180° out-of-phase. This is clearly seen in the red curves for each detector bin, although only half of the saddle shape is visible in these plots.

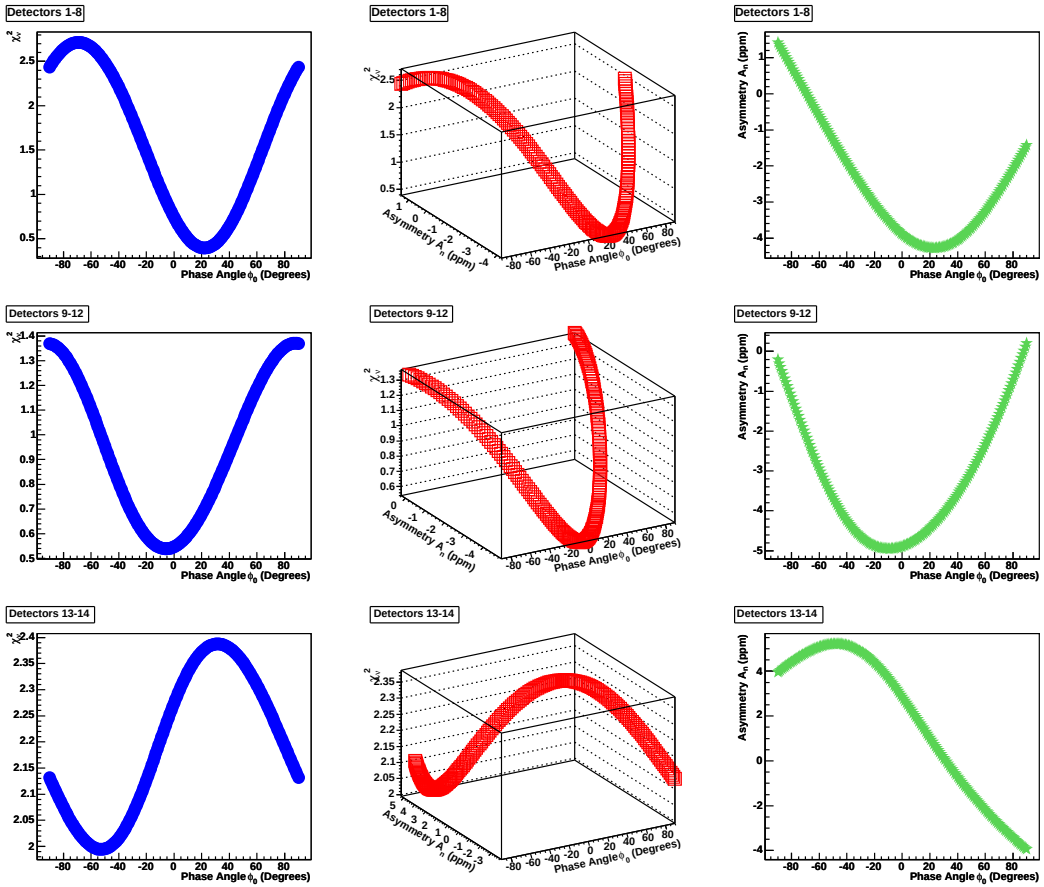

FIG. 5.70: *Plots detailing studies of the effects of the phase ϕ_0 on the extracted azimuthal amplitude of the sinusoidal fit the to asymmetries. The blue curves show the effect on the reduced χ^2 of constraining the fits to various azimuthal angles, the green curves show the effect on the asymmetry A_n of constraining the fits to various azimuthal angles ϕ_0, and the red curve shows the relationship of the phase ϕ_0, the asymmetry A_n, and the reduced χ^2. [Note: Asymmetries are not blinded.]*

The calculated precession angle due to the beam traversing the field of the Møller solenoid is about 5.3°, which does not sit far from the χ^2 minima and the A_n absolute maxima in the plots for detector bins 1 – 8 and 9 – 12, and thus does not have much of an impact on the extracted A_n. However, this is not the case with the results for detectors 13 – 14, which display a very different trend with the minimum reduced χ^2 at −58.3°. This gives support to the suggestion that there is something possibly amiss with the data from these detectors, as they favor a phase angle that is so far out of agreement with the other detectors, the luminosity monitors, and the calculated phase from the precession due to the Møller solenoid.

5.4.9 An Alternative Approach: Correcting via the Wiggles

As another consistency check, a relatively quick and completely different analysis of the data was also made. In this method, the $A_\perp$ values from each of the sinusoidal fits for the background cuts (cut1, cut2a, cut2b, and cut3) where plotted versus the average ToF of the cuts for each of the detector bins and fitted with a linear background function. The value of the background $A_\perp$ under the elastic peak was then evaluated at the elastic peak ToF from the background fit, and used to correct the $A_\perp$ from the sinusoidal fits to the measured elastic asymmetries using the elastic peak dilution factors and the now-familiar equation

$$A_{elas} = \frac{1}{f}\left(A_\perp^{meas} - (1-f)A_{bkg}\right). \tag{5.64}$$

The results of this procedure can be seen in Figure 5.71, where the background $A_\perp$ fits are shown along with a plot of the corrected elastic $A_\perp$ for each center-of-mass angle using this method, which are also listed in the first column of Table 5.20 (the asymmetries are still blinded). The extracted background $A_\perp$ values are consistent within the large error bars with the ones from the other methods, and the corrected elastic $A_\perp$ values are also consistent with the previous methods.

Figure 5.71 and the first column of Table 5.20 show the results of this method with no constraints placed on any of the fit parameters. For comparison, the second and third columns of Table 5.20 show the results for the case where the phase ϕ_0 of all the sinusoidal fits for the cuts are constrained to the calculated precession of the polarization through the Møller solenoid, and for

Detector Bin	Free	$\phi_0 = 5.3°$	$A_\perp$ (ppm) $\phi_0 = 5.3°$, $A_0 = 0$	Simultaneous Method	Two-Step Method
1 – 8	-2.45 ± 0.63	-2.24 ± 0.63	-2.25 ± 0.63	-2.55 ± 0.80	-2.52 ± 0.66
9 – 12	-3.16 ± 1.36	-3.10 ± 1.33	-3.11 ± 1.33	-3.10 ± 1.52	-3.23 ± 1.18
13 – 14	2.14 ± 1.98	1.40 ± 1.96	1.41 ± 1.97	2.97 ± 2.40	3.04 ± 1.90

TABLE 5.20: *The corrected elastic $A_\perp$ using the "correction via the wiggles" method, where the amplitudes for the detector bins are shown for sinusoidal fits where the parameters were not constrained, for fits where the parameters were constrained to the calculated Møller phase, and for fits with the parameters constrained to both zero offset and the calculated Møller precession phase. The extracted $A_\perp$ for the simultaneous fit and the two-step methods are also shown for comparison. [Asymmetries are all blinded.]*

the case where the vertical offset is constrained to zero in addition to the Møller phase constraint. The plots for this latter case are shown in Figure 5.72. As in the plots for the unconstrained case, the three plots for each detector bin show the linear fit to the asymmetry amplitudes extracted from the azimuthal sinusoidal fits from the background cut asymmetries for each octant. The closed blue circles are the background asymmetry amplitudes that are used in the linear fit, the open blue circle is the uncorrected elastic asymmetry (not in fit), and the red square is the value of the background asymmetry at the elastic peak that is determined from the fit to the background points. This value for the background asymmetry is also displayed at the top of the graphs. The fourth and final graph shows the corrected elastic asymmetry amplitude for each of the three detector bins versus their corresponding center-of-mass angle, with the values displayed at the top of the plot. The values for both constrained cases are in good agreement with the unconstrained case, expect for detectors 13 and 14, which was not unexpected. These values are also consistent with those found by the more careful and thorough analysis.

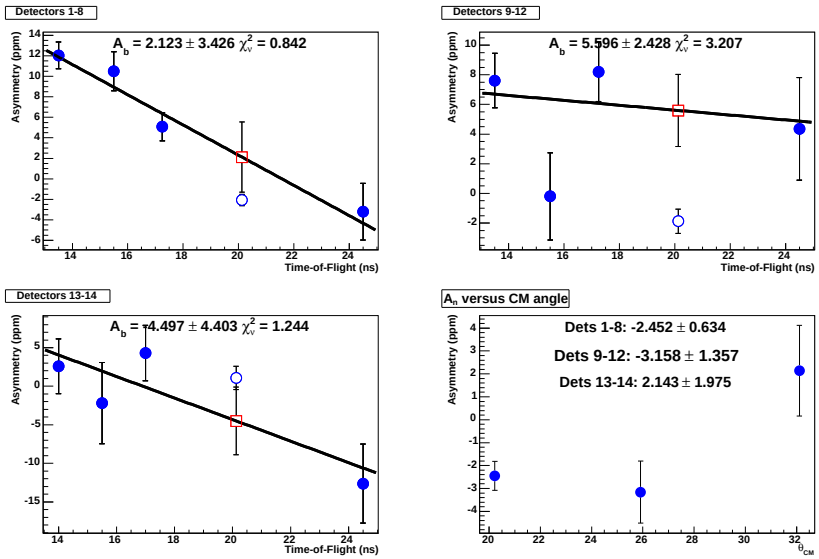

FIG. 5.71: *Plots of the linear fits of $A_\perp$ of each of the background cuts versus time-of-flight for each detector bin. The value of the $A_\perp$ asymmetry in the elastic cut extracted from the fit is shown as a red square and is displayed at the top of each plot, along with the reduced χ^2 for the fit. The open circle is the measured elastic $A_\perp$, which is included in the plots for comparison, but not included in the background fits. The closed blue circles are the $A_\perp$ data points for the background cuts: cut1, cut2a, cut2b and cut3. The bottom right plot shows the corrected elastic $A_\perp$ versus center-of-mass angle for the three detector bins, with the values displayed at the top of the plot. [Note: Asymmetries are all blinded.]*

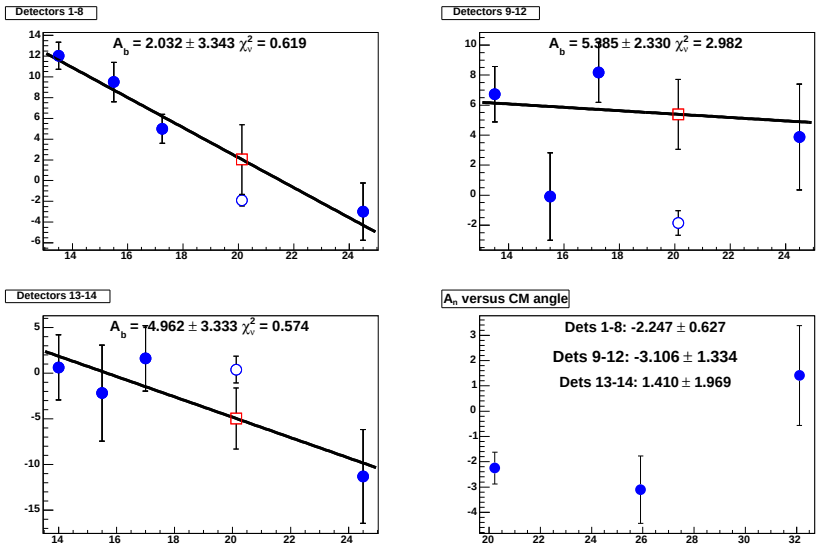

FIG. 5.72: *Plots of the linear fits of $A_\perp$ of each of the background cuts versus time-of-flight for each detector bin, where the sinusoidal fits were constrained to zero offset and the calculated Møller precession phase. The value of the $A_\perp$ background asymmetry in the elastic cut extracted from the fit is shown as a red square and is displayed at the top of each plot, along with the reduced χ^2 for the fit. The open circle is the measured elastic $A_\perp$, which is included in the plots for comparison, but not included in the background fits. The closed blue circles are the $A_\perp$ data points for the background cuts: cut1, cut2a, cut2b and cut3. The bottom right plot shows the corrected elastic $A_\perp$ versus center-of-mass angle for the three detector bins, with the values displayed at the top of the plot. [Note: Asymmetries are all blinded.]*

5.4.10 Final Physics Asymmetries

The final elastic asymmetries from the simultaneous fit analysis method, corrected for the multiplicative analysis blinding factor of 0.805619 and the beam polarization, are listed in Table 5.21 for each of the detector groups. The error bars on the asymmetries are the statistical and systematic uncertainties discussed in Section 5.4.8 combined in quadrature. These asymmetries can now be used to extract the transverse asymmetry A_n, which is the subject of the next chapter.

Octant	Detectors 1 - 8			
	A_{elas}(ppm)	σ_{stat} (ppm)	$\sigma_{sys_{pt-pt}}$ (ppm)	$\sigma_{sys_{global}}$ (ppm)
1	-4.57	2.00	0.67	0.55
2	-4.39	2.04	0.76	0.55
3	-3.30	1.88	0.67	0.55
4	2.74	1.88	0.39	0.55
5	2.25	2.00	0.71	0.55
6	4.47	1.98	0.42	0.55
7	-0.38	1.94	0.62	0.55
8	-1.15	1.84	0.49	0.55
Octant	Detectors 9 - 12			
	A_{elas}(ppm)	σ_{stat} (ppm)	$\sigma_{sys_{pt-pt}}$ (ppm)	$\sigma_{sys_{global}}$ (ppm)
1	-8.70	4.78	3.14	0.63
2	-1.67	3.18	0.87	0.63
3	-6.45	5.70	3.86	0.63
4	5.68	3.33	0.83	0.63
5	9.74	4.58	2.75	0.63
6	1.13	3.06	0.81	0.63
7	1.39	6.22	2.36	0.63
8	-1.09	3.35	1.09	0.63
Octant	Detectors 13 - 14			
	A_{elas}(ppm)	σ_{stat} (ppm)	$\sigma_{sys_{pt-pt}}$ (ppm)	$\sigma_{sys_{global}}$ (ppm)
1	8.11	4.69	1.72	0.67
2	2.88	5.68	1.50	0.67
3	-13.66	4.94	1.46	0.67
4	16.58	6.96	2.27	0.67
5	-7.44	8.34	3.36	0.67
6	3.58	6.01	2.56	0.67
7	2.33	5.21	1.88	0.67
8	6.01	6.82	1.92	0.67

TABLE 5.21: *Systematic uncertainties for the extracted elastic asymmetries, corrected for the analysis blinding factor of 0.805619.. $\sigma_{sys_{bkg}}$ is the contribution of the background syst error to the pt-pt error.*

5.5 Analysis Summary

This chapter has described the analysis techniques used to correct the raw asymmetries measured in the parity-violating, forward-angle asymmetry measurement of the G^0 experiment and the parity-conserving transverse asymmetry measurement. These asymmetries can now be used to extract the physics of interest, the linear combination of the strange form factors $G_E^s + \eta G_M^s$ in the former case, and the transverse asymmetry A_n in the latter. The next chapter is devoted to this and to a discussion of these results.

CHAPTER 6

From Physics Asymmetries to Physics Results

6.1 Longitudinal Data Set

6.1.1 Experimental Asymmetry Results

The final, published physics asymmetries that were measured in the experiment and analyzed as described in Chapter 5 are presented in Table 6.1, along with their corresponding statistical and systematic uncertainties (both point-to-point and global) [245]. These asymmetries are shown along with the "no-vector-strange" asymmetry A_{nvs}, that is, the calculated asymmetry assuming no contribution from strange quarks ($G_E^s = G_M^s = 0$ for all values of Q^2). For the calculation of the NVS asymmetry, the electromagnetic form factors of Kelly were used [279].

These experimental asymmetries are shown plotted in Figures 6.1 and 6.2 (as linear and log plots, respectively), along with the solid black line denoting the calculated values of the no-vector-strange asymmetry using the Kelly form factor parameterizations. In the plots, the inner error bar denotes the statistical uncertainty, and the outer one represents the statistical and point-to-

Q^2 (GeV/c)^2	A_{phys} (ppm)	σA_{stat} (ppm)	σA_{pt-pt} (ppm)	σA_{global} (ppm)	A_{nvs} (ppm)
0.122	-1.51	0.44	0.22	0.18	-1.96
0.128	-0.97	0.41	0.20	0.17	-2.11
0.136	-1.30	0.42	0.17	0.17	-2.29
0.144	-2.71	0.43	0.18	0.18	-2.50
0.153	-2.22	0.43	0.28	0.21	-2.75
0.164	-2.88	0.43	0.32	0.23	-3.05
0.177	-3.95	0.43	0.25	0.20	-3.44
0.192	-3.85	0.48	0.22	0.19	-3.91
0.210	-4.68	0.47	0.26	0.21	-4.47
0.232	-5.27	0.51	0.30	0.23	-5.23
0.262	-5.26	0.52	0.11	0.17	-6.31
0.299	-7.72	0.60	0.53	0.35	-7.78
0.344	-8.40	0.68	0.85	0.52	-9.66
0.410	-10.25	0.67	0.89	0.55	-12.74
0.511	-16.81	0.89	1.48	1.50	-17.96
0.631	-19.96	1.11	1.28	1.31	-24.77
0.788	-30.8	1.9	2.6	2.59	-34.57
0.997	-37.9	7.2	9.0	0.52	-48.61

TABLE 6.1: *The physics asymmetries and uncertainties measured in the forward-angle phase of the G^0 experiment, as published in [245].*

point systematic uncertainties combined in quadrature. The grey band at the top of the graph is the global systematic uncertainty for the measurement. Although not very far from zero, the asymmetries do show a systematic tendency to ride slightly above (positive) the line for no strange quark contributions.

6.1.2 The Linear Combination $G_E^s + \eta G_M^s$

The linear combination of the strange electric and magnetic form factors is determined from the difference between the measured experimental asymmetry A_{phys} and the no-vector-strange asymmetry A_{NVS}, which is calculated as described previously with $G_E^s = G_M^s = 0$ for all values of Q^2 and Kelly's electromagnetic form factors [279].

$$G_E^s + \eta G_M^s = \frac{4\pi\sqrt{2}\alpha}{G_F Q^2} \frac{\epsilon (G_E^{\gamma,p})^2 + \tau (G_M^{\gamma,p})^2}{\epsilon G_E^{\gamma,p}} \left(A_{phys} - A_{NVS}\right), \tag{6.1}$$

where $\eta(Q^2) = \tau G_M^{\gamma,p} / \epsilon G_E^{\gamma,p}$.

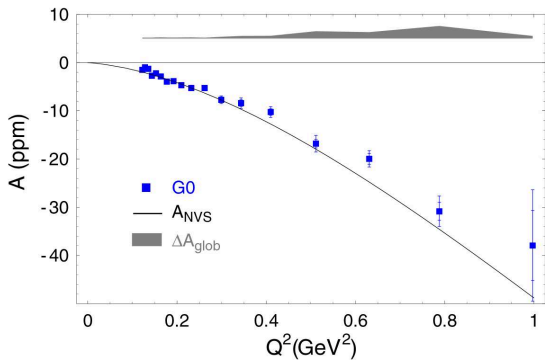

FIG. 6.1: *$A_{physics}$ (points) and A_{NVS} (solid line) versus Q^2, shown in a linear scale. The inner error bars represent the statistical error bars; the outer error bars denote the statistical and point-to-point systematic uncertainties combined in quadrature. The grey band above the plot shown the global systematic uncertainty.*

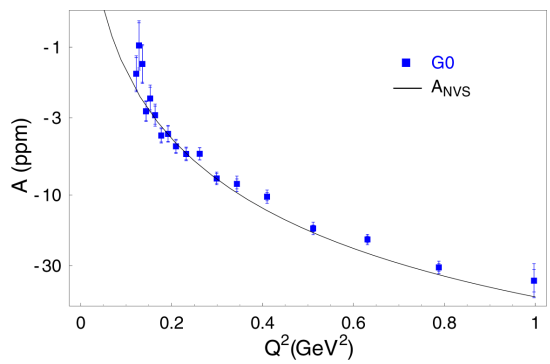

FIG. 6.2: *$A_{physics}$ (points) and A_{NVS} (solid line) versus Q^2, shown in a logarithmic scale. The inner error bars represent the statistical error bars; the outer error bars denote the statistical and point-to-point systematic uncertainties combined in quadrature. The grey band above the plot shown the global systematic uncertainty.*

The results of the calculation are shown in Table 6.2. Note that $G_E^s + \eta G_M^s = 0$ at $Q^2 = 0$ and that $\eta \sim 0.94Q^2$ for our kinematics using the Kelly parameterization. The linear combination $G_E^s + \eta G_M^s$ is shown as a function of momentum transfer in Figure 6.3. The inner error bars are the statistical uncertainty, and the outer ones are the statistical and point-to-point systematic uncertainties combined in quadrature. The grey error bands represent the global systematic uncertainties. The upper band shows the ones from the measurement, and the lower band the ones from the uncertainties in the quantities entering A_{NVS}: the calculated value of the axial-vector form factor normalization [85] (differing from g_A/g_V by electroweak radiative corrections), the same dipole momentum transfer dependence for $G_A^e(Q^2)$ as is deduced for $G_A(Q^2)$ [280], the axial-vector strangeness contribution Δs [281], and the electroweak radiative corrections [68].

These calculations have used the parameterization of the electromagnetic form factors by Kelly [279]; however, the difference in using the parameterizations by Friedrich-Walcher [282] or Arrington [283] is not large. These parameterizations are also shown in Figure 6.3, the green dashed line representing the parameterization by Friedrich and Walcher [282] and the pink dotted line denoting the combination of Arrington's parameterization for the proton [283] and Kelly's neutron parameterization [279]. These lines represent the effective zero value of A_{NVS} for these

Q^2 (GeV/c)^2	η	$G_E^s + \eta G_M^s$	σ_{stat}	$\sigma_{sys,pt-pt}$	$\sigma_{sys,global}$	$\sigma_{sys,model}$
0.122	0.098	0.037	0.036	0.019	0.015	0.003
0.128	0.103	0.090	0.032	0.016	0.014	0.003
0.136	0.109	0.074	0.032	0.013	0.013	0.003
0.144	0.116	-0.014	0.030	0.013	0.012	0.003
0.153	0.123	0.034	0.028	0.019	0.014	0.003
0.164	0.132	0.010	0.026	0.020	0.014	0.004
0.177	0.143	-0.028	0.024	0.014	0.011	0.004
0.192	0.156	0.003	0.025	0.011	0.010	0.004
0.210	0.170	-0.010	0.022	0.012	0.010	0.004
0.232	0.189	-0.002	0.021	0.012	0.010	0.004
0.262	0.214	0.038	0.019	0.004	0.006	0.005
0.299	0.245	0.002	0.018	0.016	0.011	0.005
0.344	0.283	0.033	0.018	0.022	0.014	0.005
0.410	0.341	0.053	0.014	0.019	0.012	0.006
0.511	0.431	0.019	0.014	0.024	0.024	0.006
0.631	0.543	0.060	0.014	0.016	0.016	0.007
0.788	0.700	0.036	0.018	0.024	0.025	0.008
0.997	0.932	0.076	0.052	0.064	0.004	0.008

TABLE 6.2: *The linear combination $G_E^s + \eta G_M^s$ from the G^0 forward-angle measurement.*

parameterizations; for example, the value of $G_E^s + \eta G_M^s$ at $Q^2 = 0.63$ (GeV/c)^2 would increase from 0.059 to 0.072 if the Friedrich-Walcher form factors were used.

Included on the graph are the data points from recent HAPPEX measurements [183–185], which were made at nearly the same kinematic points (the points do include small corrections to the asymmetries to adjust them to the same beam energy as G^0, < 0.2 ppm). The points are in excellent agreement with the G^0 points.

The results are also displayed on the G^0 website, along with other plots and information about the measurement.[1]

6.1.3 Discussion of Results

The results for $G_E^s + \eta G_M^s$ shown in Figure 6.3 suggest a systematic and intriguing Q^2 dependence. However, are these data consistent with zero, or do they reject this hypothesis that $G_E^s + \eta G_M^s = 0$?

To characterize the results, the hypothesis that $G_E^s + \eta G_M^s = 0$ was tested using the classic

[1] http://www.npl.uiuc.edu/exp/G0/Forward/index.html

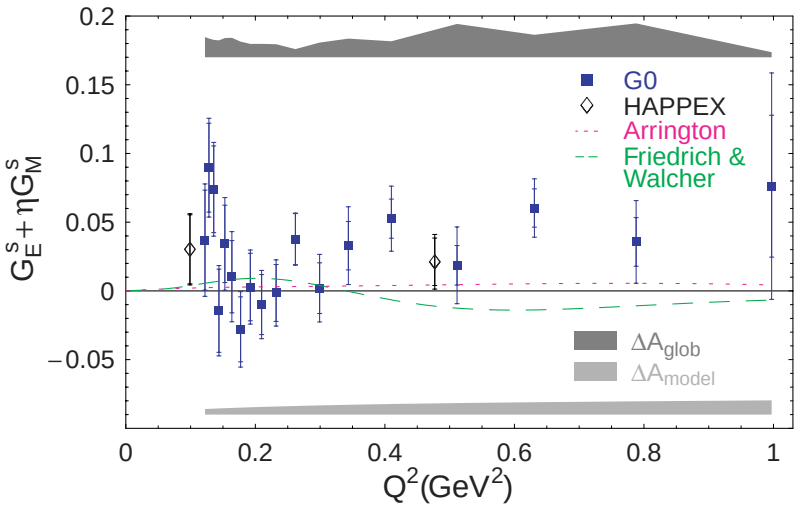

FIG. 6.3: *$G_E^s + \eta G_M^s$ versus Q^2, calculated using Kelly form factors. Inner error bars denote the statistical uncertainty; outer ones, the statistical and point-to-point systematic uncertainties combined in quadrature. The grey error bands represent the global systematic uncertainties, the upper band the ones from the measurement, and the lower band the ones from the uncertainties in the quantities entering A_{NVS}. The two lines correspond to the effective zero-line A_{NVS} using different electromagnetic nucleon form factor parameterizations. Figure from [245].*

χ^2 test. This test makes the assumption that the zero-line hypothesis is the correct physics, and then evaluates the probability that a random data set would give χ^2 values equal to or lesser than the value obtained from the measured data set if the zero-line hypothesis accurately describes the underlying physics. This was done using a Monte Carlo simulation, which generated randomized data sets with the assumption that $G_E^s + \eta G_M^s = 0$ and which were distributed according to the statistical and systematic uncertainties of the actual measurement (including correlated uncertainties). The χ^2 value for each generated data set relative to the zero-line hypothesis calculated and then compared to the χ^2 of the measured data (using Kelly's form factors). The fraction of these sets with a χ^2 value larger than that of our data set was only 11% with the assumption that the distribution is governed by the no-vector-strange hypothesis. Therefore, the nonstrange hypothesis is disfavored by the G^0 data with 89% confidence.

The Q^2 dependence of the data is very intriguing. How does this dependence compare with other measurements? A combined analysis using the world data for $Q^2 = 0.1$, 0.23, and 0.477 $(\mathrm{GeV}/c)^2$ can be done by plotting the results from the various experiment discussed in Chapter 3

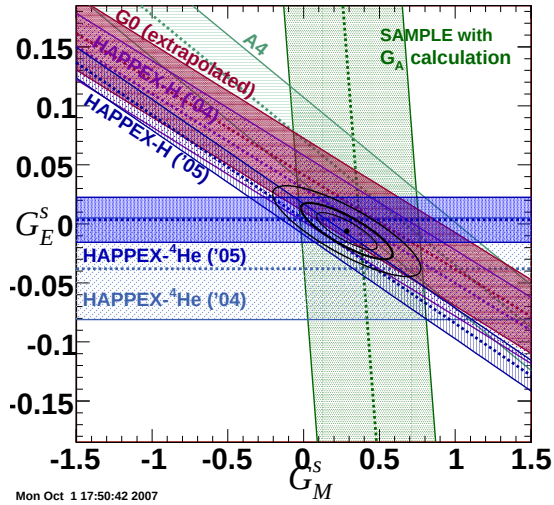

FIG. 6.4: *The world Data of $G_E^s + \eta G_M^s$ for $Q^2 = 0.1$ (GeV/c)^2. The inner and outer ellipses are the 1σ and 2σ error ellipses. Data from [178, 184–186, 189, 245]*

in (G_E^s, G_M^s) space. In these plots, each measurement is shown as a linear band, defined as

$$G_E^s + \eta G_M^s = g \pm \sigma(g), \tag{6.2}$$

where the η, g, and $\sigma(g)$ denote the values of η and the linear combination and its uncertainty for each measurement. The bands should overlap where the most probable values of G_E^s and G_M^s are located. Figure 6.4 shows this for $Q^2 = 0.1$ (GeV/c)^2, where the value for the G^0 line is from a linear interpolation between the lowest three measured Q^2 bins (0.122, 0.128, 0.136 (GeV/c)^2) and the physical constraint that at $Q^2 = 0$ the linear combination is zero. The inner and outer ellipses are the 1σ and 2σ error ellipses. The best fit to the measurements yields a value of

$$G_E^s = -0.006 \pm 0.016, \quad G_M^s = 0.284 \pm 0.200, \tag{6.3}$$

which is consistent with zero for G_E^s, but perhaps slightly positive for G_M^s.

This technique can be done using the world data at $Q^2 = 0.23$ and 0.477 (GeV/c)^2 as well. For these plots, three adjacent points of the measured G^0 data are used for the interpolation, $Q^2 = 0.210$, 0.232, 0.262 (GeV/c)^2 for the value at $Q^2 = 0.23$, and $Q^2 = 0.410$, 0.511, 0.631 for $Q^2 = 0.477$ (GeV/c)^2. These values are shown in Figures 6.5 and 6.6, along with the data from

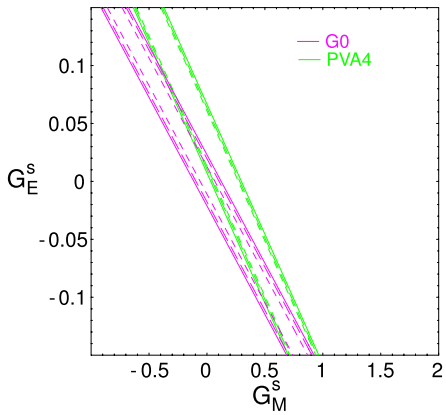

FIG. 6.5: $G_E^s + \eta G_M^s$ *at* $Q^2 = 0.23$ *(GeV/c)*^{2}. *The magenta band shows the results from the* G^0 *experiment [245]; the green band is from the PVA4 forward-angle measurement [188]. The dashed and solid lines denote the statistical and total uncertainties for each measurement.*

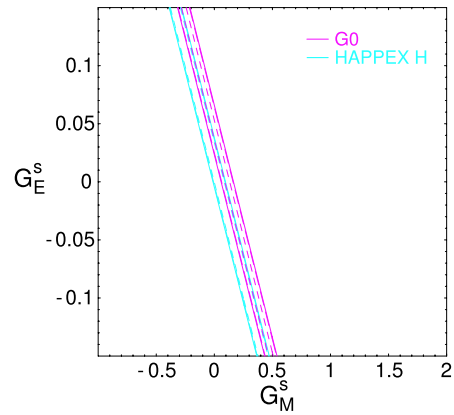

FIG. 6.6: $G_E^s + \eta G_M^s$ *at* $Q^2 = 0.48$ *(GeV/c)*^{2}. *The magenta band shows the results from the* G^0 *experiment [245]; the blue band is from the first HAPPEX measurement [183]. The dashed and solid lines denote the statistical and total uncertainties for each measurement.*

PVA4 [188] and HAPPEX [183], respectively. The best fit for Figure [188] at $Q^2 = 0.23$ (GeV/c)^2 yields [224]

$$G_E^s = -0.14 \pm 0.16, \quad G_M^s = 0.80 \pm 0.81, \tag{6.4}$$

which favors a negative G_E^s and a positive G_M^s (although both are still consistent with zero). At $Q^2 = 0.477$ (GeV/c)^2, the kinematics for the two measurements were almost the same, making the two lines parallel and unable to give an extraction for G_E^s and G_M^s. However, the agreement between the two measurements is excellent.

What about the comparison of the points themselves in the G^0 dataset? The initial rise from 0 to about 0.05 at low Q^2 is consistent with the finding that $G_M^s(Q^2 = 0.1(\text{GeV}/c)^2 \sim +0.5$ from the SAMPLE [178], PVA4 [189], and HAPPEX 2004 measurements [184, 185], although also consistent with zero like the HAPPEX 2005 measurements [186]. The kinematic factor η increases linearly throughout, so the apparent decline of the data in the intermediate region up to $Q^2 \sim 0.3$ could suggest that G_E^s may be negative in this range. This conclusion is also supported by the combination of the G^0 and PVA4 [188] results at $Q^2 = 0.23$, as seen in Figure 6.5. At higher values of Q^2, there is the suggestion of a trend to positive values of $G_E^s + \eta G_M^s$. This is also consistent

with the first HAPPEX measurement [183].

6.1.4 Summary

The first part of the G^0 experimental program measured forward-angle parity-violating asymmetries in elastic electron-proton scattering for eighteen Q^2 points between 0.12 and 1.0 (GeV/c)^2. Using these measured asymmetries, we have determined the combinations of the strange-quark contributions to these form factors, $G_E^s + \eta G_M^s$, over this Q^2 range, which allows us to see their dependence over this range. These results, along with other experiments, hint that both G_M^s and G_E^s could be non-zero, especially at higher values of momentum transfer, although the final determination of this rests with the separation planned using this data in combination with future data. These results, in conjunction with other measurements, indicate that models that predict large strange quark effects are strongly disfavored at $Q^2 = 0.1$ (GeV/c)^2. More experiments are planned to investigate this situation, including G^0 measurements at backward angles, PVA4 backward measurements, and yet another HAPPEX measurement, HAPPEX III. The combination of all these measurements should provide precise separations of G_E^s and G_M^s over a range of Q^2, which should shed some more light on this puzzle.

6.2 Transverse Experimental Results

The final elastic asymmetries from Table 6.3 can now be used to extract the transverse asymmetry A_n, which then can be compared to calculations predicting the magnitude of the transverse asymmetry at these kinematics. This section describes how the transverse asymmetry was obtained from the data and discusses the comparison of these results to the theoretical calculations.

6.2.1 Extraction of Transverse Asymmetry A_n

After the final step of the removal of the analysis blinding factor of 0.805619, the final asymmetries are obtained. The final, unblinded elastic asymmetries, $A_\perp$ (the elastic asymmetry A_{elas}

Octant	ϕ	Transverse Asymmetries $A_\perp$ (ppm) $Q^2 = 0.15$ (GeV/c)^2	$Q^2 = 0.25$ (GeV/c)^2
1	90°	$-4.57 \pm 2.00 \pm 0.67$	$-8.70 \pm 4.78 \pm 3.14$
2	135°	$-4.39 \pm 2.04 \pm 0.76$	$-1.67 \pm 3.18 \pm 0.87$
3	180°	$-3.30 \pm 1.88 \pm 0.67$	$-6.45 \pm 5.70 \pm 3.86$
4	225°	$2.74 \pm 1.88 \pm 0.39$	$5.68 \pm 3.33 \pm 0.83$
5	270°	$2.25 \pm 2.00 \pm 0.71$	$9.74 \pm 4.58 \pm 2.75$
6	315°	$4.47 \pm 1.98 \pm 0.42$	$1.13 \pm 3.06 \pm 0.81$
7	0°	$-0.38 \pm 1.94 \pm 0.62$	$1.39 \pm 6.22 \pm 2.36$
8	45°	$-1.15 \pm 1.84 \pm 0.49$	$-1.09 \pm 3.35 \pm 1.09$

TABLE 6.3: *Measured elastic asymmetries and uncertainties vs. azimuthal scattering angle ϕ, published in [278]. Uncertainties are the statistical and individual systematic uncertainties, respectively (summarized in Table 5.18); global systematic uncertainties are not included here.*

corrected for all effects, including beam polarization and the washing-out of the sinusoidal shape), for each of the eight detector arrays in each Q^2 bin were presented in Table 5.21 at the end of the last chapter, along with their (statistical, point-to-point, and global) uncertainties. The final, unblinded sources of systematic error are given in Table 6.4; the background correction dominates and varies in ϕ, although the overall uncertainty in the measurement is clearly dominated by statistics. A conservative model-dependent systematic error due to finite Q^2 bin size is also indicated in Table 6.4.

Of the systematic uncertainties shown in Table 6.4, the leakage beam, beam polarization, longitudinal systematic uncertainties, and uncertainties from finite Q^2 binning are treated as global uncertainties, and are not included in the error bars for the sinusoidal fits. The uncertainties arising from the background correction, deadtime, and helicity-correlated beam parameters are treated as point-to-point systematic uncertainties, and thus are included in the error bars for the fits. Thus we arrive at our published [278] asymmetry results in Table 6.3, which will be used to extract the transverse asymmetry.

Detectors 13 and 14, as well as detector 15, have very poor statistical precision and are not very definitive. These data perhaps show an azimuthal trend, but are also consistent with no azimuthal effect. It was not possible to perform a reliable background correction due to the inability to extract a meaningful background asymmetry. The lack of a reliable background correction precludes the

Source	Uncertainty	
	$Q^2 = 0.15$	$Q^2 = 0.25$
Deadtime	0.05 ppm	0.05 ppm
False asymmetries	0.12 ppm	0.12 ppm
Background correction	0.37 - 0.74 ppm	0.80 - 3.86 ppm
Leakage beam	0.55 ppm	0.63 ppm
Beam polarization	1.8%	1.8%
Longitudinal polarization	0.002 ppm	0.021 ppm
Finite Q^2 binning	0.03 ppm	0.03 ppm

TABLE 6.4: *Systematic uncertainties in the asymmetries, published in [278]. The first three uncertainties are treated as point-to-point; the last three are global.*

determination of a transverse asymmetry from these data, and we have chosen not to publish these results, but the analysis of these data are reported in Chapter 5.4. We can infer from these data that the transverse beam asymmetry for these detectors is likely not huge, certainly less than 15 ppm.

The octants each span about 45° in ϕ, and the average azimuthal angles corresponding to each octant in our coordinate system are shown in Figure 6.7. As the detector arrays are positioned at evenly-spaced azimuthal angles ϕ around the beamline, the asymmetries should follow a sinusoidal dependence in ϕ, *viz.*

$$A_\perp = |A_n| \sin(\phi + \phi_0) + A_0, \tag{6.5}$$

where the amplitude $|A_n|$ is the magnitude of the transverse beam spin asymmetry, the phase ϕ_0 depends on the direction of the transverse beam polarization, and A_0 is any ϕ-independent offset of the data points. The data were taken with the Wien filter set so that the electron polarization for the positive (+) helicity is in the direction of the positive x-axis of a right-handed coordinate system (positive x-axis to the beam left, positive y-axis up, and the positive z-axis in the beam direction, looking downstream). The positive x-axis corresponds to $\phi = 0°$, and ϕ increases clockwise.

Using this convention, we obtain the final plots of the sinusoidal fits to the corrected elastic asymmetries versus ϕ for each of the detector groups. This sinusoidal dependence is displayed in Fig. 6.8, where the data are shown along with the best fit to Eq. 6.5. The error bars on the

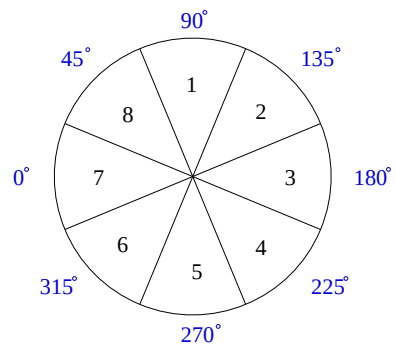

FIG. 6.7: *The average azimuthal angle corresponding to each of the G^0 octants following our defined coordinates.*

asymmetries are the statistical and point-to-point systematic uncertainties discussed in Section 5.4.8 combined in quadrature. The fits were constrained to ϕ_0 as calculated from the precession of the electron spin in the 3T solenoid used in the Møller polarimeter (5.3°) and do not allow a ϕ-independent offset, however, relaxing these constraints has negligible impact on the extracted A_n, and causes only slight changes in χ_ν and σ_{A_n}. The reduced χ^2 values for the fits were 0.63 and 0.58 for $Q^2 = 0.15, 0.25$, respectively.

However, the contributions of the statistical and systematic error bars must be unfolded from each other, as the error bar from the fit is a combination of the statistical and point-to-point uncertainties. To accomplish this, the sinusoidal fits were done for two cases: with the error bars on the data points being purely the statistical error bars, and with the error bars on the data points being the combination (in quadrature) of the statistical and point-to-point uncertainties. From this, we obtain these two results: for purely statistical error bars:

$$\text{Det } 1-8 : \mathrm{A_n} = -4.057 \pm 0.985 \text{ ppm}, \ \chi^2 = 0.700 \tag{6.6}$$

$$\text{Det } 9-12 : \mathrm{A_n} = -5.145 \pm 1.869 \text{ ppm}, \ \chi^2 = 0.717 \tag{6.7}$$

and for error bars of the statistical and point-to-point uncertainties combined in quadrature:

$$\text{Det } 1-8 : \mathrm{A_n} = -4.064 \pm 1.031 \text{ ppm}, \ \chi^2 = 0.630 \tag{6.8}$$

$$\text{Det } 9-12 : \mathrm{A_n} = -4.822 \pm 2.014 \text{ ppm}, \ \chi^2 = 0.578. \tag{6.9}$$

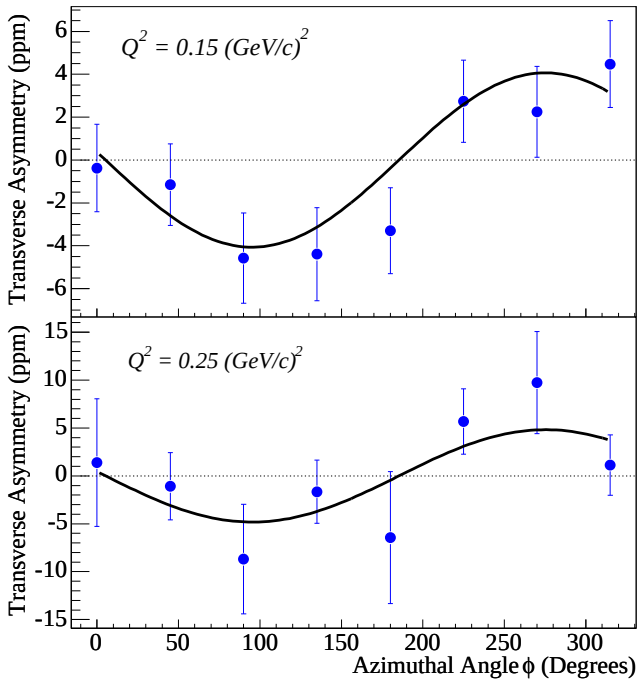

FIG. 6.8: *Measured asymmetry as a function of the azimuthal scattering angle ϕ for $Q^2 = 0.15$ (upper plot) and 0.25 $(GeV/c)^2$ (lower plot). The curves are the best fit to Eq. 6.5. Error bars are the statistical and individual systematic errors combined in quadrature.*

By comparing these two cases and working backward with the knowledge that,

$$\sigma_{syst} = \sqrt{\sigma^2_{total} - \sigma^2_{stat}}, \tag{6.10}$$

we obtain that the point-to-point systematic uncertainties are 0.305 and 0.750 for detectors 1 – 8 and 9 – 12, respectively. Thus we obtain our final results, as shown in Table 6.5. For the sake of publications and comparisons to theory, we can combine our systematic error to obtain the following:

$$\text{Det } 1-8 : \mathrm{A_n} = -4.064 \pm 0.985_{\text{stat}} \pm 0.625_{\text{syst}} \text{ ppm} \tag{6.11}$$

$$\text{Det } 9-12 : \mathrm{A_n} = -4.822 \pm 1.869_{\text{stat}} \pm 0.982_{\text{syst}} \text{ ppm}, \tag{6.12}$$

which is further reduced to

$$\text{Det } 1-8 : \mathrm{A_n} = -4.064 \pm 1.167 \text{ ppm} \tag{6.13}$$

$$\text{Det } 9-12 : \mathrm{A_n} = -4.822 \pm 2.111 \text{ ppm}. \tag{6.14}$$

Detector Bin	Q^2 (GeV/c)^2	θ_{CM}	A_n (ppm)
1-8	0.15 ± 0.02	$20.22°$	$-4.064 \pm 0.985_{stat} \pm 0.305_{pt-pt} \pm 0.546_{global}$
9-12	0.25 ± 0.03	$25.91°$	$-4.822 \pm 1.869_{stat} \pm 0.750_{pt-pt} \pm 0.634_{global}$

TABLE 6.5: *The final results for A_n, from the sinusoidal fits constrained to the calculated Møller precession and to a vertical offset of zero.*

These values are shown plotted versus their center-of-mass angle, θ_{CM} in Figure 6.9, in the next section.

The reduced χ^2 (per degree-of-freedom) values for the fits were found to be 0.630 and 0.578 for the two Q^2 points in order of increasing Q^2, corresponding to 73.12% and 77.46% confidence levels, respectively, that the data follow this dependence. In comparison, constant fits to these two data sets give values of $A = -0.444 \pm 0.718$ and $A = 0.698 \pm 1.464$ ppm with reduced χ^2 values of 2.795 and 1.365 and corresponding confidence levels of 0.66% and 22%.

6.2.2 Comparison with Theoretical Predictions

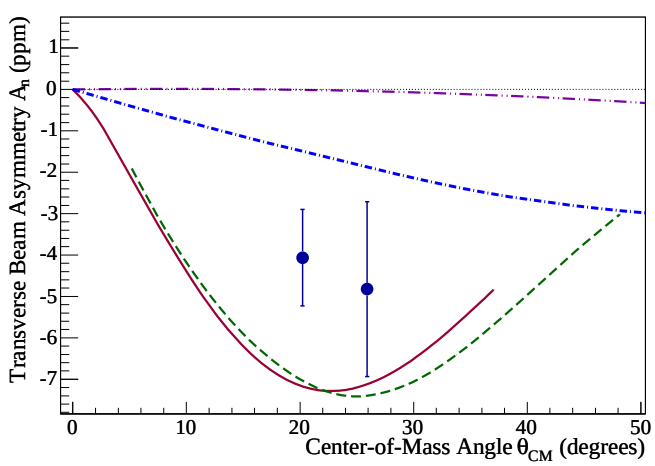

FIG. 6.9: *Published results for A_n as a function of center-of-mass scattering angle, along with calculations from Refs. [140, 148, 149] (see text for explanation).*

Including all corrections, we obtain A_n values of $-4.06 \pm 0.99_{\text{stat}} \pm 0.63_{\text{syst}}$ ppm for $Q^2 = 0.15$ (GeV/c)^2 and $A_n = -4.82 \pm 1.87_{\text{stat}} \pm 0.98_{\text{syst}}$ ppm for $Q^2 = 0.25$ (GeV/c)^2 from the sinusoidal fits, where the first error is statistical and the second is systematic in both cases. These are the

results reported in [278]. Figure 6.9 compares these results to the available calculations by Afanasev and Merenkov [148], Gorchtein [149], and Pasquini and Vanderhaeghen [140] appropriate to the kinematics of this measurement, as discussed in Section 2.8.3. The dash-double-dotted line is a calculation of the two-photon exchange contribution solely from the nucleon intermediate state (elastic contribution); the dash-dotted line represents the intermediate hadronic state for which the elastic contribution ground-state nucleon has been combined with inelastic contributions from excitation amplitudes to πN-intermediate states, both from Pasquini and Vanderhaeghen [140]. The solid line (Afanasev and Merenkov) [148] is a calculation using an optical theorem and parameterizations for the measured total photo-production cross sections ($\gamma + p \rightarrow X$) on the proton. The dashed line (Gorchtein) [149] represents a calculation where the imaginary part of the two-photon exchange amplitude is found in terms of the electron phase space integral over DIS structure functions. Clearly, the data show that the contribution of the inelastic hadronic intermediate state to the two-photon exchange amplitude is significant and that the nucleon intermediate state alone is not sufficient in calculations of the two-photon exchange amplitude. This conclusion is consistent with those reported by SAMPLE [145] and PVA4 [156]; however, as the kinematics are different, the data points cannot be compared directly.

6.2.3 Summary

These results are inconsistent with calculations using only the elastic nucleon intermediate state, and are in general agreement with calculations with significant inelastic hadronic intermediate state contributions. The data reported here, along with other measurements, help provide a valuable test of the theoretical framework of the two-photon contribution to the cross section through a comparison of the experimentally measured imaginary part of the two-photon exchange contribution to calculations of the real part, as the two are related through dispersion relations [139]. Two-photon exchange and other box diagrams are important in the interpretation of high-precision parity-violating electron-scattering experiments and in the radiative corrections for other lepton scattering experiments, making an understanding of these contributions important.

In addition, these asymmetries are potentially another tool to access information about hadron structure.

The G^0 experiment and other experiments [157] have recently obtained transverse beam spin asymmetry data at various angles on hydrogen, deuterium, and helium targets at additional Q^2 values, which will provide a further exploration of the imaginary part of the two-photon exchange amplitude (See Section 7.1.2).

6.3 Conclusions

The forward-angle phase of the G^0 experiment has measured and reported two different physics results to date, each measurement adding to the knowledge of nucleon structure. The primary measurement of the G^0 experiment yielded the linear combination of the strange electric and magnetic form factors $G_E^s + \eta G_M^s$ for the range from $0.1 \leq Q^2 \leq 1.0$ (GeV/c)^2. The data show an intriguing Q^2 dependence that, although close to zero, disfavors the no-vector-strange hypothesis with 89% confidence. However, the backward-angle measurements are necessary to completely separate the strange electric and magnetic form factors and thus answer the question of the magnitude of strange quark contributions to these quantities. The results for the forward-angle transverse beam spin data analysis show that the calculations using solely the nucleon intermediate state are not sufficient, and that the intermediate hadronic states have a significant contribution to the two-photon exchange amplitude. This conclusion is in agreement with other measurements of the transverse asymmetry at other kinematics. Both of these measurements provide more pieces to the puzzle of nucleon structure, and with future measurements (see Section 7.1), will help to form a complete picture.

CHAPTER 7

Concluding Remarks

7.1 Prospects for the Future

Although both of these measurements are clearly important and add to the world data on these topics, more work is needed in each case to fully understand and describe these phenomena. This section presents the experiments that will provide the next steps, and discusses some speculation regarding the future directions of these measurements.

7.1.1 The Future of Strange Quark Physics

With such intriguing results, but no definitive answers, clearly more must be done. As discussed in Section 2.3, to accomplish a complete separation of the strange form factors, measurements at both forward and backward angles are necessary. The G^0 experiment has recently finished taking backward-angle data at $Q^2 = 0.23$ and 0.62 $(\mathrm{GeV}/c)^2$ on both liquid hydrogen and deuterium targets. To make the measurement, the entire spectrometer was turned around, enabling the detection of backscattered electrons at $\theta = 108°$, as can be seen in the diagram in Figure 7.1. Time-of-flight could not be used to separate the elastically scattered electrons from the inelastic ones, so arrays of nine cryostat exit detectors (CEDs) were installed for each octant of the Ferris

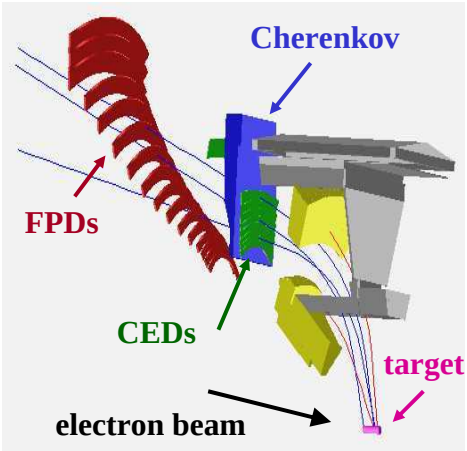

FIG. 7.1: *Schematic of the G^0 backward-angle measurement.*

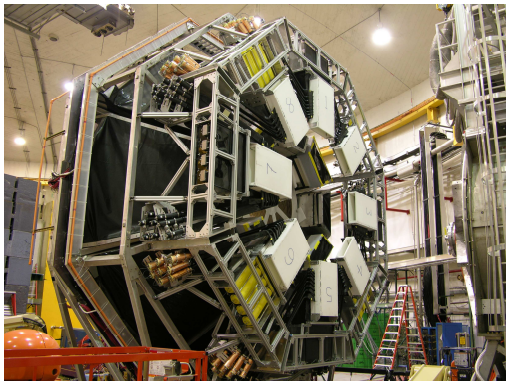

FIG. 7.2: *Photograph of the detectors for G^0 backward-angle measurement.*

Wheel, along with aerogel Čerenkov detectors used to differentiate between pions and electrons. A photograph of the detectors for the backangle measurement is shown in Figure 7.2. As time-of-flight was not used for particle identification, the beam was the standard 499 MHz CEBAF structure, greatly simplifying the beam delivery. The beam quality for both Q^2 values (at 362 and 687 MeV) was very high, as was the polarization ($\sim 85\%$), due to the use of the new superlattice photocathode. New electronics were used that formed a CED-FPD coincidence matrix to identify particles. Examples of the coincidence matrix pattern and electron data from LH_2 at 687 MeV are shown in Figures 7.3 and 7.4. For more information on the G^0 backward-angle measurements, see References [194, 284].

Using the data from these measurements, a complete separation of the strange electric, magnetic, and axial form factors (G_E^s, G_M^s, and G_A^e) will be done at $Q^2 = 0.23$ and 0.62 $(\mathrm{GeV}/c)^2$. These points were chosen for the backward-angle measurements as $Q^2 = 0.62$ is in the range where the measurement of the linear combination of G_E^s and G_M^s suggests that strange quark effects could be sizable, and $Q^2 = 0.23$ is in a region of higher precision and where the effects could be cancelling each other out. As most of the world data is at $Q^2 = 0.1$ and the form factors are not expected to vary rapidly with Q^2, these points should provide illumination on the Q^2 behaviour

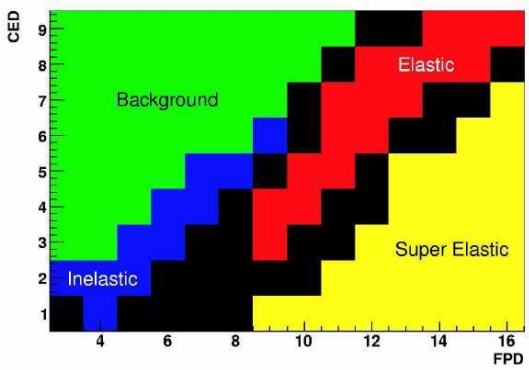

FIG. 7.3: *Schematic of the CED-FPD coincidence matrix pattern for LH_2 at a beam energy of 687 MeV.*

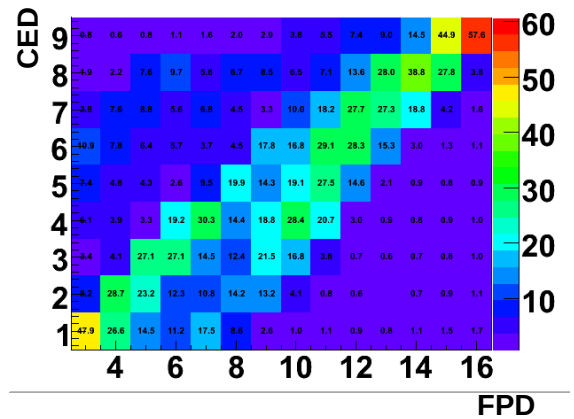

FIG. 7.4: *LH_2 electron coincidence data taken at 687 MeV.*

of these form factors. The data analysis for the G^0 backward-angle data is underway, with results possibly available within the next year.

The PVA4 experiment [285] has also taken backward-angle data at $Q^2 = 0.23$ (GeV/c)^2 [190, 191]. As with the G^0 experiment, the entire detector system was repositioned to detect elastically-backscattered electrons at 145° from the interaction of the 315 MeV beam with the liquid hydrogen target. The analysis of these data is ongoing, and will provide further illumination, especially as the data are at different kinematics than the Jefferson Lab measurements.

With the release of results that suggest there could be a non-zero contribution from the strange sea to the nucleon's properties at higher values of Q^2, there is quite a bit of interest in studying this range more thoroughly. HAPPEx III (E05-109) [286] in Hall A will measure the parity-violating asymmetry in the elastic scattering of 3.4 GeV electrons from liquid hydrogen at $Q^2 = 0.6$ (GeV/c)^2 to investigate the suggestion that the strange quark form factors could be non-zero at higher Q^2 values. A high-precision measurement in this region will help to constrain the possible contributions of strange quarks to the linear combination of G_E^s and G_M^s, especially in conjunction with the G^0 backward-angle measurements.

7.1.1.1 Other Measurements from G^0

In addition to the above measurements, the G^0 experiment is also simultaneously measuring the parity-violating asymmetry in inclusive single pion electroproduction from the proton in the range of $0.1 \leq Q^2 \leq 0.6$ (GeV/c)^2, which will be used to extract the axial vector transition form factor $G^A_{N\Delta}$ for the $N \rightarrow \Delta$ transition as a function of Q^2 [287]. The form factor $G^A_{N\Delta}$ characterizes the axial, or intrinsic spin response of the nucleon during the transition to its first excited state. This measurement is the first determination of this form factor in the neutral current sector of the weak interaction, and will help in the understanding of the Δ resonance.

7.1.2 Explorations of Two-Photon Exchange

As a part of the systematics studies for the backward-angle measurements of the G^0 experimental program, more transverse beam spin asymmetry data were taken for both targets at both the 0.362 GeV and 0.687 GeV beam energies. About 3.59 C and 2.69 C were taken at 0.23 and 0.62 (GeV/c)^2 respectively on the LH_2 target, yielding statistical uncertainties of $\sim$ 5–6 ppm and $\sim$ 15 ppm respectively, as summarized in Table 7.1. Both measurements were taken at $\theta_{CM} \sim 130°$. The transverse beam spin asymmetry $A_\perp$ is predicted to be quite large for the kinematics of the G^0 backangle running (~ -100 ppm for 0.3 GeV and ~ -42 ppm for 0.570 GeV!), making the measurement important for the constraint of the systematic errors from residual transverse polarization in the parity-violating asymmetry measurement, but also allowing a clean measurement at this precision. Plots of the calculations for the predicted transverse beam asymmetry by reference [140] with markers showing the anticipated G^0 backangle precision for these data on LH_2 are shown in Figure 7.5. Note that the calculations in the figures are not at precisely the same beam energy as the G^0 measurements; however, they serve to give a good estimate to the reader of the magnitude of the measured asymmetry. These measurements on liquid hydrogen and liquid deuterium will do much to add to the knowledge of two-photon exchange effects. In addition, these data are also of interest as they can be used to study the transverse asymmetry for pions, as these

Beam Energy	$\langle Q^2 \rangle$	Target	Accumulated Charge
0.362 GeV	0.23	LH_2	3.59 C
0.687 GeV	0.62	LH_2	2.67 C
0.362 GeV	0.23	LD_2	2.13 C
0.687 GeV	0.62	LD_2	0.14 C

TABLE 7.1: *The anticipated statistical precision of the G^0 backward-angle transverse beam spin measurements on LH_2 at each beam energy and Q^2.*

data were taken along with the elastically scattered electrons.

Other forthcoming parity-violation experiments will make measurements of the transverse beam spin asymmetry as part of their systematic studies, and will also extract the interesting physics from these data. HAPPEx III (in the same manner as HAPPEx II) and Q_{Weak} will certainly both study this effect at their respective kinematics.

In addition, there are several dedicated forthcoming experiments which will study two-photon exchange effects in various ways. Currently running in Hall C is a measurement of two-photon exchange effects in unpolarized elastic electron-proton scattering by JLab experiment E05-017 [288]. The goal of the experiment is to perform a series of high-precision Rosenbluth separation measurements over the range $1 \leq Q^2 \leq 6$ (GeV/c)^2. The experiment then will use these precise Rosenbluth measurements to study the ϵ and Q^2 dependence of two-photon exchange contributions to the elastic $e-p$ cross section by extracting the two-photon effects from the difference between the measured Rosenbluth and existing polarization transfer measurements combined with limit from existing position-proton data. This measurement studies the effects of the real part of the two-photon exchange amplitude.

A measurement of the target normal single spin asymmetry in inclusive deep-inelastic $n^{\uparrow}(e,e')$ scattering [289] will take place during the Hall A neutron transversity experiments (E06-010 and E06-011) using a vertically polarized ^{3}He target at $Q^2 = 1.3$, 2.0, 2.6, and 3.1 (GeV/c)^2. Like the beam-normal transverse asymmetry, the target-normal transverse asymmetry arises from the imaginary part of the two-photon exchange amplitude and is a good observable for two-photon

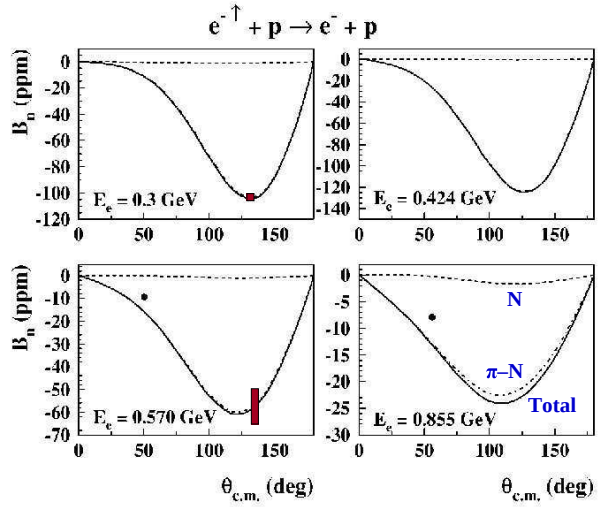

FIG. 7.5: *The anticipated G^0 backward-angle results at $\theta_{COM} \sim 130°$ on LH_2, statistical errors only, shown with predictions of the transverse asymmetry magnitude. Note that the calculations are not exactly at the G^0 beam energies, but nevertheless give an estimate for the reader. The calculation with solely the nucleon elastic state is designated as N, the calculation using the intermediate hadronic states is labeled as π–N, and the combination of both is labeled as Total. Calculations from reference [140]; data from the A4 collaboration, reference [156].*

exchange effects; furthermore, in DIS the normal spin asymmetry probes helicity-flip amplitudes at the quark level related to effects beyond the leading-twist description of DIS. The target single-spin asymmetry for the neutron in inclusive quasi-elastic ^{3}He(e, e') scattering will also be measured at $Q^2 = 1.0$ and 2.3 (GeV/c)^2 in Hall A using a vertically polarized ^{3}He target [290]. This measurement will provide new information on the dynamics of the two-photon exchange process and give new constraints on GPD models.

In Hall B, a direct measurement of the two-photon exchange contribution to lepton-proton elastic scattering is planned using the CLAS spectrometer [291] to explain the discrepancy between the Rosenbluth and polarization transfer methods of measuring the G_E/G_M ratio of the proton. The experiment will measure the cross section ratio of the elastic electron-proton and positron-proton $\left(\frac{\sigma(e^-p)}{\sigma(e^+p)}\right)$, as a function of ϵ and Q^2 for $0.5 < Q^2 < 2.5$ (GeV/c)^2. From these data, the two-photon exchange corrections to elastic scattering in this region can be extracted, and will provide important constraints for models of two-photon exchange effects. This measurement is sensitive to the real part of the two-photon exchange amplitude.

Another experiment in Hall C is also planned to study the real part of two-photon exchange effects. Experiment E04-019 [292] will measure the ϵ dependence at constant Q^2 of the recoil proton polarization in ep elastic scattering, measuring the polarization transfer components simultaneously. In the measurement, an ϵ-dependence that differs from the one-photon exchange calculation is assumed to be due to the real part of the two-photon exchange amplitude, giving a greater understanding of the effects of two-photon exchange in polarization transfer measurements.

7.1.3 The Future of PVES

In the future, PVES seems to be heading back to its beginnings, in fundamental symmetry searches. The Q_{Weak} experiment (E05-008) [293] will measure the parity-violating asymmetry in electron scattering on the proton at very low Q^2 and forward angles in Hall C at Jefferson Lab. The goal of this precision measurement is to test predictions of the Standard Model and search for new physics by looking for a significant deviation of the running of the weak mixing angle, $\sin^2\theta_W$, from the Standard Model prediction at low Q^2. This will be the first precision measurement of the proton's weak charge, $Q^p_{Weak} = 1 - 4\sin^2\theta_W$ at Jefferson Lab, and the most precise standalone measurement of the weak mixing angle at low Q^2. This experiment builds on the technical advances made in JLab's parity-violation program, as well as using the results of the G^0 and HAPPEx experiments to constrain corrections from contributions from hadronic structure (including G^s_E and G^s_M) in the measurement, making this experiment truly the next big step in the parity-violation program at Jefferson Lab.

As with the G^0 experiment and other precision parity-violation measurements, the Q_{Weak} experiment will measure the transverse asymmetry to put constraints on the possible size of any systematic contributions to the parity-violating asymmetry due to any residual transversely-polarized beam component. The azimuthally-symmetric, segmented design of the detectors allows for a lovely measurement of the sinusoidal dependence of the transverse asymmetry, and will yield another measurement of this asymmetry at a different kinematic setting.

The 12 GeV Upgrade to the accelerator at Jefferson Lab will provide the opportunity for new

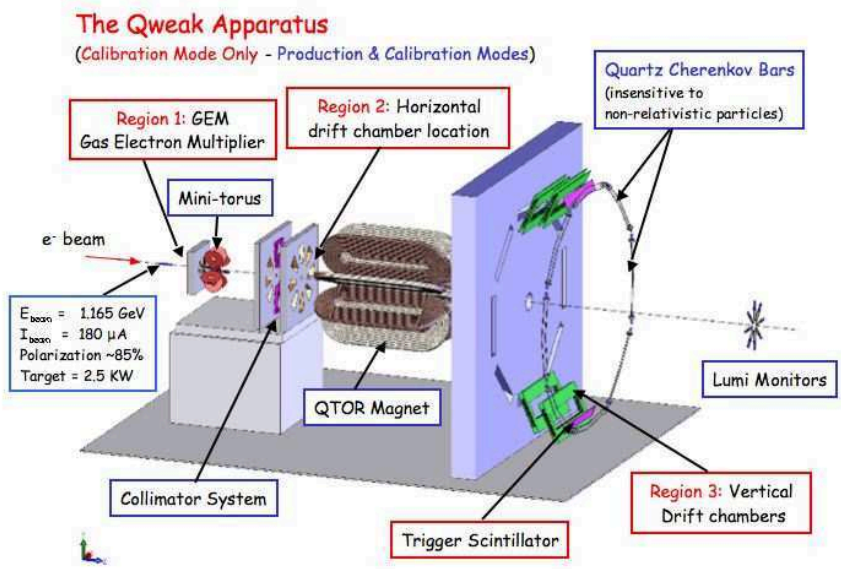

FIG. 7.6: *A CAD drawing of the Apparatus for the Q_{Weak} Experiment in Hall C at Jefferson Lab.*

precision parity-violating electron scattering experiments to further challenge Standard Model predictions and search for physics beyond the Standard Model. Two types of experiments in particular are envisioned: parity-violating deep inelastic scattering (PV DIS) and parity-violating Møller scattering.

Parity-violating deep inelastic scattering with a deuterium target, first observed by Prescott *et al.* [170, 171] in the mid-1970's, could be used either to study higher-twist structure functions or as a way of searching for new physics. Information on higher-twist structure functions could be extracted from the Q^2-dependence of the parity-violating asymmetry in the range made accessible by the upgrade. In a sense, this could be viewed as an extension of JLab's strange quark program, as parity-violation is being used to study non-perturbative nucleon structure. In the search for new physics beyond the Standard Model, PV DIS measurements would provide complementary information about the Q^2-dependence of $\sin^2\theta_W$ in the deep inelastic domain to the work of the NuTeV collaboration on deep inelastic ν ($\bar{\nu}$)-nucleus scattering from iron. The NuTeV results for the Q^2-dependence of the weak mixing angle indicate a 3σ-deviation from the standard model, sparking debates as to the size of possible non-perturbative QCD contributions to this anomaly. As

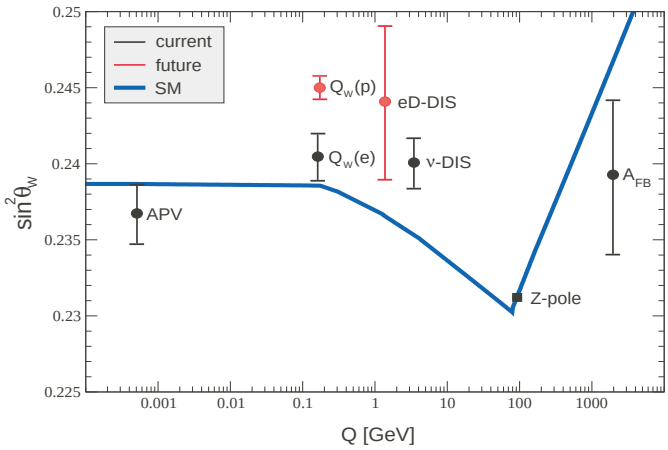

FIG. 7.7: *Calculated running of the weak mixing angle* $\sin^2(\theta_W)$ *as a function of* Q^2 *in the standard model (modified minimal subtraction scheme), where the black points are existing measurements from atomic parity violation (APV), SLAC E158 (*$Q_W(e)$*), deep inelastic neutrino-nucleus scattering (NuTeV), and from* Z^0 *pole asymmetries (LEP+SLC); the red points show the future proposed measurements for the* Q_{Weak} *Experiment in Hall C at Jefferson Lab and eD-DIS (at arbitrarily chosen vertical locations). Figure from Ref [293].*

PV DIS measurements would involve differing systematic and non-perturbative QCD effects, such measurements could help to resolve the discrepancy or verify a deviation from the Standard Model [294–297]. This experimental program could also make measurements of the parity-conserving transverse asymmetry. In deep-inelastic scattering, the collinear-photon enhancement [148] is absent in the leading-twist parton calculation, but could appear at the higher-twist level or be enhanced by nonpertubative QCD effects, and thus provide insight into QCD dynamics. QED calculations of the transverse asymmetry on a muon from the 1960's [66] can be applied to electron scattering from a point-like quark and gives an estimated effect of a fraction of a ppm in the kinematics for a JLab DIS parity experiment [297].

The parity-violating asymmetry in Møller scattering measures the weak charge of the electron, and thus is very sensitive to the value of $\sin^2\theta_W$. The interpretation is much cleaner than for PV DIS due to the lack of higher-twist contributions to the asymmetry, but the measurement is difficult due to the tiny size of the asymmetry. A 12 GeV Møller experiment at Jefferson Lab could achieve half of the anticipated uncertainty of the recent SLAC E-158 Møller experiment [168, 169], and would be the best measurement of the electron's weak charge at low energy scales [294]. Not

only could this measurement search for new physics beyond the Standard Model by challenging the prediction for the running of the weak mixing angle, but will have the precision to probe aspects of supersymmetry, such as the existence of a viable supersymmetric candidate for cold dark matter, the non-luminous and unexplained source of about 90% of the universe's mass [298, 299], by restricting the available parameter space for viable models. A 12 GeV Møller experiment would also provide an opportunity to measure the transverse asymmetry in Møller scattering at these kinematics.

Both the near future and the somewhat further future upgrade of the CEBAF accelerator to 12 GeV provide remarkable opportunities to build on the great success of previous parity-violating electron scattering experiments. Although all of these experiments will measure $\sin^2\theta_W$, they are sensitive to different possible Standard Model extensions, and provide the opportunity to search for new physics.

7.2 Conclusions

This dissertation has presented the analysis and results of the forward-angle measurement of the G^0 experiment at Jefferson Lab, plus context for backward-angle measurements. The results of this measurement, the linear combination of the strange electric and magnetic form factors $G_E^s + \eta G_M^s$, suggest possible non-zero, Q^2 dependent, strange quark contributions and provide new information to understand the magnitude of the contributions. In addition, this dissertation presented the analysis and results from the G^0 measurement of the beam-normal single-spin asymmetry in the elastic scattering of transversely polarized 3 GeV electrons from unpolarized protons at $Q^2 = 0.15, 0.25\ (\mathrm{GeV}/c)^2$. The results of the measurement indicate that calculations using solely the elastic nucleon intermediate state are insufficient and generally agree with calculations that include significant inelastic hadronic intermediate state contributions. These two measurements have helped to further the knowledge of the nucleon, and have provided information for future investigations to build upon.

BIBLIOGRAPHY

[1] E. Rutherford. The Structure of the Atom. *Nature*, 92:423, December 11, 1913.

[2] E. Rutherford. Nuclear Constitution of Atoms. *Proceedings of the Royal Society, Series A (Proceedings of the Royal Society of London. Series A, Containing Papers of a Mathematical and Physical Character (1905-1934))*, 97(686):374–400, July 1, 1920.

[3] J. Chadwick. Possible Existence of a Neutron. *Nature*, 129:312, February 27, 1932.

[4] J. Chadwick. The Existence of a Neutron. *Proceedings of the Royal Society, Series A (Proceedings of the Royal Society of London. Series A, Containing Papers of a Mathematical and Physical Character (1905-1934))*, 136(830):692–708, June 1, 1932.

[5] R. Frisch and O. Stern. Über die magnetische Ablenkung von Wasserstoff-molekülen und das magnetische Moment des Protons. I. *Zeitschrift fur Physik*, 85:4, August 1933.

[6] Luis W. Alvarez and F. Bloch. A Quantitative Determination of the Neutron Moment in Absolute Nuclear Magnetons. *Phys. Rev.*, 57(2):111–122, January 1940.

[7] Jerome I. Friedman and Henry W. Kendall. Deep Inelastic Electron Scattering. *Ann. Rev. Nucl. Part. Sci.*, 22:203–254, 1972.

[8] R. Schwitters and K. Strauch. The Physics of e^+ e^- Collisions. *Ann. Rev. Nucl. Part. Sci.*, 26:89–149, 1976.

[9] E. W. Hughes and R. Voss. Spin Structure Functions. *Ann. Rev. Nucl. Part. Sci.*, 49:303–339, 1999.

[10] J. D. Bjorken. Applications of the Chiral $U(6) \bigotimes U(6)$ Algebra of Current Densities. *Phys. Rev.*, 148(4):1467–1478, August 1966 [Erratum-ibid. 160, 1582 (1967)].

[11] J. D. Bjorken. Inelastic Scattering of Polarized Leptons from Polarized Nucleons. *Phys. Rev. D*, 1(5):1376–1379, March 1970.

[12] J. Ashman *et al.* [European Muon Collaboration]. An Investigation of the Spin Structure of the Proton in Deep Inelastic Scattering of Polarized Muons on Polarized Protons. *Nucl. Phys.*, B328:1–35, December 11, 1989.

[13] D. Adams *et al.* [Spin Muon Collaboration (SMC)]. Spin structure of the proton from polarized inclusive deep- inelastic muon proton scattering. *Phys. Rev.*, D56:5330–5358, November 1, 1997 (hep-ex/9702005).

[14] K. Abe *et al.* [E143 collaboration]. Measurements of the proton and deuteron spin structure functions g_1 and g_2. *Phys. Rev.*, D58:112003, October 27, 1998 (hep-ph/9802357).

[15] P. L. Anthony *et al.* [E155 Collaboration]. Measurements of the Q^2-dependence of the proton and neutron spin structure functions g_1^p and g_1^n. *Phys. Lett.*, B493:19–28, November 9, 2000 (hep-ph/0007248).

[16] A. Airapetian *et al.* [HERMES Collaboration]. Measurement of the proton spin structure function g_1^p with a pure hydrogen target. *Phys. Lett.*, B442:484–492, December 3, 1998 (hep-ex/9807015).

[17] G. Baum *et al.* New Measurement of Deep-Inelastic e–p Asymmetries. *Phys. Rev. Lett.*, 51:1135, September 26, 1983.

[18] John Ellis and Robert Jaffe. Sum rule for deep-inelastic electroproduction from polarized protons. *Phys. Rev. D*, 9(5):1444–1446, March 1974 [Erratum-ibid. D 10, 1669 (1974)].

[19] B. W. Filippone and Xiang-Dong Ji. The Spin Structure of the Nucleon. *Adv. Nucl. Phys.*, 26:1–88, 2002 (hep-ph/0101224).

[20] B. Adeva *et al.* [Spin Muon Collaboration (SMC)]. Polarised quark distributions in the nucleon from semi- inclusive spin asymmetries. *Phys. Lett.*, B420:180–190, February 1998 (hep-ex/9711008).

[21] K. Ackerstaff *et al.* [HERMES Collaboration]. Flavor decomposition of the polarized quark distributions in the nucleon from inclusive and semi-inclusive deep-inelastic scattering. *Phys. Lett.*, B464:123–134, October 1999 (hep-ex/9906035).

[22] D. Mason [NuTeV Collaboration]. New Strange Asymmetry Results from NuTeV. arXiv:hep-ex/0405037, May 15, 2004.

[23] D. Mason [NuTeV Collaboration]. NuTeV Strange/Antistrange Sea Measurements from Neutrino Charm Production. *AIP Conf. Proc.*, 792:851–854, 2005.

[24] G. P. Zeller *et al.* [NuTeV Collaboration]. Effect of asymmetric strange seas and isospin-violating parton distribution functions on $sin^2\theta_W$ measured in the nutev experiment. *Phys. Rev. D*, 65(11):111103, June 2002 (hep-ex/0203004) [Erratum-ibid. D 67, 119902 (2003)].

[25] T. Adams *et al.* [NuTeV Collaboration]. Strange Content of the Nucleon (NuTeV). arXiv:hep-ex/9906038, June 27, 1999.

[26] V. Barone, C. Pascaud, and F. Zomer [NuTeV Collaboration]. A New Global Analysis of DIS Data and the Strange Sea Distribution. arXiv:hep-ph/0004268, December 1999.

[27] Douglas H. Beck and Barry R. Holstein. Nucleon Structure and Parity-Violating Electron Scattering. *Int. J. Mod. Phys.*, E10:1–41, February 2001 (hep-ph/0102053).

[28] L. A. Ahrens *et al.* Measurement of neutrino-proton and antineutrino-proton elastic scattering. *Phys. Rev.*, D35:785–809, February 1987.

[29] G. T. Garvey, W. C. Louis, and D. H. White. Determination of proton strange form factors from νp elastic scattering. *Phys. Rev.*, C48:761–765, August 1993.

[30] R. L. Jaffe and C. L. Korpa. The Pattern of Chiral Symmetry Breaking and the Strange Quark Content of the Proton. *Comments Nucl. Part. Phys.*, 17:163, January 1987.

[31] J. Gasser, H. Leutwyler, and M. E. Sainio. Sigma-term update. *Phys. Lett.*, B253:252–259, January 3, 1991.

[32] J. Gasser, H. Leutwyler, and M. E. Sainio. Form factor of the σ-term. *Phys. Lett.*, B253:260–264, January 3, 1991.

[33] M. G. Olsson. The nucleon sigma term from threshold parameters. *Phys. Lett.*, B482:50–56, June 1, 2000 (hep-ph/0001203).

[34] M. M. Pavan, R. A. Arndt, I. I Strakovsky, and R. L. Workman. New Result for the Pion-Nucleon Sigma Term from an Updated VPI/GW πN Partial-Wave and Dispersion Relation Analysis. *PiN Newslett.*, 15:118–122, 1999 (nucl-th/9912034).

[35] M. E. Sainio. Low-Energy Pion-Nucleon Interaction and the Sigma-Term. *PiN Newslett.*, 13:144–149, 1997 (hep-ph/9709302).

[36] Paul Büttiker and Ulf-G. Meißner. Pion-nucleon scattering inside the Mandelstam triangle. *Nucl. Phys.*, A668:97–112, March 27, 2000 (hep-ph/9908247).

[37] R. Hofstadter and R. W. McAllister. Electron Scattering from the Proton. *Phys. Rev.*, 98:217–218, April 1955.

[38] Robert Hofstadter. Electron Scattering and Nuclear Structure. *Rev. Mod. Phys.*, 28:214–254, July 1956.

[39] Robert N. Cahn and Frederick J. Gilman. Polarized-electron-nucleon scattering in gauge theories of weak and electromagnetic interactions. *Phys. Rev.*, D17:1313–1322, March 1978.

[40] David B. Kaplan and Aneesh Manohar. Strange Matrix Elements in the Proton from Neutral-Current Experiments. *Nucl. Phys.*, B310:527–547, December 12, 1988.

[41] R. D. McKeown. Sensitivity of Polarized Elastic Electron-Proton Scattering to the Anomalous Baryon Number Magnetic Moment. *Phys. Lett.*, B219:140–142, March 16, 1989.

[42] D. H. Beck. Strange-quark vector currents and parity-violating electron scattering from the nucleon and from nuclei. *Phys. Rev.*, D39:3248–3256, June 1, 1989.

[43] Gerald A. Miller. Nucleon charge symmetry breaking and parity violating electron-proton scattering. *Phys. Rev.*, C57:1492–1505, March 1998 (nucl-th/9711036).

[44] J. Mar *et al.* Comparison of Electron-Proton and Positron-Proton Elastic Scattering at Four Momentum Transfers Up to 5.0 $(\mathrm{GeV}/c)^2$. *Phys. Rev. Lett.*, 21:482–484, August 1968.

[45] S. Hartwig *et al.* Elastic Scattering of Electrons and Positrons from Protons. *Lett. Nuovo Cim.*, 12:30–32, 1975.

[46] Luke W. Mo and Yung-Su Tsai. Radiative Corrections to Elastic and Inelastic ep and μp Scattering. *Rev. Mod. Phys.*, 41:205–235, January 1969.

[47] N. Meister and D. R. Yennie. Radiative Corrections to High-Energy Scattering Processes. *Phys. Rev.*, 130(3):1210–1229, May 1963.

[48] S. D. Drell and M. A. Ruderman. Proton Polarizability Correction to Electron-Proton Scattering. *Phys. Rev.*, 106(3):561–563, May 1957.

[49] S. D. Drell and S. Fubini. Higher Electromagnetic Corrections to Electron-Proton Scattering. *Phys. Rev.*, 113(2):741–744, January 1959.

[50] N. R. Werthamer and M. A. Ruderman. Nucleon Polarizability Correction to High-Energy Electron-Nucleon Scattering. *Phys. Rev.*, 123(3):1005–1013, August 1961.

[51] Gary K. Greenhut. Two-Photon Exchange in Electron-Proton Scattering. *Phys. Rev.*, 184(5):1860–1867, August 1969.

[52] P. A. M. Guichon and M. Vanderhaeghen. How to Reconcile the Rosenbluth and the Polarization Transfer Methods in the Measurement of the Proton Form Factors. *Phys. Rev. Lett.*, 91:142303, October 2003 (hep-ph/0306007).

[53] R. C. Walker *et al.* Measurements of the proton elastic form factors for $1 \leq Q^2 \leq 3$ (GeV/c)^2 at SLAC. *Phys. Rev.*, D49:5671–5689, June 1994.

[54] L. Andivahis *et al.* Measurements of the electric and magnetic form factors of the proton from $Q^2 = 1.75$ to 8.83 (GeV/c)^2. *Phys. Rev.*, D50:5491–5517, November 1994.

[55] M. E. Christy *et al.* [E94110 Collaboration]. Measurements of electron-proton elastic cross sections for $0.4 < Q^2 < 5.5$ (GeV/c)^2. *Phys. Rev.*, C70:015206, 2004 (nucl-ex/0401030).

[56] I. A. Qattan *et al.* Precision Rosenbluth Measurement of the Proton Elastic Form Factors. *Phys. Rev. Lett.*, 94:142301, April 2005 (nucl-ex/0410010).

[57] M. N. Rosenbluth. High Energy Elastic Scattering of Electrons on Protons. *Phys. Rev.*, 79:615–619, August 1950.

[58] M. K. Jones *et al.* [Jefferson Lab Hall A Collaboration]. G_{E_p}/G_{M_p} Ratio by Polarization Transfer in $\vec{e}p \rightarrow e\vec{p}$. *Phys. Rev. Lett.*, 84:1398–1402, February 2000 (nucl-ex/9910005).

[59] O. Gayou *et al.* [Jefferson Lab Hall A Collaboration]. Measurement of G_{E_p}/G_{M_p} in $\vec{e}p \rightarrow e\vec{p}$ to $Q^2 = 5.6$ GeV^2. *Phys. Rev. Lett.*, 88:092301, March 2002 (nucl-ex/0111010).

[60] V. Punjabi *et al.* [Jefferson Lab Hall A Collaboration]. Proton elastic form factor ratios to $Q^2 = 3.5$ GeV^2 by polarization transfer. *Phys. Rev.*, C71:055202, 2005 (nucl-ex/0501018) [Erratum-ibid. C **71**, 069902 (2005)].

[61] A. I. Akhiezer and Mikhail. P. Rekalo. Polarization effects in the scattering of leptons by hadrons. *Sov. J. Part. Nucl.*, 4:277, 1974.

[62] R. G. Arnold, Carl E. Carlson, and Franz Gross. Polarization transfer in elastic electron scattering from nucleons and deuterons. *Phys. Rev.*, C23:363–374, January 1981.

[63] J. Arrington. How well do we know the electromagnetic form factors of the proton? *Phys. Rev.*, C68:034325, September 2003 (nucl-ex/0305009).

[64] Andrei V. Afanasev and Carl E. Carlson. Two-Photon-Exchange Correction to Parity-Violating Elastic Electron-Proton Scattering. *Phys. Rev. Lett.*, 94:212301, June 2005 (hep-ph/0502128).

[65] W. J. Marciano and A. Sirlin. Some general properties of the O(α) corrections to parity violation in atoms. *Phys. Rev.*, D29:75, 1984 [Erratum-ibid. D **31**, 213 (1985)].

[66] A. O. Barut and C. Fronsdal. Spin-orbit correlations in $\mu - e$ and $e^- - e^-$ scattering. *Phys. Rev.*, 120(5):1871–1874, December 1, 1960.

[67] A. De Rujula, J. M. Kaplan, and E. De Rafael. Elastic Scattering of Electrons from Polarized Protons and Inelastic Electron Scattering Experiments. *Nucl. Phys.*, B35:365–389, December 15, 1971.

[68] M. J. Musolf *et al.* Intermediate-energy semileptonic probes of the hadronic neutral current. *Phys. Rept.*, 239:1–178, April 1994.

[69] D. H. Beck and R. D. McKeown. Parity-Violating Electron Scattering and Nucleon Structure. *Ann. Rev. Nucl. Part. Sci.*, 51:189–217, 2001 (hep-ph/0102334).

[70] K. S. Kumar and P. A. Souder. Strange Quarks and Parity Violation. *Prog. Part. Nucl. Phys.*, 45:S333–S395, 2000.

[71] F. Halzen and A. D. Martin. *Quarks and Leptons: An Introductory Course in Modern Particle Physics.* John Wiley & Sons, New York, 1984.

[72] E. J. Beise and R. D. McKeown. *Comments on Nuclear and Particle Physics*, 20:105, 1991.

[73] T. D. Lee and C. N. Yang. Conservation of Heavy Particles and Generalized Gauge Transformations. *Phys. Rev.*, 98(5):1501, June 1, 1955.

[74] T. D. Lee, R. Oehme, and Chen-Ning Yang. Remarks On Possible Noninvariance Under Time Reversal And Charge Conjugation. *Phys. Rev.*, 106:340–345, April 15, 1957.

[75] T. D. Lee and Chen-Ning Yang. Question Of Parity Conservation In Weak Interactions. *Phys. Rev.*, 104:254–258, October 1, 1956 [Erratum-ibid. 106, 1371 (June 1957)].

[76] T. D. Lee and Chen-Ning Yang. Parity Nonconservation and a Two-Component Theory of the Neutrino. *Phys. Rev.*, 105:1671–1675, March 1, 1957.

[77] C. S. Wu, E. Ambler, R. W. Hayward, D. D. Hoppes, and R. P. Hudson. Experimental Test of Parity Conservation in Beta Decay. *Phys. Rev.*, 105(4):1413–1415, February 1957.

[78] E. Ambler, R. W. Hayward, D. D. Hoppes, R. P. Hudson, and C. S. Wu. Further Experiments on β Decay of Polarized Nuclei. *Phys. Rev.*, 106(6):1361–1363, June 1957.

[79] C. S. Wu. Parity Experiments in Beta Decays. *Rev. Mod. Phys.*, 31(3):783–790, July 1959.

[80] R. L. Garwin, L. M. Lederman, and M. Weinrich. Observations of the Failure of Conservation of Parity and Charge Conjugation in Meson Decays: The Magnetic Moment of the Free Muon. *Phys. Rev.*, 105:1415–1417, February 1957.

[81] J. Arvieux *et al.* Electromagnetic radiative corrections in parity-violating electron-proton scattering. *Eur. Phys. J.*, A26:429–439, December 2005.

[82] M. A. El-Yakoubi, M. Morlet, J. Van de Wiele, J. Arvieux, R. Frascaria, S. Ong, S. Baunack, F. Maas, E. J. Beise, and J. Roche. Evaluation of Strange Form-Factors in Parity Violating Electron Scattering. *G0 Technical Note*, G0 Analysis Log 73: *Anapole corrections*, July 11, 2005.

[83] J. Arvieux, M. A. El-Yakoubi, M. Morlet, J. Van de Wiele, R. Frascaria, S. Ong, S. Baunack, F. Maas, E. J. Beise, D. Beck, and J. Roche. Towards a Common PVA4-SAMPLE Analysis: A First Step. *G0 Technical Note*, G0-doc-609-v1, July 11, 2005.

[84] M. E. Peskin and D. V. Schroeder. *An Introduction to Quantum Field Theory.* Perseus Books, Cambridge, 1995.

[85] Shi-Lin Zhu, S. J. Puglia, Barry R. Holstein, and M. J. Ramsey-Musolf. Nucleon anapole moment and parity-violating *ep* scattering. *Phys. Rev.*, D62:033008, July 2000 (hep-ph/0002252).

[86] S. Eidelman *et al.* (Particle Data Group). Review of Particle Physics. *Phys. Lett.*, B592:1–1109, July 2004.

[87] Nathan Isgur. Interpreting the Neutron's Electric Form Factor: Rest Frame Charge Distribution or Foldy Term? *Phys. Rev. Lett.*, 83:272–275, July 1999 (hep-ph/9812243).

[88] M. J. Musolf and Hiroshi Ito. Chiral symmetry and the nucleon's vector strangeness form factors. *Phys. Rev.*, C55:3066–3082, June 1997 (nucl-th/9607021).

[89] Thomas R. Hemmert, Ulf-G. Meißner, and Sven Steininger. Strange magnetism in the nucleon. *Phys. Lett.*, B437:184–190, October 1998 (hep-ph/9806226).

[90] Thomas R. Hemmert, Bastian Kubis, and Ulf-G. Meißner. Strange chiral nucleon form factors. *Phys. Rev. C*, 60(4):045501, August October 1999 (nucl-th/9904076).

[91] H.-W. Hammer, S. J. Puglia, M. J. Ramsey-Musolf, and Shi-Lin Zhu. What do we know about the strange magnetic radius? *Phys. Lett.*, B562:208–214, June 2003 (hep-ph/0206301).

[92] G. Höhler *et al.* Analysis of Electromagnetic Nucleon Form Factors. *Nucl. Phys.*, B114:505, November 8, 1976.

[93] H. Genz and G. Höhler. Validity of SU(3) and Violation of Zweig's Rule for Vector Meson-Nucleon Coupling Constants. *Phys. Lett.*, B61:389–392, April 1976.

[94] R. L. Jaffe. Stranger Than Fiction: The Strangeness Radius and Magnetic Moment of the Nucleon. *Phys. Lett.*, B229:275–279, October 1989.

[95] P. Mergell, Ulf G. Meißner, and D. Drechsel. Dispersion-theoretical analysis of the nucleon electromagnetic form factors. *Nucl. Phys.*, A596:367–396, January 1996 (hep-ph/9506375).

[96] H.-W. Hammer, Ulf-G. Meißner, and D. Drechsel. The strangeness radius and magnetic moment of the nucleon revisited. *Phys. Lett.*, B367:323–328, January 1996 (hep-ph/9509393).

[97] Hilmar Forkel. Dispersion analysis of the strange vector form factors of the nucleon. *Phys. Rev. C*, 56(1):510–525, July 1997 (hep-ph/9607452).

[98] Hilmar Forkel, Marina Nielsen, Xue-min Jin, and Thomas D. Cohen. Stranger in the light: The strange vector form-factors of the nucleon. *Phys. Rev. C*, 50(6):3108–3121, December 1994 (hep-ph/9408326).

[99] L. Hannelius, D. O. Riska, and L. Ya. Glozman. The strangeness magnetic moment of the proton in the chiral quark model. *Nucl. Phys.*, A665:353–364, February 2000 (hep-ph/9908393).

[100] J. F. Donoghue and B. R. Holstein. Improved treatment of loop diagrams in SU(3) baryon chiral perturbation theory. *Phys. Lett.*, B436:331–338, September 24, 1998.

[101] John F. Donoghue, Barry R. Holstein, and Buḡra Borasoy. SU(3) baryon chiral perturbation theory and long distance regularization. *Phys. Rev.*, D59:036002, February 1999 (hep-ph/9804281).

[102] M. J. Musolf and M. Burkardt. Stranger still: Kaon loops and strange quark matrix elements of the nucleon. *Z. Phys.*, C61:433–440, 1994 (hep-ph/9301229).

[103] W. Koepf, E. M. Henley, and S. J. Pollock. Strangeness matrix elements in the nucleon. *Phys. Lett.*, B288:11–17, August 1992.

[104] A. Chodos, R. L. Jaffe, K. Johnson, Charles B. Thorn, and V. F. Weisskopf. A new extended model of hadrons. *Phys. Rev.*, D9:3471–3495, June 1974.

[105] S. Théberge, Anthony W. Thomas, and Gerald A. Miller. Pionic corrections to the MIT bag model: The (3,3) resonance. *Phys. Rev.*, D22:2838, December 1980 [Erratum-ibid. D 23, 2106 (1981)].

[106] Anthony W. Thomas, S. Théberge, and Gerald A. Miller. The cloudy bag model of the nucleon. *Phys. Rev.*, D24:216, July 1981.

[107] Thomas D. Cohen, Hilmar Forkel, and Marina Nielsen. Just how strange? Loops, poles and the strangeness radius of the nucleon. *Phys. Lett.*, B316:1–6, October 1993 (hep-ph/9308374).

[108] Ulf-G. Meißner, V. Mull, J. Speth, and J. W. van Orden. Strange vector currents and the OZI-rule. *Phys. Lett.*, B408:381–386, September 1997 (hep-ph/9701296).

[109] M. Malheiro and W. Melnitchouk. Nucleon strange magnetic moment and relativistic covariance. *Phys. Rev.*, C56:R2373–R2377, November 1997 (hep-ph/9709307).

[110] Paul Geiger and Nathan Isgur. Strange hadronic loops of the proton: A quark model calculation. *Phys. Rev. D*, 55(1):299–310, January 1997 (hep-ph/9610445).

[111] L. L. Barz *et al.* K^* mesons and nucleon strangeness. *Nucl. Phys.*, A640:259–280, September 1998 (hep-ph/9803221).

[112] T. H. R. Skyrme. A Nonlinear Field Theory. *Proc. Roy. Soc. Lond.*, A260:127–138, 1961.

[113] Edward Witten. Baryons in the 1/N Expansion. *Nucl. Phys.*, B160:57–115, November 1979.

[114] Edward Witten. Current Algebra, Baryons, and Quark Confinement. *Nucl. Phys.*, B223:433–444, August 1983.

[115] Gregory S. Adkins, Chiara R. Nappi, and Edward Witten. Static Properties of Nucleons in the Skyrme Model. *Nucl. Phys.*, B228:552–566, December 1983.

[116] Curtis G. Callan and Igor R. Klebanov. Bound-State Approach to Strangeness in the Skyrme Model. *Nucl. Phys.*, B262:365–382, December 1985.

[117] M. Chemtob. Skyrme Model of Baryon Octet and Decuplet. *Nucl. Phys.*, B256:600–608, 1985.

[118] H. Yabu and K. Andō. A New Approach to the SU(3) Skyrme Model: Exact treatment of the SU(3) symmetry breaking. *Nucl. Phys.*, B301:601–626, May 1988.

[119] N. W. Park, J. Schechter, and H. Weigel. Electromagnetic, axial-vector and strange currents in the Skyrme model: Effects of symmetry breaking. *Phys. Rev. D*, 43(3):869–884, February 1991.

[120] N. W. Park and H. Weigel. Static properties of baryons from an SU(3) pseudoscalar vector meson lagrangian. *Nucl. Phys.*, A541:453–491, May 1992.

[121] Antonio Silva, Hyun-Chul Kim, and Klaus Goeke. Strange form factors in the context of SAMPLE, HAPPEX, and A4 experiments. *Phys. Rev.*, D65:014016, January 2002 (hep-ph/0107185) [Erratum-ibid. D 66, 039902 (2002)].

[122] H. Weigel, A. Abada, R. Alkofer, and H. Reinhardt. On the strange vector form-factors of the nucleon in the NJL soliton model. *Phys. Lett.*, B353:20–26, June 1995 (hep-ph/9503241).

[123] L. Hannelius and D. O. Riska. Strangeness form factors of the proton in the chiral quark model. *Phys. Rev. C*, 62(4):045204, October 2000 (hep-ph/0001325).

[124] Valery E. Lyubovitskij, P. Wang, T. Gutsche, and Amand Faessler. Strange nucleon form factors in the perturbative chiral quark model. *Phys. Rev. C*, 66(5):055204, November 2002 (hep-ph/0207225).

[125] Yoichiro Nambu and G. Jona-Lasinio. Dynamical Model of Elementary Particles Based on an Analogy with Superconductivity. II. *Phys. Rev.*, 124:246–254, October 1961.

[126] S. Klimt, M. Lutz, U. Vogl, and W. Weise. Generalized SU(3) Nambu-Jona-Lasinio model: (I). Mesonic Modes. *Nucl. Phys.*, A516:429–468, October 1990.

[127] U. Vogl, M. Lutz, S. Klimt, and W. Weise. Generalized SU(3) Nambu-Jona-Lasinio Model: (II). From Current to Constituent Quarks. *Nucl. Phys.*, A516:469–495, October 1990.

[128] M. J. Ramsey-Musolf and H. W. Hammer. KN Scattering and the Nucleon Strangeness Radius. *Phys. Rev. lett.*, 80:2539–2542, March 1998 (hep-ph/9705409) [Erratum-ibid. Phys. Rev. Lett. 85, 224 (2000)].

[129] H. W. Hammer and M. J. Ramsey-Musolf. Spectral content of isoscalar nucleon form factors. *Phys. Rev. C*, 60(4):045205, Sept. October 1999 (hep-ph/9812261) [Erratum-ibid. C 62, 049903 (2000)].

[130] M. J. Musolf, H. W. Hammer, and D. Drechsel. Nucleon strangeness and unitarity. *Phys. Rev.*, D55:2741–2755, March 1997 (hep-ph/9610402) [Erratum-ibid. D 62, 079901 (2000)].

[131] H. W. Hammer and M. J. Ramsey-Musolf. $K\bar{K}$ continuum and isoscalar nucleon form factors. *Phys. Rev. C*, 60(4):045204, October 1999 (hep-ph/9903367) [Erratum-ibid. C 62, 049902 (2000)].

[132] H. W. Hammer and M. J. Ramsey-Musolf. Nucleon vector strangeness form factors: Multi-pion continuum and the OZI rule. *Phys. Lett.*, B416:5–15, January 1998 (hep-ph/9703406).

[133] F. Gross. *Relativistic Quantum Mechanics and Field Theory.* John Wiley & Sons, Inc., New York, 1993.

[134] J. D. Walecka. *Theoretical Nuclear and Subnuclear Physics.* Oxford University Press, New York, 1995.

[135] S. J. Dong, K. F. Liu, and Anthony G. Williams. Lattice calculation of the strangeness magnetic moment of the nucleon. *Phys. Rev. D*, 58(7):074504, October 1998 (hep-ph/9712483).

[136] Nilmani Mathur and Shao-Jing Dong. Strange Magnetic Moment of the Nucleon from Lattice QCD. *Nucl. Phys. Proc. Suppl.*, 94:311–314, March 2001 (hep-lat/0011015).

[137] R. Lewis, W. Wilcox, and R. M. Woloshyn. Nucleon's strange electromagnetic and scalar matrix elements. *Phys. Rev.*, D67:013003, January 2003 (hep-ph/0210064).

[138] D. B. Leinweber *et al.* Precise Determination of the Strangeness Magnetic Moment of the Nucleon. *Phys. Rev. Lett.*, 94:212001, June 2005 (hep-lat/0406002).

[139] Carl E. Carlson and Marc Vanderhaeghen. Two-Photon Physics in Hadronic Processes. arXiv:hep-ph/0701272, 2007.

[140] B. Pasquini and M. Vanderhaeghen. Resonance estimates for single spin asymmetries in elastic electron-nucleon scattering. *Phys. Rev.*, C70:045206, October 2004 (hep-ph/0405303).

[141] Andrei Afanasev, Igor Akushevich, and N. P. Merenkov. Nucleon Compton Scattering with Two Space-Like Photons. arXiv:hep-ph/0208260, 2002.

[142] J. Arrington. Evidence for two-photon exchange contributions in electron-proton and positron-proton elastic scattering. *Phys. Rev.*, C69:032201(R), March 2004 (nucl-ex/0311019).

[143] J. Arrington. Extraction of two-photon contributions to the proton form factors. *Phys. Rev.*, C71:015202, January 2005 (hep-ph/0408261).

[144] A. De Rujula, J. M. Kaplan, and E. De Rafael. Optimal Positivity Bounds to the Up-Down Asymmetry in Elastic Electron-Proton Scattering. *Nucl. Phys.*, B53:545–566, March 12, 1973.

[145] S. P. Wells *et al.* [SAMPLE Collaboration]. Measurement of the vector analyzing power in elastic electron-proton scattering as a probe of the double virtual Compton amplitude. *Phys. Rev.*, C63:064001, June 2001 (nucl-ex/0002010).

[146] M. L. Goldberger, Y. Nambu, and R. Oehme. Dispersion Relations for Nucleon-Nucleon Scattering. *Annals of Physics*, 2:226–282, 1957.

[147] M. Gorchtein, P. A. M. Guichon, and M. Vanderhaeghen. Beam normal spin asymmetry in elastic lepton-nucleon scattering. *Nucl. Phys.*, A741:234–248, September 2004 (hep-ph/0404206).

[148] Andrei V. Afanasev and N. P. Merenkov. Collinear Photon Exchange in the Beam Normal Polarization Asymmetry of Elastic Electron-Proton Scattering. *Phys. Lett.*, B599:48, October 2004 (erratum in hep-ph/0407167 v2).

[149] Mikhail Gorchtein. Dispersive contributions to e^+p/e^-p cross section ratio in forward regime. *Phys. Lett.*, B644:322–330, January 2007 (hep-ph/0610378).

[150] N. F. Mott. The polarisation of electrons by double scattering. *Proceedings of the Royal Society of London, Series A: Containing Papers of a Mathematical and Physical Character (1905-1934)*, 135(827):429–458, March 1, 1932. Many thanks to the Royal Society for directing me to their online preservation journal archives from 1665 to the present for this article - http://www.pubs.royalsoc.ac.uk/index.cfm?page=1373.

[151] N. F. Mott. The scattering of fast electrons by atomic nuclei. *Proceedings of the Royal Society of London, Series A: Containing Papers of a Mathematical and Physical Character (1905-1934)*, 124(794):425–442, June 4, 1929. Many thanks to the Royal Society for directing me to their online preservation journal archives from 1665 to the present for this article - http://www.pubs.royalsoc.ac.uk/index.cfm?page=1373.

[152] J. S. Price *et al.* 5-MeV Mott polarimeter development at Jefferson Lab. *Given at 7th International Workshop on Polarized Gas Targets and Polarized Beams, Urbana, IL*, August 18-22, 1997.

[153] L. Diaconescu and M. J. Ramsey-Musolf. The vector analyzing power in elastic electron-proton scattering. *Phys. Rev.*, C70:054003, November 2004 (nucl-th/0405044).

[154] Luca R. Diaconescu. *Applications of Effective Field Theory to Electron Scattering.* PhD thesis, California Institute of Technology, January 7, 2005.

[155] D. Drechsel, O. Hanstein, S. S. Kamalov, and L. Tiator. A unitary isobar model for pion photo- and electroproduction on the proton up to 1 GeV. *Nucl. Phys.*, A645:145–174, January 1999 (nucl-th/9807001).

[156] F. E. Maas *et al.* [A4 Collaboration]. Measurement of the Transverse Beam Spin Asymmetry in Elastic Electron-Proton Scattering and the Inelastic Contribution to the Imaginary Part of the Two-Photon Exchange Amplitude. *Phys. Rev. Lett.*, 94:082001, March 2005 (nucl-ex/0410013).

[157] L. Capozza [A4 Collaboration]. Transverse single spin asymmetry at the A4 experiment: Preliminary backward-scattering results. *The European Physical Journal A*, 32:497–499, June 2007 (PAVI06 Proceedings).

[158] Mikhail Gorchtein. Doubly virtual Compton scattering and the beam normal spin asymmetry. *Phys. Rev.*, C73:035213, March 2006 (hep-ph/0512106).

[159] Mikhail Gorchtein. Beam normal spin asymmetry in the quasireal Compton scattering approximation. *Phys. Rev.*, C73:055201, May 2006 (hep-ph/0512105).

[160] Andrei V. Afanasev and N. P. Merenkov. Large logarithms in the beam normal spin asymmetry of elastic electron-proton scattering. *Phys. Rev.*, D70:073002, October 2004 (hep-ph/0406127).

[161] L.J. Kaufman [HAPPEX Collaboration]. Transverse beam spin asymmetries measured from ^{4}He and hydrogen targets. *The European Physical Journal A*, 32:501–503, June 2007 (PAVI06 Proceedings).

[162] Y. C. Chen, A. Afanasev, S. J. Brodsky, C. E. Carlson, and M. Vanderhaeghen. Partonic Calculation of the Two-Photon Exchange Contribution to Elastic Electron-Proton Scattering at Large Momentum Transfer. *Phys. Rev. Lett.*, 93:122301, September 2004 (hep-ph/0403058).

[163] Andrei V. Afanasev, Stanley J. Brodsky, Carl E. Carlson, Yu-Chun Chen, and Marc Vanderhaeghen. Two-photon exchange contribution to elastic electron-nucleon scattering at large momentum transfer. *Phys. Rev.*, D72:013008, July 2005 (hep-ph/0502013).

[164] Lester L. DeRaad, Jr. and Yee Jack Ng. Electron electron scattering: Spectral forms for the invariant amplitudes to order e^4. *Phys. Rev.*, D10:683–693, July 1974.

[165] Lester L. DeRaad, Jr. and Yee Jack Ng. Electron-electron scattering. II. Helicity cross sections for positron-electron scattering. *Phys. Rev.*, D10:3440, November 1974.

[166] Lester L. DeRaad, Jr. and Yee Jack Ng. Electron-electron scattering. III. Helicity cross sections for electron-electron scattering. *Phys. Rev.*, D11:1586, March 1975.

[167] Lance J. Dixon and Marc Schreiber. Radiative corrections to the azimuthal asymmetry in transversely polarized Møller scattering. *Phys. Rev.*, D69:113001, June 2004 [Erratum-ibid. D 71, 059903 (2005)].

[168] P. L. Anthony *et al.* [SLAC E158 Collaboration]. Precision Measurement of the Weak Mixing Angle in Møller Scattering. *Phys. Rev. Lett.*, 95:081601, August 2005 (hep-ex/0504049).

[169] P. L. Anthony *et al.* [SLAC E158 Collaboration]. Observation of Parity Nonconservation in Møller Scattering. *Phys. Rev. Lett.*, 92:181602, May 2004 (hep-ex/0312035).

[170] C. Y. Prescott *et al.* Parity Non-Conservation in Inelastic Electron Scattering. *Phys. Lett.*, B77:347–352, August 1978.

[171] C. Y. Prescott *et al.* Further Measurements Of Parity Nonconservation In Inelastic Electron Scattering. *Phys. Lett.*, B84:524–528, July 1979.

[172] W. Heil et al. Improved limits on the weak, neutral, hadronic axial vector coupling constants from quasielastic scattering of polarized electrons. *Nucl. Phys.*, B327:1–31, 1989.

[173] P. A. Souder et al. Measurement of parity violation in the elastic scattering of polarized electrons from C-12. *Phys. Rev. Lett.*, 65:694–697, 1990.

[174] Damon T. Spayde. *Measurement of the Strange Magnetic Form Factor of the Proton Using Elastic Electron Scattering.* PhD thesis, University of Maryland, College Park, 2001.

[175] Bryon Alan Mueller. *Measurement of the Strange Quark Contribution to the Magnetic Moment of the Proton*. PhD thesis, California Institute of Technology, May 1997.

[176] D. T. Spayde *et al.*, SAMPLE Collaboration. Parity violation in elastic electron proton scattering and the proton's strange magnetic form-factor. *Phys. Rev. Lett.*, 84:1106–1109, 2000.

[177] R. Hasty *et al.*, SAMPLE Collaboration. Strange magnetism and the anapole structure of the proton. *Science*, 290:2117, 2000.

[178] D. T. Spayde *et al.* [SAMPLE Collaboration]. The strange quark contribution to the proton's magnetic moment. *Phys. Lett.*, B583:79–86, March 2004 (nucl-ex/0312016).

[179] T. M. Ito *et al.*, SAMPLE Collaboration. Parity-violating electron deuteron scattering and the proton's neutral weak axial vector form factor. *Phys. Rev. Lett.*, 92:102003, 2004.

[180] E. J. Beise, M. L. Pitt, and D. T. Spayde. The sample experiment and weak nucleon structure. *Prog. Part. Nucl. Phys.*, 54:289–350, 2005.

[181] K. A. Aniol *et al.*, HAPPEX Collaboration. Measurement of the neutral weak form factors of the proton. *Phys. Rev. Lett.*, 82:1096–1100, 1999.

[182] K. A. Aniol *et al.*, HAPPEX Collaboration. New measurement of parity violation in elastic electron proton scattering and implications for strange form factors. *Phys. Lett.*, B509:211–216, 2001.

[183] K. A. Aniol *et al.* [HAPPEX Collaboration]. Parity-violating electroweak asymmetry in $\vec{e}p$ scattering. *Phys. Rev.*, C69:065501, June 2004 (nucl-ex/0402004).

[184] K. A. Aniol *et al.* [HAPPEX Collaboration]. Constraints on the nucleon strange form factors at $Q^2 \sim 0.1$ GeV^2. *Phys. Lett.*, B635:275–279, April 2006 (nucl-ex/0506011).

[185] K. A. Aniol *et al.* [HAPPEX Collaboration]. Parity-Violating Electron Scattering from ^{4}He and the Strange Electric Form Factor of the Nucleon. *Phys. Rev. Lett.*, 96:022003, January 2006 (nucl-ex/0506010).

[186] A. Acha *et al.* [HAPPEX Collaboration]. Precision Measurements of the Nucleon Strange Form Factors at $Q^2 \sim 0.1$ GeV^2. *Phys. Rev. Lett.*, 98:032301, January 2007 (nucl-ex/0609002).

[187] F. E. Maas, A4 Collaboration. Parity violating electron scattering at the MAMI facility in Mainz: The strangeness contribution to the form-factors of the nucleon. *Eur. Phys. J.*, A17:339–343, 2003.

[188] F. E. Maas *et al.* [A4 Collaboration]. Measurement of Strange-Quark Contributions to the Nucleon's Form Factors at $Q^2 = 0.230$ (GeV/c)^2. *Phys. Rev. Lett.*, 93:022002, July 2004 (nucl-ex/0401019).

[189] F. E. Maas *et al.* [A4 Collaboration]. Evidence for Strange Quark Contributions to the Nucleon's Form Factors at $Q^2 = 0.108$ (GeV/c)^2. *Phys. Rev. Lett.*, 94:152001, April 2005 (nucl-ex/0412030).

[190] B. Glaser, A4 Collaboration. Rearrangement of the A4 Calorimeter for the Backward Angle Measurement. In *From Parity Violation to Hadronic Structure and more... (Part III)*. PAVI06, May 16-20, 2006.

[191] S. Baunack, A4 Collaboration. The Parity Violation A4 Experiment at Forward and Backward Angles. In *From Parity Violation to Hadronic Structure and more... (Part III)*. PAVI06, May 16-20, 2006.

[192] E. D. Cooper and C. J. Horowitz. Vector analyzing power in elastic electron-nucleus scattering. *Phys. Rev.*, C72:034602, September 2005 (nucl-th/0506034).

[193] A. V. Afanasev. Private communication.

[194] D. S. Armstrong *et al.* G0 NIM Paper. *Nucl. Instrum. Methods (in preparation)*.

[195] Mark Pitt. Helicity control requests from the G^0 experiment. Technical report, G^0 Collaboration, August 20, 2001.

[196] C. W. Leemann, D. R. Douglas, and G. A. Krafft. The Continuous Electron Beam Accelerator Facility: CEBAF at the Jefferson Laboratory. *Ann. Rev. Nucl. Part. Sci.*, 51:413–450, December 2001.

[197] Joseph M. Grames. *Measurement of a Weak Polarization Sensitivity to the Beam Orbit of the Cebaf Accelerator*. PhD thesis, University of Illinois at Urbana-Champaign, 2000.

[198] J. Grames et al. Status of the Jefferson Lab polarized beam physics program and preparations for upcoming parity experiments. *AIP Conf. Proc.*, 675:1047–1052, 2003. Prepared for Workshop on Polarized Electron Sources and Polarimeters (PESP 2002), Danvers, Massachusetts, 4-6 Sep 2002.

[199] M. Poelker et al. Polarized source performance and developments at Jefferson Lab. *AIP Conference Proceedings*, 570:943–948, June 1, 2001. Prepared for 14th International Spin Physics Symposium (SPIN 2000), Osaka, Japan, 16-21 Oct 2000.

[200] R. A. Mair et al. Anisotropies in strain and quantum efficiency of strained GaAs grown on GaAsP. *Phys. Lett.*, A212:231–236, 1996.

[201] D. H. Beck and M. L. Pitt. Beam optics for electron scattering parity-violation experiments. *Eur. Phys. J.*, A24S2:115–118, 2005.

[202] Yu-Chiu Chao et al. Achieving beam quality requirements for parity experiments at Jefferson Lab. *Proceedings of the 9th European Particle Accelerator Conference (EPAC 2004), Lucerne, Switzerland*, July 5–9, 2004. Presented at 9th European Particle Accelerator Conference (EPAC 2004), Lucerne, Switzerland, 5-9 Jul 2004.

[203] Paul King. Electronic logbook entry for the G^0 Collaboration, March 16, 2004. G0log entry 79358.

[204] V. Bargmann, Louis Michel, and V.L. Telegdi. Precession of the Polarization of Particles Moving in a Homogeneous Electromagnetic Field. *Physical Review Letters*, 2(10):435–436, May 15, 1959.

[205] John David Jackson. *Classical Electrodynamics*. John Wiley and Sons, Inc., New York, New York, third edition, 1999.

[206] D.A. Engwall, B.M. Dunham, L.S. Cardman, D.P. Huddle, and C.K. Sinclar. A spin manipulator for electron accelerators. *Nuclear Instruments and Methods in Physics Research*, A:409–420, 1993.

[207] Sarah K. Phillips, Dave Gaskell, Damon T. Spayde, and Tanja Horn. Møller Polarimetry in the G^0 Forward Angle Measurement. Technical Report G0-doc-614-v1, G^0 Collaboration, April 7, 2005.

[208] Matthias Loppacher. *Møller Polarimetry for CEBAF Hall C*. PhD thesis, Universität Basel, April 1996.

[209] M. Hauger *et al*. A high-precision polarimeter. *Nucl. Instrum. Meth.*, A462:382–392, April 2001 (nucl-ex/9910013).

[210] Dave Gaskell. Spin dance results - new wien angle setting. Electronic logbook entry for the G^0 Collaboration, February 10, 2004. G0log entry 76002.

[211] Dave Gaskell. Transverse polarization drift 2. Electronic logbook entry for the G^0 Collaboration, March 26, 2004. G0log entry 80432.

[212] Dave Gaskell. Moller leakage tests. Electronic logbook entry for the G^0 Collaboration, May 1, 2004. G0log entry 83734.

[213] G. Niculescu. Resonant Cavities Used as Beam Current Monitors. CEBAF Internal Report (unpublished), 1995.

[214] C. Armstrong. Beam Current Measurement in Hall C. CEBAF Internal Report (unpublished).

[215] David G. Meekins. *Coherent π^0 Photoproduction on the Deuteron*. PhD thesis, The College of William and Mary, 1998.

[216] K. B. Unser. The Parametric Current Transformer: A Beam Current Monitor Developed for LEP (CERN-SL-91-42-BI). *AIP Conf. Proc.*, 252:266–275, 1991.

[217] Walter Barry. A general analysis of thin wire pickups for high frequency beam position monitors. *Nucl. Instrum. Meth.*, A301:407–416, 1991.

[218] G. Krafft and A. Hofler. How the Linac Beam Position Monitors "Work". Technical Report CEBAF-TN-93-004, CEBAF Technical Note, 1993.

[219] R. Abbott, B. Bowling, and E. Woodworth. HARP User's Manual. Technical Report CEBAF-TN-92-050, CEBAF Technical Note, 1992.

[220] C. Yan et al. Superharp: A wire scanner with absolute position readout for beam energy measurement at CEBAF. *Nucl. Instrum. Meth.*, A365:261–267, 1995.

[221] R. Carlini, S. Page, and M. Pitt. Beam Parameter Specifications for the G^0 Experiment. Technical Report G0-doc-237-v1, G^0 Collaboration, December 17 2001.

[222] Sarah K. Phillips. Beam Halo in the G^0 Forward-Angle Measurement. Technical Report G0-doc-000-v1, G^0 Collaboration, Pending.

[223] Sarah K. Phillips. Beam Halo in the First G^0 Engineering Run. Technical Report G0-doc-434-v1, G^0 Collaboration, October 27, 2003.

[224] Jianglai Liu. *A Measurement of the Strange Quark Contributions to the Electromagnetic Form Factors of the Nucleon*. PhD thesis, University of Maryland, College Park, 2006 (G^0 Document Number G0-doc-650-v3).

[225] C. Yan, N. Sinkine, and R. Wojcik. Linear beam raster for cryogenic targets. *Nucl. Instrum. Meth.*, A539:1–15, 2005.

[226] C. Yan et al. Target raster system at CEBAF. *Nucl. Instrum. Meth.*, A365:46–48, 1995.

[227] S.D. Covrig, E.J. Beise, R. Carr, K.K. Gustafsson, L. Hannelius, M.-C. Herda, C.E. Jones, J. Liu, R.D. McKeown, R. Neveling, A.W. Rauf, and G. Smith. The Cryogenic Target for the G^0 Experiment at Jefferson Lab. *Nuclear Instruments and Methods in Physics Research*, A(551):218–235, May 13, 2005. nucl-ex/0502019.

[228] Silviu Doru Covrig. *A Measurement of Parity-Violating Asymmetries in the G^0 Experiment in Forward Mode*. PhD thesis, California Institute of Technology, Pasadena, California, 2004 (G^0 Document Number G0-doc-483-v1).

[229] EPICS: Experimental Physics and Industrial Control System. http://www.aps.anl.gov/epics/.

[230] Jeffery A. Secrest. *Measurement of Parity-Violating Electroweak Asymmetries in $\vec{e}p$ Scattering at* $0.1 < Q^2 < 0.4$ *(GeV/c)*^{2}. PhD thesis, The College of William and Mary, Williamsburg, Virginia, November 2005 (G^0 Document Number G0-doc-671-v1).

[231] J. Roche, J. Secrest, D. S. Armstrong, T. Averett, C. Cheze, M. Finn, K. Griffioen, S. K. Phillips, A. Powell, H. Breuer, and P. Roos. Tests of the G^0 North American Focal Plane Detectors. G^0 Internal Document G0-doc-310-v1, G^0 Collaboration, August 7, 2002.

[232] V. Popov. Design and study of photomultiplier pulse-shaping amplifier powered by the current flowing through a voltage divider. *Nucl. Instrum. Meth.*, A505:316–319, 2003.

[233] Guillaume Batigne. *Mesure du contenu étrange du nucléon : expérience G^0*. PhD thesis, Université Joseph Fourier, Laboratoire de Physique Subatomique et de Cosmologie, Grenoble, France, 5 Décembre 2003 (G^0 Document Number G0-doc-478-v1).

[234] G. Batigne, C. Furget, S. Kox, E. Liatard, E. Penel, G. Quéméner, J-S Réal, and R. Tieulent. Characterization of the signals delivered by the french FPD's: Cosmic and LED measurement of Octant #2. G^0 Internal Document G0-doc-192-v1, G^0 Collaboration, April 2001.

[235] G. Batigne, L. Bimbot, C. Furget, S. Kox, E. Liatard, G. Quéméner, J-S Réal, and R. Tieulent. Study of the second French Octant from measurements with cosmic muons. G^0 Internal Document G0-doc-202-v1, G^0 Collaboration, April 2001.

[236] G. Batigne, C. Furget, S. Kox, E. Liatard, G. Quéméner, J-S Réal, and R. Tieulent. Study of the third French Octant from measurements with cosmic muons. G^0 Internal Document G0-doc-211-v1, G^0 Collaboration, July 2001.

[237] G. Batigne, C. Furget, S. Kox, E. Liatard, G. Quéméner, J-S Réal, and R. Tieulent. Study of the fourth French Octant from measurements with cosmic muons. G^0 Internal Document G0-doc-230-v1, G^0 Collaboration, October 2001.

[238] David McKee, Stephen Pate, and Glen MacLachlan. G^0 GMS Technical Reference. Technical Report G0-doc-477-v1, G^0 Collaboration, October 18, 2004.

[239] D. Marchand *et al.* G^0 Electronics and Data Acquisition (Forward-Angle Measurements). *Nucl. Instrum. Methods (submitted)*, 2007 (nucl-ex/0703026).

[240] John Musson, Trent Allison, Arne Freyberger, Joachim Kuhn, and Brian Quinn. YO! A time-of-arrival receiver for removal of helicity-correlated beam effects. *Nuclear Instruments and Methods in Physics Research A*, 540:448–454, 2005.

[241] Brian Quinn. G^0 Forward Angle NA Electronics. Technical Report G0-doc-577-v1, G^0 Collaboration, January 2003.

[242] W. A. Watson, J. Chen, G. Heyes, E. Jastrzembski, and D. Quarrie. CODA: A scalable, distributed data acquisition system. *Prepared for 8th Real-Time Computer Applications in Nuclear, Particle and Plasma Physics (RT 93), Vancouver, British Columbia, Canada*, pages 296–303, 8-11 Jun 1993.

[243] G. Heyes et al. The CEBAF On-line Data Acquistion System. In *Proceedings of the CHEP conference*, pages 122–126, April 1994. See http://coda.jlab.org.

[244] Jeffrey A. Secrest. *Measurement of Parity-Violating Electroweak Asymmetries in $\vec{e}p$ Scattering at* $0.1 < Q^2 < 0.4$ *(GeV/c)*^{2}. PhD thesis, The College of William and Mary, Williamsburg, Virginia, 2006 (G^0 Document Number G0-doc-671-v1).

[245] D. S. Armstrong *et al.* [G0 Collaboration]. Strange Quark Contributions to Parity-Violating Asymmetries in the Forward G0 Electron-Proton Scattering Experiment. *Phys. Rev. Lett.*, 95:092001, August 2005 (nucl-ex/0506021).

[246] W. R. Leo. *Techniques for Nuclear and Particle Physics Experiments: A How-to Approach.* Springer-Verlag, New York-Berlin-Heidelberg, second edition, 1994.

[247] Damon T. Spayde. Beam polarization. Personal webpage at Jefferson Lab, April 28, 2003. http://www.jlab.org/∼spayde/beam-polarization.html.

[248] Sarah K. Phillips. Transverse Beam Spin Asymmetries in the G^0 Forward-Angle Measurement. Technical Report G0-doc-674, G^0 Collaboration, October 11, 2006.

[249] Sarah K. Phillips. Finding the True Electron Beam Helicity for the G^0 Experiment Using the Hall C Møller Polarimeter. Technical Report G0-doc-616-v1, G^0 Collaboration, November 24, 2004.

[250] Kazutaka Nakahara. *Measurement of the Strange Quark Contribution to Proton Structure Through Parity Violating Electron-Proton Scattering.* PhD thesis, University of Illinois at Urbana-Champaign, 2006 (G^0 Document Number G0-doc-657-v1).

[251] Emmanuel Rollinde de Beaumont. G0-GEANT Manual. G^0 Internal Document G0-doc-101-v1, G^0 Collaboration, June 1999.

[252] Lars Hannelius. Beam Position Sensitivities from MC. G^0 Internal Document G0-doc-612-v1, G^0 Collaboration, 2004.

[253] Kazutaka Nakahara. Linear Regression. G^0 Internal Document G0-doc-556-v1, G^0 Collaboration, March 28, 2005.

[254] Jianglai Liu. G^0 Leakage Correction. G^0 Internal Document G0-doc-551-v1, G^0 Collaboration, September 8, 2005.

[255] P. King, S.P. Wells, and the G0 Collaboration. Measurement of the vector analyzing power in e-p scattering using the G^0 forward angle apparatus. *Proposal to PAC*, December 2003 (G0-doc-437-v1).

[256] S.P. Wells, P. King, and the G0 Collaboration. Measuring the two-photon exchange amplitude with vector analyzing powers in elastic electron-proton scattering. *Proposal to PAC 26*, PR-04-103, July 12, 2004 (G0-doc-442-v1).

[257] P. M. King. Normal beam spin asymmetries during the G^0 forward angle measurement. *Presentation at the APS/DNP Fall 2004 Meeting, Chicago*, October 27–30, 2004 (G0-doc-521-v1).

[258] J. Grames. Study of the Vertical Component of the Beam Polarization for the 2004 HAPPEX-2 Run. Jefferson Lab Technical Note JLAB-TN-05-028, TJNAF, February 14, 2005.

[259] Jianglai Liu. A collection of the systematic uncertainty evaluation for G^0 forward-angle experiment. G^0 Internal Document G0-doc-550-v1, G^0 Collaboration, November 11, 2005.

[260] Benoît Guillon *et al.* Determination of the yield coming from the target walls through an experimental approach. G^0 Internal Document G0-doc-444-v1, G^0 Collaboration, May 2004.

[261] Lars Hannelius. G0 Geant Simulation Update. G^0 Internal Document G0-doc-458-v1, G^0 Collaboration, June 2004.

[262] J. W. Lightbody and J. S. O'Connell. Modeling single arm electron scattering and nucleon production from nuclei by GeV electrons. *Computers in Physics*, 2(3):57, 1988.

[263] M. Morlet, S. Ong, and J. Van de Wiele. Electroproduction generator in the forward scattering configuration of $G0$ experiment. G^0 Internal Document G0-doc-212-v1, G^0 Collaboration, July 2001.

[264] J. Arvieux, H. Guler, M. Morlet, and J. Van de Wiele. Simulations of the SOS data from December 1999. G^0 Internal Document G0-doc-374-v1, G^0 Collaboration, June 2003.

[265] D. S. Carman *et al.* [CLAS Collaboration]. First Measurement of Transferred Polarization in the exclusive $\vec{e}p \rightarrow e'K^+\vec{\Lambda}$ Reaction. *Phys. Rev. Lett.*, 90:131804, April 4, 2003 (hep-ex/0212014).

[266] Jianglai Liu. G^0 hyperon simulation. G^0 Internal Document G0-doc-552-v2, G^0 Collaboration, February 9, 2006.

[267] T. Mart, C. Bennhold, H. Haberzettl, and L. Tiator. KAON-MAID: An effective Lagrangian Model for Kaon Photo- and Electroproduction on the Nucleon. http://www.kph.uni-mainz.de/MAID/kaon/kaonmaid.html, version 2002.

[268] M. Q. Tran *et al.* [SAPHIR Collaboration]. Measurement of $\gamma p \to K^+\Lambda$ and $\gamma p \to K^+\Sigma^0$ at photon energies up to 2 GeV. *Phys. Lett.*, B445:20–26, December 31, 1998.

[269] R. Lawall et al. Measurement of the reaction $\gamma p \to K^0\Sigma^+$ at photon energies up to 2.6 GeV. *Eur. Phys. J.*, A24:275–286, May 2005 (nucl-ex/0504014).

[270] Benoît Guillon. *Contribution du quark étrange à la structure électromagnétique du nucléon : Les premiers résultats de l'expérience G^0*. PhD thesis, Université Joseph Fourier, Laboratoire de Physique Subatomique et de Cosmologie, Grenoble, France, 4 Octobre 2005 (G0 Document Number G0-doc-619-v1).

[271] P. R. Bevington and D. K. Robinson. *Data Reduction and Error Analysis for the Physical Sciences*. McGraw-Hill, Boston, 1992.

[272] Jacques Arvieux, Hayko Guler, Marcel Morlet, Silvia Niccolai, Saro Ong, and Jacques Van de Wiele. Calculation of the electromagnetic radiative corrections for G^0. G^0 Internal Document G0-doc-608-v1, G^0 Collaboration, June 9, 2005.

[273] Hayko Guler. *Contribution à l'expérience G^0 de violation de parité : calcul et simulation des corrections radiatives et étude du bruit de fond*. PhD thesis, Université Paris XI Orsay, Institut de Physique Nucléaire d'Orsay, France, Décembre 17, 2003 (G^0 Document Number G0-doc-438-v1).

[274] Yung-Su Tsai. Pair production and bremsstrahlung of charged leptons. *Rev. Mod. Phys.*, 46:815–851, October 1974 [Erratum-ibid. 49, 421–423 (April 1977)].

[275] Gilles Quéméner. Q^2 Determination in the G^0 Experiment. G^0 Internal Document G0-doc-548-v1, G^0 Collaboration, January 2005.

[276] Serge Kox. Q^2 Determination: Status Report. G^0 Internal Document G0-doc-543-v1, G^0 Collaboration, A Presentation at the January 2005 G0 Collaboration Meeting, January 2005.

[277] G. Batigne, C. Furget, S. Kox, F. Merchez, and J-S Réal. Q^2 Determination in the first phase of the G0 experiment. G^0 Internal Document G0-doc-330-v1, G^0 Collaboration, February 13, 2003.

[278] D. S. Armstrong *et al.* [G0 Collaboration]. Transverse Beam Spin Asymmetries in Forward-Angle Elastic Electron-Proton Scattering. *Phys. Rev. Lett.*, 99:092301, August 2007 (arXiv:0705.1525 [nucl-ex]).

[279] J. J. Kelly. Simple parametrization of nucleon form factors. *Phys. Rev.*, C70:068202, December 2004.

[280] Véronique Bernard, Latifa Elouadrhiri, and Ulf.-G. Meißner. Axial structure of the nucleon. *J. Phys.*, G28:R1–R35, January 2002 (hep-ph/0107088).

[281] Elliot Leader, Aleksander V. Sidorov, and Dimiter B. Stamenov. Role of higher twist in polarized deep inelastic scattering. *Phys. Rev.*, D67:074017, April 2003 (hep-ph/0212085).

[282] J. Friedrich and Th. Walcher. A coherent interpretation of the form factors of the nucleon in terms of a pion cloud and constituent quarks. *Eur. Phys. J.*, A17:607–623, August 2003 (hep-ph/0303054).

[283] J. Arrington. Implications of the discrepancy between proton form factor measurements. *Phys. Rev.*, C69:022201(R), February 2004 (nucl-ex/0309011).

[284] Stephanie L. Bailey. *Parity Violation in Elastic Electron Scattering: A First Measurement of the Parity-Violating Asymmetry at $Q^2 = 0.631$ (GeV/c)^2 at Backward Angle*. PhD thesis, The College of William and Mary, Williamsburg, Virginia, 2007.

[285] F. E. Maas, spokesperson. PVA4 Backangle Measurement. *DFG proposal SFB 443:H7*, 2005?

[286] K. D. Paschke and P. A. Souder, spokespersons. HAPPEX III. *JLab Experiment E05-109*.

[287] S. P. Wells and N. Simicevic, spokespersons. Measurement of the Parity-Violating Asymmetry in the $N \to \Delta$ Transition. *JLab Experiment E04-101*.

[288] "A Measurement of Two-Photon Exchange in Unpolarized Elastic Electron-Proton Scattering". J. Arrington, spokesperson. *JLab Experiment E-05-017*, December 6, 2004.

[289] "Target Normal Single-Spin Asymmetry in Inclusive DIS $n^{\uparrow}(e, e')$ with a Polarized ^{3}He Target". X. Jiang, spokesperson. *JLab PAC31 Experimental Proposal PR-07-013*, January 30, 2007.

[290] "Measurement of the Target Single-Spin Asymmetry in Quasi-Elastic $^3\mathrm{He}^{\uparrow}(e, e')$". T. Averett, spokesperson (E05-015). *JLab PAC27 Experimental Proposal PR-05-015*, January 12, 2005.

[291] "Beyond the Born Approximation: A Precise Comparison of $\mathrm{e}^+\mathrm{p}$ and $\mathrm{e}^-\mathrm{p}$ Elastic Scattering in CLAS". A. V. Afanasev, spokesperson (E07-005). *JLab PAC31 Experimental Proposal PR-07-005*, December 11, 2006 (former experiment number E-04-116).

[292] "Measurement of the Two-Photon Exchange Contribution in *ep* Elastic Scattering Using Recoil Polarization". R. Gilman, spokesperson (E04-019). *JLab PAC25 Experimental Proposal PR-04-019*, December 3, 2003.

[293] "The Q^p_{Weak} Experiment: A Search for New Physics at the TeV Scale via a Measurement of the Proton's Weak Charge", R. Carlini, spokesperson. Q_{Weak} Collaboration. *JLab Experiment E02-020 (or E-05-008?)*, December 6, 2004 (http://www.jlab.org/Qweak/).

[294] "Pre-Conceptual Design Report (pCDR) for The Science and Experimental Equipment for The 12 GeV Upgrade of CEBAF". Jefferson Lab. Report to the DOE Office of Science, June 11, 2004 (unpublished).

[295] "Conceptual Design Report: Hall C 12 GeV/c Upgrade". Hall C Collaboration, Jefferson Lab. November 27, 2002 (unpublished).

[296] K. Hafidi and R. J. Holt and P. E. Reimer and P. Bosted and R. Ent. "Search for New Physics Using Parity Violation in DIS". Hall C Collaboration, Jefferson Lab, June 27, 2002 (unpublished).

[297] "Hall A 12 GeV Upgrade Pre-Conceptual Design Report". Hall A Collaboration, Jefferson Lab. March 28, 2005 (unpublished).

[298] A. Kurylov, M. J. Ramsey-Musolf, and S. Su. Probing supersymmetry with parity-violating electron scattering. *Phys. Rev.*, D68:035008, August 2003 (hep-ph/0303026).

[299] A. Kurylov, M. J. Ramsey-Musolf, and S. Su. Parity-Violating Electron Scattering as a Probe of Supersymmetry. *hep-ph/0205183*, May 2002.